The Analysis and Imaging of Lipids from Complex Samples by Matrix-Assisted Laser Desorption/Ionisation Mass Spectrometry

by

Claire Louise Carter

A thesis submitted to the University of Birmingham for the degree of

Doctor of Philosophy

School of Chemistry
University of Birmingham
Edgbaston
Birmingham
B15 2TT
September 2011

Abstract

Matrix assisted laser desorption/ionisation mass spectrometry (MALDI-MS) is a relatively new technique for imaging lipids directly in tissue, with useful applications in disease state profiling, bacterial typing and forensics. This thesis describes optimisation and evaluation of sample preparation procedures for MALDI-MS and MS imaging of lipids in complex samples.

Direct analysis of fresh samples is shown to result in higher ion counts than analysis of desiccated tissues but thickness of tissue sections was shown to have a minimal effect on imaging results. Extracts of lipids from rat brain samples were used to optimise matrix selection for MALDI-MS of lipids. DHB was found to be the optimum matrix, in accordance with literature, for extract analysis; however, superior imaging results were obtained using αCHCA. An automated matrix deposition robot is compared to a manual airspray method. The robotic method demonstrated enhanced sensitivity, superior image resolution and reduced variability between different sample plates compared to traditional manual methods. Optimised methods were applied to analysis of formalin fixed tissue. Successful imaging of phospholipids in fixed samples is demonstrated for the first time. Lipids in formalin fixed samples were found to be predominantly detected as sodium adducts (due to high levels of sodium in the buffered formalin). This was exploited to offer enhanced structural information afforded by collision induced dissociation (CID) of sodium rather than potassium adducts, which is well reported to increase the number of useful product ions detected.

Methods for analysis and imaging of non-mammalian lipids by MALDI-MS were considered. Members of the *Mycobacterium tuberculosis* complex (MTBC) are important human pathogens. The cell wall of mycobacteria contains a number of lipids, which contribute largely to the virulence of pathogenic species. Preliminary research showed relatively poor sensitivity for these complex lipids but improved results were obtained by direct analysis of TLC plates. A binary matrix solvent system was developed offering considerably improved sensitivity. Successful detection of numerous lipids species involved in virulence, along with several previously unreported molecules is presented.

Declaration

I hereby declare that the work presented in this thesis is entirely my own, except where indicated by specific reference in the text, this includes samples that where provided externally. I also declare that this thesis has not been submitted for a degree at any other university.

Work presented in Chapter 4 of this thesis has been published in the following:

Carter C; McLeod CM; Bunch J. Imaging of Phospholipids in Formalin Fixed Rat Brain Sections by Matrix Assisted Laser Desorption/Ionization Mass Spectrometry. *Journal of the American Society for Mass Spectrometry*, 2011. **22**(11): p. 1991-1998.

Fonville JM; Carter C; Cloarec O; Nicholson JK; Lindon JC; Bunch J; Holmes E. Robust Data Processing and Normalization Strategy for MALDI Mass Spectrometric Imaging. *Analytical Chemistry*, 2012. **84**(3): p.1310-1319.

This thesis is dedicated to Emma Bliss and Sue Harris, whose guidance and influence put me on the path to where I am today.

Acknowledgements

First and foremost I offer my sincerest gratitude to my supervisor, Dr Josephine Bunch, for her support and guidance over the years, without you this thesis would not have been possible. You work so hard and care so much; you truly are an inspiration.

I am indebted to Covance Laboratories Ltd, AstraZeneca, and the Medical Schools at the University of Sheffield and the University of Birmingham, for a constant supply of samples and solutions. I would like to thank AppliedBiosystems for loan of the instrument, Alain Creissen from HTX Technologies for loan of the TM sprayer and EPSRC/RSC for funding.

I wish to thank Professor Cameron McLeod and my old group at the Centre for Analytical Sciences, University of Sheffield, for their support and games of corridor golf. I would like to thank my friends and colleagues at the University of Sheffield, particularly the residents of E81 and members of the No Balls football team; you have made life fun and interesting over the years. Special thanks to Zoe Bellamy for answering every chemistry question I have, for amusing stories and sharing a love of all food unhealthy. Huge thanks to Ruth Davidson, Claire Hurley, Jo Cook, Lindsay Hewison and Jenny Louth, for nearly doing it and 'I have never'.

I would like to express my gratitude to everyone at the School of Chemistry, University of Birmingham, for helping my transfer be a swift and pain-free one. Thanks go to my group, Sarah Turker, Rian Griffiths, Andrew Palmer and Rory Stevens. Particular thanks to Andrew Palmer and Rory Stevens for their last minute help and input, and for their constant mockery, which continues to amuse me. Thanks to Laura Rowley for her help with my list of tables and figures. Special thanks and sincerest of gratitude to Antoine (Adonis) Vallatos, you made my move to Birmingham easy, you are an amazing person, thank you for all the interesting discussions and for keeping me grounded. I wish to thank Myrto Arapinis and Ornella Smila-Castro for your directness and advice, it is needed and appreciated. An additional thanks to Ornella Smila-Castro for reminding me no matter how bad my punctuality is; there is always someone worse.

Away from academia and a science setting I would like to thank the following people for keeping me sane, letting me moan endlessly when needed and shutting me up when it is not. I would like to thank all of the Friday's girls, Kate Wallis, Jessica Jenkins, Charlotte Rae, Hayley Jennings, Carla Schramm, Helen Glynn and Claire Brooke, for fun shifts and all round good times. Special thanks to Roxy Dunbar-Stuart and Scott Frankham, we dance and laugh a lot. I would like to thank Alina Zhubrina for so many amusing emails that always brighten up my day; you are possibly the funniest person I know. Thank you, Tiffany Porta, for introducing me to snowboarding, allowing me to nearly kill myself on a mountain, and for the hilarious emails in broken English, I promise to learn French one day.

I owe my deepest gratitude to my extended family, Karen Hodgson, Scarlett 'now we know' Drury, Alice Gledhill, Flower Pot, Claire Daniels, Linda 'ginger' Hennessy, Maria Rudden and Laura Barrett, so many wonderful memories. To thank you all properly would take more space than I have and possibly bore the reader, so I will simply say this, I love you all dearly.

Last but not least, I would like to thank my parents for their continued support, for trying to understand what I do, and for finally knowing the difference between PhD and M.D.

Table of Contents

List of Figures

which is at *m/z* 1530 and represents the major homologue of PGL. The cluster of peaks seen at the higher mass range *m/z* 1677-1756 are believed to be cell envelope associated lipids with a similar structure, but are yet to be identified.

List of Tables

List of Abbreviations

The following table lists the abbreviations and acronyms used throughout this thesis, along with the page number in which each one is first used/defined.

Abbreviations	Meaning	Page
αCHCA	α-cyano-4-hydroxycinnamic acid	4
AA	arachidonic acid	37
CID	collision induced dissociation	34
DCM	dichloromethane	167
DHA	decosahexaenoic acid	37
DHB	2,5-dihydroxybenzoic acid	4
EA	ethyl acetate	167
ESI	electrospray ionisation	25
FA	fatty acid	26
FF	formalin fixed	113
FFPE	formalin fixed paraffin embedded	36
GC	gas chromatography	25
GPL	glycerophospholipid	25
HPLC	high performance liquid chromatography	25
IHC	immunohistochemistry	23
IPA	2-propanol	167
IR	infrared	1
MA	mycolic acid	43
MALDI	matrix-assisted laser desorption/ionisation	1
MAME	mycolic acid methyl ester	46
M. bovis	*Mycobacterium bovis*	137
M. bovis BGC	*Mycobacterium bovis* Bacillus Calmette-Guérin	137
M. tb	*Mycobacterium tuberculosis*	42

MS	mass spectrometry	12
MSI	mass spectrometry imaging	20
MS/MS	tandem mass spectrometry	12
m/z	mass-to-charge ratio	1
N_2	nitrogen	7
NBF	neutral buffered formalin	115
Nd:YAG	neodymium: yttrium-aluminum garnet	7
NL	neutral loss	128
OCT	optimal cutting temperature	36
PA	phosphatidic acid	27
PC	phosphatidylcholine	27
PCA	principal component analysis	37
PDIM	phthiocerol dimycocerosate	44
PE	phosphatidylethanolamine	27
PG	phosphatidylglycerol	27
PGL	phenoglycolipid	44
PI	phosphatidylinositol	27
PL	phospholipids	25
PS	phosphatidylserine	27
PUFA	polyunsaturated fatty acid	26
QqTOF	quadrupole time-of-flight	13
QqQ	triple quadrupole	20
SM	sphingomyelin	34
TDM	trehalose dimycolates	44
TFA	trifluoroacetic acid	54
THAP	2’, 4’, 6’-trihydroxyacetophenone monohydrate	4
THF	tetrahydrofuran	167
TLC	thin layer chromatography	25
TMM	trehalose monomycolates	44
TOF	time-of-flight	12
UV	ultraviolet	1

1. Introduction

1.1 Basic Principles of the MALDI Technique

MALDI (matrix-assisted laser desorption/ionisation) is a soft ionisation technique introduced by Karas and Hillenkamp[1] and Tanaka[2] simultaneously in the late 1980's. The method involves the use of a matrix compound, usually a low molecular weight organic acid, which is mixed in molar excess with the analyte/s of interest to facilitate in desorption/ionisation. For optimum results a molar ratio of 1:1000 to 1:10000 (analyte:matrix) are often recommended. The simplest and most commonly used sample preparation method is the dried droplet[1]. In this method the analyte and matrix are mixed in (ideally) the same solvent system and 0.25-1 µl of this mixture is deposited onto a stainless steel MALDI target plate. Upon evaporation of the solvent a co-crystallised structure of matrix/analyte is formed. This is then placed in the MALDI ion source and interrogated with a pulsed UV or IR laser. Energy transfer into the co-crystallised structure results in the desorption of both the matrix and analyte species from the surface, and the formation of the 'MALDI plume', which contains gas phase (de)protonated and cationised species of matrix and analyte. Charged species are extracted into the mass analyser using a known electrical field, traditionally a time-of-flight instrument, where they are separated and detected according to their mass-charge ratio (*m/z*). A simplified overview of the MALDI process is presented in figure 1.

Investigations presented in this thesis focused on UV-MALDI, thus only aspects related to this will be discussed in detail.

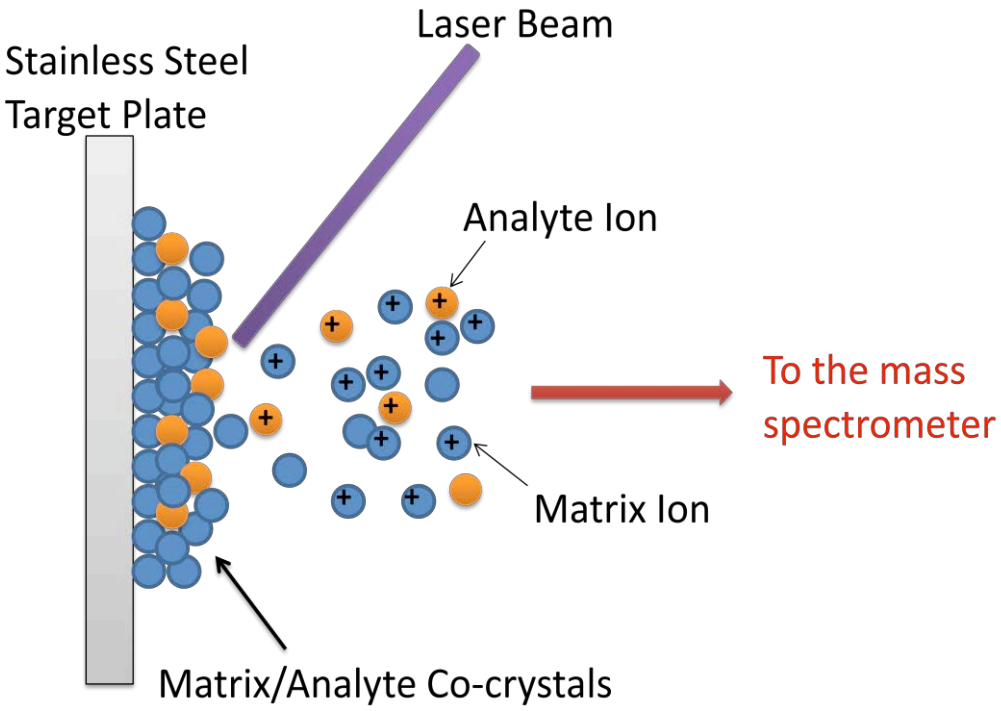

Figure 1. Simplified overview of the MALDI technique. Matrix:analyte crystal on the MALDI target plate are irradiated with a pulsed laser, this causes rapid heating of the matrix molecules, resulting in energy transfer into the analyte molecules and local sublimation/ablation of the solid material. Gas-phase protonation occurs in the expanding MALDI plume. Charged species are then extracted into the mass spectrometer.

1.1.2 MALDI Matrices

Since the MALDI technique was pioneered, numerous molecules have been tried and tested for their suitability as a MALDI matrix[3]. However, of the numbers tried and tested relatively few of these proved successful. Generally speaking, a MALDI matrix is usually a low molecular weight organic acid that has two important functions: (1) absorption of energy from the laser beam and transferring it into excitation energy, and (2) isolation of the analyte molecules from one another, thus holding analyte aggregation to a minimum. A successful MALDI matrix also requires the following characteristics:

- High molar absorptivity at the lasers wavelength
    - Removes the need to tune the laser to the wavelength of the analyte and protects the analyte from the laser energy, thereby minimising fragmentation.

- Solubility in the solvent compatible with the analyte.
    - For enhanced analyte incorporation into the matrix crystals

- Vacuum stability
    - To ensure the matrix does not sublime in the high pressure of the MALDI source

- The ability to promote ionisation by acting as a proton donor and receptor.

In recent years matrices have been grouped or categorised depending on the compounds/molecules they ionise. Table 1 lists the common MALDI matrices, their structure and applications.

Compound	Structure	Applications
α-cyano-4-hydroxycinnamic acid (αCHCA)	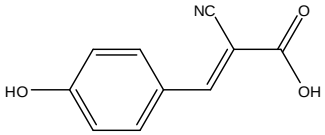	Peptides [4, 5] Oligonucleotides [6] Pharmaceuticals [7-9] Lipids [10]
2,5-dihydroxy benzoic acid (DHB)	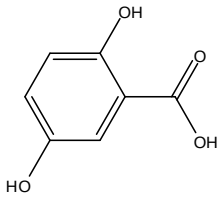	Peptides [11] Lipids [12-14] Carbohydrates [15-17] Oligonucleotides [18, 19]
3,5-dimethoxy-4-hydroxycinnamic acid (sinapinic acid, SA)	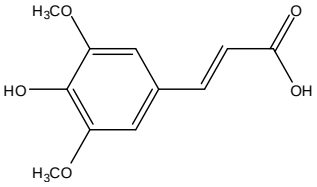	Proteins [20-22] Peptides [23]
Picolinic acid (PA)	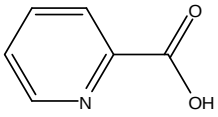	Oligonucleotides [24]
3-hydroxy-picolinic acid (3-HPA)	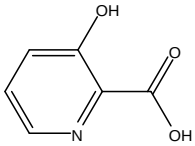	Oligonucleotides [18, 25-27]
2,4,5-trihydroxyacetophonone (THAP)	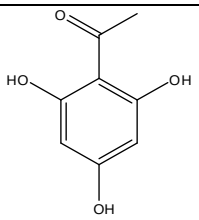	Oligonucleotides [28-30] Lipids [31, 32] Carbohydrates [15, 17, 33]

Table 1. Common MALDI matrices, their structure and applications.

There are a number of sample preparation methods that have been published since the original dried droplet method[1]; this is largely due to the poor spot-to-spot reproducibility associated with this method. As the solvent evaporates from the sample spot the formation of analyte-doped matrix crystals is inhomogeneous, resulting in crystals of varying shapes and sizes, that may either contain high concentrations of analyte molecules, or low to no analyte molecules. These effects also influence the quality of the mass spectra acquired, regarding mass resolution and signal intensity[34]. Techniques presented to improve crystal homogeneity and thus reproducibility include; the two-layer method[35], crushed crystal method[36], seeding method[37], fast evaporation method[38], electrospray deposition of the mixed matrix:analyte solution [39] and sublimation of the dried matrix material[40]. In the two-layer method the matrix is first deposited onto the target plate and allowed to crystallise, this is then followed by deposition of the sample onto the target plate[35]. The crushed crystal method involves crushing of formed matrix crystals to use as a 'template' for further matrix:analyte crystal growth[36]. The seeding method is similar to the two-layer method, a low concentration of matrix solution is first deposited onto the target and allowed to dry, a higher concentration of matrix solution mixed 1:1 (v/v) with the analyte is then applied on top of the first spot in the same manner as the dried droplet method[37]. The fast evaporation technique is again similar to the two-step method, with this method a high concentration of matrix is deposited onto the target plated in a highly volatile organic solvent, the rapid spread and evaporation of the solvent results in smaller crystals, the analyte solution is then applied after the matrix crystals have formed[38]. A pre-mixed solution of matrix:analyte is sprayed over the target surface for electrospray deposition, resulting in a thin layer of matrix:analyte crystals[39]. For sublimation the analyte is first applied to the target plate, followed by sublimation of the matrix solid[40]. All of the aforementioned methods have been shown to increase crystal homogeneity and reproducibility, or enhance detection sensitivity and spectral quality compared to the dried droplet method.

Sample preparation concerning matrix:analyte deposition onto the target plate is just one factor that can affect both the reproducibility and the quality of the mass spectrum acquired. The solvent composition of the matrix and sample (if different) solution can also greatly affect reproducibility and spectral quality; this is discussed further in chapter 5.

1.1.3. Lasers

MALDI-MS has successfully employed a variety of UV and IR lasers. These are shown in table 2. The energy deposition between the two wavelengths differs, with UV-MALDI; the matrix compound absorbs the lasers energy, whereas energy deposition in IR-MALDI occurs through excitation of the functional groups of the matrices. UV-MALDI is the most widely used of the two techniques; however, IR-MALDI does offer some advantages. Metastable fragmentation has been shown to be much lower in IR-MALDI compared to UV, thus would be a better choice for the analysis of very labile biomolecules. Spectral reproducibility is also superior in IR-MALDI compared to UV-MALDI this is mainly due to the type of matrices used for each. IR-MALDI utilises liquid matrices whereas UV-MALDI uses matrix:analyte co-crystals which can have a high degree of heterogeneity, however, liquid matrices have also been used in UV-MALDI analysis[41].

Ultraviolet Lasers (UV)	Frequency quadrupled Nd:YAG, 266 nm [1] Nitrogen (N_2), 337 nm [42, 43] Frequency tripled Nd:YAG, 355 nm [42-44] Nd:YVO_4, 355 nm [45]
Infrared Lasers (IR)	Er:YSGG, 2.79 µm [46] Er:YAG, 2.94 µm [47] CO_2, 10 µm [46] Wavelength-tuneable free-electron laser (FEL) [48]

Table 2. Lasers employed for both UV and IR MALDI.

Original MALDI experiments were carried out using quadrupled Nd:YAG lasers (266nm)[1]. These were soon replaced with the less expensive and smaller nitrogen lasers, which until relatively recently, were the most widely used and published. The introduction of solid state lasers, particularly the diode-pumped frequency-tripled Nd:YAG laser (355nm) offered an alternative to the nitrogen laser[44]. Nd:YAG lasers have two major advantages, they offer high-throughput or more sensitive analysis in MALDI imaging studies, due to achievable repetition rates of 1000 Hz, compared to the nitrogen laser which is limited to 50 Hz. The Nd:YAG laser also offers a longer life span compared to the nitrogen laser. The nitrogen laser has been shown to ionise certain molecules/sample preparation procedures more efficiently than the Nd:YAG laser. Holle *et al.* 2006 has published a good paper comparing the UV-lasers to date.

Laser fluence, beam or spot diameter, and the type and length of the optical fibres used have all been shown to greatly influence ion signals in MALDI-MS investigations[43, 49-51].

1.1.4 Desorption/Ionisation

The desorption/ionisation process in MALDI is incredibly complex and involves a magnitude of physical and chemical events, these processes have been the focus of many research groups[49, 50, 52-73]. To fully outline or discuss all the theoretical, molecular dynamic and experimental models presented to date, is out of the scope of this thesis, thus the main/key points for desorption/ionisation will be presented only.

1.1.4.1 Desorption

Upon irradiation by the laser, the phase transition of the bulk matrix-analyte material from solid to gas is rapid, the resulting MALDI plume expands out taking many microseconds to expand to a collision-free environment, if it does at all[54, 67]. The two main models for desorption are the thermal spike and the pressure pulse models, which have been discussed in an excellent review by Dreisewerd (2003)[49]. Desorption is affected by a number of sample parameters, matrix absorption, sample surface characteristics, and most importantly, laser fluence[49]. The laser fluence defines whether desorption occurs, or ablation of the bulk matrix:analyte material[73]. Desorption in the form of evaporation/sublimation, resulting in individual gas particles, is observed at low laser fluence. At low laser fluence phase transition is observed as a smooth evaporation of the bulk material from the surface. This process, according to literature, rarely happens in MALDI, thus desorption is not really a suitable word to describe this part of the technique[49, 67]. At higher laser fluencies, ablation of the bulk material from the surface occurs, causing what is known as ‘phase explosion’, this results in the ejection of gas particles and clusters from the upper layers of the matrix-analyte crystals. This reportedly is a more common occurrence during the MALDI processes, thus ablation is more

suitable to describe this part of the MALDI process[49, 54, 58, 67]. The laser fluence also impacts the velocity of the expanding plume, as demonstrated by Knochenmuss and Zhigilei (2009)[62].

1.1.4.2 Ionisation

Much research has focused on the specific mechanisms of the MALDI ionisation process, whilst numerous theories and models have been put forward, there are now two generally agreed and accepted models, the Two-Step model[60] and the Lucky Survivor model[71]. The two stages of the Two-Step model involve primary matrix ionisation, and secondary analyte ionisation. Secondary ionisation mechanisms have been widely accepted for some time as they are believed to follow basic condensed phase 'plume' kinetic and thermodynamic rules[60, 64, 72]. Primary ionisation is still an area of much discussion, the theory of the Lucky Survivor model developed from the idea of pre-formed analyte ions, this was a method originally presented to describe primary ionisation. The model of primary ionisation that has attracted the most interest and has increasingly become accepted is the two-photon energy 'pooling' model. Only these models will be discussed.

1.1.4.2.1 Primary Ionisation-The Energy Pooling Model

Many models/theories have been put forward to explain the mechanisms of primary ionisation; they have been discussed in an excellent review by Knochenmass[60], and will not be discussed here. The two-photon energy pooling model, is also known as the gas phase protonation model[58, 60-62, 65, 67]. The theory for this method is based on energy pooling between excited neighbouring matrix molecules within the solid state

crystals, this energy pooling is essential for the following reason. Typical MALDI lasers are operated at 337 and 355 nm for the N_2 and Nd:YAG lasers respectively, with laser photon energies of 3.6 eV for nitrogen and 3.3 eV for Nd:YAG[72]. These energies are lower than those required for the resonant two photon absorption of many MALDI matrices[72]. For photoionisation of matrix molecules to occur, 2-3 photons are necessary, thus interaction of the electronic states of two excited neighbouring molecules, the energy 'pooling' process, enables this. These excitations are not said to be fixed, they can 'wander' or 'hop' around, thus at typical laser fluencies, these excitations frequently collide and are ionised[60, 67]. It has also been postulated that matrix ionisation potentials (IPs) may also be lower in the solid phase of the crystals and/or thermal energy impact may contribute to the gas phase protonation model[67]. This model can demonstrate many of the features observed experimentally for MALDI-MS. One such feature is the matrix suppression and analyte suppression effects, the depletion of the primarily formed matrix ions by analyte ions, when present at high concentrations results in the presence of incredibly low or no matrix ions in the mass spectrum[60, 63, 67]. The opposite is seen for analyte suppression effects.

1.1.4.2.2 Secondary Ionisation

Secondary ionisation occurs in the expanding plume, the three key reactions for the production of analyte ions have been reported as[60, 72]:

Proton transfer:

- Positive ion mode – $mH^+ + A \text{ ----> } m + AH^+$
- Negative ion mode – $(m\text{-}H)^- + A \text{ ----> } m + (A\text{-}H)^-$

Cation transfer:

- Positive ion mode – $mNa^+ + A \text{ ----> } m + ANa^+$

Electron transfer:

- Positive ion mode – $m^+ + A \text{ ----> } m + A^+$
- Negative ion mode – $m^- + A \text{ ----> } m + A^-$

1.1.4.2.3 The Lucky Survivor Model

The 'lucky survivor' model is based on the theory of ejected clusters of preformed analyte ions from the solid state[55, 56, 71, 74]. Evidence for this was presented by Kruger *et al.* (2001), who observed pH indicator molecules retaining their colour, and thus charge state, within acidic, neutral and basic matrix crystals[69]. These results indicate proteins and other analyte molecules may also retain their charge state upon co-crystallisation. This model assumes, for instance, that peptides carrying multiple positive charge sites, are incorporated in a partially solvated form, and kept separate from their counterions, which would include matrix anions. Once in the expanding plume of clusters, these peptides are then believed to undergo neutralisation of all charges except the excess charge (only remaining) by proton transfer with counterions such as matrix/solvent molecules[55, 56, 69]. Hence the term 'lucky survivors', these singly charges species are thought to be the surviving molecules of neutralisation processes [74]. This model can explain the presence of only/mainly singly formed ions in MALDI mass spectra, in addition to this, this model can be applied to both IR and UV MALDI[56, 74].

A recent research article published by Jaskolla and Karas (2011)[74] provided evidence, for the first time, that verifies both ionisation models. The extent or ratio of which model

was predominant depended on a number of experimental factors, and analyte and matrix characteristics, including; laser fluence, matrix and analyte proton affinity, analyte composition and size, and the protonated-to-neutral analyte ratio embedded in the matrix crystal.

It would be naive to believe that for such a multitude of complex reactions, that these two models are solely responsible for ionisation in MALDI, but to date they are the best described and most experimentally researched models.

1.1.5 Mass Analysers

Mass analysers are used to separate and detect pre-formed ions according to their mass-to-charge (*m/z*) ratio. Generally speaking they fall into two distinct categories: 1) scanning or sector instruments that continuously analyse, include quadrupole and magnetic sector instruments, and 2) pulsed instruments which include time-of-flight, ion cyclotron resonance and ion trap analysers. Scanning instruments only allow for the separation and detection of one *m/z* value at a time, whereas pulsed instruments allow for the simultaneous measurement of pulsed ion packets, giving the *m/z* values of all ions transmitted[75-80].

MALDI was traditionally used as an ion source for time-of-flight (TOF) mass analysers. This was largely due to the nature of the ion source, producing pulsed ion packets which were suitably measured and analysed using a TOF analyser[77].

There has been a constant drive within the mass spectrometry community to produce instruments with greater resolving power, sensitivity and tandem MS capabilities (MS/MS)[81-84]. Mass resolution is seen as the dimensionless ratio of the mass peak

divided by its width, and is taken as the full width at half maximum intensity (FWHM). Tandem MS (MS/MS) instruments (two or more mass spectrometers placed together) have been developed to allow for structural information and identification of molecules of interest.

Work herein is carried out on a hybrid quadruple time-of-flight (QqTOF) mass spectrometer; therefore this will be discussed in detail. A QqTOF instrument combines the high accuracy and sensitivity of a TOF reflectron analyser, with the stability of the triple quadrupole mass analyser, and its ability to select a particular ion of interest for tandem analysis[85]. In order to fully understand the mechanisms of the QqTOF instrument, it will be necessary to first look at them individually.

1.1.5.1 Quadrupole Mass Analysers

First described by Paul and Steinwegen in 1953, quadrupole mass analysers consist of four cylindrical rods used to separate ions according to their trajectories in oscillating electric fields[86]. The mass analyser electrodes or rods must have exactly hyperbolic profiles to achieve maximum transmission and resolution of the oscillating ions about the positional axis[87]. Ions are transmitted according to these oscillations and depend entirely upon the radio frequency (r.f.) and direct current (d.c.) voltages that are applied to the electrodes. The electrodes of the analyser are connected in opposing pairs, with a differing r.f voltage being applied to each pair, combined with a superimposed d.c voltage.

The application of the potentials to the rods is as follows:

Equation 1. $\Phi_0 = +(U - V\cos\omega t)$ and $-(U - V\cos\omega t)$

Where Φ_0 represents the potential applied to the rods, ω is the angular frequency (in rad s^{-1}) = $2\pi v$, v is the frequency of r.f. field, U is the d.c. potential, and V is the 'zero to peak' amplitude of the r.f. voltage[88, 89].

Variation of the electrical parameters for a specific ion of interest allows its trajectory through to the mass detector. All the other ions with a different *m/z* value to the selected ion/ion of interest are deflected by the electrical field and collide with the electrodes, which in turn neutralises them [86-88]. Hence they follow an unstable trajectory and are never detected. This means that only one *m/z* value can be transmitted to the detector at a time, thus quadrupole analysers are often termed mass filters.

Under constant operating conditions ion trajectories in a quadrupole mass analyser are determined by the Mathieu equation:

Equation 2. $a = 8eU/m\omega^2 r_o^2$ $\quad q = 4eV/m\omega^2 r_o^2$

In which e is the charge of an electron, m is the *m/z* ratio of the ion, $V\cos(\omega t)$ is the applied r.f. voltage between the opposite rods, U is the d.c. voltage, and r_o is the radius of the quadrupole field, which remains constant for a given instrument[90].
Quadrupole mass analysers offer the advantage of fast scanning times along with high ion transmission efficiency. However, they are limited to unit mass resolution, are unable to carry out a full-scan across a wide mass range and have an upper mass limit of *m/z* 4000.

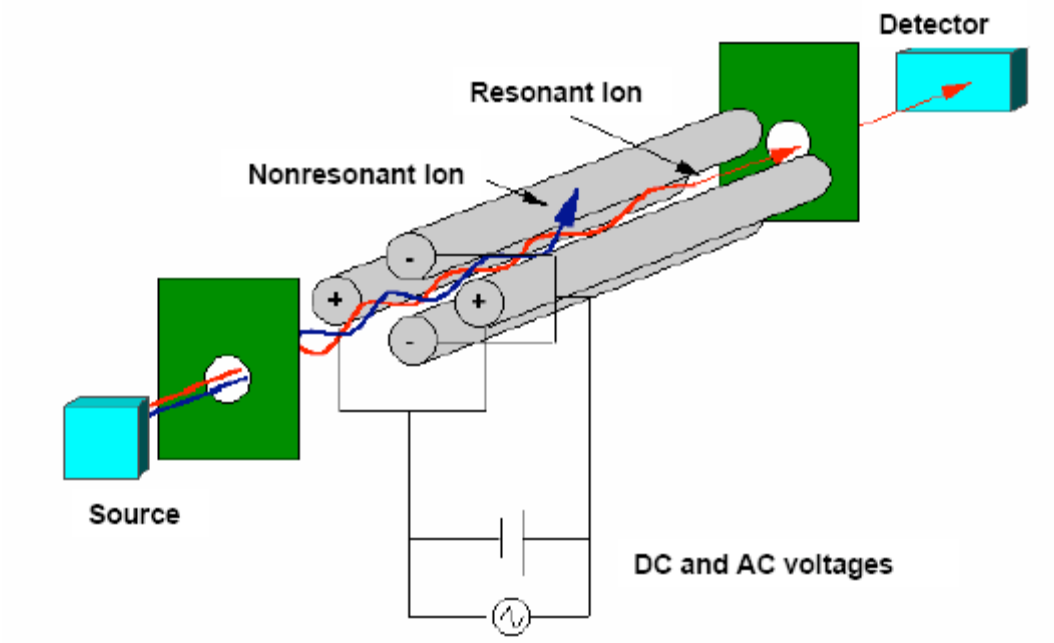

Figure 1.2. Illustration of a quadrupole mass analyser showing the source, focusing lenses, quadrupole rods and the detector. Transmitted ions oscillate in the resulting quadrupolar field, ions with an unstable trajectory (nonresonant) are filtered out. Figure taken from www.huygensgcms.gsfc.nasa.gov (accessed July 2011).

1.1.5.2 Time-of-Flight Mass Analysers

TOF mass spectrometry was first proposed by nuclear physicist William E. Stephens in 1946. In the 1950s that the instrument was adapted for use in biomolecular analysis and was commercially produced[91, 92]. Time-of-flight mass analysers are probably the simplest analysers in design; they separate ions in time as they travel down a field-free flight tube. Short ion packets are produced by a pulsed ion source, which are then

accelerated to a constant energy by the application of a known electric field. As all ions experience the same electric potential, they all have the same kinetic energy on entrance to the flight tube[93]. The velocity of an ion and thus the time it takes to travel the distance of the flight tube depends upon its *m/z* ratio. Equation 3 shows the acceleration of an ion before it leaves the source, by conversion electric potential energy into kinetic energy.

Equation 3 $E_k = \frac{mv^2}{2} = qV_s = zeV_s = E_{el}$

Equation 3 shows the conversion of an ions electric potential energy E_{el} into kinetic energy E_K. An ion with a mass m and total charge $q=ze$ is accelerated by a potential V_s.

Equation 3 can be rearranged to give the velocity (*v*) of the ion leaving the source; this is shown in equation 4.

Equation 4 $v = (2zeV_s/m)^{1/2}$

The ion travels to the detector at a constant velocity, the time it takes for the ion to reach the detector can be calculated by equation 5.

Equation 5 $t = \frac{L}{v}$

Where t = time and L is the distance the ion travels, which will be the length of the flight tube.

The *m/z* of the ion can thus be calculated by:

Equation 6 $t^2 = \frac{m}{z}\left(\frac{L^2}{2eV_s}\right)$

As smaller masses are lighter they will traverse the field-free drift tube faster due to their higher velocities, with larger molecules taking longer. The velocity of a singly charged ion is inversely proportional to the square root of its mass-to-charge ratio[94].

TOF instruments offer the following advantages:

- Very high sensitivity
- Minimal ion loss due to increased transmission efficiency
- Complete mass spectrum of all ions transmitted
- Theoretical unlimited mass range

Linear instruments are associated with poor mass resolution for the following reasons[94]:

- Spatial width of the initial ion packed produced (spatial distribution)
- Variation of the initial kinetic energy of the ions (kinetic energy distribution)
- Temporal spread over which the ions are formed (time distribution)

A number of instrument developments have resulted in improvements to the original TOF design and has solved some of these mass resolution issues. These include using an ion mirror as a reflectron to increase the length of the flight tube, and delayed extraction (DE) of the ion packets[91, 95].

Reflectron TOF analysers minimise the effects of the initial spread in kinetic energy. Ions are in effect decelerated, stopped and reaccelerated in a static electric field (ion mirror) before they reach the detector[95]. Ions with a higher kinetic energy be retarded and repelled compared to ions with less kinetic energy. This results in high and low energy ions that share the same *m/z* arriving at the detector at the same time, thus increasing the resolution of the instrument[94-96].

The method of delayed extraction is based on the theory of “time lag energy focusing”, which was described by Wiley and Mclaren in 1955[91] to reduce the kinetic energy spread among ions sharing the same m/z ration[91]. A time delay is introduced between ion formation and ion extraction into the instrument. Ions are formed in a weak electric field and then extracted after a time specific delay by the application of a high voltage pulse[97-99].

1.1.5.3 Quadrupole Time-of-Flight Mass Spectrometer

A quadrupole time-of-flight mass spectrometer (QqTOF) is a hybrid instrument. Q refers to the mass resolving quadrupole, q refers to an r.f-only quadrupole or hexapole and TOF refers to a time of flight mass analyser as previously discussed. The instrument can be regarded as the replacement of Q3 in a triple quadrupole instrument with a TOF mass analyser, as shown in figure 1.1.5.3 [100].

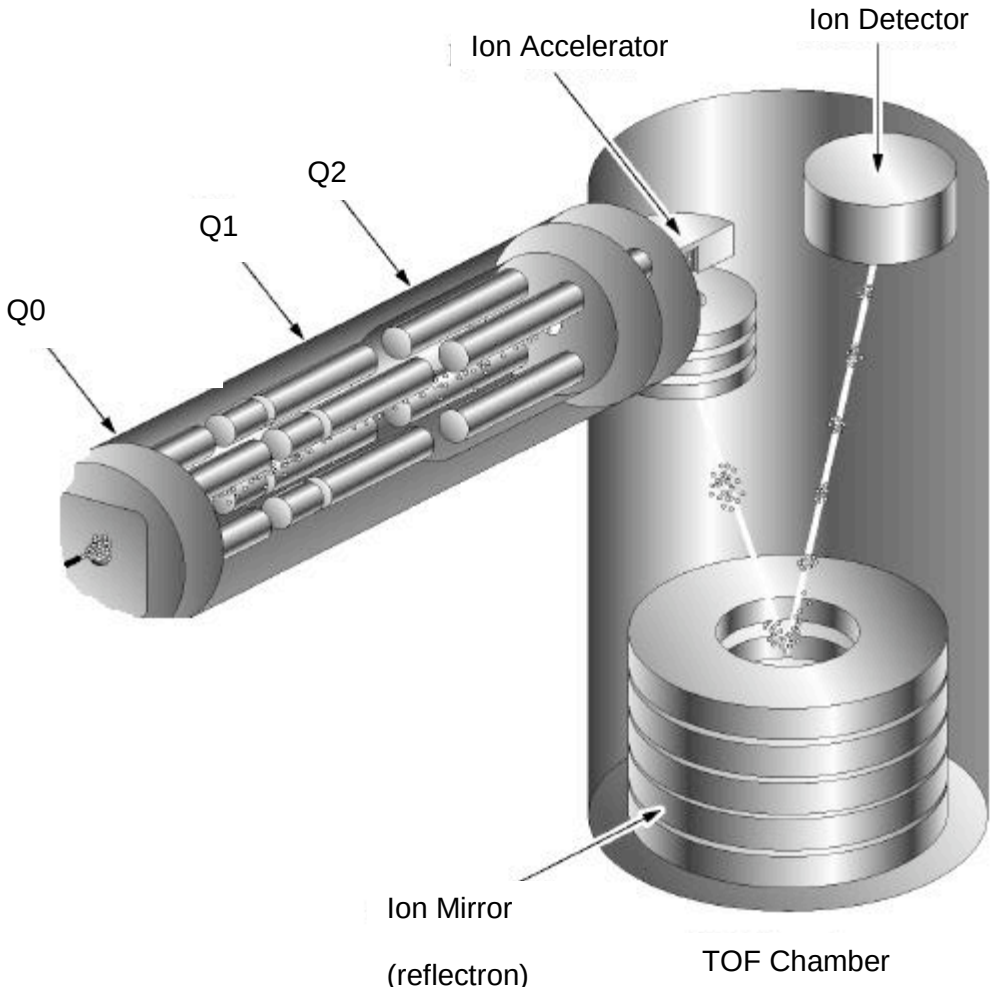

Figure 1.3. Representation of a QqTOF mass spectrometer. Image taken from the Hardware Overview for the QStar mass spectrometer supplied by Applied Biosystems.

Q0 is an r.f-only quadrupole used for collisional cooling of the ions to suppress fragmentation, and focusing the ion into Q1[101]. The rf voltage of Q0 is a fraction of the rf voltage applied to Q1 to ensure optimal ion transfer through the quadrupoles. Q1 can be operated in the r.f-only mode for MS analysis, in this mode ions are transmitted through the quadrupoles and separated and detected in the TOF chamber (TOF analysis). Q1 can also be operated in the mass selective mode for MS/MS analysis, for this mode of analysis a resolving DC voltage is applied to the electrodes to select or resolve the ion of interest. Q2 is also an r.f-only quadrupole, but is also the collision cell of the instrument. In

MS/MS mode, Q1 functions as a mass selector for the ion of interest, which is then transmitted into the collision cell (Q2) for fragmentation. Fragmentation usually occurs within the first few collisions with a neutral gas, nitrogen or argon and the resultant fragments are transmitted into the TOF section for analysis[85].

QqTOF instruments offer the advantage of high sensitivity, mass resolution and mass accuracy for full scan measurements and tandem analysis modes. These are attributed to the features of the TOF section of the instrument. The disadvantages to this instrument are associated with the loss of numerous functions a QqQ mass spectrometer has. These include single ion monitoring and multiple reaction monitoring, the inability to perform neutral loss and parent ion scans. The need for a pulsed ion source also limits the duty cycle of the instrument and there is also a limited dynamic range not usually seen with a TOF instrument[100].

1.2 Overview of the MALDI Imaging Technique

Caprioli and co-workers pioneered the MALDI mass spectrometric imaging (MALDI-MSI) technique in 1997, in which they demonstrated imaging of proteins in tissue[102].
The basic MALDI technique applies, in which a matrix is required to co-crystallise with the anaylte/s of interest. For imaging investigations, organs/tissues of interest are sectioned using a cryostat, usually at a thickness between 5 and 20µm. The sectioned tissue is then transferred onto a MALDI stainless steel sample plate, glass slide or other solid substrates, and allowed to dry onto the plate prior to matrix application. Matrix deposition for imaging experiments is more commonly carried out using an artistic airbrush; this is discussed in more detail in chapter 3. Briefly, the matrix solution is deposited over the

target plate and tissue area in the form of a fine mist, with an aim to cover the entire tissue section with a homogenous coating. The sample is then ready for MALDI-MSI analysis. Within the ion source the sample plate moves in x and y dimensions, under a fixed laser. A pre-determined data acquisition grid pattern controls the movement of the sample plate within these dimensions. The number of laser shots or rasters per grid co-ordinate is set prior to the start of the experiment, with a fixed distance between each grid spot. The distance selected is dependent upon the diameter of the laser spot, the stepping distance capability of the sample plate motor and the image resolution required. These are generally set between 50-300 µm stepping distances, with a smaller distance giving higher resolution. All processes are controlled by specialised computer software. Individual *m/z* values are determined at each raster location, giving rise to a mass spectrum of compounds at each location. The acquired data files are then converted or transferred to an image processing application programme. Each laser spot or individual spectrum now becomes a pixel. Imaging applications allow the selection of the *m/z* or mass spectrum of the analyte/s of interest and enables visualisation of its distribution over the defined area of interest. Pixel intensity (given in colour in many cases) of the analyte/s of interest thus corresponds to ion intensity. Images can also be overlaid such that a protein, lipid or drug compound in a selected area of tissue can be placed over an optical image of that tissue, indicating its anatomical position. The workflow from sample preparation to image and spectral analysis is shown in figure 1.4.

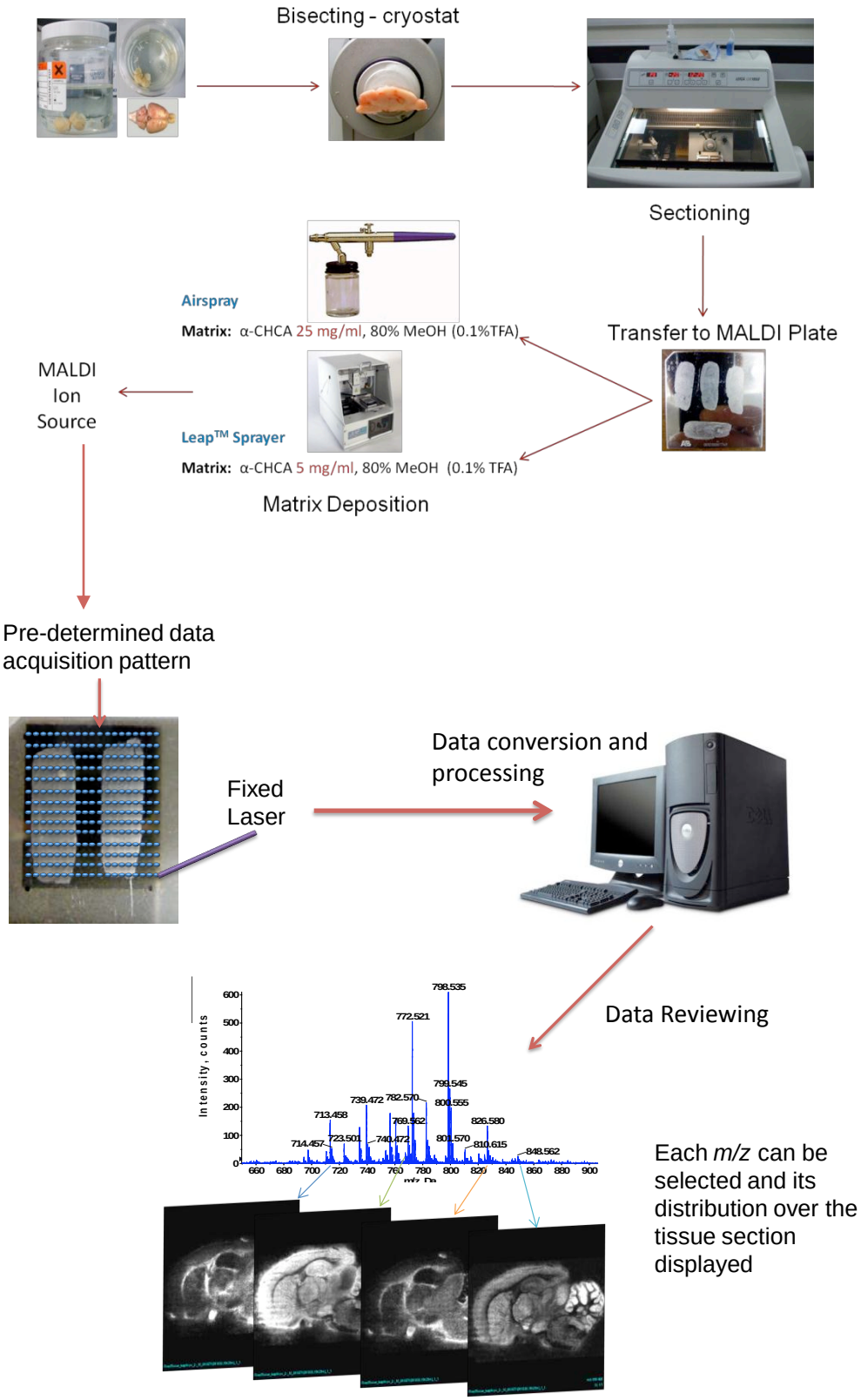

Figure 1.4 MALDI-MSI workflow from sample preparation to analysis.

1.2.1 Imaging and profiling of Proteins by MALDI-MS

The following section reviews the key research articles, including the pioneering article, that where important in establishing MALDI imaging as a viable technique.

The first application of MALDI-MSI (Caprioli, 1997) was used in the analysis of tissue via direct and indirect methods[102]. For the indirect methods the tissue was blotted onto specially prepared carbon coated membranes or with C_{18} coated resin beads. All imaging experiments were carried out on a MALDI-TOF-MS instrument, equipped with delayed extraction (DE) and nitrogen laser (337mn). The group successfully imaged and localised insulin in a section of rat pancreatic tissue, mapped hormone peptides from rat pituitary tissue and a small protein bound on the surface of human endothelial cells. By comparing the results of different matrix application methods, the group also found that optimum results were achieve by electrospraying the matrix onto the tissue. This prevented analyte migration (to an extent) thus allowing the compounds investigated to be mapped to specific locations within the tissue sections analysed. However, care must be taken when interpreting these results as two completely different matrices and solvent systems were used for each method. Therefore it is not known whether the method of matrix deposition or the matrix of choice was responsible for the results achieved by electrospray deposition. The pioneering authors also commented on the need for methods/instrumentation and software to improve the spatial resolution of the images achieved in this first paper.

Stoeckli and co-workers (2001) used MALDI-TOF-MS to investigate human brain tumour xenograph sections[103]. The group distinguished subgroups of gliomas from each other as well as distinguishing between two tumours that shared the same histological features but had different origins. The results lack a histological stained section for comparison, making it difficult to visualise the distribution of these proteins within the tumour and non tumour sections/tissue areas.

Stoeckli and co-workers (2002) used MALDI-MSI to investigate brain sections from transgenic mice models of Alzheimer's disease[104]. This investigation was carried out on a DE MALDI-TOF instrument equipped with an Nd:YAG laser. The group successfully imaged and localised plaques that contained increasing concentrations of amyloid β (Aβ) peptides, as well as differentiating between the different Aβ isoforms present. These peptides are central to the pathogenesis of Alzheimer's disease. The acquired images from this investigation strongly correlated with immunohistochemical (IHC) results obtained on a section of the same brain tissue. Although the group demonstrated the specificity of MALDI-MSI in terms of imaging peptides and being able to do this simultaneously in a single imaging run, the spatial resolution of the images obtained here are poor. This is mainly due to the choice of method for matrix application. As stated by the authors, the slow crystal drying process that accompanies this method resulted in crystal sizes of up to 200 µm in some cases. This would drastically affect the achievable resolution as this is affected by laser diameter and matrix crystal size. Despite the laser irradiation being set at 100 µm increments, a crystal size above this, as is occurring here would inhibit the ability of the resolution to reach that level. There was also crystal migration during the matrix drying process which would cause analyte migration, thus affecting the specificity with respect to mapping analyte distribution within tissue.

1.3 Lipidomics

The term 'lipidomics' began appearing in literature in 2003 and is seen as a subsection of metabolomics[105]. Lipidomics, much like genomics and proteomics, is said to be the systems-biology analysis of lipids and their interacting moieties[106]. The study of lipids has seen a rapid increase in interest over recent years. This is owed in part to the

understanding of their involvement in physiological and pathological processes, and in part to the development of analytical tools and instrumentation that enable rapid high-throughput analysis. The development of soft ionisation techniques, MALDI and ESI has greatly contributed to the vast amount of knowledge we now have on these molecules[107-119]. Prior to ESI and MALDI, techniques included, fluorescence-based assays, anti-PL antibodies, TLC, HPLC, NMR and GC/MS, whilst these techniques are useful they are non-specific and/or extremely time consuming, due to the extensive separation process which was often necessary before analysis[120-124].

Every living cell, be it eukaryotic or prokaryotic, is enclosed by a protective plasma membrane containing phospholipids, proteins, carbohydrates and cholesterol. The main constituents of plasma membranes are phospholipids (PLs), also called glycerophospholipids (GPLs).

Bacteria, in addition to having a plasma membrane, also have protective outer cell wall containing a number of unique lipids, including highly complex methyl-branched, and/or cyclopropane containing fatty acids[125-128]. The cell wall lipids in bacteria have been shown to be involved in virulence and resistance to antibiotics by providing incredibly low fluidity[125-129]. Of particular interest are cell wall lipids from the genus *Mycobacterium*, for two reasons, firstly the species from this genus comprise the *Mycobacterium tuberculosis* complex, and secondly, these cell wall lipids are highly unique to the *Mycobacterium* genus, they are not observed in any other bacterium, and contribute greatly to the virulence and intracellular survival of the slow-growing pathogenic *Mycobacterium[127, 130-139]*.

This thesis is separated into two parts, the first three experimental chapters describe routes to optimised sample preparation for MALDI-MS of PLs, the final two experimental chapters describe efforts made to analyse slow-growing pathogenic mycobacterial cell wall lipids from complex solutions.

1.4 Glycerophospholipids

Glycerophospholipids are amphiphilic in nature and contain a polar head group attached to non-polar acyl chains. The polar head group, which defines the subgroup or class of the lipid, contains a phosphate group esterified to the *sn-3* of a glycerol backbone[116]. The main head group classes are phosphatidylcholine, phosphatidylethanolamines, phosphatidylserines, phosphatidylinositols, and phosphatidylglycerol[140]. The glycerol backbone is acylated or alkylated with long-chain fatty acids (FAs), typically 14-24 carbons in length at the *sn-1* and *sn-2* positions[141]. The *sn-1* position of the glycerol backbone usually has a saturated or monounsaturated FA esterified, whereas polyunsaturated FAs (PUFAs), typically 2-6 double bonds, are usually located at the *sn-2* position[141]. The structural diversity that exists due to the different combinations of fatty acids with the different head groups gives rise to hundreds of different molecule species. The different structures of GPL head groups are presented in figure 1.5

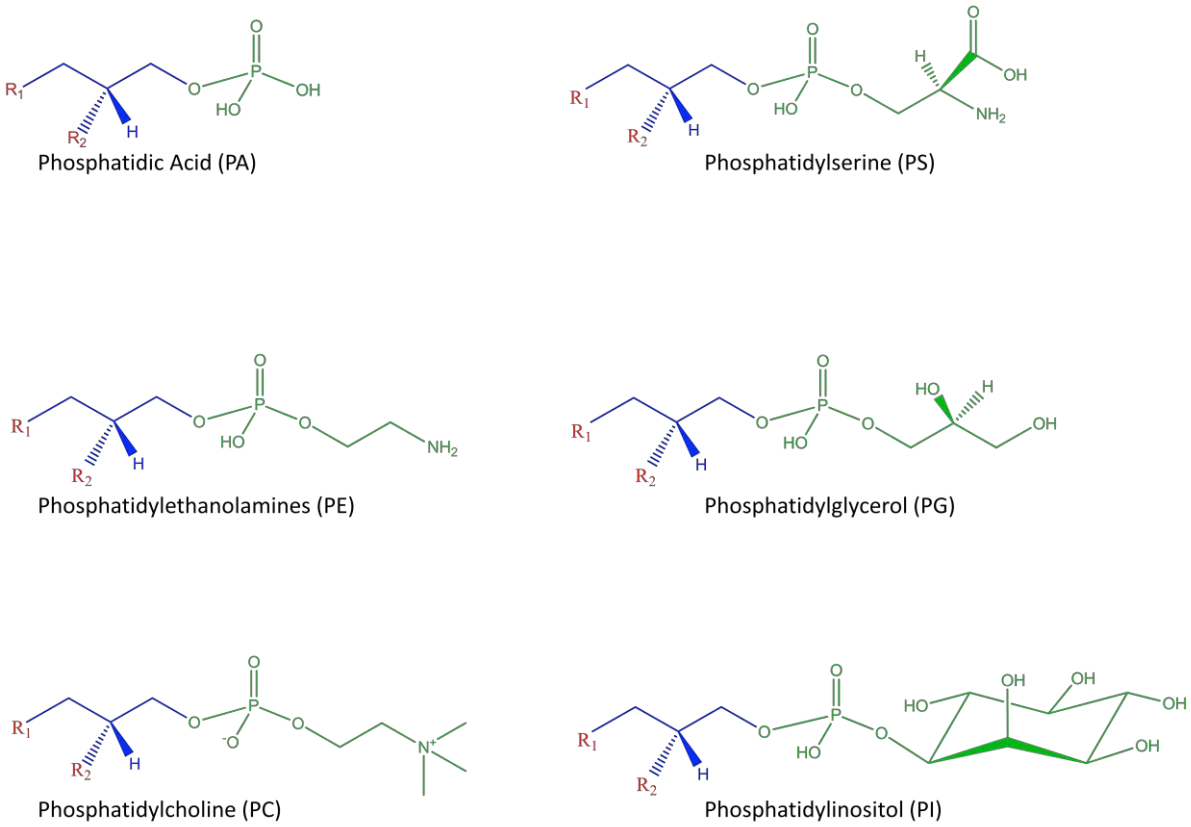

Figure 1.5. Structures of the different classes of Glycerophospholipids according to their polar head group, drawn in green, with the glycerol backbone in blue, R1 and R2 represent acyl chains.

A comprehensive classification system for lipids was published in 2005 by Fahy *et al* to establish a universal nomenclature for lipids[142]. From this glycerophospholipids are recognised by their polar head group and type and location of their fatty acid residues. For instance, a choline containing head group will be termed a glycerophosphocholine, or simply phosphatidylcholine, if *sn-1* and *sn-2* contained palmitic acid (hexadecanoic acid) and arachidonic acid (5Z,8Z,11Z,14Z-eicosatetraenoic acid) respectively, would have a systemic name of 1-hexadecanoyl-2-(5Z,8Z,11Z,14Z-eicosatetraenoyl)-sn-glycero-3-phosphocholine, commonly called PC(16:0/20:4(5Z,8Z,11Z,14Z)), which can then be further abbreviated to PC 36:4. The structure of this lipid is presented in figure 1.6, GPLs should always be drawn with the head group on the right[142].

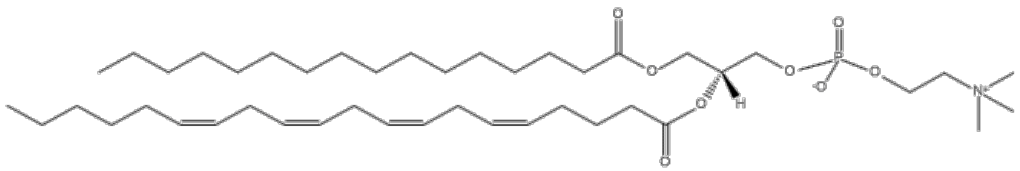

Figure 1.6. Structure of 1-hexadecanoyl-2-(5Z,8Z,11Z,14Z-eicosatetraenoyl)-sn-glycero-3-phosphocholine, commonly known as PC 36:4.

GLPs are abundant in cellular systems and the main constituents of cellular membranes. The fluid mosaic model for cell membranes was proposed in 1972 by Singer and Nicholson, in which the phospholipids are distributed on either side of the membrane in an asymmetrical manner, organised as a bilayer[143]. GLPs were previously thought to serve merely as membrane barriers and reservoirs for biological energy. It is now known that they are involved in numerous physiological processes, including membrane trafficking and cell signalling[141]. PUFAs are hydrolysed from membrane GPLs and are further metabolised into numerous biologically active molecules[108]. Figure 1.7 depicts the fluid mosaic model of cell membranes, with a simplified overview of lipid involvement in physiological processes.

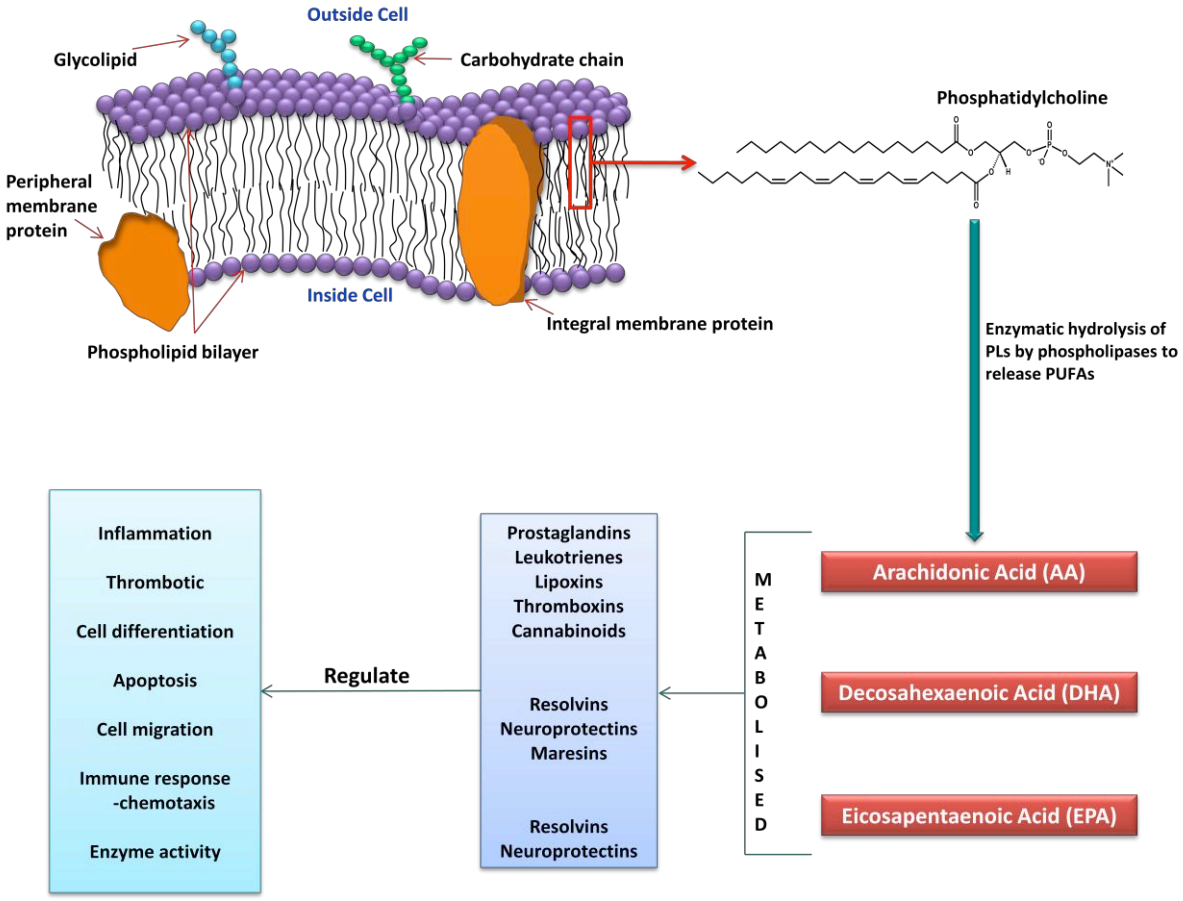

Figure 1.7 Schematic representation of the fluid mosaic model of cell membranes, adapted from[143], addition information collected from[108, 144-146].

With the involvement of lipids in numerous physiological processes it is unsurprising that lipid distribution has also been shown to be altered in a number of pathological conditions. These include, diabetes, Alzheimer's, cancer, heart disease, and numerous metabolic diseases, and the list is still growing [108, 144-154]. It is yet to be understood as to whether these changes occur prior to, or are the cause of, initial disease states.

1.4.1 Analysis of Glycerophospholipids by MALDI-MSI

Sample preparation and Instrument Evaluation

One of the first lipid imaging papers was by Garrett and co-workers (2007)[155], who analysed phospholipids in 10 µm rat brain sections to assess the feasibility of a number of MALDI parameters, and a new intermediate-pressure MALDI linear ion-trap mass spectrometer (MALDI LTQ-MS). High resolution images were produced of PC (18:0, 18:1) *m/z* 810, $[M+Na]^+$, on both conductive and non-conductive microscope slides, and PC 36:4, *m*/*z* 804, $[M+Na]^+$ and PC 38:6, *m*/*z* 828, $[M+Na]^+$. An important feature of this article is the ability to show and separate isobaric species by tandem MS analysis. This is shown in by the images presented, which showed the differential distribution of product ions recorded from the fragmentation of the ion at *m/z* 828. Three different spatial distributions were produced, meaning three different species were fragmented at *m/z* 828, if only one species was present the same image, would be present for all product ions produced. The ability to perform MS^3 enabled structural identification of the lipids. Lipid species were identified as PC (16:0, 22:6) $[M+Na]^+$, PE (18:0, 20:4) $[M-H+Na+K]^+$ and PS (16:0, 18:1) showing the benefit of this instrument platform for PL analysis.

The use of MALDI-Ion-mobility time-of-flight mass spectrometry (IM-TOF-MS) in imaging investigations of PLs from rat brain sections was presented for the first time by Jackson *et al.* (2007)[156]. This instrument separated ions according to their mobility, based on gas-phase density of ions, prior to TOF analysis. Images illustrating the distribution of *m*/*z* 798.6, assigned (PC 34:1 + K), *m*/*z* 826.6 assigned (PC 36:1 + K), and *m*/*z* 844.6, assigned (PC 38:6 +K) were presented, demonstrating the differential distribution of lipids in grey and white matter regions of the brain.

In 2008 Shimma and co workers used PLs as a way of assessing another new instrument platform, a MALDI quadrupole-ion-trap time-of-flight (QIT-TOF) instrument[157]. Images of two PCs at *m/z* 798.5 and 826.7 were recorded in positive ion mode and two species at *m/z* 885.5 and 904.7 in negative ion mode. The MS^3 spectra for the positive ion mode species allowed for the identification of phosphocholine head group fragments, alkali-metal adducts and proper structural identification of the fatty acid chains. PC 16:0/18:1 and PC 18:0/18:1 was structurally identified for *m/z* 798 and 826 respectively; the former displayed an omnipresent distribution in the brain, and the latter showed higher intensity within white matter regions. Upon fragmentation the ions recorded in negative mode at *m/z* 885 and 904 were found to be PI 18:0/20:4 and ST d18:1/24h:1 respectively. The image at *m/z* 904 showed clear anatomical specificity for white matter regions, whereas the ion at *m/z* 885 displayed an omnipresent distribution. Images presented are of rather poor quality, as the authors commented on the whole area scanned and not the resolution it is unknown whether the image quality is due to intentionally low resolution images being acquired.

Prior to these investigations the majority of MALDI imaging studies were carried out using MALDI-TOF, MALDI-TOF/TOF and MALDI QqTOF mass spectrometers[7, 158-163].

MALDI-LTQ-MSI of a specific phospholipid was used to assess a new matrix deposition method[164]. PC 36:1 at *m/z* 810, representing $[M+Na]^+$, was used to compare a new automated inkjet printer to the commonly used airbrush and electrospray deposition methods. Three images of this PC were presented, one for each method for comparison of image resolution afforded by all, images representing inkjet and airbrush deposition demonstrated a higher intensity of this lipid within the white matter regions of the brain. Electrospray deposition resulted in images of poor resolution; the inkjet printer deposition resulted in higher quality images, and increased reproducibility.

A MALDI-QqTOF-MS study showing PC images was published by Murphy *et al*. (2007), with the aim of assessing a new method of matrix deposition. This time the method was sublimation, and comparisons were made to electrospray deposition. Species detected included PC 32:0, at *m/z* 734, PC 34:1 at *m/z* 760, both representing the protonated molecule, PC 34:1 at *m/z* 798 for the sodium adduct, and PC 36:1, *m/z* 826, representing the potassium adduct. The images presented displayed the potassium adduct of PC 36:1 at *m/z* 826, slightly outlining grey matter features such as the corpus callosum.

Another imaging study using phospholipid distribution in brain as a way of assessing matrix deposition methods rapidly followed the former paper[165]. This was carried out by Wang and co-workers (2008) who compared the use of a TLC reagent sprayer, collision nebuliser and an artistic airbrush for matrix deposition followed by MALDI-TOF-MS analysis. Images of phosphatidylinositols and sulfatides were acquired in negative ion reflectron mode, while phosphatidylcholines were acquired in positive ion, reflectron mode. The group identified a total of 11 lipid species in negative ion mode and 6 in positive. Positive ion mode images were of PC 32:0, *m/z* 772, $[M + K]^+$ PC 36:1, *m/z* 826, $[M + K]^+$ and PC 34:1, *m/z* 760, $[M + H]^+$ showed a grey, white and omnipresent distribution respectively. Negative ion mode images of PI 38:4, followed the grey matter contours of the brain such as the cerebral cortex and the hippocampus, whereas ST 24:1 and ST 24:1 (OH) followed white matter regions of the brain, such as the corpus callosum. Airbrush deposition was found to generate at more homogenous matrix distribution with enhanced analyte extraction and co-crystallisation compared to the other two methods evaluated.

Phospholipids were imaged directly from 12 µm sagittal mouse brain sections for the assessment of a newly developed dry matrix application protocol using MALDI-TOF/TOF-MS[166]. DHB was finely ground and deposited onto the tissue section through a 20 µm

stainless steel sieve; results were compared to those obtained using a thin layer chromatography (TLC) reagent spray gun for matrix application. Phospholipid patterns in mouse brain cerebellum were determined by overlaying the extracted lipid images onto an adjacent haematoxylin and eosin stained optical image. The overlaid image showed the localization of *m/z* 872, PC 40:6, in the cerebellar cortex, *m/z* 826, PC 36:1 and *m/z* 810, PC 38:4 in the cerebellar nucleus and *m/z* 844, PC 38:6 in the granule cell layer.

The use of alkali metal salts in mass spectrometric analysis has been proven to aid in either the reduction of complexity of the mass spectra for lipid analysis or in the case of lithium, in enabling enhanced PL fragmentation for identification by MS/MS[112, 167]. Alkali metal salts were first shown to be of use in the analysis of polymers by MALDI-MS[168, 169], eventually leading to MALDI profiling and imaging investigations[165, 170]. In 2009 Sugiura *et al.* published an investigation into the use of alkali metal additives in matrix solutions, to enable the selective ionisation of GLPs directly from tissue, using MALDI TOF/TOF mass spectrometry[171]. Mass spectra of lipid species acquired directly from tissue are complex due to the presence of multiple adducts ($[M+H]^+$, $[M+Na]^+$ and $[M+K]^+$), leading to overlapping *m/z* values for several lipid species. The group showed that the addition of 10 mM of potassium acetate simplified the resulting mass spectra by shifting the ionised PCs to a single ion, the $[M+K]^+$ ion. They also showed the addition of sodium acetate did not have the same effect as multiple adducts were still present. The authors concluded that K^+ formed stronger adducts than Na^+, however this may not be the case. There are high concentrations of sodium and potassium already present in organ systems, which is why these adducts are often observed when analysing PLs directly from tissue sections. Therefore the results seen may be due to a higher concentration of potassium already being present in the tissue analysed, meaning a higher concentration of K^+ is readily available. Images of PC 32:0, *m/z* 772, PC 34:2, *m/z* 796, PC 34:1, *m/z* 798, PC 36:4, *m/z* 820, PC 38:6, *m/z* 844, and PC 38:4, *m/z* 848, all representing $[M+K]^+$

were presented, displaying differential distributions across the cortex, medulla and pelvis renalis regions of a kidney section. CID experiments were conducted out using lithium additives to enable structural identification. The group then went on to analyse the distribution of PUFA containing PLs during growth; this part of the research paper is discussed in the physiological studies presented below.

Shanta *et al.* (2011) have recently reported the combination of DHB and CHCA as a binary matrix for enhanced analysis and imaging of lipids by MALDI TOF/TOF-MS, with the addition of both TFA and piperidine (an acid and a base) they gave the matrix ionic properties[172]. Combining equal amounts of DHB and CHCA, 1:4 ratio of TFA:PIP the group carried out both positive and negative ion made MSI studies on the same 12 um section of rat brain, resulting in the detection of over 100 peaks relating to lipid species, including PC, SM, PA, PE, PI and ST. Multiple ion forms of the same lipid species are detected during MSI analysis, thus this number is by no means the total number of individual species detected. The binary matrix proved more sensitive when comparing to DHB or CHCA used alone. For the 3 commonly detected lipid species in positive ion mode, *m/z* 798, $[PC\ 34:1+K]^+$, *m/z* 734, $[PC\ 32:0+H]^+$, *m/z* 772, $[PC\ 32:0+K]^+$, and *m/z* 826, $[PC\ 36:1+K]^+$, the binary matrix showed a three-fold increase in signal intensity compared to the individual matrices. For analysis in negative ion mode the binary matrix detected more peaks and showed increased intensities for ions at *m/z* 784, 806, 878, 906 and 920, which were identified as PS 36:3, ST 18:0, ST OH-20:0, ST OH-40:1, ST OH-42:1 and ST 44:0 respectively. The differential distribution of numerous lipid species across the brain were presented after principal component analysis (PCA) had been carried out.

A study by Cerruti and co-workers (2011) evaluated five different lithium salts, citrate, acetate, trifluoroacetate, iodide and chloride, for their suitability for MSI analysis, with

respect to crystal formation, detection sensitivity of lithium adducts and image quality[10]. Results were compared to one another and CHCA without additive. Lithium acetate produced large elongated crystals that although was the most sensitive, in terms of yielding the highest proportions of lithium lipid adducts, produced images of extremely poor quality, thus was deemed unsuitable for MSI. Lithium citrate was also unsuitable for MALDI-MSI as crystals produced with this additive were that of large irregular plaques, that required increased laser fluencies for obtaining only weak signals. Lithium chloride, iodide and trifluoroacetate all produced crystals of small size with good homogeneity over the tissue, however, lithium chloride adducts did not exceed 65 % of the ions formed. Lithium trifluoroacetate was shown to give a three-fold increase in sensitivity compared to lithium iodide. Lithium trifluoroacetate was also shown to give a two-fold increase in sensitivity of PC 32:0 and PC 34:1 compared to αCHCA alone, these lipids were chosen because they are commonly observed in MALDI-MS and display different distributions in the cerebellum. Images presented using αCHCA as the matrix solution were of *m/z* 734, $[PC\ 32:0+H]^+$, *m/z* 760, $[PC\ 34:1+H]^+$, *m/z* 731, $[SM\ 18:0+H]^+$, displaying grey matter distributions, whereas *m/z* 806, $[PE\ 38:4+K]^+$ or $[PC\ 38:6+H]^+$, *m/z* 812, $[PC\ 38:3+H]^+$, [PE 38:1+K]+, or $[PE\ 38:4+2Na\text{-}H]^+$, *m/z* 816.6, $[PE\ 42:8+H]^+$, and *m/z* 834, [PE 38:1+Na+K–H]$^+$, displayed white matter distributions. The same images were produced for lithium iodide and lithium trifluoroacetate, showing more resolved images for the latter two, however, it should be noted that the images presented for αCHCA without additive are of extremely poor quality. It is suggested in this thesis that the poor quality results presented by this group using αCHCA without additive, may be due to acetonitrile being used as the solvent system. Images presented in chapter 3 of this thesis, which used the same matrix compound and deposition method, but different solvent system presents high quality molecular images of PLs.

The majority of lipid MS imaging experiments, regarding sample preparation, have been carried out on brain tissue sections, more recently a report has been published detailing efforts made to analyse PLs from lung tissue.

The sectioning of lung tissue for analysis is problematic due to its spongy nature, frozen non-inflated lungs result in sections with compromised morphology[173]. Histological preparation of lung tissue employs agarose inflation followed by FFPE or OCT-embedding for sectioning. These preparations are not suited to MALDI-MS and MSI investigations of lipids due to two factors; the processing of tissue for paraffin embedding, and then removal after sectioning involves grades of alcohol, in which lipids are soluble and thus washed away, whilst OCT contains benzalkonium salt as a preservative, which is known to cause ion suppression of analytes and thus spectral interference during the MALDI process. Berry *et al.* (2011) modified the OCT cryoembedding agent with a mixture of 10 % PVA 6-98 and 8 % PPG 200 and evaluated its use in MALDI QqTOF-MSI investigations[173]. The results obtained from the analysis of tissue inflated with and embedded in the modified OCT (mOCT) were compared to FFPE and OCT-embedded preparations and lung lipid extracts. As expected MALDI-MSI analysis of FFPE produced no signals representing PLs. The analysis of agarose-inflated OCT-embedded tissue detected the presence of a few PL species, with images showing some definition of the lipid airway, however the signals for these lipids were low and thus was the image quality was poor. Numerous PL species were detected from mOCT-embedded tissue sections, including the commonly observed ions at *m/z* 706, 734, 760, 782 and 810. In addition to this, pulmonary morphology of the lung section was conserved, with far superior image quality, as evidenced by comparison to a stained section. MSI images revealed several lipids were distinctly located within specific lung regions, for instance, *m/z* 782, 806 and 810 were found to be highly abundant along the edge of the putative airways, whilst *m/z* 725 was found to have higher signal intensity at the edge of pulmonary blood vessels. Further MS/MS investigations identified these as PC (16:0/20:4), for *m/z* 782, PC

(16:0/22:5), for *m/z* 806 and PC (18:0/20:4), for *m/z* 810, the ion at *m/z* 725 was assigned SM d18:1/16:0. This is the first study demonstrating increasing amounts of PUFA containing PLs within specific distributions of pulmonary tissue. Little is known about the change in arachidonic acid (AA) and decosahaexanoic acid(DHA) containing lipids during lung disease and environmental toxicants; methods presented in this work provides a possible route to investigate such changes.

Physiological Changes

PUFAs have been proven to be involved in numerous physiological processes, and have high abundance in the CNS. A study by Suguira and co-workers (2009) used MALDI-QIT-TOF MSI, with the addition of potassium acetate to the matrix system, as described above, to show the specific distribution of PUFA containing GPLs within distinct anatomical regions of the rat brain[171]. Specifically, the distribution of arachidonic acid (AA) and decosahexaenoic acid (DHA) containing GPLs were investigated. Principle component analysis was used to investigate whether there are changes observed in the distribution of these lipid species with increasing age. Three trends in distribution of GPLs were observed, all of which presented as MS images. The first scores were for spectra that displayed higher counts in the infant brains (1 and 12 days old) compared to the adult brains (7 and 96 weeks old), and a PC that showed increasing intensity in white matter regions of the brain with increasing age. Specifically, PC (14:0/16:0), *m/z* 744 (cerebral cortex distribution), and PC (16:0/16:1), *m/z* 770 (omnipresent distribution), showed high intensity in the 1 day old brain, which decreased with age, showing lower intensity in the 12 day old, followed by no or low counts observed in the 7 and 96 week old brains. Conversely PC (18:0/18:1), *m/z* 826 displays low signal intensity in the 1 day old brain, which increases in intensity with age, showing high abundance in the white matter regions

of the 7 and 96 week old brains. The second trend represented the accumulation of AA-PCs during the formation of the hippocampus, cerebral cortex, corpus striatum and the granular layer of the cerebellum. The images produced of this PCA showed PC (16:0/24:4), *m/z* 820, and PC (18:0/20:4), *m/z* 848 were only faintly observed within the hippocampus in the infant brains but were clearly defined in the adult brains. The third and final trend reported the accumulation of DHA-PCs in the cerebellar cortex. The PCs attributed to this were PC (16:0/22:6), *m/z* 844 and PC (18:0/22:6), *m/z* 872, which increased in intensity with the developing brain. PC (18:0/22:6) was said to be contained in the soma and dendrites of the Purkinje cells and was detected in the 1 day old brain at the surface of the cerebellum, an area where immature Purkinje cells are located. Due to the addition of potassium into the matrix solvent system this group reported these ions as $[M+K]^+$. This report highlights the importance of MALDI-MSI in spatially mapping the distribution of PCs containing two biologically active and important PUFAs. In addition, the report gives insight into how the distributions of PUFA containing PCs change with age.

Kobayashi and co-workers (2010) have recently published a report imaging PLs in the placental villus. The group detected and imaged numerous PLs, however, the focus of the report was on two specific ions due to them showing distinct differential distribution within the tissue[174]. The ions at *m/z* 785.6 and 804.7 were identified as sphingomyelin (d18:1/16:0) and PC (16:0/20:4), both being detected as the sodium adduct $[M+Na]^+$. SM (d18:1/16:0) was found to be predominantly located in the stem villi, but not in the terminal villi, whereas PC (16:0/20:4) showed the opposite distribution. Terminal villi are responsible for hormone secretion and nutrient transportation, thus the identification of the distribution of PLs containing AA within this region may be of importance. AA metabolism into eicosanoids is believed to play a key part in normal/abnormal growth, and vasodilation/constriction of vessels in the placental villus, thus mapping the distribution of these lipids may provide key insight into both physiological and pathological changes.

Difference in the composition of PCs between placentas from normally grown and growth-restricted newborns have been shown, however, this is the first study mapping differential distribution of PCs within such tissues.

The liver has a remarkable capacity to regenerate; Miyamura *et al.* (2011) used MALDI-TOF-MS imaging to investigation the difference in lipid composition/distribution in rodents that had received a partial hepactomy (PH), the experimental model used to investigate liver regeneration[175]. MALDI-MS analysis of mice liver tissue, acquired 0, 6, 12 or 24 h post-operative showed differences in lipid distribution compared to sham (control) post-operative tissue. This investigation demonstrated an increase in 6 PC species, including PC 34:1, PC 34:2, PC 36:0, PC 36:2, PC 36:5 and PC 38:6, along with a decrease in LPC 16:0, PC 40:6 and PC 40:8 in the regenerating liver compared to the control. Care needs to be taken with the interpretation of these results, as images produced and the table generated, showing the differences in lipid composition, were based on *m/z* values representing either $[M+H]^+$, $[M+Na]^+$ or $[M+K]^+$. The report does not take into consideration the sum of these ions for a given lipid species, and then compare this across the samples, thus results are not a true representation of PL composition, the differences observed may be due to different levels of salts in the samples. It should also be noted that there are no recognisable anatomical features in the MALDI-MS images presented.

Pathological Changes

In a study by Shimma and co workers (2007), images of tumour and non tumour areas of colon cancer liver metastases were compared[176]. Whilst numerous lipid species where detected, the authors constructed three images focusing on two differentially distributed ions; the first was of a lipid at *m/z* 725 showing higher accumulation within the cancerous

area. The second was of a lipid at *m/z* 616 which showed higher ion counts in the normal area and the third image was an overlay of the former two. The authors also stated these lipid species were of equal distribution in the stroma area of the biopsy sample, demonstrated by the overlay image of the two. Tandem MS analysis and the use of the database Lipid Search suggested the ion observed at *m/z* 725 was that of the sodium adduct of SM 16:0. This study demonstrates the feasibility of MALDI-MS imaging as a viable tool for the comparative analysis of lipid distribution between physiological and pathological specimens. The reader should note that this particular study appeared to only analyse one biopsy sample, thus reproducibility is not shown.

Immunoglobin IgA is the most common glomerular disease worldwide. Kaneko *et al.* (2011), using a MALDI-QIT-TOF mass analyser, successfully identified eight dominant peaks that were present in the kidneys of HIGA mice, the widely used animal model of this disease, but absent from controls[177]. These were reported as, *m/z* 792, 814 and 830, assigned to PC O-16:0/22:6, representing the protonated molecule and the sodium and potassium adduct respectively. The peak at *m/z* 840 was assigned to PC O-18:0/22:4, $[M+Na]^+$, and *m/z* 854, 852, 880 and 882, were unidentified due to insufficient fragment peaks; however, the authors believed they were related structures. It must be noted however, that the images produced from the control samples show signal intensity outside the tissue area, which at times equals that found in the tissue area. In addition to this, the stained sections presented are either of poor quality or presented badly as anatomical features are unrecognisable, it is difficult to see if the section for the control includes the cortex, medulla and pelvic areas. The group also analysed urine samples in parallel and demonstrated the lipids observed in the kidneys of HIGA mice were secreted in the urine of both healthy and disease models. Unilateral urethral obstruction (UUO), which causes artificial urinary stag, was carried out on control mice. Kidneys from these experiments were said to mimic the results obtained from the HIGA disease model. This

is not the case, the distribution of *m/z* 792, 814, 830, 840, 854, 856, 880, and 882 are mainly confined within what appears to be the medullar region of the HIGA kidneys, whereas the images produced of these values in the kidneys of the UUO mice show an omnipresent distribution, and again there is evidence of increased signal intensity outside of the tissue area.

The investigation of PL distribution in rat models of ischemic brain injury, induced by middle cerebral artery occlusion (MACO), was carried out using a MALDI-QqTOF mass spectrometer[178]. Koizumi *et al.* (2010) compared images and mass spectra of the injured and normal hemisphere. The group focused on the differential distribution and signal intensities of three ions at *m/z* 760, identified and $[PC\ 34:1+K]^+$, *m/z* 798 identified as $[PC34:1+K]^+$ and *m/z* 496 identified as $[LPC\ 16:0+H]^+$. Images, spectra and statistical analysis presented by the group show a reduction in signal intensity for *m/z* 760 and 798 for PC 34:1, and an increase in signal intensity for *m/z* 496, for LPC 16:0, in the ischemic area compared to the normal brain regions. They concluded there is a reduction of PC 34:1 in the ischemic area, and an increased in LPC 16:0, possibly resulting from the biodegradation of PC by lipases to release LPC. What the group fail to comment on, or indeed investigate, is the signal intensity representing $[PC\ 34:1+Na]^+$, which, in the spectrum presented from the ischemic area, shows a large increase in signal intensity compared the spectrum taken from the normal area. As is the case of other PCs detected in this spectrum, there is a noticeable difference in the ratios of $[M+K]^+$ and $[M+Na]^+$ across the two sample areas. There is not believed to be a difference in the intensity of this PC across the two areas.

The differences in the ratio of PL sodium to potassium adduct formation in brain injury models was later reported by Hankin *et al.* (2011)[179]. The analysis of fluid percussion injury (FPI) using MALDI-QqTOF-MSI identified key changes in lipid distribution and metal

adduct formation. Highly abundant phospholipids commonly detected in brain tissue were detected during this MALDI-MSI investigation; however there was a distinct difference in adduct formation within the region of injury. There was a clearly visible increase in Na adduct formation for common lipid species, which directly correlated to a decrease in K formation. The authors demonstrated this by presenting images of *m/z* 782 $[PC34:1+Na]^+$, which showed high signal intensity within the injured region of the brain and lower intensity across normal brain anatomy, and *m/z* 798 $[PC34:1+K]^+$, which displayed to opposite distribution. This finding was observed across all sections analysed for the FPI model, the authors attributed this difference to the loss of the Na/K ATPase pump/activity and cell death.

1.5 Mycobacterium

The *Mycobacterium* genus comprises many species responsible for disease in humans, the most problematic and widely known being *Mycobacterium tuberculosis (M.tb*), the aetiological agent of tuberculosis (TB). Once thought to be a disease that was on the verge of eradication, the World Health Organisation (WHO) statistics show that TB kills nearly 2 million people annually, with 9 million new cases each year, 1.5 million of these among people living with HIV, and over half a million are multidrug-resistant (MDR-TB) strains. The resurgence of the disease is thought to be due to inadequate compliance with drug treatment along with the appearance of drug- and multidrug-resistant strains, and immunocompromised individuals. In 2006 the WHO launched the new Stop TB Strategy with a global plan to eliminate TB 2006-2015, which consists of six main components, the sixth being – “enable and promote research, by which improved practices and elimination depend on new diagnostics, drugs and vaccines”[180].

1.5.1 Cell Envelope Components

The *Mycobacterium* cell envelope structure has been extensively studied as the components play a central role in the growth, survival and thus pathogenicity of disease-causing *Mycobacterium* species. The cell envelope is unique compared to other Gram-positive bacterium and non-*Mycobacterium*. It contains an unusually high number of lipids, which comprise up to 60 % of the bacterial cell wall dry weight, and are responsible for the extremely hydrophobic nature of the cell envelope. Structurally, from the plasma membrane to the surface, the *mycobacterium* cell envelope contains a cell wall core composed of 3 covalently bound macromolecules; peptidoglycan, which is covalently bound to arabinogalactan via a linker unit; and the mycolic acids (MAs), which are esterified to the arabinose termini of the arabinogalactan[181]. Collectively these macromolecules have been termed the mycolyl-arabinogalactan-peptidoglycan (mAGP) complex, which is, in turn, capped by a layer of non-covalently bound lipids and glycolipids. The outer-most component of the cell envelope is a capsule of polysaccharides, proteins and lipids[182]. The most intensively studied of the mycobacterial cell envelope lipids to date, are the mycolic acids. Over half a century of research has proven their structural and functional importance: they are responsible for the highly hydrophobic and extremely low fluidity of the cell, making the cell impermeable to many detergents, toxins and pharmaceuticals, and their involvement in virulence has shown they are key to the success of *Mycobacterium* as intracellular pathogens[125, 183-189].

1.5.1.2 Mycolic Acids

MAs are signature lipids of mycobacterium due to their unique structure; they are extremely long-chain α-alkyl-branched, β-hydroxylated fatty acids, which vary according to their chain length (C_{60}-C_{90}) and functional group[125, 184, 190-192]. *M.tb* and some strains of *M. bovis* produce three types of MAs, the alpha-mycolates and oxygenated methoxy- and keto-mycolates, with the functional group being at the distal position of the merocolate chain. The MAs of *M.tb* and other slow-growing pathogenic *Mycobacterium* are cyclopropanated, with the alpha-mycolates containing two *cis* or *trans* cyclopropane rings (di-cyclopropanated), and the oxygenated MAs have a methoxy- or ketone- group and a proximal *cis* or *trans* cyclopropane ring[134, 188, 193-195]. In addition to the free MAs and those bound to the arabinogalactan, mycolic acids are also present in the cell envelope as sugar esters known as trehalose monomycolates and dimycolates, TMM and TDM respectively. These larger non-covalently bound lipids form part of the outer leaflet of the lipid bilayer, and contribute highly to the pathogenicity of mycobacteria[133, 196, 197]. The biosynthesis of MAs is the target of several first line anti-microbial drugs, such as isoniazid, which acts on several enzymes involved in their biosynthesis[185, 198].

1.5.1.3 Non-Covalently Bound Lipids – PDIMs, PGLs and MMGs

In addition to the covalently bound MAs, several non-covalently bound lipids have been shown to contribute to the permeability barrier of the *Mycobacterium* cell envelope, and are thus also involved in virulence. Of these, two structurally related families of lipids which are predominantly found in slow-growing pathogenic mycobacterium have been identified. These are the phthiocerol dimycocerosates, PDIMs or DIMs for short and phenolphthiocerol dimycolates, also called phenoglycolipids or PGLs[128]. PDIMs are

composed of a mixture of long-chain β-diols esterified by multimethyl-branched fatty acids called mycocerosoc acids. The major PDIM produced by *M.tb* is termed PDIM A or DIM A. Minor structural variants of these lipids are also present, termed PDIM B or DIM B[199, 200]. PGLs have a chemical structure similar to that of PDIMs, with a lipid core formed by long-chain β-diols, the structural difference is that this phthiocerol chain is ω-terminated by an aromatic nucleus (phenolphthiocerol), which is glycosylated[132, 201]. In *M.tb* the major form of PGL is termed PGL-tb, in *M. bovis* it is termed PGL-1. PDIMs and PGLs constitute part of the outer membrane component of the envelope; their FAs are believed to interact with the covalently bound MAs, with their sugar moiety interacting with the capsule. Mutant knock-out models have shown PDIMs are required for the multiplication of *M.tb* during the acute phase of TB infection in both the lung and spleen of mouse models[128]. Although these lipids are structurally similar and are observed together, not all strains of *M.tb* synthesise PGLs, this is due to a natural frame shift mutation in the *pks15/1* gene. These lipids are thought to be involved in the hyper-virulence of certain *M.tb* strains[132]. MAs are organised with other lipids, including PGLs, PDIMs, monomycolated glycerol (MMG), sphingomyelin (SM), and triacylglycerides (TAGs) to form an outer barrier with extremely low fluidity, that confer very low permeability to mycobacteria.

1.5.2 MALDI-MS of Mycobacterium Cell Wall Lipids

The analysis of mycolic acids using MALDI-TOF-MS was carried out for the first time by Laval *et al.* (2001)[193], who successfully analysed various types of purified mycolates from a number of representative *Mycobacterial* species and showed that chain lengths corresponded to the growth rate of strains, i.e rapid- and slow-growers. For analysis the group converted the extracted MAs into methyl esters with an ethereal solution of

diazomethane prior to TLC separation into MAME subgroups, and MALDI-TOF analysis. Mycolic acids are non-polar molecules, their methyl esters (MAMEs) ionise more readily than the free acids, thus enhancing detection of these species, which is the reason methylation is carried out. This investigation evaluated seven matrix solutions for their suitability in MALDI-MS analysis of MAMEs and found DHB 10 mg/mL in methanol:chloroform (1:1,v/v) gave the best results. From the analysis of the extracts from *M. tuberculosis* H37Rv the group detected four clear α-MAMEs, at *m/z* 1146, 1174, 1202, and 1230, which they designated carbon chain lengths C_{76}, C_{78}, C_{80}, and C_{82} respectively. Four methoxy-MAMES were also detected at *m/z* 1262, 1290, 1318 and 1346, assigned C_{83}, C_{85}, C_{87}, C_{89}. The keto-MAMEs detected from this species were, *m/z* 1246, 1274, 1288, 1302, 1316, and 1330, designated C_{82}, $C_{84,}$ C_{85}, C_{86}, C_{87}, and $C_{88.}$ All peaks detected in this study were designated $[M+Na]^+$ ions. The group then went on to detail the differences observed in MAME composition between rapid- and slow-growing *Mycobacterium*. The most important part of this study however, was the proof of viability of MALDI-MS as a technique that can analyse complex FA mixtures from pathogenic species, and comparing results to those obtained from mutant strains, devoid of certain mycolate biosynthesis. The group detected alpha-methoxy- and keto-MAMEs from a mixture, detecting the same species as was observed in the analysis of single mycolate extracts. Results obtained from the analysis of a mutant model, showed this species to be devoid of both methoxy- and keto-MAMEs, compared its parent strain; this was evidenced by a mass spectrum containing one series of peaks from *m/z* 1118 to 1250. This investigation was important as it demonstrated, for the first time, the feasibility of MALDI-MS as a tools to provide accurate molecular mass information, and a more direct and rapid route for the analysis of MAs.

During the same year Watanabe and co-workers[195] used MALDI-TOF-MS alongside NMR, the former revealing the chain length with the latter revealing the type and location

of the double bonds, along with the cyclopropane ring content of MAs from 24 representatives of the *Mycobacterium* genus. This was an exhaustive study comparing differences in mycolate type, double bond location, configuration and degree of cyclopropane content, not only between a number of species in the MTBC, but also at different growth stages of cultivation. Much of this report however, is concerned with NMR results obtained. MALDI-MS was used as a confirmatory tool; results presented by the group were for the detection of alpha- and methoxy-MAMEs from *M. tuberculosis* H37Ra, an attenuated strain, which demonstrated distinct differences in mycolate profiles compared to virulent strains. All peaks presented by the authors represented $[M+Na]^+$, α-MAMEs were detected at *m/z* 1133, 1161, 1173, 1189, 1201, 1217, 1229, and 1257, methoxy-MAMEs were detected at *m/z* 1235, 1263, 1275, 1291, 1303, 1319, 1331, and 1359.

A comprehensive analysis of MA subclass and molecular species composition of *M. bovis* BCG Tokyo 172 has used MALDI-TOF-MS for the determination of the molecular weight of the species detected[194]. After initial extraction of the lipids from the bacterial cells the group methylated the MAs, MAMEs were then separated into alpha-, methoxy- and keto-subgroups by HPTLC. Each subgroup was then further separated by $AgNO_3$ coated silica gel TLC and designated, α1, α2, methoxy 1-6 (m1-6) and keto 1-5 (k1-5). MALDI-MS analysis of α1 detected peaks at *m/z* 1117-1229 which the group assigned carbon chain lengths of C_{74}, C_{76}, C_{78},C_{80}, and C_{82} respectively, the major homologue is shown in bold. Peaks detected from α2 were observed at *m/z* 1131, 1159, 1187, and 1215, which the group assigned as C_{75}, C_{77}, C_{79}, and $C_{81.}$ MALDI-MS data presented by the group for the detection of the methoxy sub-subgroups were as follows; m1, *m/z* 1233, 1261, 1289, 1317, and 1345, assigned C_{81}, C_{83}, $C_{85,}$ C_{87}, and C_{89} homologues; m2, *m/z* 1275, 1303, and 1331, assigned C_{84}, C_{86}, and C_{88}; m3, *m/z* 1233, 1261, 1289, and 1317, assigned C_{81}, C_{83}, $C_{85,}$ and C_{87}; m4, *m/z* 1217, 1245, 1273, 1301, and 1329, assigned C_{80}, C_{82}, $C_{84,}$

$C_{86,}$ and C_{88}; m5, *m/z* 1233, 1247, 1261, 1275, 1289, 1303, 1331, and 1345, assigned C_{81} through to C_{89}; finally, m6, *m/z* 1259, 1287, 1315, and 1343, assigned C_{83}, $C_{85,}$ C_{87}, and $C_{89.}$ Similarly, MALDI-MS data for keto- sub-subgroups were presented as follows; k1, *m/z* 1217, 1245, 1273, 1301, and 1329, assigned C_{80}, C_{82}, $C_{84,}$ $C_{86,}$ and C_{88}; k2, *m/z* 1259, 1287, 1315, and 1343, assigned C_{83}, $C_{85,}$ C_{87}, and C_{89}; k3, *m/z* 1217, 1245, 1273, and 1301; k4, *m/z* 1203, 1231, 1259, 1287, and 1315; k5, *m/z* 1271, 1299, and 1327. With the aid of fast atom bombardment-MS and NMR analysis the group were able to structurally identify each species detected.

MALDI-TOF MS has since been applied to the analysis of the MA content of MA containing glycolipids, including TMM[196] and TDM[133, 197], with both the free acids and the whole glycolipids being analysed from a number of mycobacterium species. MALDI-TOF-MS was used in the analysis of mycolic acid content of TDM from nine species of *Mycobacterium*, five slow-growing virulent strains and four rapid-growing non-virulent strains. Analysis was again using MAMEs and all species were detected as $[M+Na]^+$. The group presented results detected from the analysis of MAMEs after alkali hydrolysis from TDMs. MALDI mass spectral data presented by the authors showed, *M. tb* H37Rv and *Aoyama B* strains to have similar MAME profiles. Peaks detected representing α-MAMEs were at *m/z* 1145-1285 for C_{76}-C_{86}, methoxy-MAMEs were at *m/z* 1219-1387 for C_{80}-C_{92}, and keto-MAMEs were detected at *m/z* 1203-1387 for C_{79}-C_{92}. The peak profiles observed for the *M. bovis BCG Tokyo* 172 were detected at *m/z* 1145-1257 (28 u difference) for α-MAMEs with carbon chain lengths C_{76}-C_{84}, methoxy-MAMEs were detected by the group at *m/z* 1233-1359 for C_{81}-C_{90}, and keto-MAMEs at, *m/z* 1217-1343 for C_{80}-C_{89}. The MALDI-MS results presented by the authors for the analysis of *M. bovis BCG Connaught* differed from those present for the other pathogenic strains due to this strain not being able to synthesis methoxy-MAMEs. Peaks for α-MAMEs were detected at *m/z* 1117-1257 assigned C_{74}-C_{84} by the authors, and keto-MAMEs were detected at *m/z*

1175-1371, assigned C_{77}-C_{91} by the authors. The MALDI mass spectra presented for the analysis of TDMs from these species is highly complex due to the numerous combinations of possible MAs within their structure. Using the compositional *m/z* acquired from the analysis of the hydrolysed MAs, coupled with the *m/z* obtained from their parent TDMs the authors deduced possible MA structures of TDMs for each respective species. This is the first report of such a study, and provides useful information of the structure-virulence relationship of TDMs in pathogenic *Mycobacterium*.

Other cell envelope lipid species, including PDIMs and PGLs, have been structurally investigated using MALDI-TOF MS in combination with NMR to identify lipid species involved in growth and virulence[132, 199-201].

1.6 Aims and Objectives

MALDI-MS and MSI investigations has widespread application across many research areas, but is limited by poor sensitivity and reproducibility in many instances. This can be partially addressed through optimisation of sample preparation methods. Investigations into sample preparation are aimed at increasing sensitivity, resolution, reproducibility, and techniques that enable MSI to be used alongside clinical pathology procedures to investigate disease processes.

The choice of matrix compound, a range of section thickness and storage parameters will be considered. There is little research in this area for lipid analysis to date; results from these investigations will be presented in chapter 2. Optimised matrix deposition methods aimed at enhancing sensitivity, mass and spatial resolution, increasing throughput times and reducing variability will be presented in chapter 3. This chapter will compare a robotic matrix deposition method to a manual airspray method. The analysis of archival tissue is highly desirable to study disease pathology. MALDI imaging of lipids from formalin fixed tissue, as prepared by clinical pathology laboratories is investigated. To the best of the author's knowledge, this has never been carried out before; results from this study form chapter 4 of this thesis.

The analysis and imaging of non-polar lipids by MALDI-MS proves to be somewhat difficult, due to their nature. MALDI-MS analysis and imaging of non-polar cell wall lipids from the *Mycobacterium tuberculosis* complex will be considered. The investigation of a variety of samples, including complex lymph and blood extracts, full lymph nodes and TLC plates, for MALDI-MS analysis and imaging of these lipids will be presented in chapter 5. Methods that enhance MALDI-MS sensitivity in the detection of non-polar lipids, particularly with regard to cell wall components of the *Mycobacterium tuberculosis* complex, are needed. Development and optimisation of matrix solvent systems is one way this can be achieved. The screening or evaluation of numerous solvent systems, with the aim of developing an optimised system, will be carried out. Comparisons will be made to those currently used in literature for these and other non-polar lipids, applications to complex bacterial extracts will be considered, results from this study will be presented in chapter 6.

2. An Investigation into the Effects of Sample Storage Parameters and Section Thickness for MALDI-MSI

2.1 Introduction

It is widely accepted that sample preparation is key to the success of a MALDI-MSI investigation; affecting both sensitivity and spectral and image quality[202, 203]. As sample preparation greatly influences the quality of results, every step of the preparation process must be carefully and correctly carried out in order to maintain as much spatial and chemical information as feasibly possible[204]. The choice of matrix compound and solvent system are crucial, and this is always the first procedure to be evaluated for MALDI-MS and MSI investigations[205-211]. As discussed in chapter one, the most suitable solvent system is one in which both the matrix and analyte/s are soluble. The matrix compound of choice is largely dependent on the type of molecules/analyte/s of choice, common MALDI matrices and their compound applications have been discussed in chapter 1. There is great diversity that exists not only between organs/tissues of interest, but also between molecules/species of interest from within these samples, and so no two experiments are the same[160, 212-224]. In general investigators optimise their experiments by varying sample preparation parameters before analysis of specific analyte/s of interest are investigated. Numerous reviews have been published with recommended guidelines for sample preparation procedures, such as range of tissue section thickness; section embedding; storage and storage temperatures, however these vary from investigator to investigator[21, 202-204, 218, 225]. It is generally accepted that tissue sections between thicknesses of 5-20 µm are suitable for MALDI-MSI experiments, with respect to extractable analytes and resulting spectral and image quality, with 10-20

μm being reported as optimal[204, 218]. Many investigators also desiccate samples for varying time periods after tissue sectioning, but prior to matrix deposition, this is to dehydrate the tissue sections[202, 203, 226, 227]. To the best of the author's knowledge no investigation has been reported on a comparison of the effects of sample storage or preparation prior to matrix deposition, such as to desiccate or not, and the length of time samples are in the desiccator. There have been two investigations published to date assessing sample thickness. The first investigated the effects of sample thickness on the sensitivity and signal and image quality of proteins detected from tissue[227]. The second assessed the effects of section thickness on laser profiling depth, and thus detection sensitivity and signal quality for both large and small compounds[228]. The two studies produced conflicting results.

In this chapter αCHCA and DHB, two commonly used matrices for the investigation of small molecules[165, 210, 229-231], were evaluated for the analysis of previously reported GPL species[13, 14, 155, 156, 165, 171, 196, 205, 230-233]. Initial investigations used rat brain lipid extracts to assess which matrix produced the best overall results. They were then both assessed for their suitability for MALDI-MSI studies. The selected matrix was then used in MALDI-MS imaging of GPLs to investigate the effects of varying sample thickness, between 5-50 μm. The effect of sample desiccation prior to MALDI matrix application is concluded.

2.2 Experimental

2.2.1 Materials

Alpha-cyano-4-hydroxy cinnamic acid (α-CHCA), 2, 5-dihydroxybenzoic acid (DHB) and trifluoroacetic acid (TFA) were purchased from Sigma-Aldrich (Dorset, UK). Methanol and chloroform were purchased from Fisher Scientific (Loughborough, UK). Whole control rat brains were supplied by Covance, (Harrogate, UK).

2.2.2 Matrix Evaluation for GPL Investigations

Whole brain lipid extracts were prepared using the Folch[234] method and stored at -20°C until analysis. For analysis, 1 µL of extract was deposited onto a stainless steel MALDI target plate and allowed to air dry at room temperature, 1 µL of either αCHCA 10 mg/mL or DHB 12.5 mg/mL (80% MeOH, 0.1% TFA) was deposited on top of the extract.

Serial sagittal rat brain sections were taken at 12 µm on a Leica CM 1800 cryostat, and transferred to stainless steel MALDI target plates prior to matrix deposition and analysis.

2.2.3 Sample Storage and Section Thickness

MALDI plates were prepared with serial sagittal sections of rat brain tissue; sectioned at 12 and 40 µm on a Leica CM 1800 cryostat. Plate A was immediately sprayed (10 min after sectioning, to allow temperature equilibration) with matrix and analysed. Plate B was stored for 24 h at -20°C, on removal from the freezer the sections were left for 10 min to allow temperature equilibrium before matrix deposition and analysis. Plate C was placed in a desiccator for 1 h, and Plate D was stored in a desiccator for 24 h prior to matrix application and analysis.

In further investigation on the effects of tissue thickness the cerebellum of rat brain tissue was bisected along the midline of the sagittal plane, and embedded on a cryostat chuck using water-ice slush. Serial sections at 5, 10, 14, 20, 25, 30, 35, 40, 45 and 50 µm were taken and transferred to a stainless steel MALDI target plate for analysis. Matrix deposition was carried out as described below.

2.2.4 Matrix Deposition for MALDI-MSI

Matrix deposition was via an artistic airbrush (Badger Airbrush Ltd, UK), the MALDI target insert was held in a fume hood using a clamp, 25 mg/mL αCHCA matrix material solution, (prepared in 80% methanol (0.1% TFA)) was deposited over each plate in cycles, allowing time to dry between each cycle. Deposition was carried out from a distance of 15-20 cm, the plate was rotated 90° between each cycle to ensure an even distribution, deposition was deemed optimal when 9 mL had been deposited.

2.2.5 MALDI-MS

Analysis of the lipid brain extract was carried out using an Applied Biosystems (Toronto, Canada) hybrid quadrupole time-of-flight (QqTOF) instrument (Qstar XL). The instrument was fitted with an orthogonal MALDI ion source and a nitrogen laser (337nm), operated at 20 % available power with a repetition rate of 20Hz. The instrument was operated in the positive ion reflectron mode, recording all signals between *m/z* 50-1000. Data collection was via an automated pre-determined pattern analysis over the sample spot, using a Q1 scan time of 1 s, summing 15 scans per spectrum obtained. Mass spectral data was analysed using Analyst software supplied by Applied Biosystems.

2.2.6 MALDI-MSI

MALDI mass spectrometric analysis was carried out using a QqTOF (Qstar XL – Applied Biosystems, Toronto, Canada) mass spectrometer fitted with an orthogonal MALDI ion source. The nitrogen laser (337nm) energy was operated at 20% available power for CHCA and 30% for DHB, with a repetition rate of 20 Hz. MALDI-QqTOF mass spectra were collected at 150 µm intervals, with a laser dwell time of 2 s at each location. A dwell time of 2 s is optimal before the matrix is completely ablated and the signal is lost. The resulting two-dimensional ion density maps were generated using the TissueView software, after conversion of the raw data into the format required using the 'wiff to analyse' script, provided by applied biosystems.

In the subsequent analysis of tissue section thickness, sections of cerebella were analysed using QqTOF (Qstar Elite – Applied Biosystems, Toronto, Canada), operated in positive ion reflectron mode. Instrument parameters had been previously optimised for the analysis of PCs from rat brain, data was acquired between the mass range *m/z* 50-1000. The Nd:YAG (355nm) laser was operated at 20 % available power (2.1 µJ), with a repetition rate of 500 Hz. The target plate stepping distance was set to 100 µm for both the x and y dimension using the imaging acquisition software. Data were acquired using the 'dynamic pixel' setting, which involves the laser being moved within the 100 μm^2 pixel area and resultant data being summed to give an accumulated mass spectrum over one second for each pixel area. The resulting two-dimensional ion density maps were generated using the TissueView software, after conversion of the raw data into the format required using the 'wiff to analyse' script, provided by Applied Biosystems.

2.3 Results and Discussion

2.3.1 Matrix Evaluation for MALDI-MS and MSI Analysis of Lipids

To evaluate the most suitable matrix compound to use for MALDI-MS investigations of lipid species from tissue, αCHCA and DHB were used as matrix compounds in analysis of brain lipid extract. Each matrix was assessed on spectral quality, species present and ion counts/sensitivity. The spectral complexity differs remarkably for the two different matrices assessed, as shown by the overlay spectrum presented in figure 2.1. There are a much higher number of peaks present in the mass spectrum for αCHCA (red trace) compared to DHB (blue trace). This is believed to be due to αCHCA forming a higher number of matrix clusters or associated peaks compared to DHB. In addition to this αCHCA is what is termed a 'hot' matrix, in that is causes a higher degree of analyte fragmentation compared to 'cold' matrices such as DHB[49, 70, 72]. This is visible in the spectrum presented in figure 1, when focusing on the mass range between *m/z* 300-650, *m/z* within this range represent the neutral losses of PC head groups and fatty acids from GPLs and SMs[235]. The ion counts for the lipid fragments are much lower for DHB (labelled blue peaks) compared to αCHCA (red peaks), for which ion counts for *m/z* 478 and 504 go into the thousands. DHB appears to show a two-fold increase in ion counts for common lipid species, which is demonstrated by the mass spectra presented in figure 2.2. When observing the two most common species detected from rat brain sections, PC 32:0 and PC 34:1 at *m/z* 734 and 760 representing $[M+H]^+$, *m/z* 756 and 782 for $[M+Na]^+$, and *m/z* 772 and 798 representing $[M+K]^+$ for these lipids, the increase is clearly visible when using DHB. The ion counts for PC 32:0 at *m/z* 734 were 225 counts for αCHCA and 609 counts for DHB from the spectra present in figure 2.2. The same trend was observed for

the protonated ion of PC 34:1 at *m/z* 760, where the ion counts using αCHCA as the matrix were 505 counts compared to 1124 counts for DHB.

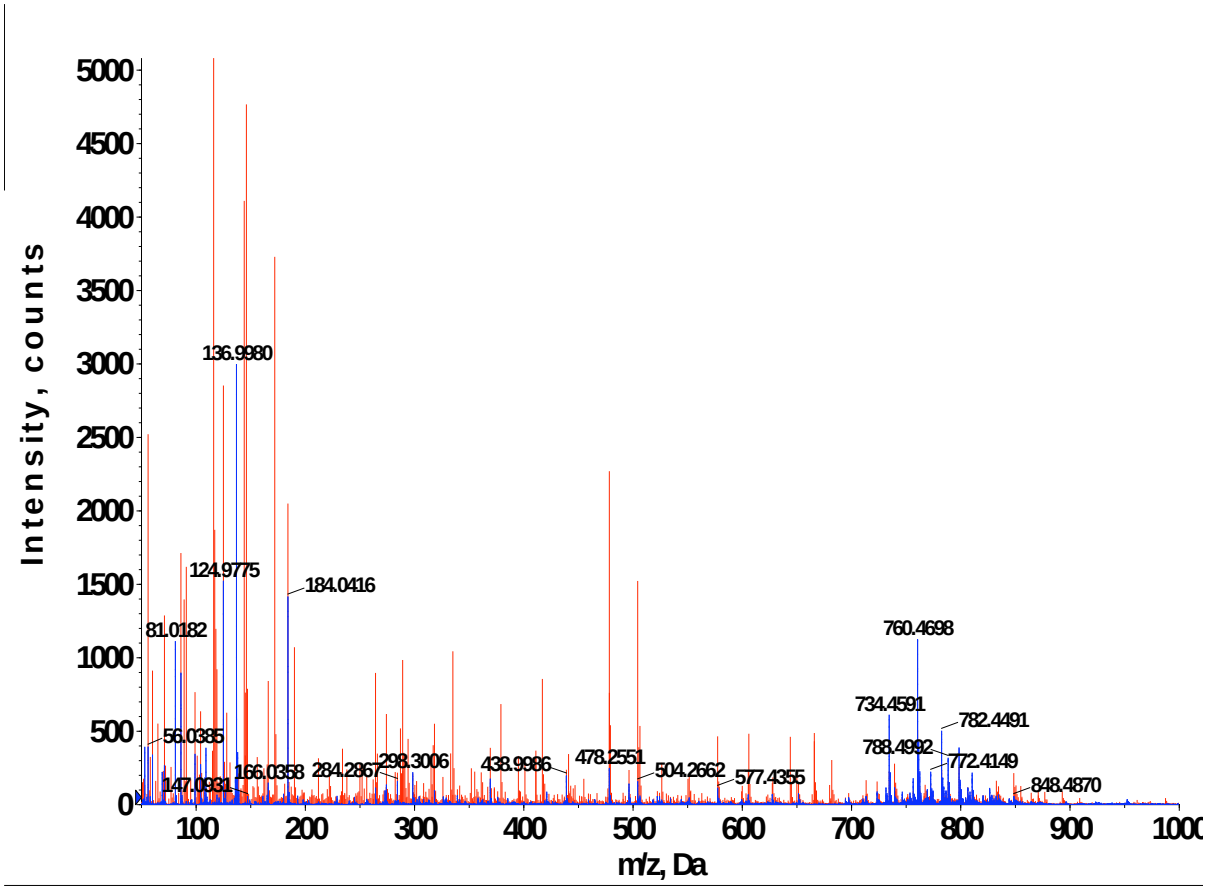

Figure 2.1. MALDI mass spectral overlay of brain lipid extract for αCHCA (red trace) and DHB (blue trace). A large difference in spectral complexity is visible due to the high number of αCHCA peaks, shown in red. Conversely, DHB shows not only reduced spectral complexity but also produced higher ion counts for lipids species of interest as shown by the labelled blue peaks *m/z* 700-900.

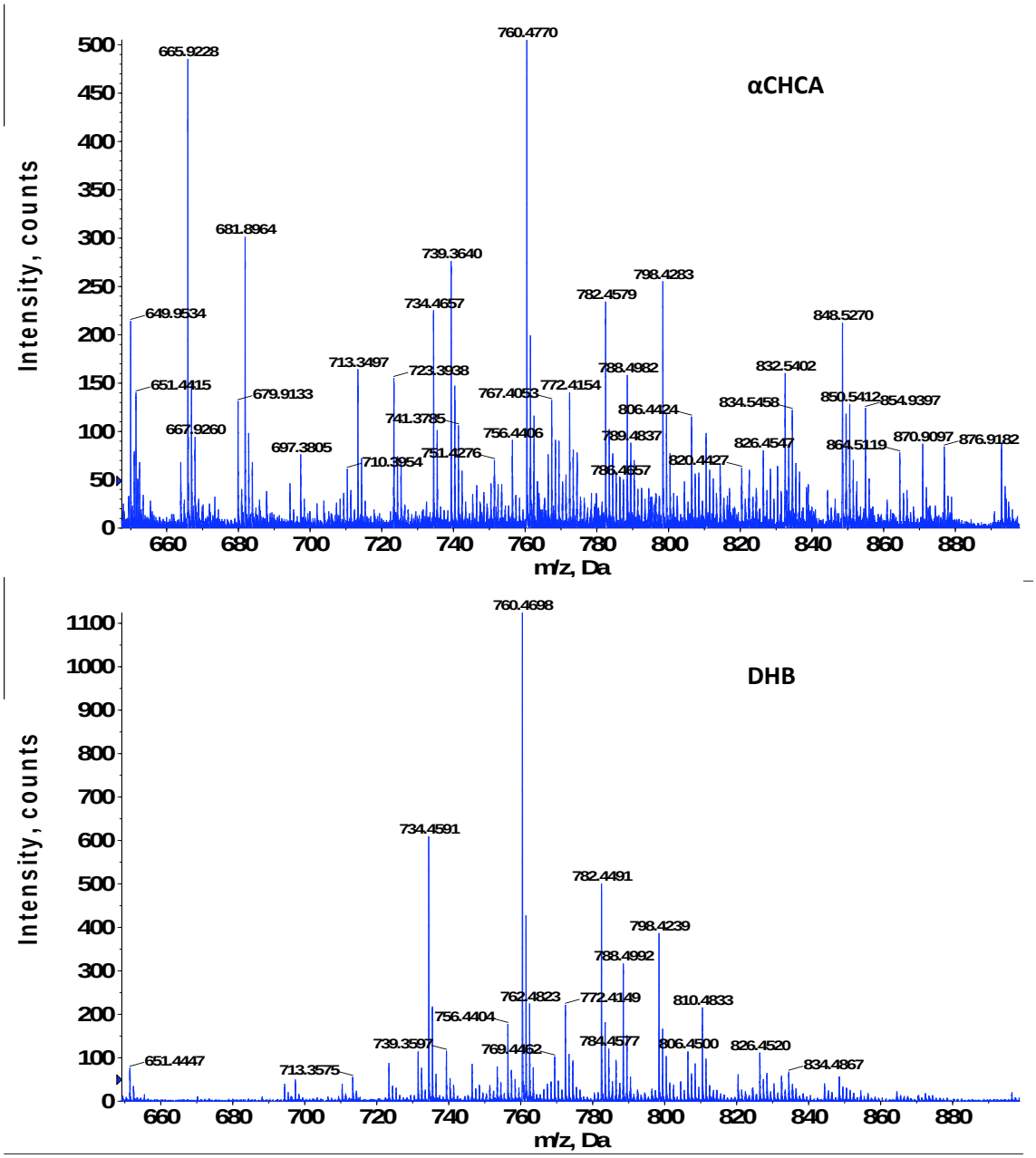

Figure 2.2. MALDI mass spectra of brain lipid extract acquired using αCHCA (top spectrum) and DHB (bottom spectrum). The increased spectral complexity observed with αCHCA is clearly visible. There appears to be a two-fold increase in ion counts for lipid species of interest using DHB as the matrix system compared to αCHCA.

The analysis of the lipid extract was repeated five times and the mean ion counts for several lipid species were recorded. The mean ion counts for the $[M+H]^+$ of three different lipid species, PC 32:0, PC 34:1 and PC 36:1, for αCHCA and DHB is presented in figure 2.3. For all lipid species DHB proved to be the most sensitive matrix compound to use. This matrix produced over a three-fold increase in ion counts for PC 32:0 and PC 36:1 and over a two-fold increase in ion counts for PC 34:1. Brain tissue contains high concentrations of sodium and potassium, thought to be due to the Na^+/K^+ ATPase (also known as the sodium/potassium pump)[179, 236], this increases spectral complexity when analysing lipids from brain tissue, as the $[M+H]^+$, $[M+Na]^+$ and $[M+K]^+$ adducts are commonly detected in MALDI-MS analysis. To evaluate total ion yields from single molecules, all ions for a given lipid species were summed, the results are presented in the graph in figure 2.4. Review of the sum of ion counts for $[M+H]^+$, $[M+Na]^+$ and $[M+K]^+$ revealed the same trends were observed as for the $[M+H]^+$, with DHB giving over a two-fold increase in counts for PC 34:1 and over a three-fold increase for PC 32:0 and 36:1. These results show the improvement is not linear across all species, preferential ionisation of certain lipid species if apparent, this could be attributed to the different matrix used, however, it could also be a laser affect, as DHB requires a higher laser power for optimal ionisation. Previously reported lipid species detected from the lipid extracts using both matrices are presented in table 3.

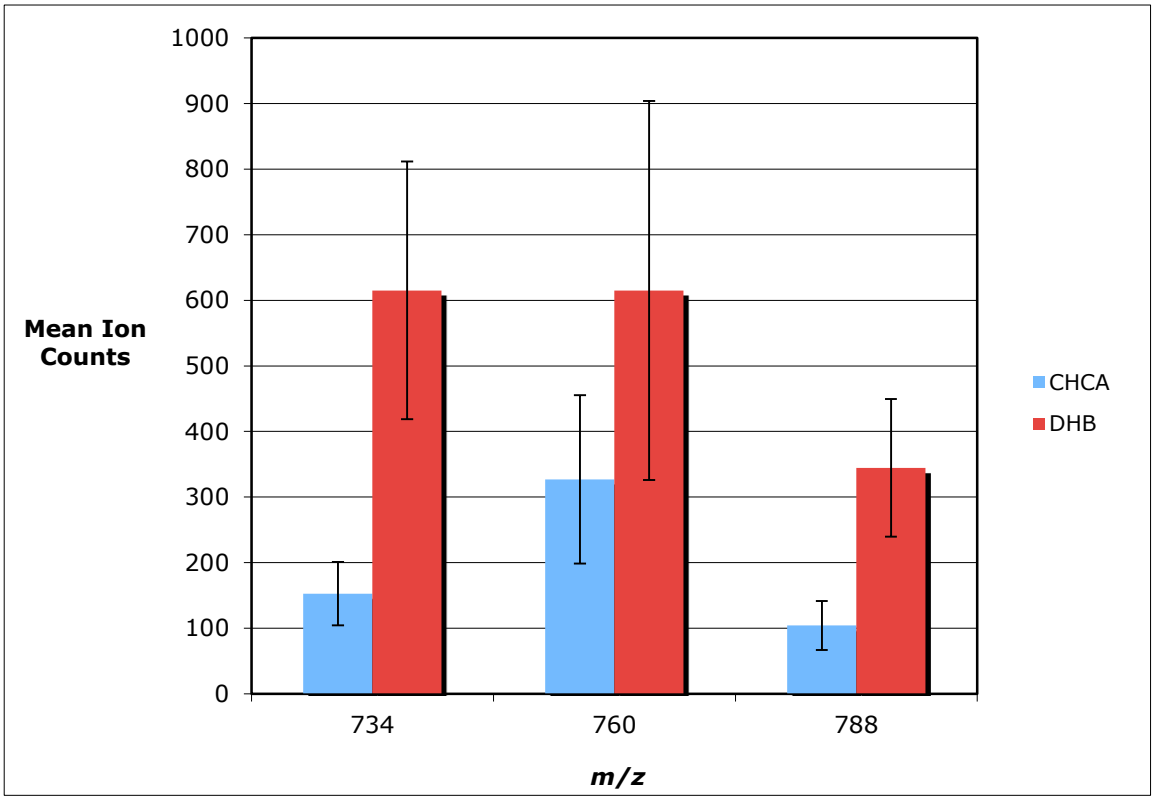

Figure 2.3. MALDI-MS data from the analysis of brain lipid extract using αCHCA and DHB as the matrices. The selected *m/z* values represent the $[M+H]^+$ for PC 32:0, PC 34:1 and PC 36:1 from left to right respectively. Values presented are the mean ion counts ± SD taken from 5 repeat analyses. For all species DHB produced the highest ion counts.

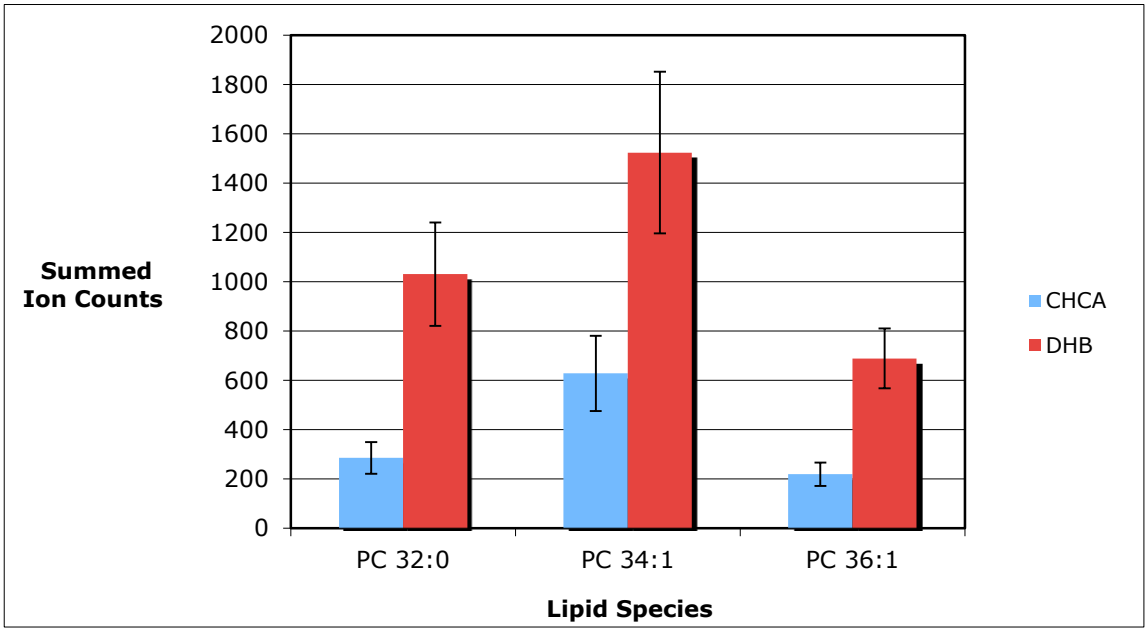

Figure 2.4. MALDI-MS data summing the mean ion counts (n=5) for the $[M+H]^+$, $[M+Na]^+$ and $[M+K]^+$ ions for PC 32:0, PC 34:1 and PC 36:1. DHB shows over a two-fold increase in signal intensity in analysis of dried droplet lipid extracts.

Species	[M+H]+	[M+Na]+	[M+K]+	References
SM 18:0	731	753	769	[14, 165, 166, 232]
SM 20:0	759	781	797	[232]
PC 32:1	732	754	770	[205, 231]
PC 32:0	734	756	772	[14, 165, 166, 205, 231, 232]
PC 34:1	760	782	798	[165, 166, 205, 231, 232]
PC 34:0	762	784	800	[14, 232]
PC 36:4	782	804	820	[165, 166, 205, 231]
PC 36:3	784	806	822	[205, 231]
PC 36:2	786	808	824	[205, 231]
PC 36:1	788	810	826	[165, 166, 231, 232]
PC 38:6	806	828	844	[165, 166, 231]
PC 38:5	808	830	846	[205, 231]
PC 38:4	810	832	849	[205, 231]
PC 38:3	812	834	851	[205]
PE 36:2	744	766	782	[205]
PE 36:1	746	768	784	[205]
PE 38:4	768	790	806	[14]
PE 40:6	792	814	830	[205]

Table 3. List of *m/z* of SM, PC and PE species detected using both αCHCA and DHB as the matrix compounds, along with their previously published record. Isobaric ions are colour coded.

Analysis of solutions on a spot plate and analysis of tissue in an imaging experiment are very different, tissue sections are highly complex compared to solutions and sufficient extraction of the analyte/s can be difficult. A key factor when considering a matrix compound for MALDI-MSI investigations is crystal size and morphology and homogeneity, as these factors affect resolution, and spectral/image quality. Although DHB proved to be the most suitable matrix for spot analysis of lipid extracts, both matrices must be evaluated for their suitability for MALDI-MS imaging studies of lipids.

Contrary to results from the analysis of lipid extracts from spot samples, the direct analysis of rat brains using DHB at the matrix did not produce any recordable analyte ions. The optimisation of DHB for imaging studies was thus unsuccessful; DHB crystals appear white when deposited over the MALDI target plate, which made it quite difficult to evaluate how much material was being deposited on the tissue. The formation of DHB crystals within the airbrush column and at the tip caused repeated blockages and spluttering of the gun. DHB is known to form large needle like crystals, the size of the matrix crystals influence the image resolution, if they are larger than the laser spot size then resolution is compromised[41, 164, 237]. The results obtained using αCHCA as the matrix system were of high quality, image resolution was clear and defined for airbrush deposition, high numbers of lipid species were detected (all corresponding to those previously published and those detected from the extract). The facile detection of lipid species using αCHCA resulted in high ion counts, and the lateral distribution of PLs across the brain section showed clear anatomical differentiation for a number of species. The crystal size and morphology using αCHCA is that of small rounded crystals, establishing good coverage on the sample surface and greatly increased homogeneity compared to DHB. These results, combined with the much lower laser power needed for desorption/ionisation, lead to the decision of αCHCA being the most suitable matrix to take forward for all imaging studies of lipids from tissue sections. For these reasons DHB was not optimised further. A direct comparison of image resolution achieved with the two

matrices has recently been published, much more highly resolved images are observed for αCHCA[172].

2.3.2 Sample Preparation and Thickness

Images of *m/z* 772 (potassium adduct of PC 32:0) presented in figure 2.5 clearly show well defined anatomical regions that correspond to those previously published for the MALDI-MSI analysis of this lipid[165]. This lipid is highly abundant in rat brain, readily ionises in positive ion mode, and its anatomical distribution has been published[12, 14, 156, 164-166, 205, 230-232, 238], which is why this *m/z* was chosen to compare data obtained from the analysis of the different sample preparation methods. Initial results demonstrated that analysis of 40 µm sections of fresh-frozen tissue yielded marginally higher ion counts than those observed in analysis of sections prepared at 12 µm (figure 2.5, plates A and B). Little difference was found between the 12 and 40 µm sections that were desiccated, as demonstrated by the relatively similar ion intensity across the tissues for these plates, presented in figure 2.5, plates C and D.

In order to achieve high ion counts for a given analyte, the analyte must be incorporated sufficiently within the matrix crystals (co-crystallisation) during the crystal drying process. A slower crystal drying time increases this process but also increases crystal size which in turn decreases image resolution[34, 239]. If the crystals dry too fast the analyte/s have less time to migrate into the crystals and sensitivity is often compromised[238, 239]. Images from the sample prepared immediately after sectioning and the sample stored in the freezer display a much higher signal compared to the desiccated samples, as shown by the pixel intensity in figure 2.5. This may be attributed to the desiccated samples being much dryer upon matrix deposition compared to the samples that were prepared for analysis after sectioning/removal from the freezer. In these samples the solvent system

used for the deposition of matrix material may have evaporated much faster than in the fresh samples, reducing the time available for the analyte/s to incorporate into the matrix crystals. The images also illustrated slightly higher ion counts are observed in the sample desiccated for 24 h compared to the sample desiccated for 1 h.

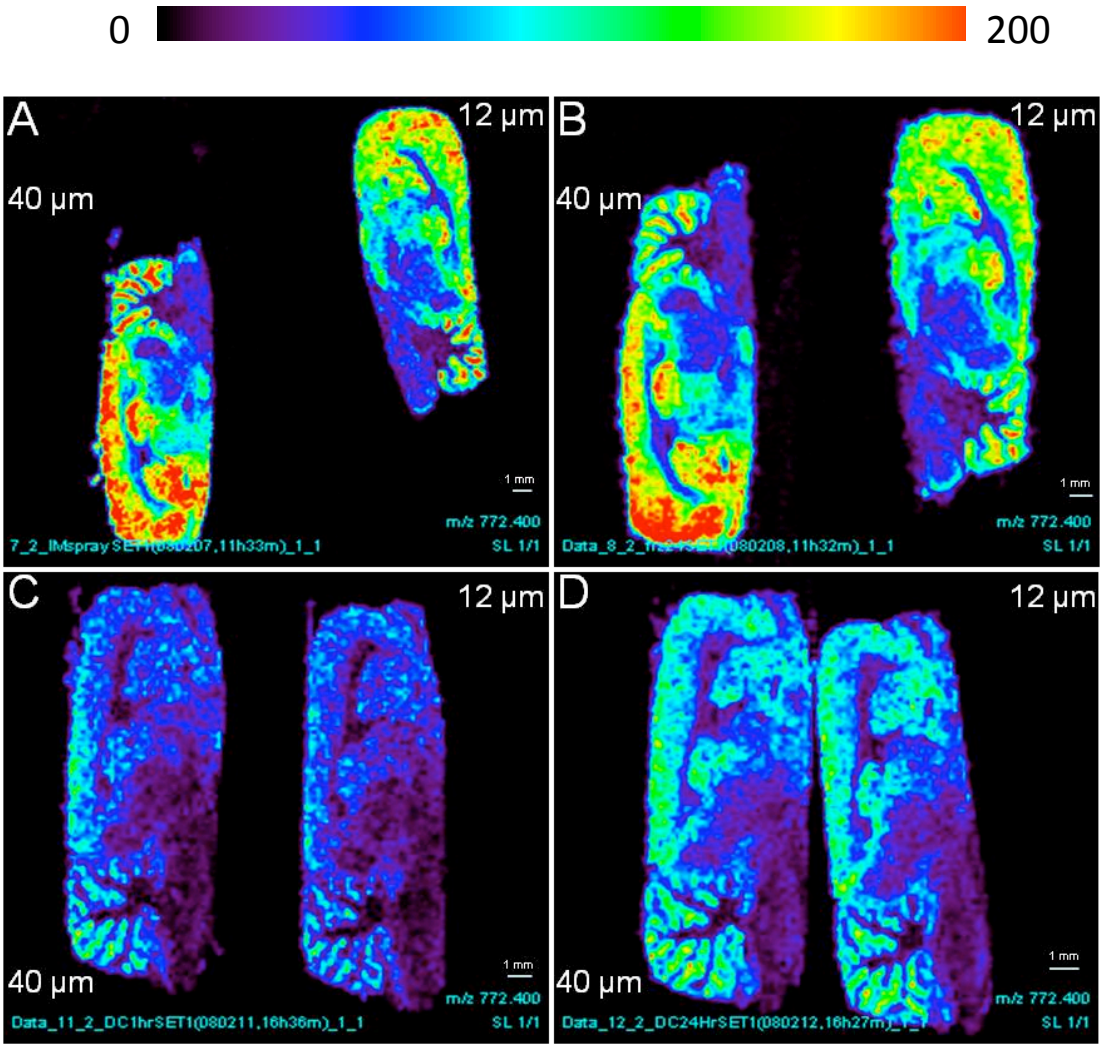

Figure 2.5. MALDI-MS images of m/z 772 $[PC32:0+K]^+$. Plate A sprayed immediately, plate B frozen for 24 h, plate C desiccated for 1 h and plate D desiccated for 24 h. In all cases the 40 µm section is on the left and the 12 µm section on the right. The sample prepared immediately after sectioning (A) and the sample stored in the freezer for 24 h (B) display the highest signal intensities, with similar pixel intensities seen for both. These are significantly higher than the samples that were desiccated (C and D).

To further assess the effects of sample preparation single point spectra were taken from 10 different anatomical regions of the cerebral cortex for each sample preparation method. The mean ion counts of two commonly detected lipids species, PC 32:0 and PC 34:1 were calculated to investigate the difference in signal intensity, results are presented in figure 2.6. The sample prepared immediately after sectioning displayed a two-fold increase in ion counts compared to both of the samples that were desiccated prior to matrix deposition. The sample stored in the freezer for 24 hrs prior to matrix deposition showed higher ion counts than both of the desiccated samples, but lower ion counts than the freshly prepared plate. The lower signal intensity may be signs of slight degradation, even after 24 h, which would not normally be noticeable because the signal quality is still good. The sample desiccated for 24 h prior to matrix deposition displayed marginally higher ion counts than the sample desiccated for 1 h; the difference is not high enough to be significant.

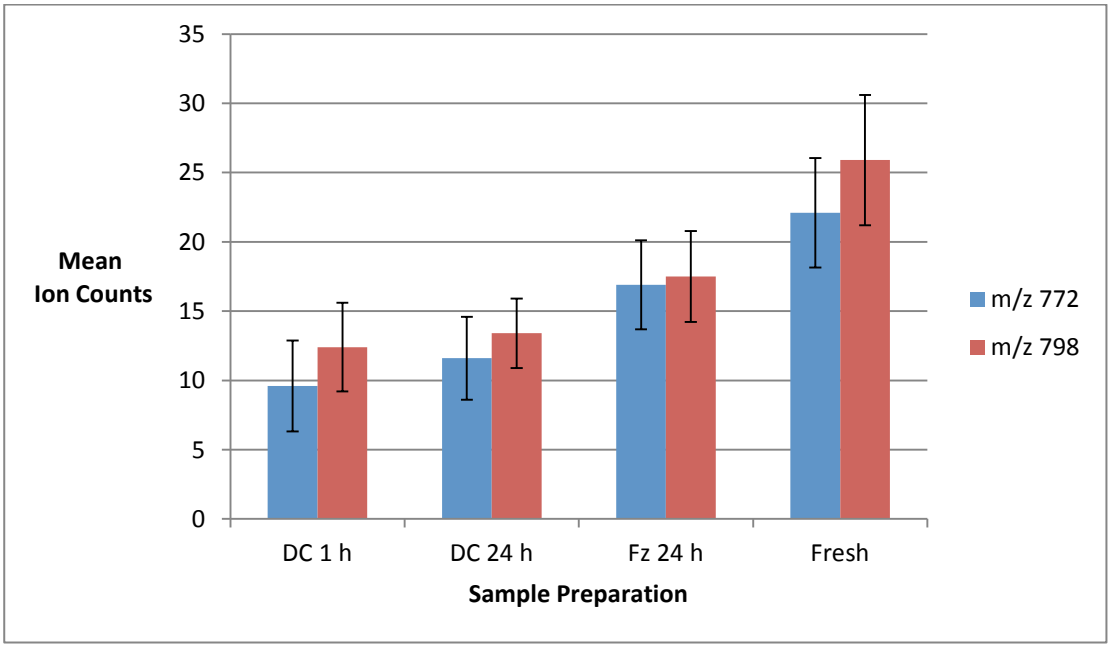

Figure 2.6. MALDI-MS single point spectral data taken from 10 different anatomical regions of the cerebral cortex for each sample preparation method. The mean ion counts ± SD for PC 32:0, *m/z* 772 and PC 34:1, *m/z* 798 are displayed, both are $[M+K]^+$. Lower ion counts are seen in the desiccated samples.

It should be noted that the matrix selection and concentration remained fixed for a given experiment, but matrix deposition for each experiment or plate was carried out individually. The comparison of ion intensities for section thickness across a given sample plate therefore remained constant. There may however be slight differences in the amount of matrix applied to each plate, as deposition was carried out manually and thus difficult to reproduce. To investigate whether the effects observed with the different sample preparation methods were a result of varying amounts of matrix being deposited onto the plates, and not the storage conditions, single point spectra were analysed from ten different regions on each plate (off tissue). As αCHCA forms many clusters in addition to the protonated, dehydrated ion and sodium and potassium adducts, all matrix peaks above 10 % relative intensity were summed. The sample desiccated for 1 hour prior to matrix deposition displayed the highest mean ion counts (n=10) for matrix ions on the plate; followed by the samples prepared immediately after sectioning/removal from the freezer; with the sample desiccated for 24 h displaying the lowest, as presented in figure 2.7. There is a three-fold increase in summed matrix ions for the sample prepared immediately after sectioning and the sample prepared after removal from the freezer compared to the sample desiccated for 24 h prior to matrix deposition. The sample desiccated for 1 h prior to matrix deposition showed a four-fold increase in summed matrix ions compared to the sample desiccated for 24 h. This finding was not expected as this sample preparation method displayed the lowest ion counts across all lipid species, as more matrix was deposited, higher analyte signals might be expected. The low ion counts seen with the sample desiccated for 1 h could be due to analyte suppression effects caused by high concentrations of matrix ions. The matrix ion counts from this sample, however, were not much higher than those from the sample prepared after sectioning, and the sample prepared after storage in the freezer for 24 h prior to matrix deposition, thus similar analyte/s signals would have been expected. The latter two preparation methods displayed similar matrix ion counts and relatively similar lipid ion

counts. The sample desiccated for 24 h displayed much lower matrix ions on the plate compared to all other preparation methods, indicating less was deposited onto this plate. If a low a concentration of matrix was deposited on this plate it would lead to inefficient extraction and incorporation of the analyte molecules into the matrix crystals, which in turn would greatly affect signal quality. An interesting observation however, is that the ion counts for lipid species of interest are higher in this sample than the sample desiccated for 1 h, which appears to have had the highest amount of matrix deposited on the plate. The poor results observed with the samples that were desiccated prior to matrix deposition could thus be attributed to different amounts of matrix being deposited on each plate. It is rather difficult to achieve the same amount each time when depositing the matrix manually via airbrush deposition, hence the need for fully automated systems.

Crystal formation on stainless steel target plates and tissue surfaces are very different, for this reason matrix ion intensity on tissue was assessed. The most abundant matrix ion detected on tissue is observed at *m/z* 265, representing $[M+2K-2H]^{+\cdot}$, the protonated species is detected with low intensity, if it is detected at all on tissue, thus *m/z* 265 was used for comparison. The mean ion counts taken from single point spectral data from ten different anatomical locations were again used here. Interestingly the results do not correlate to the amount of matrix deposited on each plate, as seen by comparing the data presented in figure 2.8 for matrix on tissue, to the data in figure 2.7 for matrix off tissue. The sample desiccated for one hour, which appeared to have the highest amount of matrix deposited over the plate, display the lowest ion counts for matrix on tissue. Results presented here correspond to those observed for analyte detection in each sample preparation method. Collectively these results suggest that desiccating samples prior to matrix deposition affects the surface properties of the tissue, resulting in reduced analyte extraction compared to samples that had not been desiccated. Results observed may

also be due to matrix crystals forming differently on each sample, with poorer analyte incorporation and co-crystalisation in the desiccated samples.

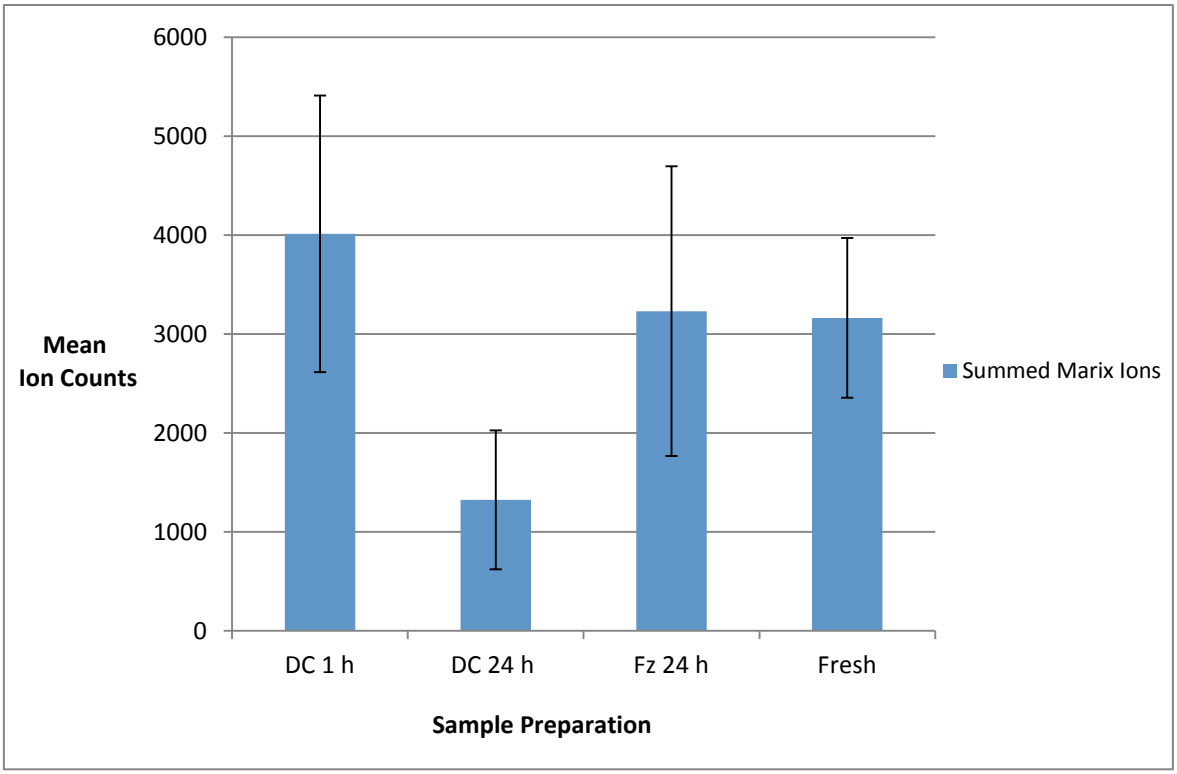

Figure 2.7. MALDI-MS single point spectral data taken from 10 different regions on the plate (away from tissue areas), for each sample preparation method. Every matrix peak above 10 % of the relative intensity was summed and the mean ion counts from this displayed. The sample desiccated for 1 h appears to have a the highest concentration of matrix deposited, the freshly prepared and the sample stored in a freezer for 24 h have a similar amount, with the sample desiccated for 24 h showing the lowest matrix ion counts on the MALDI target plate.

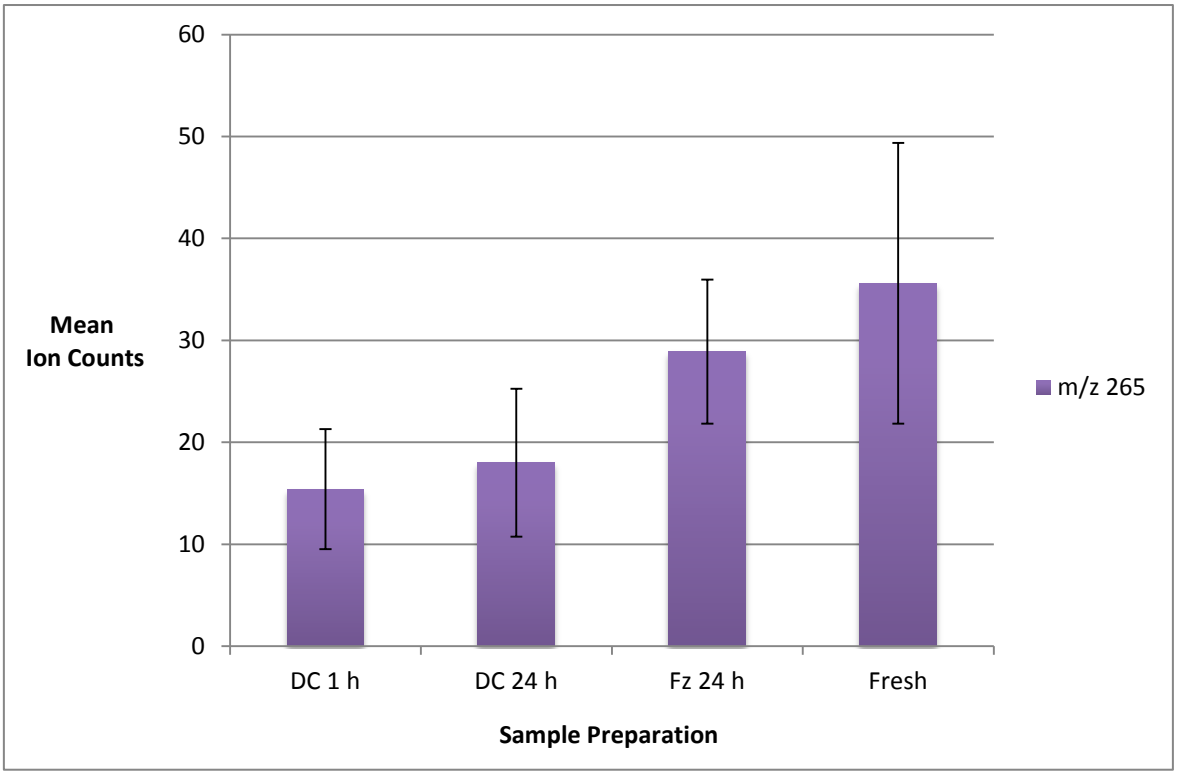

Figure 2.8. MALDI-MS single point spectral data taken from 10 different anatomical regions of the cerebral cortex for each sample preparation method. The mean ion counts ± SD of a matrix ion at *m/z* 265 are displayed. Lower ion counts are seen in the desiccated samples.

2.3.3 Sample Thickness

Next a more detailed study into sample thickness was carried out. The aim of this experiment was to investigate a wider range of thicknesses than in the previous experiment, to evaluate an Nd:YAG laser and a newer more sensitive QqTOF instrument. Two lipids were chosen that displayed a differential distribution over the cerebella grey and white matter regions. The distribution of PC 32:0, *m/z* 772 clearly highlights the outer molecular and inner granular layers (grey matter regions) of the cerebellar cortex. There was little difference observed in signal intensity for the 5-40 μm sections, the sections taken at 45 and 50 μm show slightly higher signal intensities, with 50 μm showing the highest overall, as demonstrated in figure 2. 9 (left image). The images of PC 34:0, *m/z* 784, show this lipid following the contours of white matter regions, including the *arbour vitae*, fourth ventricle and Purkinje cells which run through the junction of the inner granular layer of the cerebellum. Images presented show a similar trend to those observed with PC 32:0, in that there is little difference in signal intensity for section 5-40 μm, with 45 and 50 μm sections showing slightly higher signal intensities, as shown in figure 2.9 (right image). This trend was observed for every *m/z* investigated.

Single point spectra were taken from 10 different anatomical regions of the cerebellum, 5 from white matter regions (*arbour vitae* and fourth ventricle), and 5 from grey matter regions (molecular and granular layers). Mean ion counts of *m/z* 772 and 784 were recorded for each of the sample thicknesses, results not shown. Although not entirely accurate as these are single point spectra and thus a degree of variability exists, results do correspond with those observed in figure 2.5, in that there is little difference in signal intensity for most section thicknesses, with the 50 μm section showing higher ion counts across the sample. No difference was observed in the detection efficiency, with respect to the number of lipid species observed in both the mass spectra and resulting 2D images from each of the sample thicknesses.

Results here are not in agreement with a previously published paper by Sugiura and co-workers (2006)[227], who found thinner tissue sections produced greater ion counts, and improved spectral quality with a higher number of proteins being identified. The group determined 2 µm sections to be more efficient and anything above 10-20 µm having drastically reduced ion counts and greater spectral interference from tissue related molecules, as well as a decrease in S/N ratio. It must be noted that sectioning at a thickness of 2 µm by cryomicrotomy (as described by this group) is quite difficult to achieve, this is rather thin for a frozen section and the parameter settings are not an exact measurement. The group concluded that the charging effect on tissue sections increased with thicker sections, as well as greater interference from biological compounds, including salts, lipids and other proteins that are not washed away efficiently during the washing stages of sample preparation, due to the section thickness. This in turn resulted in a loss of ionisation, efficiency of detection and thus reduced spectral quality. It must be noted that the study in this chapter did not use pre-washing steps and the analysis was carried out for highly abundant small molecular weight compounds rather than large molecular weight compounds such as proteins, as presented by Sugiura *et al* (2006)[227].
Results found here are in agreement with a study published by Crossman and co-workers (2006)[228], who carried out experiments on profiling depths in MALDI analysis. The group successfully ionised both large (protein, cytochrome c) and small (drug, prozasin) molecular weight molecules from liver sections covered by two 20 µm control brain sections. This demonstrated that laser profiling depth of MALDI analysis is greater than 40 µm. This group postulated that profiling depth is dependent on the size and velocity of matrix droplets during deposition, cell density of the tissue under interrogation, and dissociation efficiency of the analyte from its binding tissue. These theories can be used to explain why the results obtained here do not correspond to those previously published in the former study. The concentration of matrix used here is higher, as is the number of deposition cycles compared to the method used in the Sugiura paper, which may account

for some of the variation seen. Rather than charging effects and biological interferences being responsible for decreased spectral quality and ion counts seen in thicker sections; decreased penetration of matrix and solvent into the tissue leading to insufficient extraction of the analyte/s could well be responsible.

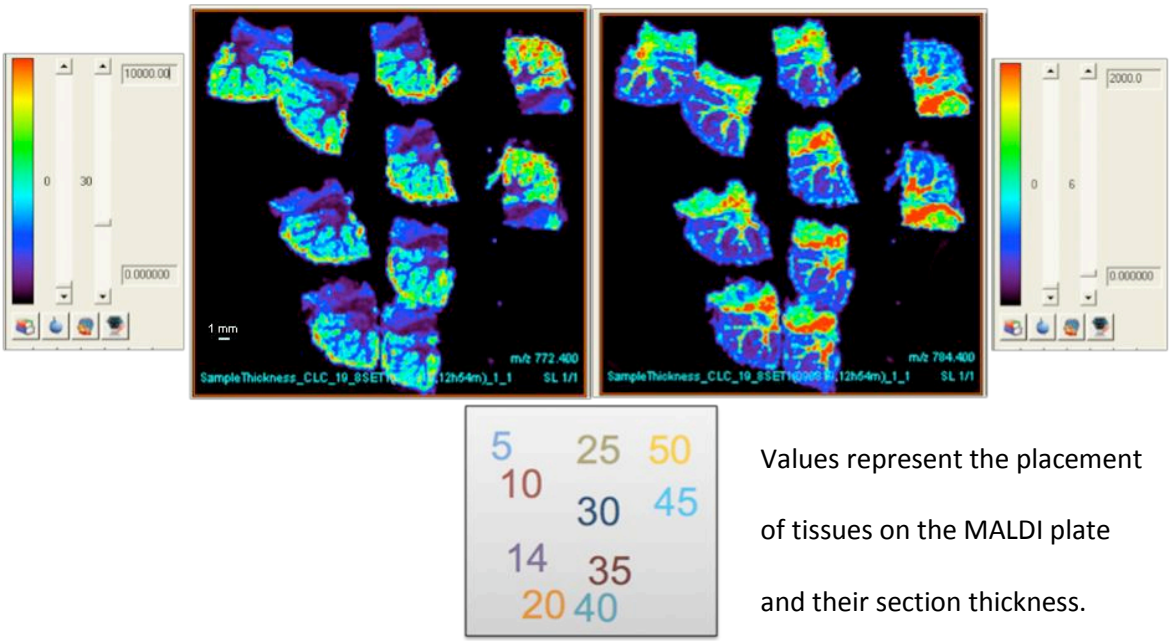

Figure 2.9. MALDI-MS images showing the differential distribution of PC 32:0, *m/z* 772 $[M+K]^+$ (left image), and PC 34:0, *m/z* 784 $[M+Na]^+$ (right image) across cerebellar sections. Sections range from 5-50 µm as indicated by the schematic below the images. Little difference is observed in the signal across the tissue for the sections ranging 5-40 µm, indicated by similar pixel intensity distribution across the sections. The cerebellum sectioned at 45 and 50 µm show a higher signal is detected from these sections.

The use of two different instrument platforms, the Qstar XL (commercially available in 2002) and the Qstar Elite (commercially available in 2006) along with the configuration of two different lasers lends the opportunity to assess the difference in sensitivity afforded by both. Although a direct comparison cannot be made with regard to the lasers, as they were operated on different instrument platforms, the nitrogen on the XL and the Nd:YAG on the Elite, some information can be gained. The Qstar Elite is a newer version of the XL, with a reported 10 times increase in sensitivity (manufacturer information), which is clearly visible when comparing the images produced from the distribution of *m/z* 772 across the tissue sections for the cerebella section thicknesses, figure 2.9 and the sample preparation plates in figure 2.5. There is a fifty-fold increase in the intensity scale representing the former compared to the latter, however the images produced do vary in colour intensity, thus this is not an accurate measurement. Five single point spectra were taken from grey matter regions of the cerebella and five from the white, from the plate analysed on the Elite and the sample plate prepared immediate and analysed on the XL, all spectra were taken from the 40 μm sections. The mean ion counts from the two lipid species used for the comparison of sample thickness were again used here, for two reasons, firstly they display a differential distribution across the brain, and secondly because they are detected at different abundances. The lipid at *m/z* 772 is detected with high abundance, whereas *m/z* 784 is detected with a much lower abundance. The mean ion counts for these species showed a 15 fold increase for *m/z* 772 and a 30 fold increase for *m/z* 784, as presented in figure 10. For all lipid species detected a large increase in sensitivity was observed for the Elite compared to the XL. The images acquired using the Elite were also at a lower resolution compared to the XL, 100 μm^2 compared to 150 μm^2, lower resolution is known to have a negative effect on spectral quality, this was not observed here. The laser dwell time for the nitrogen laser on the XL was also double that of the Nd:YAG on the Elite, thus such a large difference in sensitivity would not have been expected. The manufacturers state the Elite is 10 times more sensitive than the XL,

results here show a much greater increase in sensitivity, even at a lower resolution and shorter dwell time. The high rep laser could well be responsible for this for the greater increase in sensitivity observed, however, this cannot be said with certainty as the different lasers were operated on different platforms. It should also be noted that again the amount of matrix on each plate could vary as deposition was manually by airbrush, this would affect the results. Nonetheless, the superior sensitivity of the newer instrument platform and laser configuration is highlighted in this work.

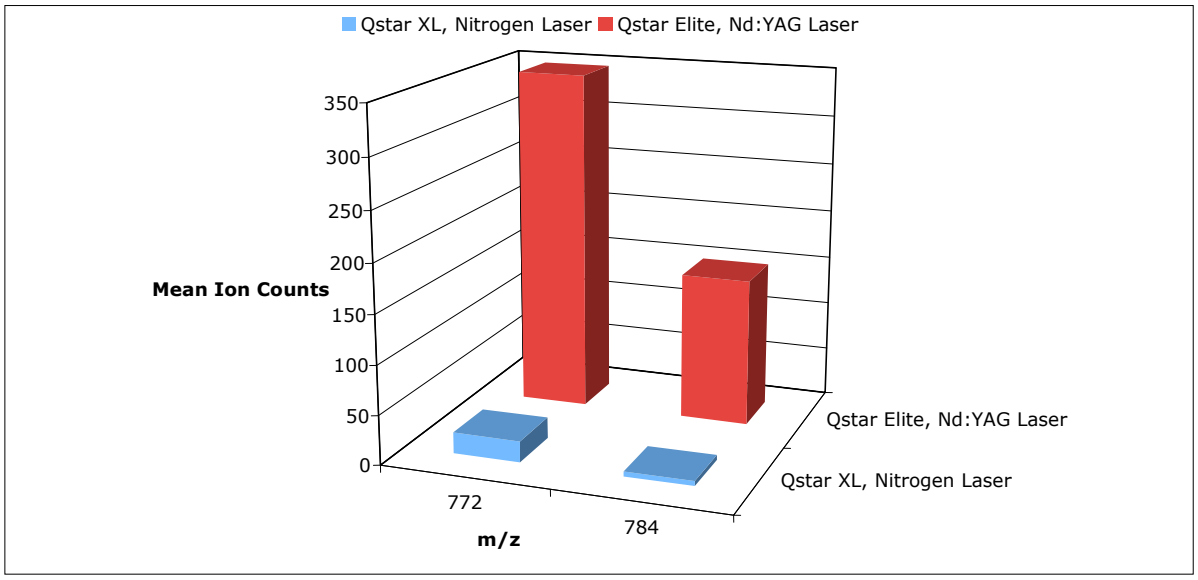

Figure 2.10. Single point spectral data (n=5) from cerebella grey matter regions, *m/z* 772 and cerebella white matter regions, *m/z* 784. Data was acquired on two different instrument platforms, using two different lasers.

2.4 Conclusion

This thesis chapter highlights the importance of matrix evaluation and optimisation for both solution/spot analysis and imaging studies. It has been demonstrated that although a given matrix may prove more suitable for the MALDI-MS analysis of complex solutions, this result does not necessarily carry over to imaging studies. Whilst DHB provided over two-fold improvement in sensitivity for the analysis of lipids from brain extracts and has been applied to numerous lipid imaging investigations, αCHCA was shown to be more suitable for MALDI-MSI in this laboratory. The mass spectra obtained with αCHCA were high quality and well defined images of lipids were obtained, matrix coverage over tissue sections was complete, and it was far easier to achieve a homogenous distribution. Furthermore, the lower laser power required for facile detection of lipid species using αCHCA is beneficial.

Results presented in this chapter show that tissue preparation and storage prior to matrix deposition greatly affects the quality of MALDI-MS image data. Tissue sections that had been dehydrated showed much lower ion intensities compared to those that had not. Fresh tissue may absorb the matrix more effectively thus allowing greater and more efficient co-crystallisation on its surface therefore giving better resolution and imaging results. Alternately the application of matrix onto a fresh sample may decrease the solvent evaporation time, which in turn would decrease the crystal drying process allowing more time for the analyte/s to be incorporated into the matrix crystals[206, 239]. These results agree with those postulated by Crossman *et al.* (2006)[228], that experimental conditions that decrease matrix solvent evaporation may increase analyte extraction efficiency, and in turn increase sensitivity of analysis. There was a difference in the amount of matrix deposited on each plate, this is a known issue associated with manual deposition methods, which highlights the need for automated matrix deposition methods, to decrease the variability and thus increase the reproducibility of MALDI-MSI investigations, and this

is a current focus of many research groups[12, 164, 166, 238, 240] and manufacturing companies[241-243]. The difference observed between the amounts deposited on each plate, although thought to impact the results, are not believed to be solely responsible for the large variation in signal intensity. The difference in matrix ion counts for the sample desiccated for 1 h, and the samples prepared after sectioning, is not thought to be significant enough to be responsible for such drastic variations in signal intensity. This was further evidence by comparing matrix ions on tissue, in which the sample plate desiccated for 1 h displayed the lowest ion counts on tissue despite displaying the highest counts off tissue. The different sample preparation procedures are believed to play a large role in the differences seen in image quality.

The initial investigation into sample thickness showed 40 µm sections had a marginal increase in ion counts compared to the 12 µm sections. As these results conflicted those previously published for the investigation into sample thickness for MALDI-MSI[227], a more in-depth investigation was carried out using a wider range of thicknesses. The analysis of sections of cerebellum ranging from 5-50 µm further supported the evidence of thicker sections giving slightly higher signal intensities. The increase in ion counts was however, only detectable in the thicker sections of 45 and 50 µm, the results obtained for the 5-40 µm were comparable. Although only two lipid species were chosen to demonstrate these findings it should be noted that the same results were observed for all species analysed. These findings are in conflict to those reported by Sugiura *et al.* (2006)[227]; there may be several reasons for this. The concentration of matrix used in their study was rather low for an imaging experiment, sinapinic acid (SA) was used at 12.5 mg/mL, this may have been too low a concentration for sufficient matrix:analyte co-crystalisation, which would greatly affect sensitivity and signal quality. In a review of sample preparation Schwartz *et al.* (2003)[21] reported SA at 30 mg/mL showed the highest number of ion signals and best resolution compared to both 20 and 10 mg/mL solutions. The number of matrix deposition cycles used is also of concern in this paper,

although the amount deposited with each cycle is unknown (as many authors do not report the amount deposited), 4 cycles seems incredibly low for an imaging study, most authors report 15-20 cycles per deposition[214, 228, 244]. Four cycles at a concentration of 12.5 mg/mL may have resulted in inefficient extraction of analytes, particularly in the thicker samples, and poor crystal coverage over the tissue sections. The study carried out by Crossman *et al*. (2006)[228], showed sufficient extraction, desorption/ionisation and good signal intensity of small and large molecules from beneath 40 µm sections. This group did use a similar concentration of SPA, however, matrix deposition was carried out over 15 cycles. This may account for the differences reported between the two papers and those observed here. This indicates matrix application and not sample thickness greatly affects the sensitivity and quality of a MALDI-MSI study.

Whilst the 50 µm section did show increased ion counts, the tissue integrity on the plate was rather poor. Sections over 30 µm in thickness showed evidence of sample drying and crusting off the target plate, a process which would be sped up under the vacuum environment of the orthogonal MALDI source used here. Sections thinner than 10 µm tend to be quite fragile and thus can split or rip when being manipulated, particularly if being handled by someone inexperienced. As there was little difference observed in the sections ranging from 5-30 µm, a section thickness of 10-12 µm is recommended, sections at this thickness show good sensitivity and thus resulting spectral quality, in addition to being easy to handle on the cryostat anti-roll plate, this thickness produces sections with good integrity.

The use of two different instrument platforms showed the Qstar Elite to be a much more sensitive instrument, which was expected as this is an upgrade of the Qstar XL. The large increase in signal intensity observed with the Elite, however, greatly exceeded what was expected according to manufacturers information. Applied Biosystems reports an ten times increase in sensitivity for the Elite compared to the XL, much higher increases were seen here, up thirty times for some analytes. The difference in sensitivity observed could

thus be attributed to the use of the high rep laser; without comparing the lasers on the same platform this cannot be said with 100 percent certainty. There are a number of clear advantages to using the high rep laser, including much faster analysis times, longer laser life span, and the smaller laser spot diameter enhances the spatial resolution for MALDI-MSI applications.

Whilst MALDI-MSI is proven as a viable tool for the analysis of lipids in both normal and disease states, method development and sample preparation protocols are still very young. Work presented here has shown how sample preparation is vital to a successful MALDI-MSI experiment. Future work will involve the evaluation of sample preparation methods that could be applied to pathological specimens/problems. This is with an aim to use MALDI-MSI as a complimentary technique to traditional clinical methods in cellular pathology departments, such as histology and immunohisitochemistry. Automated matrix deposition methods are needed to ensure *inter*- and *intra*-laboratory reproducibility. Automated methods would reduce the problems associated with manual deposition as the amount deposited on the target plate is carefully controlled. Future work will aim to evaluate automated matrix deposition methods and apply them to MALDI-MSI investigations of samples prepared for histology.

3. A Comparison of Automated and Manual Matrix Deposition Methods for Imaging of Tissues by MALDI-MS

3.1 Introduction

An important aspect of all imaging studies is the method for matrix deposition, as this greatly influences the MALDI-MS image quality in terms of mass resolution, detection sensitivity, spatial resolution of resulting images and the reproducibility of results[21, 40, 52, 166, 245]. It is known that a smaller crystal size and a homogenous layer over tissue sections lead to greater reproducibility and higher spatial resolution of images[164, 246]. Matrix deposition has to be carefully controlled, as an insufficient deposition will result in minimal analyte signals, with poor resolution thus resulting in images of poor quality. Conversely, a matrix deposition that is too wet will lead to analyte migration and result in images representing molecules that are highly delocalised from their original tissue region, leading to inaccurate results[41, 240]. In addition to these two problems there are also issues associated with an uneven matrix deposition, as this would result in local variations in extraction and thus desorption/ionisation[245]. These so called ‘sweet spots’ would have higher signal intensities than the surrounding tissue even though the distribution or concentration of the analyte within this area is the same. In recent years a number of studies have reported the use and credibility of numerous matrix deposition methods, all of these were touched upon in chapter 1, and can be divided into two main techniques, spotting and spraying. All methods to date have advantages and disadvantages.

Spraying techniques include the airbrush[155], electrospray nebulisers[247], oscillating capillary nebuliser (OCN)[164], TLC reagent sprayers[165] the commercially available vibrational sprayer[248] and the automated TM-sprayer. Spraying deposition methods are

the most commonly used to date, owing to their speed of sample preparation, small crystal size and homogeneity, and ease of use. That said, they are not without their own problems. Electrospray nebulisers and TLC reagent sprayers produce good crystal homogeneity but have problems with reproducibility and the droplets drying in transit, meaning the crystals are formed before they reach the tissue, resulting in poor analyte signals[240, 249]. The OCN produces results comparable to the manual airbrush method, in that it achieves good homogenous matrix coverage, small crystal size, with high analyte signals, and once optimised deposition is relatively fast. The OCN also offers the advantage of being an automated system, once the flow rate and deposition distance has been optimised, the sample plate moves under the nozzle in pre-determined diameters, meaning all matrix is deposited onto the plate in a fully automated and controlled manner[164, 250]. The vibrational sprayer (ImagePrep, Bruker Daltonics), is a commercially available automated device which utilises a piezo-electric spray head. The system evaluates matrix coverage using an optical scattering-light sensor to measure matrix thickness at off tissue positions[242]. Although reported to produce a homogenous layer that is reproducible, achieving high resolution images, the ImagePrep device has recently been reported as producing a matrix coverage that is far from homogenous, having issues with ‘sweet spots’[244]. In addition to this, because of the optical sensor used to measure matrix deposition, this device is limited to the application of glass sides, which is not compatible with many instrument platforms. Another commercially available spray device is the TM-sprayer (HTX Technologies), which uses a heated capillary pneumatic spray. The temperature, flow rate and deposition cycles must be previously optimised. The sample stage moves under the spray device in a predetermined pattern, at a predetermined distance from the nozzle, meaning this device is fully automated and thus thought to be more reproducible than manual spraying devices. The TM-sprayer sample stage is also adapted to fit many types of MALDI targets; as such it is not limited to one vendor or one platform[241].

To date, the most widely used and accepted matrix deposition method remains the artistic airgun. This method provides a homogenous layer of crystals, with small crystal size and complete tissue coverage, as well as yielding high ion counts. It is easy to operate and cost effective as well as producing fast sample turnaround times, of around 20 minutes. Matrix deposition with the artistic airgun is not without its own issues. Over wetting of the tissue during application can cause analyte delocalisation, conversely a deposition too dry will result in poor analyst signals. The matrix crystal homogeneity, concentration and amount deposited, are all operator dependent and therefore vary from investigator to investigator, resulting in *inter-* and *intra*-laboratory variation. Chapter 2 highlighted the reproducibility problems associated with this method.

This chapter will assess a new automated spraying method for matrix deposition, the TM-sprayer (HTX Technologies, North Carolina, USA). The results obtained from this method will be compared to the widely used and accepted artistic airbrush method, which produces high ion counts and high spatial resolution images. Investigations will focus on spectral and image quality, mass and spatial resolution, and detection sensitivity. As the distribution of numerous phospholipid species in the rat brain is already known[41, 155, 165, 166, 171, 230-232], and already used in the assessment of matrix deposition methods[12, 164, 166], they will also be used here.

3.2. Experimental

3.2.1 Materials

Alpha-cyano-4-hydroxy cinnamic acid (α-CHCA) and trifluoracetic acid (TFA) were purchased from Sigma-Aldrich (Dorset, UK). Methanol was purchased from Fisher Scientific (Loughborough, UK). Whole control rat brains were supplied by Covance, (Harrogate, UK). The automated matrix TM-sprayer was supplied on loan by Leap Technologies, Inc (North Carolina, USA).

3.2.2 Tissue Preparation

A whole rat brain, wet weight 1.916 g was homogenised in 3 mL of distilled water, giving a 40 % homogenate. This was frozen at -80°C for 24 h. Upon removal from the freezer the homogenate was allowed to defrost and using a pipette small amounts were added to a cryostat chuck. This was carried out in such a way as to build a sufficient enough amount to be sectioned. Serial sections of homogenates were then taken at 20 µm on a Leica cryostat, transferred to a stainless steel MALDI target plate.

A whole rat brain was removed from the -80°C freezer and transferred to the -20°C cryostat chamber and allowed to equilibrate. The rat brain was then bisected and half was mounted onto a cryostat chuck, using water-ice slush. Serial sagittal sections of the brain were taken at 12 µm and thaw mounted onto stainless steel MALDI target plates. The MALDI plates were placed in a -80°C freezer until analysis.

3.2.3 Matrix Application

The automated matrix TM-sprayer was supplied on loan by HTX Technologies, LLC. For deposition using the TM-sprayer, several plates were coated in 5 mg/mL αCHCA matrix material, prepared in 80% methanol (0.1% TFA). Plates were sprayed at 150°C, 10 psi, a flow rate of 0.25 mL/min with a stage velocity of 500 mm/min, as optimised for this matrix and solvent system. Each target insert was sprayed with 4 or 8 cycles.

For airbrush deposition (Badger Airbrush Ltd, UK), the MALDI target insert was held in a fume hood using a clamp, 25 mg/mL αCHCA matrix material solution, (prepared in 80% methanol (0.1% TFA)) was deposited over each plate in cycles, allowing time to dry between each cycle. Deposition was carried out from a distance of 15-20 cm, the plate was rotated 90° between each cycle to ensure an even distribution, deposition was deemed optimal when 9 mLs had been deposited.

3.2.4 Instrumentation

The homogenate samples were analysed using an Applied Biosystems (Toronto, Canada) hybrid quadrupole time-of-flight (QqTOF) instrument (Qstar XL). The instrument was fitted with an orthogonal MALDI ion source and a nitrogen laser (337nm), operated at 20 % available power with a repetition rate of 20Hz. The instrument was operated in the positive ion reflectron mode, recording all signals between *m/z* 50-1000. Data collection was via an automated pre-determined pattern analysis over the tissue, using a Q1 scan time of 1 second, summing 9 scans per spectrum obtained. Mass spectral data was analysed using Analyst software supplied by Applied Biosystems.

For imaging investigations MALDI mass spectrometric analysis was carried out using an Applied Biosystems (Toronto, Canada) hybrid quadrupole time-of-flight (QqTOF) instrument (Qstar Elite), operated in positive ion reflectron mode. Instrument parameters had been previously optimised for the analysis of PCs from rat brain, data was acquired

between the mass range *m/z* 50-1000. The Nd:YAG (355nm) laser was operated at 20 % available power (2.1 µJ), with a repetition rate of 500 Hz. The target plate stepping distance was set to 100 µm for both the x and y dimension using the imaging acquisition software. Data were acquired using the 'dynamic pixel' setting, which involves the laser being moved within the 100 μm^2 pixel area and resultant data being summed to give an accumulated mass spectrum over one second for each pixel area. The resulting two-dimensional ion density maps were generated using the TissueView software, after conversion of the raw data into the format required using the 'wiff to analyse' script, provided by applied biosystems.

3.3 Results and Discussion

3.3.1 Optimisation of the TM-Sprayer

Matrix deposition via airbrush application is a widespread commonly used technique that has been discussed in detail elsewhere. It will therefore only be discussed as a comparison to the automated Leap TM-sprayer. The TM-sprayer has a number of parameters that can be adjusted for a given matrix and solvent system to ensure a fine even distribution of matrix crystals. These parameters include; adjustable nozzle height; the block temperature; matrix deposition rate; air pressure; stage speed and offset/line spacing of deposition. The precision robot that controls the x-y sample stage has a variety of spray pattern designs that can be applied for deposition. All parameters were controlled by a Microsoft Windows™ interface that was relatively easy to operate. Due to time constraints and to reduce the time taken for optimisation, the nozzle height was kept at distance of 40 mm from the sample plate, and the stage velocity was kept at 500 mm/min,

all other parameters where optimised around these. Initial optimisation used single line deposition methods to establish parameters that appeared to deposit the matrix without being too wet or too dry. Over wetting was seen as spluttering along, and increasing out from the edges of the deposition line. A deposition was considered too dry if the matrix colouring on the plate was very light, or the deposition showed no signs of wetness upon contact with the plate. The psi, flow rate and temperature were varied until a smooth densely coloured line was achieved along the MALDI target plate. A flow rate above 0.25 mL/min resulted in deposition lines with increased diameter, when coupled with a lower temperature this often caused spluttering and blocking of the capillary nozzle. A psi and flow rate too low resulted in insufficient levels of matrix deposition on the plate. The optimal psi and flow rate was determined to be 10 psi and 0.25 mL/min. The optimal temperature was then determined from these parameters, starting at 80 °C the temperature was increased in increments 10 °C, until matrix deposition appeared as an even, smooth line on the plate. It was critical for the matrix to appear wet on deposition, for optimal analyte extraction, but with rapid solvent evaporation, as to minimise analyte delocalisation. This was optimised as 150 °C. The vertical line spacing between depositions was set to 3 mm, this was determined to be the thickness of the deposition line. The line offset stepping distance between each full deposition cycle was then set to 25 mm, on observation it was noted the outer areas of deposition lines had a slightly thinner matrix deposition, thus a slight overlap was chosen to ensure these areas had similar amounts deposited. Deposition of matrix via the TM-sprayer produced what appeared to be a thick dense film of bronze coloured matrix, evenly distributed over the target plate and tissue area. Once optimised matrix deposition was carried out in minutes for each plate.

Airbrush deposition produced finely dispersed droplets, which are built up in an almost ‘seeding’ technique; resulting in a near homogenous distribution of minute crystals over the target plate. Deposition using the airbrush usually takes around 20 min per plate. The

entire matrix is deposited directly onto the plate with the TM-sprayer, whereas with airbrush application, it is impossible to accurately calculate how much matrix gets deposited onto the plate, and thus the tissue surface.

3.3.2 Comparison of Deposition Methods for MALDI-MS

Tissue homogenates were used for the optimisation of the TM-sprayer. Homogenates were chosen as they enable analysis of a sample with the same properties of tissue, but with even analyte distribution throughout. This ensures differences that may occur are not due to variations of analyte distribution within the tissue sections, such as regional changes of PLs within the different anatomical compartments of the brain, but are a true representation of the different matrix deposition methods. Firstly the number of robotic deposition cycles was optimised for the TM-sprayer, this involved a comparison of 4 and 8 repeated cycles. These automated methods were compared to the previously optimised airbrush deposition method. Similar peaks were detected in MALDI-MS analysis of tissue homogenates prepared by each deposition method; however the ion intensities were extremely different, as shown in figure 3.1. The base peak was the same for all spectra acquired at *m/z* 265, however, at over 7000 counts for the airbrush deposition method, this peak was over three-fold higher for the TM-sprayer 4 cycle method, and two-fold higher for the 8 cycle method. The base peak at *m/*z 265 and the peak at *m/z* 221, are matrix salt adduct peaks that are usually observed above all other matrix peaks on tissue. These peaks are thought to be predominantly observed from brain tissue due to the high concentration of salts found within the brain. The difference in signal intensity observed for these peaks is believed to be due to the different concentration of αCHCA used for each method, 25 mg/mL for airbrush deposition, compared to 5 mg/mL for deposition by the TM-sprayer. The high signal intensity for *m/*z 265 observed with the airbrush method

dominates the spectra and masks many of the lipid species detected, as shown in the top spectrum of figure one. The region between *m/z* 650-900 had to be enlarged within this spectrum for these species to be clearly visible. The commonly reported lipid species that usually dominate this region of mass spectra when analysing brain tissue[41, 155, 165, 166, 171, 230-232], are not the most abundantly observed here. For example, *m/z* 772, 798 and 826, representing $[M+K]^+$ for PC 32:0, PC 34:1 and PC 36:1, are all present but their intensities were incredibly low with airbrush deposition, at 30, 69 and 32 counts. These species were detected with much higher signal intensity for the TM-sprayer, for both deposition cycle methods, as shown in figure 3.1. The 4 cycle method produced a seven-fold increase for *m/z* 772, over a six-fold increase for *m/z* 798 and over a three-fold increase for *m/z* 826 compared to airbrush deposition method. The TM-sprayer applying 8 deposition cycles, showed over a thirteen-fold increase for both *m/z* 772and 798, and over a nine-fold increase for *m/z* 826 compared to the airbrush method.

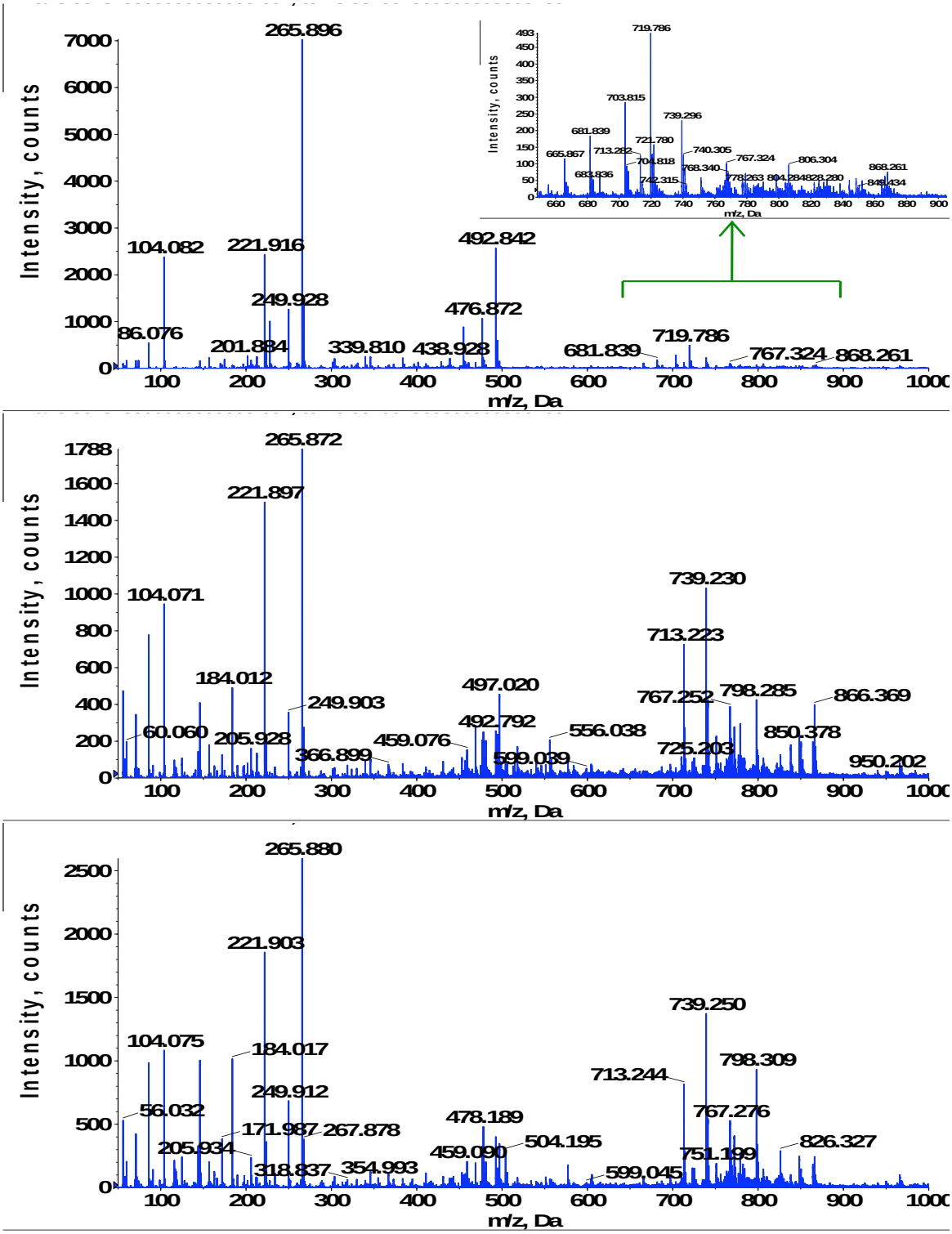

Figure 3.1. MALDI mass spectra of rat brain homogenate acquired using the manual airbrush (top spectrum), automated TM-sprayer, 4 cycles (middle spectrum), and automated TM-sprayer, 8 cycles (bottom spectrum). The difference in ion intensity for the base peak and lipids of interest, between *m/z* 700-900 is clearly visible.

As previously mentioned, the region of interest for lipid analysis, *m/z* 700-900, shows a very different lipid profile for the analysis of brain homogenates, compared to those usually observed in MALDI-MS analysis of whole rat brain sections. The most abundant peaks within this region of the mass spectrum are predominantly odd numbered *m/z,* rather than the commonly observed even numbered species reported in chapter 2 and literature[41, 155, 165, 166, 171, 230-232]. These peaks are believed to be fragment peaks of the commonly observed species, resulting from the neutral loss (NL) of trimethylamine from the phosphocholine head group. Trimethylamine ($N(CH_3)_3$) has a mass of 59 u, thus *m/z* 713, 739 and 767 are $[M+K-N(CH_3)_3]^+$ for the three commonly observed lipids, PC 32:0, PC 34:1 and PC 36:1. This fragmentation pathway is more commonly observed in the analysis of brain tissue by SIMS[251]. The difference in signal intensities for these peaks, for the different matrix deposition methods, follows the same trend as when observing the intact molecules, with the TM-sprayer 8 cycle deposition method giving the highest signal intensities. The increase in signal intensities however, is smaller when reviewing these peaks, with a six-fold increase for *m/z* 713 and 739, and a five-fold increase for *m/z* 767, for the TM-sprayer 8 cycle method compared to the airbrush method. Due to the presence of multiple ions for a given lipid species, it is necessary to monitor the sum of all ions for a more accurate assessment of the difference in sensitivity for each method. The summation of ion counts for a specific lipid species, for example, the sum of $[M+H]^+$, $[M+Na]^+$, $[M+K]^+$ and $[M+K-N(CH_3)_3]^+$, for PC 32:0, showed the same difference in signal intensity was observed, as when reviewing the fragment peaks, $[M+K-N(CH_3)_3]^+$. The TM-sprayer, using 8 deposition cycles proved far more sensitive than both the 4 cycle deposition and the manual airbrush, regarding spectral quality, detection sensitivity and mass resolution, which is clearly demonstrated by the green trace in the overlay spectrum presented in figure 3.2. The peaks at *m/z* 713, 739, 798 and 826 have been enlarged, the peak height and shape for airbrush deposition is of extremely low quality as shown by the blue trace. The peak height is greatly increased for

the TM-sprayer 4 cycle method, as shown by the red trace, however the resolution for the peak at *m/z* 826 is still rather poor, as demonstrated by the peak shape. For all other investigations the TM-sprayer 8 cycle method was used, as this gave better overall results compared to the 4 cycle deposition method.

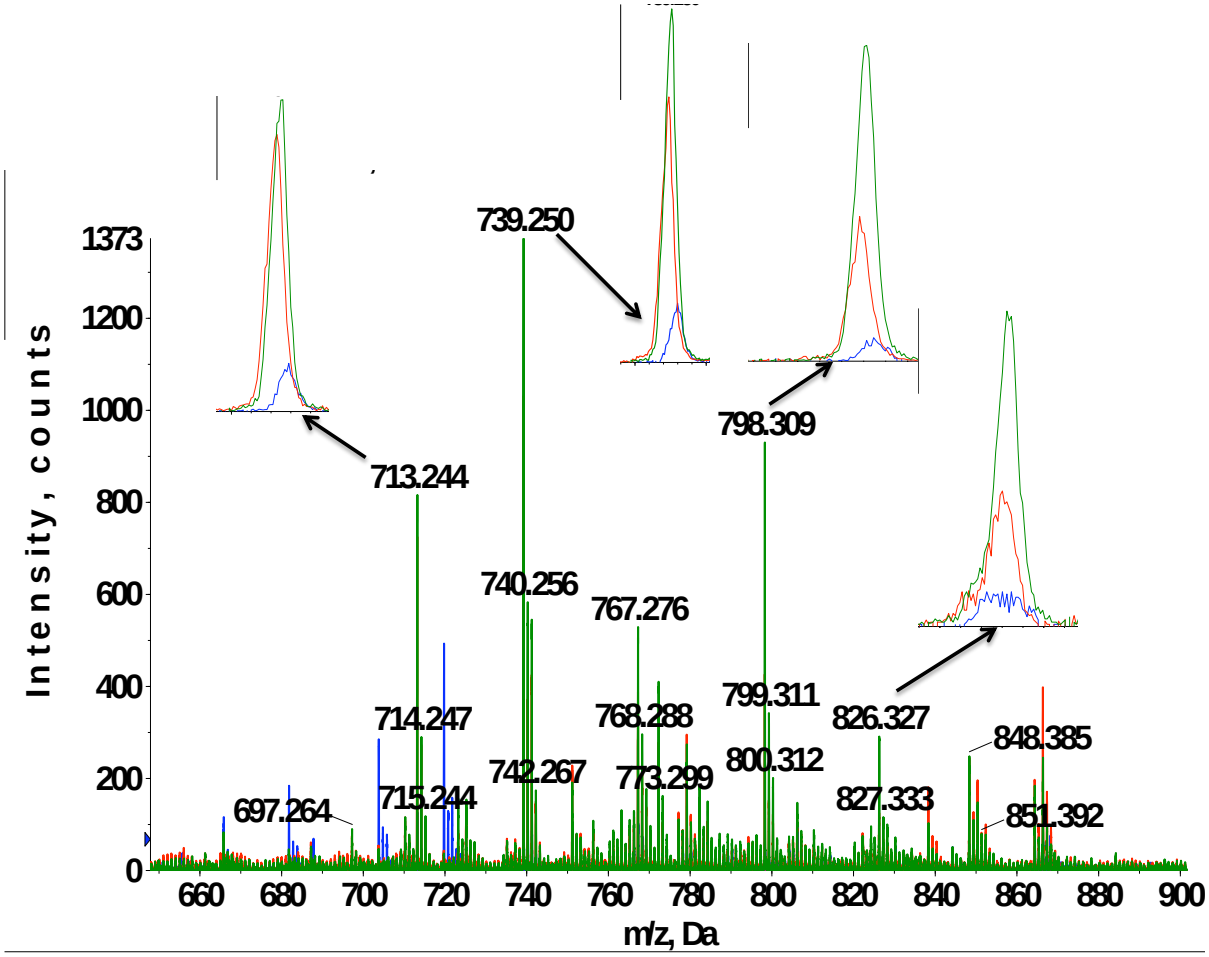

Figure 3.2. MALDI mass spectral overlay acquired from a rat brain homogenate for the airbrush deposition method (blue trace), TM-sprayer 4 cycle deposition (red trace) and the TM-sprayer 8 cycle deposition (green trace). The difference in spectral quality is clearly visible when observing the enlarged peaks at *m/z* 713 for $[PC32:0+K\text{-}N(CH_3)_3]^+$, *m/z* 739 representing $[PC34:1+K\text{-}N(CH_3)_3]^+$, *m/z* 798 for $[PC34:1+K]^+$, and *m/z* 826 representing $[PC36:1+K]^+$.

3.3.3 Evaluation of Reproducibility

To assess or compare the reproducibility of the TM-sprayer against the airbrush method, three MALDI plates were prepared for each method and analysed as described in the matrix deposition and instrumentation (imaging) section of the method. Single point spectra were analysed from ten different locations on each plate for each method, comparisons were made for *inter*- and *intra*-plate variability. Due to the high abundance of matrix peaks along with their high signal intensities, all peaks with a signal above 100 counts were summed. For the investigation of laser spot-to-spot reproducibility, or *inter*-plate variability, the summed ions at each location for an individual plate were compared for each method. The mean of the summed ions for each plate was then calculated (n=10) to investigate the plate-to-plate variability for each method. The irreproducibility issues associated with the manual airbrush deposition method are known, and were highlighted in chapter 2. The investigation of the spot-to-spot reproducibility across each plate, for each method, showed both methods suffer with variability. The data obtained from the analysis of plates 2 and 3 for airbrush deposition show areas of high and low ion counts, as show in figure 3.3, demonstrating so called ‘sweet spot’ areas, and areas of low matrix deposition. The results from plate 1 for this method show a high reduction in the variability of ion counts at each location on the plate.

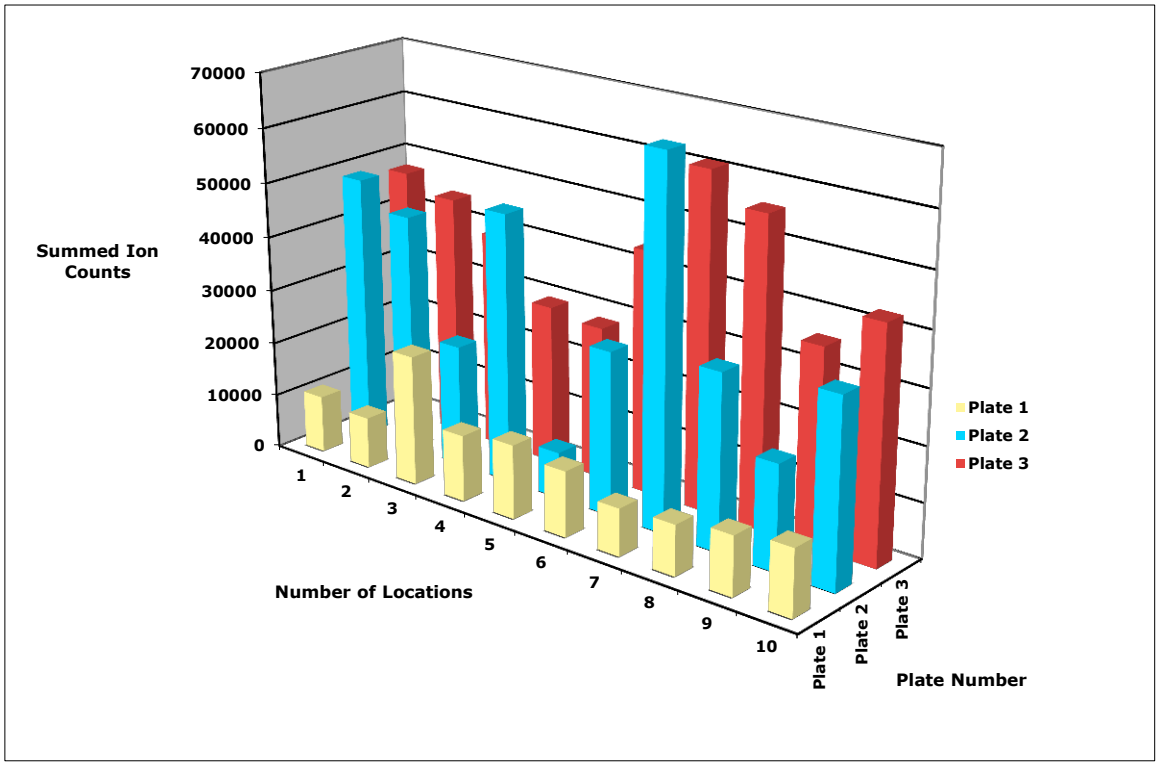

Figure 3.3. MALDI-MSI single point spectral data taken from 10 different regions on the MALDI target plate, for airbrush deposition. All matrix peaks above 100 counts were summed for each location. Results show quite high spot-to-spot variability for plates 2 and 3, *inter*-plate variability is greatly reduced for plate 1.

Similar results were obtained from the spectra from plates 1 and 3 for TM-sprayer deposition, these plates also showed high spot-to-spot variability; this is particularly evident in the data presented for plate 1 in figure 3.4. There is an incredibly high spike in ion counts at location 4 of plate 1, indicative of a higher concentration of matrix within this area; again this is the ‘sweetspot’ effect. The review of plate 2 from this deposition method shows reduced variability of ion counts between each location on the plate.

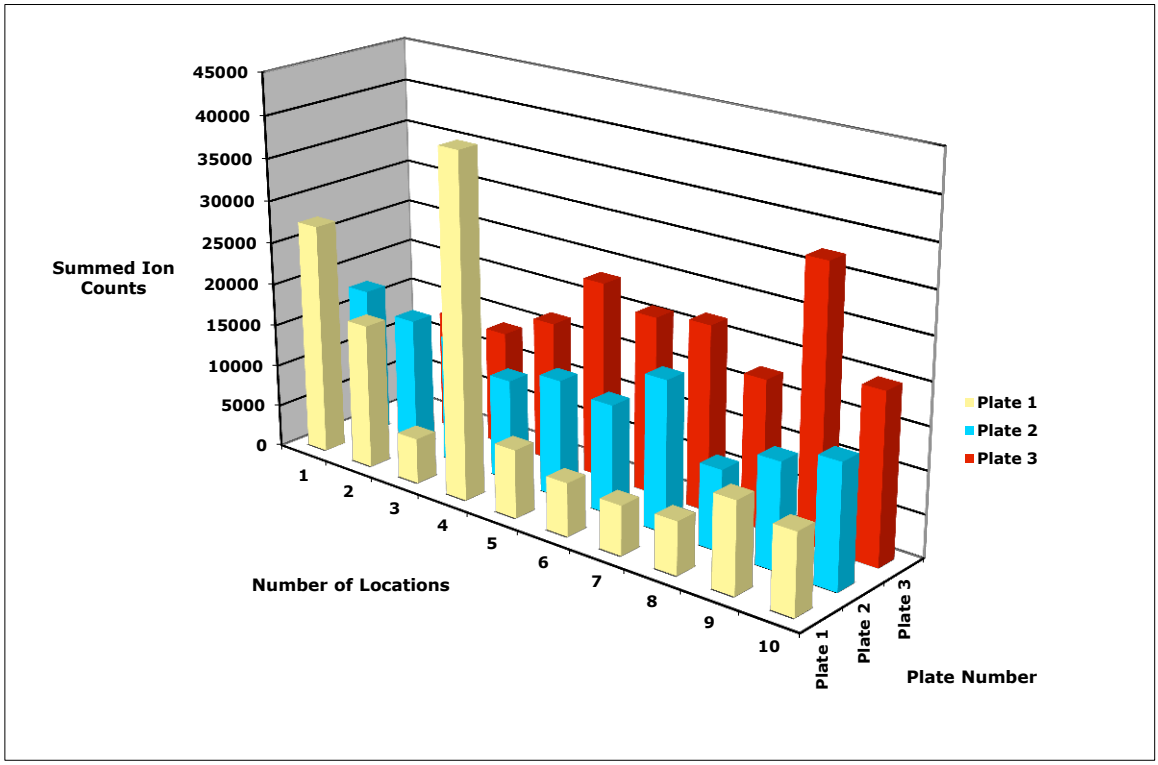

Figure 3.4. MALDI-MSI single point spectral data taken from 10 different regions on the MALDI target plate, for the TM-sprayer deposition method. All matrix peaks above 100 counts were summed for each location. Results show quite high spot-to-spot variability for plates 1 and 3, *inter*-plate variability is greatly reduced for plate 2.

On observation it would appear that plate 1 for airbrush deposition shows a higher degree of spot-to-spot reproducibility across the plate compared to plate 2 for TM-sprayer deposition, figures 3.3 and 3.4 respectively. This is not the case, it appears this ways because of the high *intra*-plate variability for the airbrush method, the scale difference caused by the large range between ion counts across the plates, gives plate 1 the appearance of a near homogenous matrix distribution, apparent by near equal columns representing each location. Comparison of coefficient of variation (CV) for plate 1, airbrush deposition, and plate 2, TM-sprayer, showed the latter to be more reproducible across the plate. The CV for plate 1, airbrush deposition was 36 %, compared to 18 % for plate 2 TM-sprayer. Interestingly, plate 3 using airbrush deposition had the lowest CV of the 3 plates analysed for this method, at 24 %, this, however, is still higher than that achieved with the TM-sprayer.

The *Intra*-plate reproducibility for each method was assessed by summing the ions taken from the single point spectral analysis, and calculating the mean from the 10 locations. The TM-sprayer was shown to be far more reproducible across plates than deposition by airbrush, as shown by figure 3.5. The coefficient of variation (CV) between the plates for the automated TM-sprayer was 18 %, whereas the CV for the manual airbrush method was 53 %, thus the TM-sprayer shows over a two-fold reduction in variability compared to the widely used airbrush method.

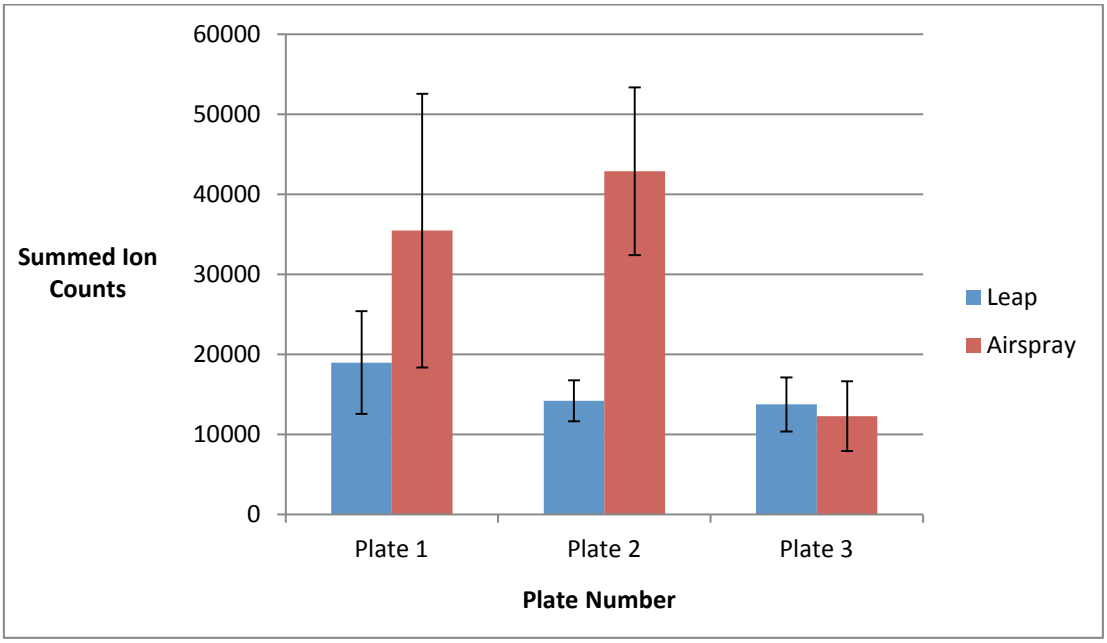

Figure 3.5. MALDI-MS single point spectral data taken from 10 different regions on the plate, for 3 different plates. Every matrix peak above 100 counts was summed and the mean ion counts ± SD (n=10) displayed. There is less variance between the amounts of matrix deposited using the TM-sprayer (blue columns) compared to the airbrush method (red columns).

3.3.4 Comparison of Deposition Methods for MALDI-MSI

The comparison of matrix deposition methods thus far has shown spectral quality, regarding detection sensitivity, S/N, mass resolution and reproducibility, were enhanced with the TM-sprayer. The next investigation sought to assess whether these results were translated to imaging studies, producing the same spectral and thus image quality, with high image spatial resolution, without causing analyte delocalisation. The images of sagittal rat brain sections acquired using the TM-sprayer and airbrush deposition methods are presented in figure 3.6 and show mutual distributions. Images of *m/z* 772 representing $[PC\ 32:0+K]^+$, clearly follow the contours of grey matter regions of the brain, as found in chapter 1 and literature[12, 165, 166, 171], demonstrating little or no analyte delocalisation has occurred. The image presented for airbrush deposition shows well defined brain anatomy, however, the appearance is rather grainy, as is commonly observed with this method. Conversely, the image presented using the TM-sprayer shows well defined anatomy, without the grainy appearance that was seen with airbrush deposition, this image is smooth, displaying a much improved resolution. The signal intensity is again higher for the TM-sprayer compared to the airbrush method, as shown by the intensity bars for each image. The image of *m/z* 772 for airbrush deposition displays an area of higher signal intensity around the tissue; this has previously been observed in MALDI imaging experiments and is known as the 'halo' effect. It is thought to be associated with tissue shrinking during sample preparation or once in the vacuum of the MALDI source. Images of *m/z* 826 show higher signal intensities within white matter regions of the brain, which is in agreement to the previously reported distribution of this lipid by MALDI-MSI[165, 166, 171]. Images are again more highly resolved, and the signal intensity is higher for the TM-sprayer compared to airbrush deposition. Spatial resolution is controlled or limited by a number of factors, including the size of the laser spot, the size of the matrix crystals and the coverage of matrix on the tissue[248-250]. As the laser was

the same for both applications the higher resolution images seen with the TM sprayer is attributed to the method used for the matrix application, and thus the formation of crystals and crystal size on the tissue. That is that the TM sprayer produced finer crystals. This could be due to a number of factors, including the lower concentration used, the controlled pressure and flow rate, the velocity of the sample stage during deposition and finally, the temperature used during deposition. These are all key factors affecting the way the matrix is deposited on the tissue surface.

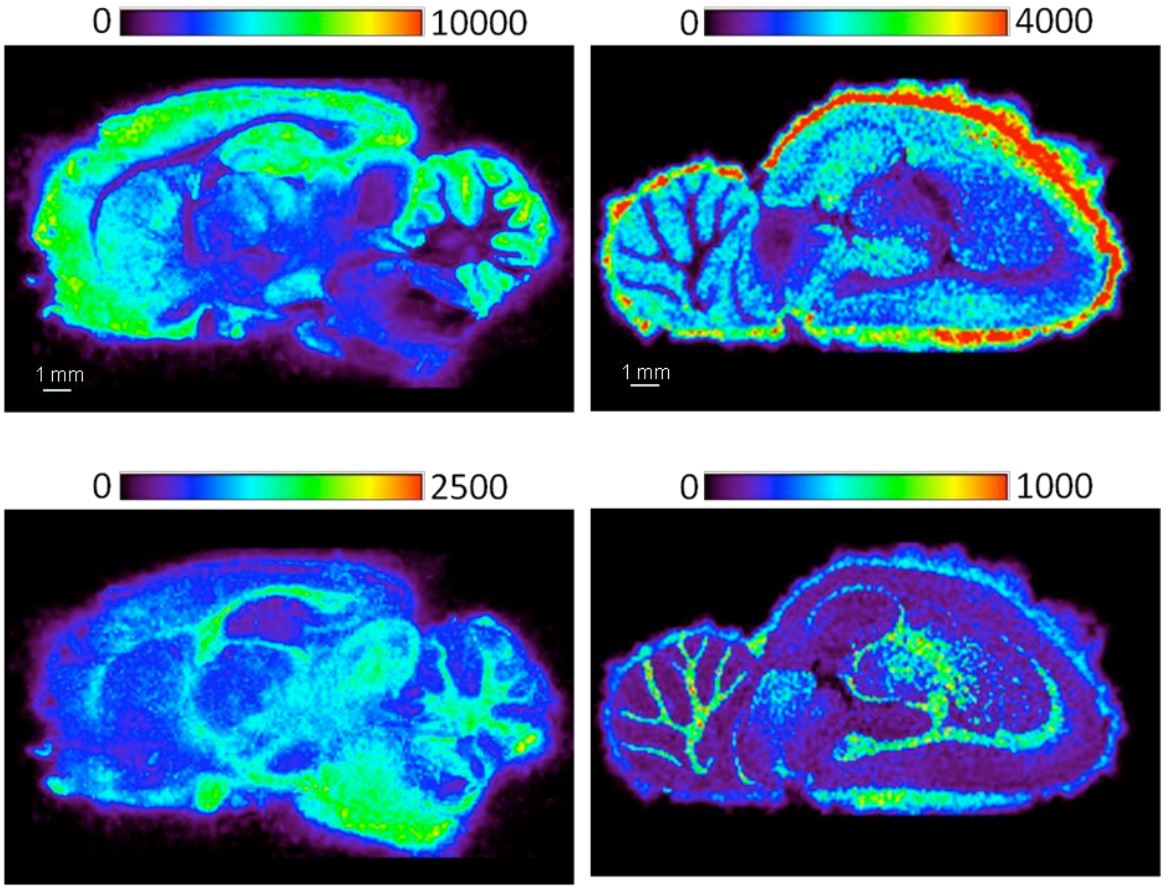

Figure 3.6. MALDI-MS images of *m/z* 772, top images and *m/z* 826, bottom images. Images representing the automated TM-sprayer are displayed on the left, and images for the manual airbrush deposition method are displayed on the right. There is over a two-fold increase in signal intensity for the TM-sprayer compared to the airbrush.

It should be noted that images presented are the raw, unprocessed data, and many groups do apply normalisation and smoothing algorithms, that enhance the appearance of MALDI-MS images produced using airbrush deposition[155, 252, 253].

The commonly reported lipid species listed in table 3 of chapter 2 are all detected with both deposition methods; however the detection sensitivity was far superior with the TM-sprayer, as shown by the spectra presented in figure 3.7. The TM-sprayer demonstrates a 5-10 fold increase in sensitivity depending on which lipid species is observed from the analysis of single point spectra, both of which were taken from the cerebral cortex of the brain. The spectral quality is far superior for the TM-sprayer, showing higher S/N, and a much cleaner spectrum compared to airbrush deposition, the latter is thought to be predominantly due to the lower concentration of matrix used, resulting in less spectral interference from matrix peaks.

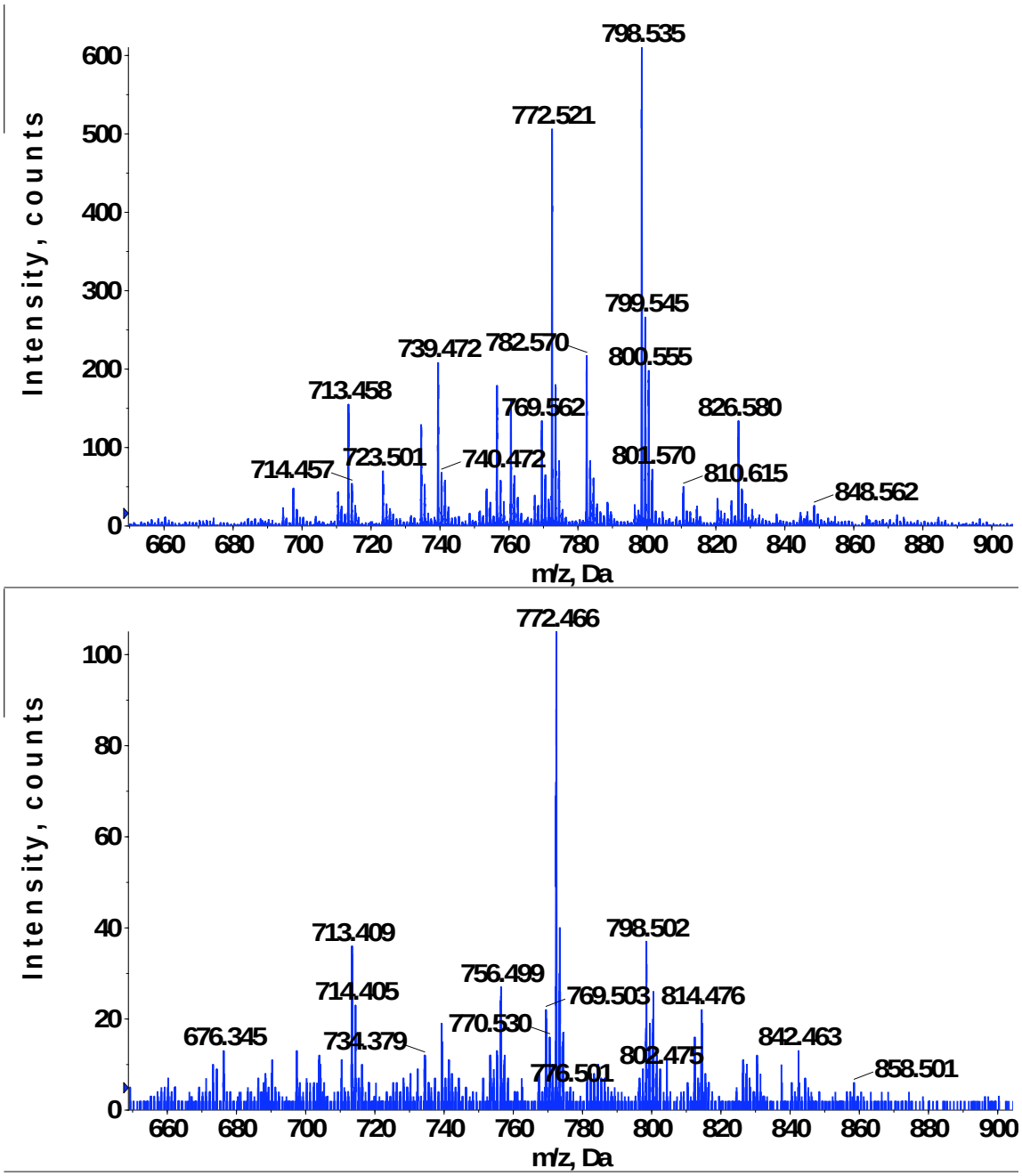

Figure 3.7. Single point MALDI mass spectra taken from the cerebral cortex of rat brain sections, for the TM-sprayer (top spectrum) and airbrush (bottom spectrum) deposition methods. The increased signal intensity, S/N, and detection sensitivity, along with decreased spectral complexity for the TM-sprayer is evident.

3.4 Conclusion

The MALDI-MS analysis of brain homogenates for profiling studies and whole serial sagittal sections for imaging studies, proved the automated TM-sprayer to be superior across all experiments, when compared to the traditional airbrush method for matrix deposition. This deposition method demonstrated small crystal size and a homogenous coverage, high analyte extraction and co-crystallisation, and no analyte delocalisation. This was evidenced throughout this chapter, initially with the investigation of tissue homogenates, in which the TM-sprayer showed over a five-fold increase in detection sensitivity, and far greater mass resolution compared to airbrush deposition, across all species analysed. The spectral profile for the analysis of tissue homogenates differed from those usually observed for the MALDI-MS analysis of rat brain material in positive ion mode[12, 41, 164-166, 171, 230]. The characteristic even numbered peaks, particularly those representing PC 32:0 and PC 34:1, usually the most abundant peaks, as shown in literature, chapter 2 and the spectrum presented in figure 6 of this chapter, where not the most abundant here. The most abundant peaks in the analysis of tissue homogenates were odd numbered, at *m/z* 713 and 739, PC 32:0 and 34:1 are the most abundant phospholipids in rat brain, and thus these peaks are attributed to fragment products of these lipids, resulting from the loss of trimethylamine from the phosphocholine head group. The nature of the tissue homogenates, or the way in which they were prepared is believed to have resulted in lipid degradation. This is further evidenced by the high abundance of peaks between *m/z* 350-550, peaks within this range result from the neutral losses of fatty acids and trimethylamine[114, 254]. MALDI-MSI investigations also demonstrated spectral quality, detection sensitivity, S/N and image resolution were all far superior with the samples prepared using the TM-sprayer for matrix deposition. There was also minimal interference from matrix clusters found within the same *m/z* range of lipids species of interest; this is a common occurrence with airbrush deposition. The

difference in matrix concentration is thought to be attributed to the cleaner spectra observed after deposition by the TM-sprayer, as it uses a concentration five times less than airbrush methods. A concentration of 25 mg/mL αCHCA was found to be optimum for MALDI-MSI within this group, thus lowering the concentration would have resulted in lower analyte signals. The TM-sprayer is equipped with a number of adjustable parameters, which are all believed to contribute to the production of a finely dispersed mist of minute matrix-solvent droplets. These include the flow rate, line spacing between depositions, sample stage speed and particularly the heated nozzle/gas flow. The high temperature applied during deposition ensures the solvent evaporates rapidly, minimising analyte delocalisation, but resulting in a fine sheet of co-crystals, which improves image rsolution. The TM-sprayer showed over a two-fold reduction in variability compared to airbrush deposition, reproducibility is one of the biggest drawbacks for the latter method. A more reproducible deposition method, as presented here, will aid in minimising the problems associated with *inter-* and *intr-* laboratory variability, due to irreproducible matrix deposition methods.

At the time of investigation (early 2008) the only literature available on the application of the TM-sprayer for MALDI-MSI was the technical note, which showed high resolution images for peptides and proteins in tissue. A study has been published more recently using the TM-sprayer for the MALDI-MSI investigation of a drug, results presented correspond well to those observed in this chapter. The study by Yamada *et al.* (2010), analysing chloroquine distribution in rat ocular tissue by MALDI-MSI, found the TM-sprayer resulted in much improved sensitivity, showing a fourteen-fold increase in signal compared to the airbrush method[255]. Collectively these results have proven the TM-sprayer can be applied to the MALDI-MSI of large (peptides and proteins), and small (drugs and lipids) molecules, enhancing the spectral and image quality, detection sensitivity, mass resolution and reproducibility. Once optimised for a solvent system this

method is both fast and efficient, and a much lower concentration and thus consumption of matrix material also make the TM Leap sprayer attractive tool for MALDI-MSI.

4. Imaging of Phospholipids in Formalin Fixed Rat Brain Sections by Matrix Assisted Laser Desorption/Ionisation Mass Spectrometry

4.1 Introduction

Traditional analysis of pathological specimens employs histological staining procedures to investigate tissue anatomy[256, 257]. Labelled antibodies are often used in conjunction with staining protocols for the visualisation of specific biomarkers that aid in the diagnosis and prognosis of diseases; this is a subset of histology known as immunohistochemistry (IHC)[256-259]. IHC, as with other molecular labelling methods, are often limited in their ability to yield information on multiple species in a single section. Mass spectrometry imaging offers simultaneous label free analysis of multiple species in a single experiment, providing significant insights into disease pathogenesis[4, 104, 176, 203, 219, 225, 260-264]. Conventional methods for collection and storage of tissue for histological evaluation uses formalin fixation to chemically preserve the tissue by preventing proteolytic degradation[265]. Formalin fixation (FF) causes inter and intra cross-linking between proteins and proteins and nucleic acids, which presents issues for direct analysis of proteins by IHC and mass spectrometry[266-268]. This cross linking is thought to predominantly involve hydroxymethylene bridges, but it has also been suggested that formation of coordinate bonds for calcium ions may play a role[269]. The net result is the masking of epitopes (antibody binding sites). There are several techniques for reversing this cross-linking, to ‘un-mask’ these epitopes, which are widely used in IHC and referred to as ’antigen retrieval methods’. These methods involve enzymatic digestion, protein denaturation, heat treatment and heat-induced antigen retrieval (HIAR)[267, 269, 270].

Investigators attempting to analyse proteins in fixed tissue via MALDI-MSI have explored the use of enzymatic digestion prior to analysis[162, 268, 271, 272]. Research has also involved development of MALDI compatible staining protocols[204] as well as performing MALDI prior to histological staining[273]. These studies have aimed to establish methods that would permit direct comparison and correlation of images from microscopy and mass spectrometry. Compatible protocols would facilitate full correlation of spectral data with areas of interest highlighted in high resolution microscopy and enable analysis of proteins in archival material by MALDI. Analysis and imaging of lipids from formalin fixed tissue sections would improve correlation of MS lipid data with histological findings, and permit MALDI analysis of sections prepared from organs stored in formalin. Lipid profiles have been investigated from formalin fixed bovine lens tissue[274], but imaging of phospholipids directly from formalin fixed tissue sections has not been presented.

This chapter investigates the effects of formalin fixation on analysis and imaging of phospholipids in tissue sections. Several studies have already reported the distribution of the commonly known phospholipids within the anatomical regions of the brain in fresh tissue sections[10, 12, 14, 155, 165, 166, 172, 205, 230, 232, 233, 238, 275-278]. Results from these studies provide a useful basis for the assessment of new sample preparation methods for MALDI-MSI. MS images and spectral data obtained from analysis of formalin fixed tissue are compared directly to data from fresh tissue. The effects of formalin fixation are considered with respect to image quality, sensitivity and the localisation of selected species. Studies were also conducted to assess the differences in salt adduct formation of lipid species ionised from fresh and fixed tissue. Prolonged storage in formalin is also evaluated.

4.2. Experimental

4.2.1 Materials

Alpha-cyano-4-hydroxy cinnamic acid (α-CHCA) and trifluoracetic acid (TFA) were purchased from Sigma-Aldrich (Dorset, UK). 10% neutral buffered formalin (NBF) was supplied by the Histology Department of the Medical School at the Royal Hallamshire Hospital, (Sheffield, UK). Methanol was purchased from Fisher Scientific (Loughborough, UK). Whole control rat brains were supplied by Covance, (Harrogate, UK).

Tissue Preparation for MALDI MSI of Phospholipids

A whole rat brain was removed from the -80°C freezer and allowed to thaw at room temperature. Once thawed the brain was placed in 10% NBF and fixed for 48-72 h, 3 weeks, 12 months and 18 months. Fixed and fresh brains were bisected and half of each was mounted onto a cryostat chuck, using water-ice slush. Serial sections of each brain were taken at 12 µm and thaw mounted onto stainless steel MALDI target plates for mass spectrometry and glass slides for histology. For formalin spiked tissue analysis, 12 µm serial sections of fresh brain were prepared as above and subsequently spiked with 0.1 µl of formalin in 9 locations.

4.2.2 Matrix Deposition

For the initial evaluation of formalin fixation, following standard histological processes of fixation for 48-72 h, and for MS/MS analysis, tissue samples were coated in 5 mg ml^{-1} αCHCA matrix material, prepared in 80% methanol (0.1% TFA) using the automated TM-sprayer (HTX Technologies, LLC, North Carolina, USA). Plates were sprayed at 150°C, 10 psi, a flow rate of 0.25 ml/min with a stage velocity of 500 mm/min. Each target insert was sprayed with 8 cycles, as optimised in Chapter 3.

Matrix deposition for the analysis of formalin spiked tissue samples, and the investigation into the effects of prolonged storage in formalin fixative, was carried out via airbrush deposition (Badger Airbrush Ltd, UK), the MALDI target insert was held in a fume hood using a clamp, 25 mg/mL αCHCA matrix material solution, (prepared in 80% methanol (0.1% TFA)) was deposited over each plate in cycles, allowing time to dry between each cycle. Deposition was carried out from a distance of 15-20 cm, the plate was rotated 90° between each cycle to ensure an even distribution, deposition was deemed optimal when 9 mL had been deposited.

4.2.3 Mass Spectrometry

Experiments were carried out on a QqTOF (Qstar Elite) mass spectrometer (Applied Biosystems, Foster City, USA), operated in positive ion reflectron mode. Instrument parameters had been previously optimised for the analysis of PCs from rat brain, data were acquired between the mass range *m/z* 50-1000. The Nd:YAG (355nm) laser was operated at 20 % available power (2.1 µJ), with a repetition rate of 500 Hz. The target plate stepping distance was set to 100 µm for both the x and y dimension using the imaging acquisition software. Data were acquired using the 'dynamic pixel' setting, which involves the laser being moved within the 100 μm^2 pixel area and resultant data being summed to give an accumulated mass spectrum over one second for each pixel area. The resulting two-dimensional ion density maps were generated using the TissueView software, after conversion of the raw data into the format required using the 'wiff to analyse' script, provided by applied biosystems.

For MS/MS analysis instrument parameters and laser power were as described above, the collision gas was argon, used at a collisional activation energy of 35 V, this was optimised from tandem profiling analysis of lipids directly from rat brain. Images were acquired at 50 µm for both the x and y dimension, using oversampling as previously described [247]. The number of data points within a data set for these imaging

experiments were too high to be converted using the ‘wiff to analyse’ script, the images from these investigation were processed using oMALDI 5.1 software (supplied by MDS Analytical Technologies, Ontario, Canada).

For the investigation into the effects of prolonged storage in formalin, experiments were conducted on a QqTOF (Qstar XL, Applied Biosystems, Foster City, USA) mass spectrometer equipped with a nitrogen laser (337 nm), operated at 25 µJ with a repetition rate of 20 Hz. TOF-MS data were acquired in the positive ion reflectron mode, over the *m/z* range 50-1000. The spatial resolution was set to 200 µm in both the x and y dimensions and a summed spectrum from each area was collected using ‘dynamic pixel’ (oMALDI 5.1, MDS Sciex). Ion images where generated using BioMap (MALDI-MSI.org).

4.3 Results and Discussion

4.3.1 MALDI-MSI of Formalin Fixed Rat Brain Sections

Analysis of formalin fixed rat brain sections, without any pre-treatment, yielded high quality molecular images for several phosphatidylcholine (PC) and sphingomyelin (SM) species. MALDI-MS images of selected lipid species clearly highlight the specific anatomical regions of the brain, as illustrated by comparing the labelled H&E stained section in figure 4.1 with MALDI-MS images (figure 4.1). For example, PC 36:4, *m/z* 804, is highly localised within the hippocampus, as shown by the ion intensity within this region. Lower ion counts for this species are observed in the cerebral cortex, striatum and molecular/granular layer of the cerebellum. The corpus callosum, thalamus, midbrain, pons, and medulla regions are outlined by very low or zero intensity regions. Conversely

PC 38:/40:4 (*m/z* 838), was not detected or displayed very low counts in the hippocampus, molecular and granular layers of the cerebellum, cerebral cortex and striatum regions (grey matter regions). High ion counts for this lipid were observed within the corpus callosum, optic chiasm and arbour vitae area of the cerebellum (white matter regions of the brain).

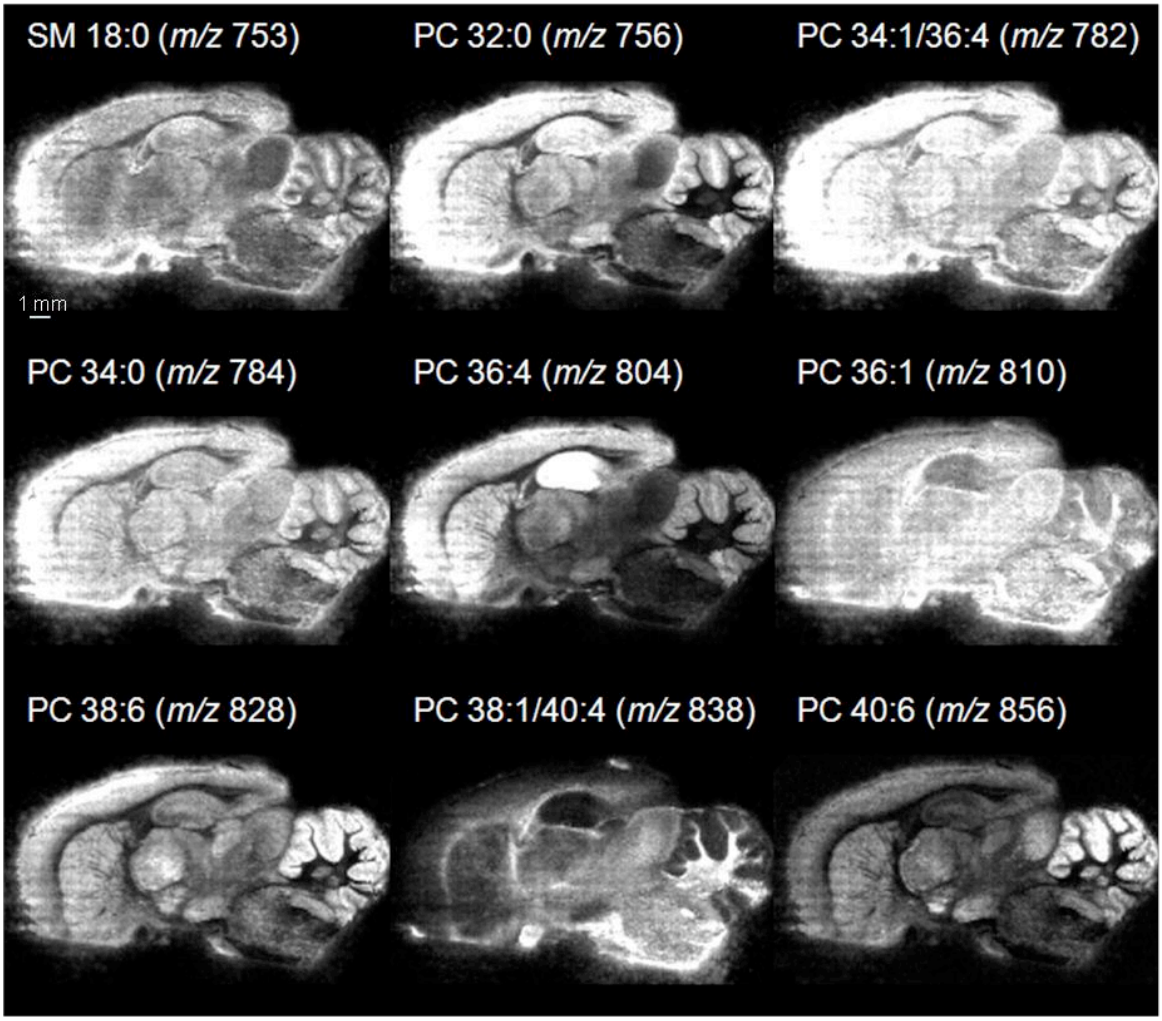

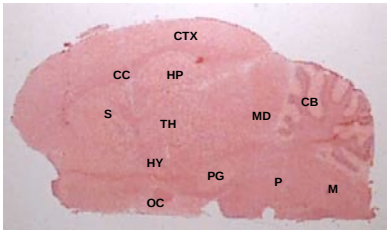

CTX=cerebral cortex, CC=corpus callosum, HP=hippocampus, S=Septum, TH=thalamus, MD=mid brain, CB=cerebellum, M=medulla, P=pons, PG=pituitary gland, HY=hypothalamus and OC=optic chiasm.

Figure 4.1. MALDI-MS images of PC and SM species from formalin fixed sagittal rat brain sections with a haematoxylin and eosin (H&E) stained sagittal section. Regions of anatomical interest are labelled. Image intensity ranges from 500-10,000.

The lipid images presented in figure 4.1, from formalin fixed tissue, correspond well with previously published data[10, 12, 14, 155, 165, 166, 172, 205, 230, 232, 233, 238, 275-278] and unpublished data obtained in this laboratory, for the analysis of lipid species directly from fresh rat brain sections. The three most commonly imaged lipid species within the rat brain to date, PC 32:0, PC 34:1, and PC 36:1, all display similar distributions to data published by Wang and co-workers (2008) [165]. The MALDI image of *m/z* 760 $[PC\ 34:1+H]^+$ shows an omnipresent distribution in the brain (data not shown), however images of *m/z* 782 and 798, which represent the sodium and potassium adduct respectively, show decreased ion counts within the corpus callosum and arbour vitae region of the cerebellum. These results indicate that multiple species are detected within this spectral region. Similar results for freshly prepared sagittal sections have been obtained within our laboratory. The sodium adduct for PC 34:1, *m/z* 782 shares the same m/z as the protonated species of PC 36:4 and with the growing number of lipid species being identified it is highly possible that numerous other lipid species share this mass range.

The image of PC 32:0 (*m/z* 756) displays high ion counts outlining the grey matter regions of the brain. This is one of the most predominant PC species ionised in positive ion mode and all adducts of this lipid share the same lateral distribution. In contrast to Wang et al (2008) [165], data presented here for the distribution of PC 36:1 (*m/z* 810) show this lipid is not confined mainly within white matter regions of the brain. An even distribution of PC 36:1 across most areas of the brain is presented in figure 4.1, but lower intensity counts are seen within the hippocampus and the cerebellar cortex. It should be noted that this study used sagittal rat brain sections whereas Wang and co-workers (2008) [165] analysed coronal sections. In addition, we have employed a different matrix system which may account for the differences seen. The sodium adduct for PC 36:1 is detected at the same m/z as the protonated species of PC 38:4. The occurrence of overlapping species

in the spectral region of interest highlights that care must be taken in the interpretation of MS images.

The images presented show some evidence of laser ‘oversampling’[247], which results in areas of lower ion intensity, in a geometric arrangement across the image area. This is often seen in high resolution MALDI-MS images.

A list of the lipid species ionised from both fixed and fresh tissue preparation is shown in table 4.

Peak Assignments for Fixed and Fresh Tissue	
m/z	**Assignment**
725.50	SM 16:0 + Na
734.57	PC 32:0 + H
741.50	SM 16:0 + K
753.50	SM 18:0 + Na
754.58	PC 32:1 + Na
760.59	PC 34:1 + H
769.50	SM 18:0 + K
770.57	PC 32:1 + K
781.60	SM 20:0 + Na
782.56	PC 34:1 + Na
784.57	PC 34:0 + Na
786.58	PC 36:2 + H
788.61	PC 36:1 + H
798.55	PC 34:1 + K
800.55	PC 34:0 + K
804.55	PC 36:4 + Na
808.59	PC 36:2 + Na
810.60	PC 36:1 + Na
820.54	PC 36:4 + K
824.62	PC 36:2 + K
826.58	PC 36:1 + K
828.56	PC 38:6 + Na
832.61	PC 38:4 + Na
835.60	SM 24:1 + Na
838.63	PC 38:1 + Na
844.52	PC 38:6 + K
848.60	PC 38:4 + K
851.60	SM 24:1 + K
856.58	PC 40:6 + Na

Table 4. Tentative assignment of lipid species detected in both fresh and fixed tissue with their respective *m/z* values.

The images presented in figure 4.2 along with spectral examination of these samples (figure 4.3) revealed different ionisation pathways are favoured with FF tissue compared to fresh. The sodium adduct is the most abundant species in the former compared to the potassium adduct in the latter. This was observed for all lipids that have previously been reported by MALDI-MSI. There are also clear differences in the spectra obtained for the fixed and the fresh sections, as demonstrated by the spectral overlay presented in figure 4.3. The $[M+Na]^+$ is the most abundant ion in fixed tissue as shown by the red peaks in the spectra, whereas the $[M+K]^+$ ion is the predominant in fresh tissue as shown by the blue peaks in the spectra. The mass shift of 16 mass units (u) is clearly visible for each lipid species detected, particularly in the enlarged spectral region, in which the $[M+Na]^+$ and $[M+K]^+$ adducts of PC 32:0 and PC34:1 are labelled. This was further investigated by comparing single point spectra obtained from eight different anatomical regions of the brain, for fixed and fresh tissue (data not included). The ion counts for the $[M+H]^+$, $[M+Na]^+$ and $[M+K]^+$ ions of PC 32:0, PC 36:1, and SM 18:0 for fixed and fresh were compared. For all species and every location investigated the $[M+Na]^+$ ion is the dominating species for fixed tissue and the $[M+K]^+$ ion was found to be the most abundant ion detected in fresh tissue. The salt content in brain is high, which could be why sodium and potassium adducts are often seen when analysing brain tissue. The sodium content of the buffered formalin may be responsible for the increase in sodium adduct formation seen. This would explain the difference observed in the ionisation pathways for the respective sample preparation methods. A recent report published by Sugiura and co-workers (2009)[171] shows selective ionisation pathways are observed with the addition of alkali metals to the matrix solution. This supports the theory of the sodium in the buffered formalin being responsible for the change in ion species seen for the fixed tissue analysis.

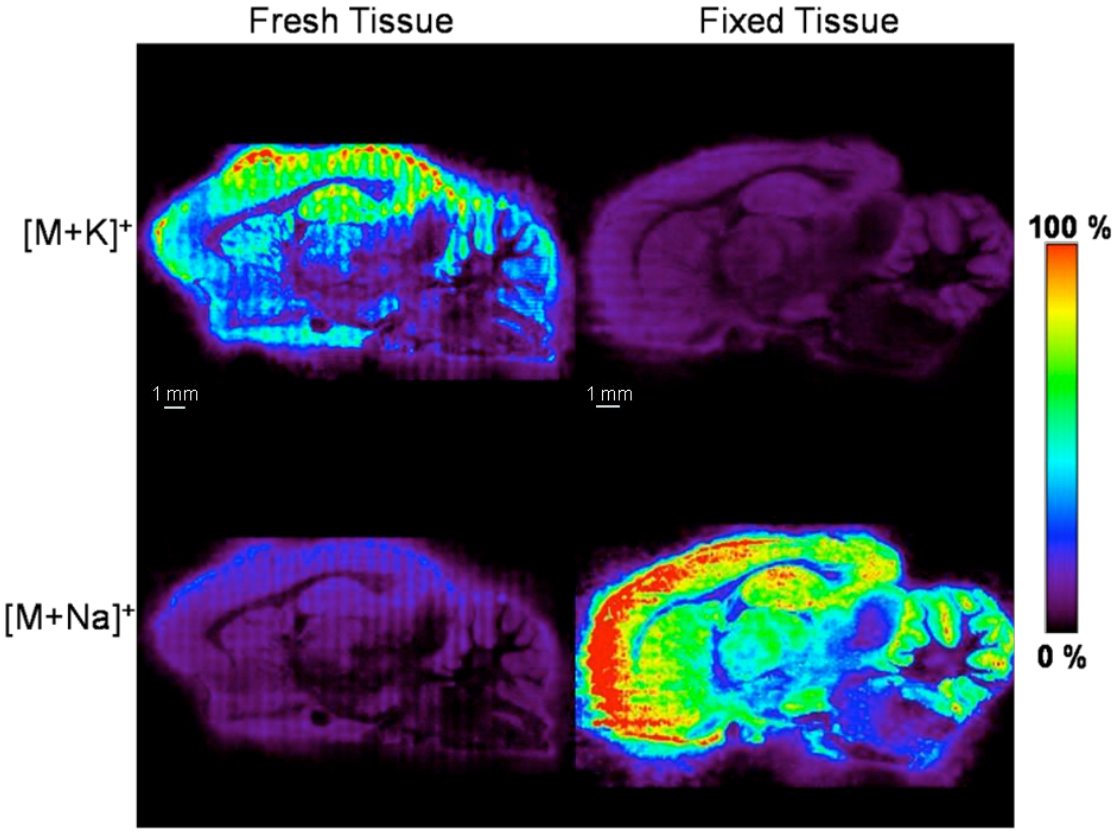

Figure 4.2. MALDI-MS images of PC 32:0 in sagittal rat brains sections of fixed and fresh tissue, for the automated matrix deposition method. Images on the left represent the $[M+K]^+$ against the $[M+Na]^+$ in fresh sections, whilst images on the right represent the $[M+K]^+$ against the $[M+Na]^+$ in fixed sections.

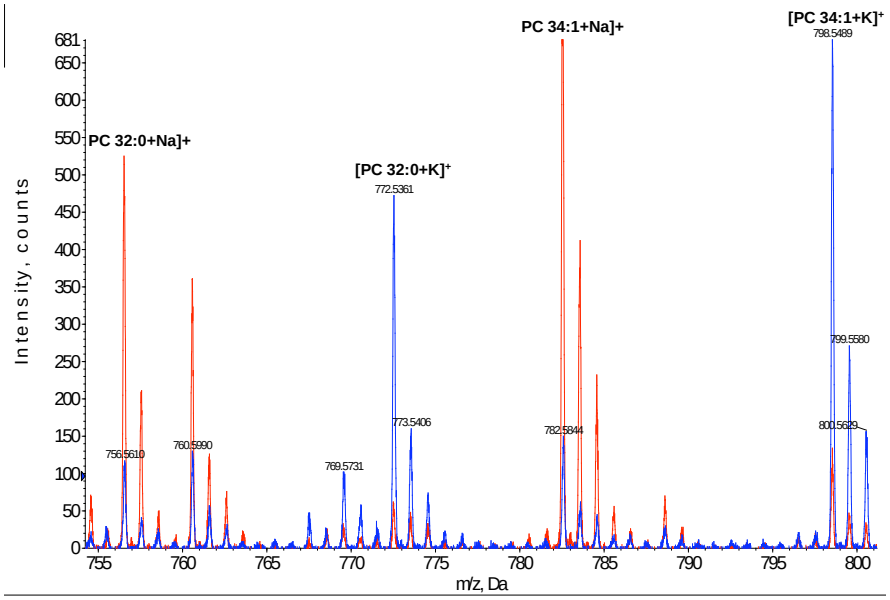

Figure 4.3. MALDI-MS single point spectra taken from the cerebral cortex area of fresh (blue) and fixed (red) tissue. An enlarged spectral region of interest (*m*/z) is presented (bottom), ions relating to PC32:0 and PC 34:1 are labelled.

4.3.2 Analysis of Formalin Spiked Tissue

The increase in sodium adduct formation in fixed tissue was further shown in the analysis of formalin spiked fresh tissue samples (top sections, figure 4.4). The image of [PC 32:0 + Na]$^+$ has a much greater ion intensity within the spiked areas compared to the surrounding tissue, as shown by the pixel intensity. This appears to directly correlate with ion suppression of [PC 32:0 + K]$^+$ within the formalin spiked areas, as shown by the change in ion intensity presented in figure 4.4. The difference in the intensity charts next to each image is due to the potassium adduct being predominantly formed in fresh tissue analysis, as previously discussed. Results from this spiking experiment indicate that formalin fixation does not causes migration or delocalisation of imaged lipids. This is illustrated by examining the formalin spike that covers part of the corpus callosum (top left spot of spiked section, [M+Na]$^+$), an area where PC 32:0 is less abundant. The spike also straddles part of the neighbouring cerebral cortex. It is postulated that if analyte migration occurred as a result of formalin spiking (and hence fixation) then lipids from the cerebral cortex may have been detected within the corpus callosum. Low ion counts within the corpus callosum indicate that no migration of PC 32:0 from the cerbebral cortex has occurred.

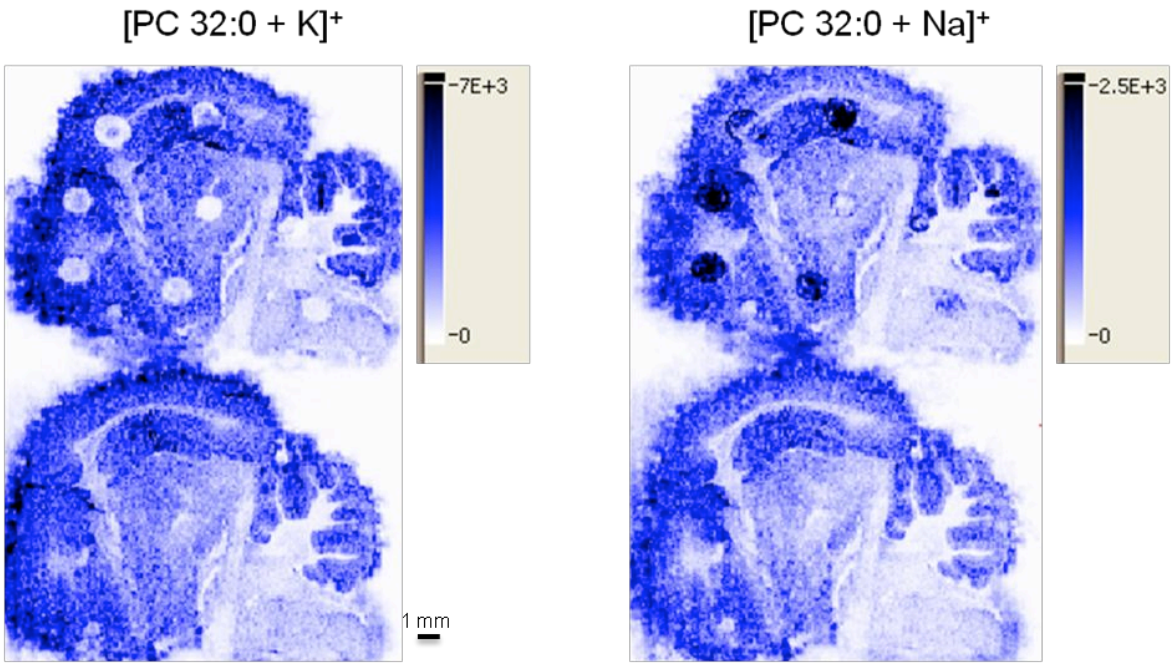

Figure 4.4. MALDI-MS images of PC 32:0 taken from formalin spiked sagittal rat brain section, top images, and fresh control section, bottom images. The $[M+K]^+$ species is represented on the left and the $[M+Na]^+$ species on the right.

4.3.3 Tandem Analysis

High resolution (50 µm) MS/MS imaging analysis of the ion at *m/z* 756, $[PC\ 32:0 + Na]^+$, and 772, $[PC\ 32:0 + K]^+$, was carried out for fixed and fresh tissue respectively. Images produced from the fragment ions for each analysis displayed the same distribution over the tissue sections; an example of the high resolution image achieved is presented in figure 4.5 for fixed tissue analysis. The analysis of single point CID spectra taken from the cerebral cortex for fixed and fresh tissue, demonstrated a more enriched fragment spectra for the dissociation of the sodium adduct, compared to the potassium adduct, as present in figure 4.6. Peaks common to both spectra are head group related peaks and are observed at *m/z* 86 representing choline, $N(CH_3)_3(CH_2)_2$, *m/z* 184 for the phosphocholine head group, *m/z* 146 and 162 corresponds to the five-membered cyclophosphane ring ($C_2H_50_4P$) with the addition of a sodium adduct for fixed tissue, and potassium adduct for fresh respectively. A peak corresponding to the neutral loss (NL) of trimethylamine, $N(CH_3)_3$, can also be observed in both spectra at *m/z* 697 for fixed tissue and *m/z* 713 for fresh. The difference in mass between the same fragment peaks in each spectrum is attributed to the mass difference between sodium and potassium. These peaks are common in CID spectra of phospholipids and sphingomyelins and agree with those previously reported[10, 105, 114, 172, 279]. There is a large difference in intensity for peaks representing the NL of the head group with and without the alkali adduct. This is evident when comparing the peaks at *m/z* 573 and 589 for the sodium (top spectrum) and potassium (bottom spectrum) adducts, which correspond to the NL of the head group, and the peak at *m/z* 551 which corresponds to the NL of the head group with the alkali adduct. As mentioned, these peaks in the CID spectrum from fresh tissue show incredibly low intensity, they are not considered to be above an acceptable S/N ratio. The peak at *m/z* 441, which is present in the CID spectrum from fixed tissue, but absent from the fresh tissue spectrum, represents a NL of 325 u, corresponding to the NL of trimethylamine and

palmitic acid (hexadecanoic acid) from the head group and glycerol backbone respectively, and thus represents [PC 32:0 + Na- $C_{16}H_{32}O_2$- $N(CH_3)_3]^+$, this is in agreement with literature[10, 105, 114, 172, 279]. Peaks representing fatty acid molecules or their NLs are not usually detectable above an acceptable S/N ratio in MALDI CID spectra of $[M+H]^+$, $[M+Na]^+$ and $[M+K]^+$, as demonstrated by the absence of a acceptable peak at *m/z* 500 (fixed tissue), which would represent the NL of palmitic acid. Cation adducts are known to induce greater fragmentation compared to the protonated molecule, which, when dissociated by low-energy CID, as is commonly used, results in a CID spectrum containing minimal peaks, the most intense signal is the phosphocholine head group peak at *m/z* 184[13, 114, 279]. The degree of fragmentation of selected adducts appears to be proportional to the arrangement in the periodic table, as can be observed when comparing the CID spectra of PC 32:0 obtained from the sodium adduct, to the potassium adduct. This is further evidenced in literature and by results obtained from this group. The addition of lithium to the matrix solvent system, in the case of MALDI, or to the electrospray solvent solution, in the case of ESI, has shown the dissociation of the lithium cation of PLs causes greater fragmentation, resulting in peaks representative of the fatty acid side chains, enabling structural identification[10, 13, 105, 114].

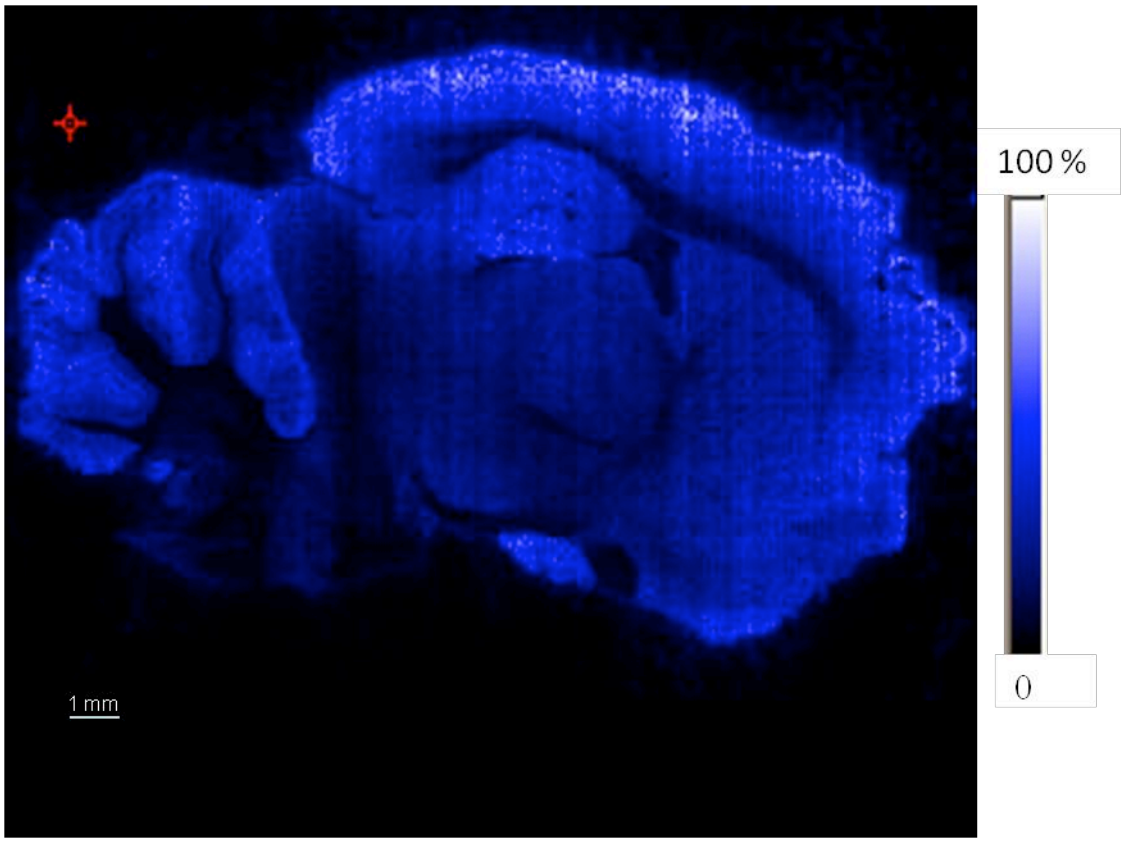

Figure 4.5. High resolution MALDI-MS/MS image of *m/z* 756, $[PC\ 32:0+Na]^+$ from formalin fixed tissue. The image is of the fragment ion at m/z 573. The image clearly outlines the anatomical regions of the brain where this ion is and is not present, due to the change in pixel intensity.

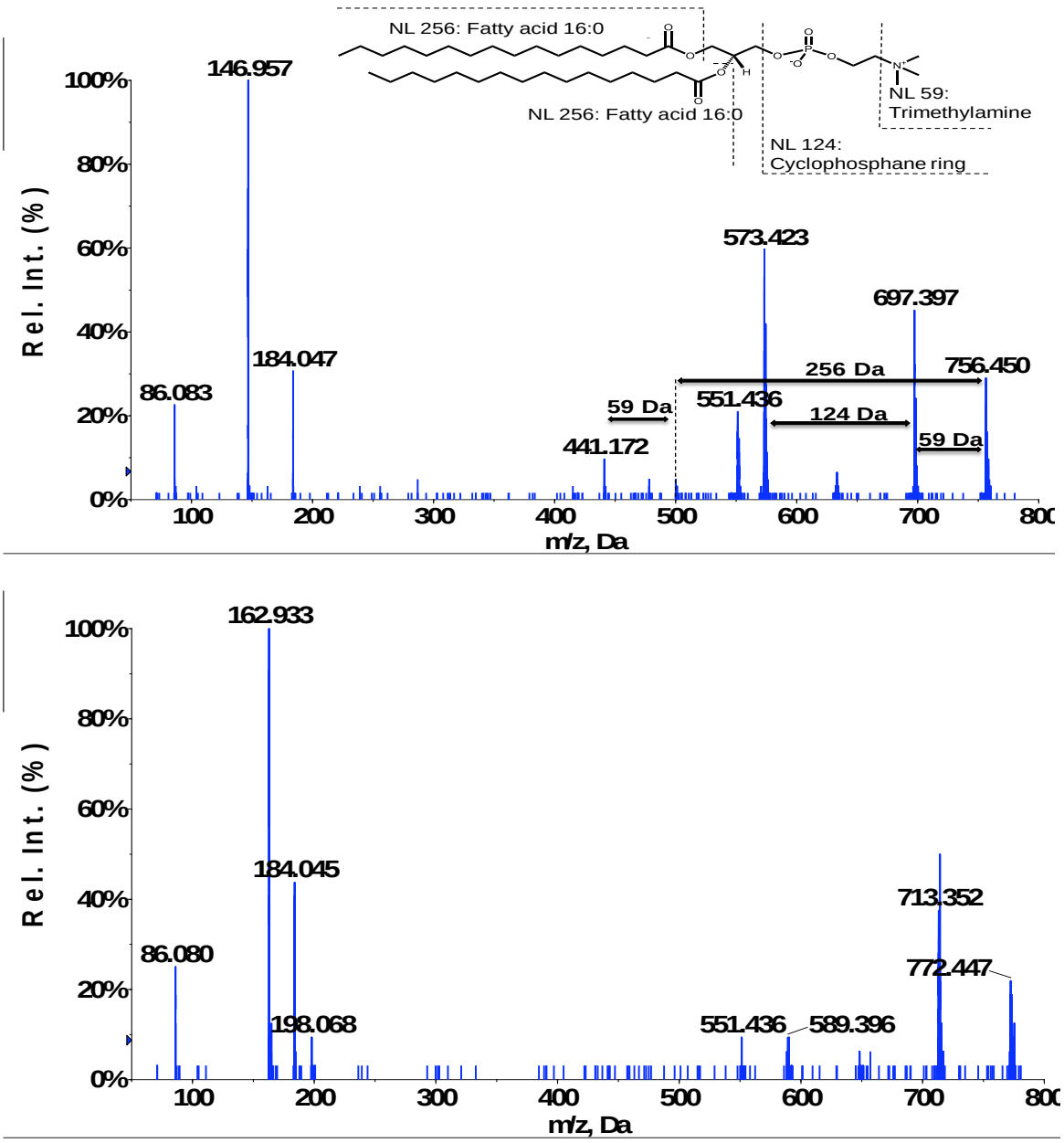

Figure 4.6. MALDI MS/MS mass spectra showing the fragment ions produced from the dissociation of $[PC\ 32:0+Na]^+$, m/z 756 from fixed tissue, top spectrum, and $[PC\ 32:0+K]^+$, *m/z* 772 from fresh tissue, bottom spectrum. There is a significant increase in the intensity of peaks associated with the NL of the phospholipid head group, *m/z* 551, 573 for $[PC\ 32:0+Na]^+$ compared to *m/z* 551 and 589 for $[PC\ 32:0+K]^+$. There is also a peak at *m/z* 441 in the spectrum from fixed tissue with is not present in fresh, A schematic of PC 32:0 is shown in the top spectrum, with labelled fragmentation pathways.

4.3.4 Prolonged Storage in Formalin

The MALDI-MSI investigation of tissue stored in formalin for prolonged periods showed such procedures to be unsuitable for MS, or MSI analysis, as shown by the spectra and corresponding images presented in figure 4.7. The image of PC 32:0 in fresh tissue and tissue fixed for 3 weeks display a defined distribution that correspond to those reported throughout this thesis, and in literature[10, 12, 14, 155, 165, 166, 172, 205, 230, 232, 233, 238, 275-278], as shown by the images presented within the top and middle spectra in figure 4.7, for fresh and fixed respectively. The distribution of PC 32:0 in the section of brain fixed for one year appears to show signs of analyte delocalisation. This is evident by the increase in signal intensity for this lipid within the white matter regions of the brain, such as the corpus callosum and arbour vitae of the cerebellum. The anatomical features of this section are also no longer clearly defined, the hippocampus and corpus callosum are just recognisable, and the granular layer of the cerebellar cortex appears defocused. This may be due to analyte delocalisation; however it could also be due to the accumulation of high concentrations of salt within the tissue. The analysis of single point spectra taken from the cerebral cortex of tissue fixed for three weeks, middle spectrum in figure 4.7, shows reduced spectral complexity within the region of interest, *m/z* 700-900, compared to fresh tissue, top spectrum in figure 4.7. This is thought to be due to the high concentration of sodium in this sample, and thus a shift to the sodium adduct for PL species, as previously demonstrated in this chapter. The most abundant peak within this spectrum can be seen at *m/z* 656, this is believed to be a matrix associated cluster, the high abundant matrix associated peaks at *m/z* 265 and 221, observed in fresh tissue analysis, are not observed with high abundance in fixed tissue, thus different matrix adducts are also believed to be formed. The single point spectrum from the analysis of tissue stored in formalin for twelve months is rather complex, as demonstrated by the bottom spectrum in figure 4.7. This may be caused by an increase in the formation of salt

adducts, however this is highly unlikely, it is believed to be primarily due to lipid fragmentation, either in source or prior to ionisation, as a result of lipid degradation within the tissue. The analysis of tissue stored in formalin for eighteen months was not possible as the integrity of the tissue was extremely poor, upon sectioning the tissue crumbled and fell apart, thus it was not possible to obtain a section.

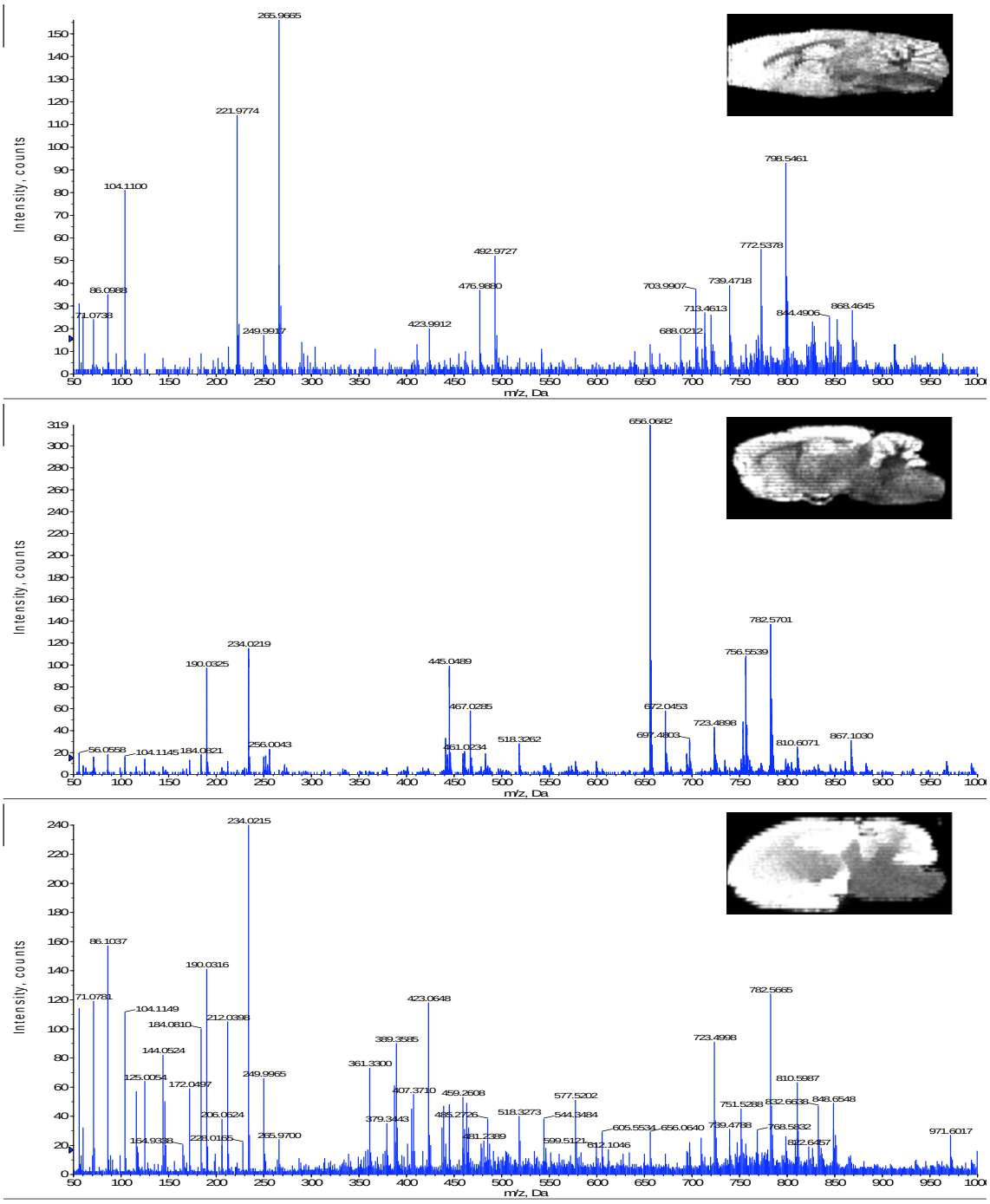

Figure 4.7. MALDI single point spectra taken from the cerebral cortex of fresh tissue (top spectrum), tissue fixed for three weeks (middle spectrum) and tissue fixed for twelve months (bottom spectrum), the corresponding MALDI-MS images for PC 32:0 are also presented.

4.5 Conclusion

Lipid species have been successfully ionised directly from formalin fixed tissue without any pre-treatment that could interfere with the distribution of these molecules. High quality molecular lipid images were obtained, showing mutual distribution to fresh tissue preparation [10, 12, 14, 155, 165, 166, 172, 205, 230, 232, 233, 238, 275-278], indicating no signs of analyte delocalisation, or interference from the formalin itself. Sodium buffers associated with the formalin fixation protocol caused a change in previously reported ionisation pathways [10, 12, 14, 155, 165, 166, 172, 205, 230, 232, 233, 238, 275-278], and the $[M+Na]^+$ was found to be the most readily detected ion for each lipid species investigated. This was evidenced in the images and spectra presented in this chapter, and by the investigation of formalin spiked tissue, which showed an increase sodium adduct formation directly correlated to a decrease in potassium adduct formation, within the spiked areas.

As the sodium adducts in fixed tissue were detected with the highest abundance, this ion was selected for tandem MS analysis. Dissociation of *m/*z 756, $[M+Na]^+$ in fixed tissue produced a more enriched CID mass spectrum, compared to those obtained from fresh tissue for the analysis of *m/z* 772, $[M+K]^+$. The peak at *m/z* 441 in the CID spectrum from fixed tissue, although present with low abundance, corresponds to the NL of palmitic acid and trimethylamine [10, 105, 114, 172, 279], thus aiding in structural identification of this ion.

Results presented in this chapter show tissues stored for prolonged periods in formalin fixative are not suitable for MALDI-MS investigations. MALDI-MSI images of PL distribution in brains stored for up to a year were poorly resolved, showing signs of analyte delocalisation and/or high accumulation of salt within the tissue. The mass spectra from these sections showed signs of lipid degradation, indicated by a highly complex spectrum. As lipids are not directly affected by formalin, they are not ‘fixed’, it is believed that over time they degrade.

As the involvement of lipids has now been proven in numerous physiological and pathological processes, the ability to analyse these species directly from and compare to, clinical histological specimens could provide a plethora of additional information.

5. Steps Towards MALDI-MS Analysis of Cell Envelope Components of Mycobacterium Bovis *Extracted from Infected Cattle.*

5.1 Introduction

The *Mycobacterium tuberculosis* complex includes the slow-growing pathogenic species *M. bovis*, the causative agent for tuberculosis in cattle. In addition to being a zoonotic pathogen, *M. bovis* is also known to be the causative agent of TB in a large spectrum of mammals, including, goats, seals, llama and oryx[280-282]. Human outbreaks of tuberculosis caused by *M. bovis* (bTB) have been attributed to infected dairy produce, direct transmission from cattle to dairy farm/abattoir workers, and as opportunistic pathogens in immunocompromised individuals [281]. In addition to the health risks associated with this bacterium, the economic cost as a result of infected cattle is incredibly high[283]. The Department for Environment Food and Rural Affairs placed this cost at £108.4 million in 2008/2009, compared to £8.2 million for 1998/99, the cost over the decade totalling at a staggering £603.3 million [284]

M. bovis BCG, an attenuated version of *M. bovis* is also the only licensed TB vaccine that is currently used in immunisation projects globally, according to the World Health Organisation (WHO) programme of immunisation [285]. The efficacy of the BGC vaccine is, however, uncertain, investigations have shown different subcultures used for vaccination show large variations in their immunoprotective capabilities[285]. Immunisation does not necessarily confer immunity to pulmonary TB. *Mycobacterium bovis* and *Mycobacterium tuberculosis* share 99.95 % genomic identity at the nucleotide level, and a cell wall composition that is common among all slow-growing pathogenic *Mycobacterium*.[280, 286] Although phenotypes and virulence are clearly different

between the two strains, demonstrated by different host infections, the similarities in the genome and cell wall composition undoubtedly indicate that the investigation of one species will provide a wealth of information on the other. The importance of the unique lipids that constitute mycobacterial cell wall were discussed in chapter 1. They are key to the intracellular survival, and contribute hugely to their virulence; they provide potential targets for pharmaceuticals, as well as being possible vaccine candidates. Investigations of mycobacterial lipids are either carried out on purified lipids from bacterial extracts, or by evaluating their contribution to growth and virulence by monitoring animal models infected with strains carrying specific mutations for the biosynthesis one or more of these lipids. MALDI-MS investigations of cell wall associated lipid species to date have been for the investigation of the effects of mutant models, and structural identification/mass determination of lipids purified from bacterial cell extracts. Research presented in this chapter investigates the feasibility of MALDI-MS detections of cell wall lipids, including mycolic acids, PDIMS, PGLs and MMGs, directly from lymph and blood extract taken from cattle infected with *M. bovis*. This may offer a more rapid first stage diagnostic tool, as the need for the growth stages that are necessary to identify many slow-growing pathogenic *Mycobacterium* are not needed for the analysis here.

5.2 Experimental

5.2.1 Materials

Alpha-cyano-4-hydroxy cinnamic acid (α-CHCA), 2,5-dihydroxybenzoic acid (DHB), 2',4',6'- trihydroxyacetophenone monohydrate (THAP) and trifluoroacetic acid (TFA) were purchased from Sigma-Aldrich (Dorset, UK). Methanol, chloroform and acetonitrile were purchased from Fisher Scientific (Loughborough, UK). Standards of free mycolic acids,

mycolic acid methyl esters and the lipids, phthiolcerol dimycocerosatic (PDIMs), phenolic glycolipid (PGLs) plus mono mycoloyl glycerol (MMG) were supplied by Professor D. Minnikin, Department of Biosciences, University of Birmingham.

5.2.2 Lipid Extracts from Infected Cattle

The following samples were supplied by Professor D. Minnikin, Department of Biosciences, University of Birmingham, as dry samples; cattle lymph extracts 4469 and 4465 A (PDIMs) and B (PGLs/MMG); cattle blood extracts 5005 A (PDIMs) and B (PGLs/MMG); and cattle lymph non-polar extracts, PDIMs samples A1 (4465), 2 (4472) and 3 (4479), MAMEs samples B1 (4465), 2 (4472) and 3 (4479), and PGL + MMG samples C1 (4465), 2 (4472) and 3 (4479). TLC plates, designated control plates 1 and 2, and sample plates A, B and C, contained species specific lipid extracts and blood and lymph extracts.

5.2.3 Lipid Standards and Lipid Sample Extract Preparation

Standards were prepared at a concentration 2 mg mL^{-1} in chloroform and mixed 1:1 (v/v) with the matrix solution. Lymph and blood extracts were re-suspended in 10, 50, 100, 200 and 400 µL of chloroform and either mixed 1:1 (v/v) with the matrix solution or applied to the target plate using the overlay method.

5.2.4 Matrix Compounds and Solvent Systems

A number of different matrix solutions were evaluated for the analysis of the mycolic acid and lipid standards, they were as follows; αCHCA at a concentration of 25 mg mL^{-1} in 80 % MeOH (0.1 %TFA); DHB at a concentration of 25 mg mL^{-1} in 80 % MeOH (0.1 %TFA); THAP at a concentration of 20 mg mL^{-1} in 80 % MeOH (0.1 %TFA) and DHB at a concentration of 12 and 25 mg mL^{-1} in 1:1 (v/v) MeOH:$CHCl_3$ (v/v), (0.1 %TFA).

5.2.5 Tissue Preparation

Lymph nodes were excised from infected cattle and autoclaved (sterilised) to remove the risk of infection. These were then frozen to -80 and stored until analysis. Upon analysis the lymph nodes were transferred to a cryostat chamber and left for 30 min to allow temperature equilibration. The lymph node was then embedded on a cryostat chuck using water-ice-slush and sectioned. A range of thicknesses were evaluated. The sections used for MALDI-MSI analysis were sectioned at 5 µm and transferred to a stainless steel MALDI target plate.

5.2.6 Matrix Deposition

Matrix deposition was carried out in a fume hood using an artistic airbrush as previously described. For lymph node analysis, DHB at 12.5 mg mL^{-1} (100 % acetonitrile (1 % TFA)), was deposited over the target insert using an artistic airbrush, from a distance of 15-20 cm in repeated cycles. Deposition was deemed optimal when a dense coating of white crystals covered the target plate and tissue area. A larger amount was used for the preparation of TLC control plates and sample plate C, 15-20 mL^{-1} of DHB at 12.5 mg mL^{-1} (100 % acetonitrile (1 % TFA)) was deposited in repeated cycles from a distance of around 20 cm. Sample plates A and B were sprayed from a distance of roughly 15 cm with a much wetter deposition achieved than the previous plates.

5.2.7 Mass Spectrometry

Lipid standards and extracts were analysed using an Applied Biosystems (Toronto, Canada) hybrid quadrupole time-of-flight (QqTOF) instrument (Qstar XL). The instrument was fitted with an orthogonal MALDI ion source and a nitrogen laser (337nm), operated at 25 µJ, unless otherwise stated, with a repetition rate of 20Hz. The instrument was operated in the positive ion reflectron mode, recording all signals either between *m/z* 200-2000 or *m/z* 1000-2000. Data were acquired using a Q1 scan time of 1 second, summing

30 scans per spectra obtained. Mass spectral data were analysed using the Analyst software supplied by Applied Biosystems.

For TLC analysis, the plates were analysed as an 'imaging experiment', with a target plate stepping distance set to 1 mm for both the x and y dimension. Acquisition was carried out using the dynamic pixel setting; this moves the laser within the 1 mm^2 area, summing the data to give an accumulated mass spectrum for each pixel area. The nitrogen laser (337nm) was operated at 50 µJ, unless otherwise stated, with a repetition rate of 20Hz. Data were acquired using a dwell time of 2 or 4 seconds, over a mass range of *m/z* 1000-2000, to enhance detection over this *m/z* range. The resulting two-dimensional ion density maps were generated using TissueView software, after conversion of the raw data into the format required using the 'wiff to analyse' script, provided by Applied Biosystems.

For MALDI-MS imaging analysis of cattle lymph node, the nitrogen laser (337nm) was operated at 30 µJ, with a repetition rate of 20Hz. Data were acquired using a dwell time of 1 second, over a mass range of *m/z* 700-2000. The target plate stepping distance was set to 100 µm for both the x and y dimension using the imaging acquisition software. Data were acquired using the 'dynamic pixel' setting, which involves the laser being moved within the 100 μm^2 pixel area and resultant data being summed to give an accumulated mass spectrum over one second for each pixel area. The resulting two-dimensional ion density maps were generated using the TissueView software, after conversion of the raw data into the format required using the 'wiff to analyse' script, provided by applied biosystems.

5.3 Results and Discussion

5.3.1 Matrix Evaluation for the Analysis of Mycolic Acids and Lipid Standards

The initial evaluation of matrix compounds suitable for MALDI-MS analysis of *Mycobacterium* cell wall associated lipids involved the screening of DHB, αCHCA and THAP, in 80 % MeOH (0.1 % TFA). The mass spectra acquired from the analysis of the lipid standards when using THAP as the matrix did not contain any peaks (results not shown), thus no further studies were carried out with this matrix. The mass spectra acquired using αCHCA as the matrix system did not reveal peaks within the desired *m/z* range that differed by multiples of 14 mass units. MAs and other cell wall associated lipids from these species occur in nature as structurally related molecules that differ from one another by one or two methylene groups; hence a difference of 14 or 28 *m/z* should be present in the spectra. These results indicated αCHCA is not a suitable matrix for the analysis of these lipids, thus no further studies were carried out with this matrix. The MALDI-MS analysis of the standard of mycolic acid methyl esters using DHB at 25 mg mL^{-1} (80 % MeOH, 0.1 TFA), was successful in the detection of alpha-, methoxy-, and keto-MAMEs, shown by the spectrum presented in figure 5.1. Peaks representing the major homologues for the alpha-, methoxy-, and keto-MAMEs can be observed at *m/z* 1173, 1289, and 1317 respectively, these results correspond well with those previously reported for the MALDI-MS analysis of these lipids[193-197]. Ion counts for these species were found to be low, with relatively high background noise. Free MA standards were not desorbed, ionised and detected efficiently using this system as demonstrated by the mass spectrum presented in figure 5.2, the spectrum is predominantly noise with ion counts only reaching 16. Free mycolates are particularly difficult to ionise due to their non-polar nature, especially the alpha-mycolic acids which are the least polar of the species, this is

possibly why most literature to date reports the MALDI-MS analysis of MAMEs, as these derivatives are more readily ionisable.

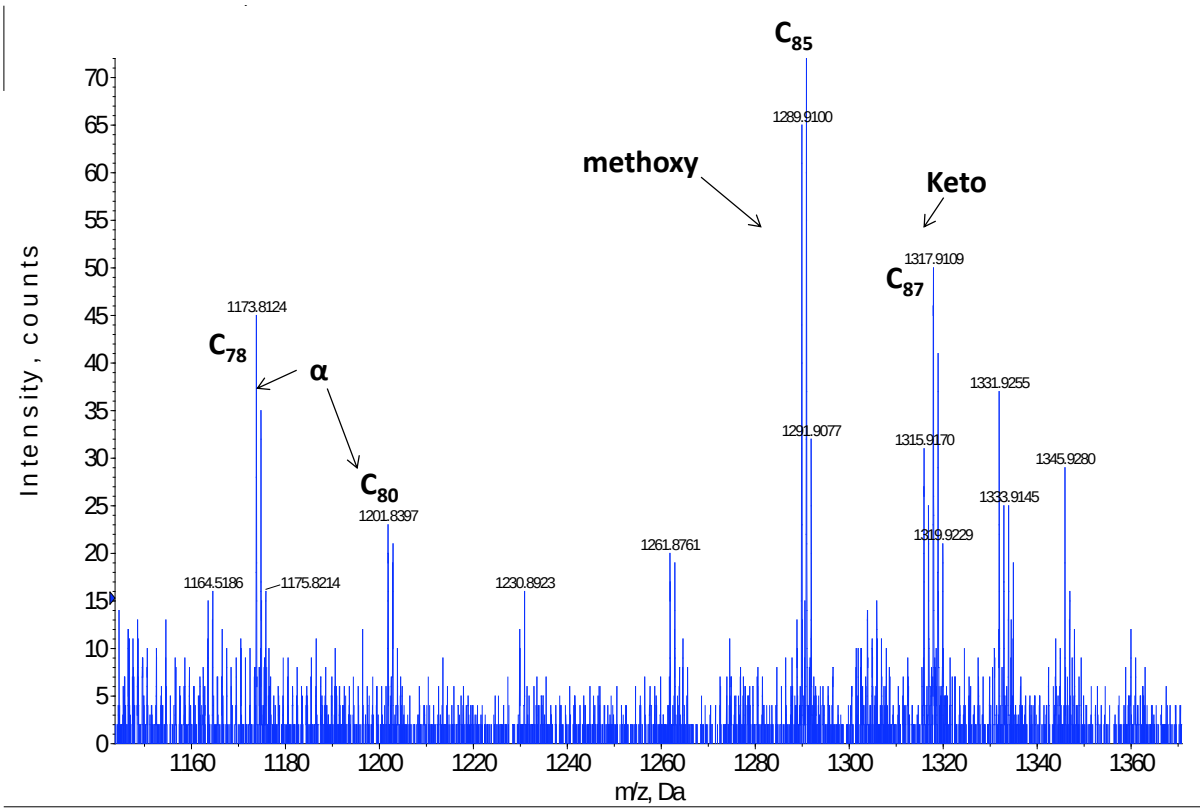

Figure 5.1. MALDI mass spectrum of mycolic acid methyl esters using DHB 25 mg mL^{-1} (80 % MeOH (0.1 %TFA)). Peaks representing the major homologues of the alpha-, methoxy-, and keto-MAMEs along with their carbon chain lengths are labelled. All peaks are believed to be $[M+Na]^+$ ions.

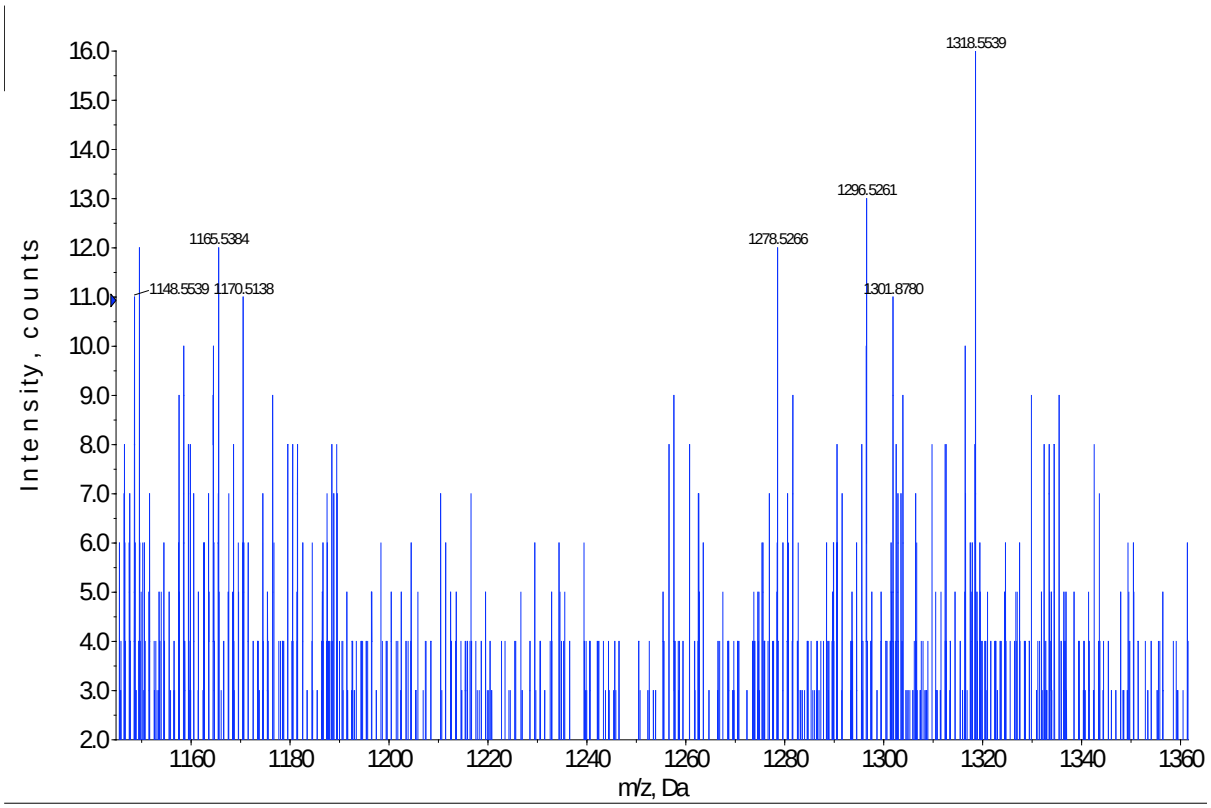

Figure 5.2. MALDI mass spectrum of free mycolic acids using DHB 25 mg mL^{-1} (80 % MeOH (0.1 %TFA)). The ion counts are extremely low and the S/N ratio is poor.

The spectrum recorded from analysis of the extract containing PDIMs using DHB at 25 mg mL^{-1} (80 % MeOH, 0.1 TFA), shows a clear pattern of peaks that differ from one another by 14 u, from *m/z* 1306 to 1460, as shown in figure 5.3. The masses detected here correspond to those previously published for PDIM type A, for carbon chain lengths C_{87} to $C_{97,}$ in MALDI-MS analysis of extracts purified from *M. bovis BCG* wild type, and *M.tb* H37Rv (wild type) and Beijing strains [132, 200, 201]. The mass spectrum acquired from the analysis of PGLs and MMGs using this matrix system show relatively low ion counts for these species, as presented in figure 5.4. Major homologues of MMGs can be observed in the spectrum at *m/z* 1333 and 1362, which correspond to the previously reported masses of keto-MMGs as $[M+Na]^+$ [287]. Peaks representing PGLs can be observed in this spectrum centring around the major homologue at *m/z* 1530, and agree with those in literature [201], however, the quality of the spectrum is rather poor, showing low ion counts and low signal-to-noise ratio (S/N).

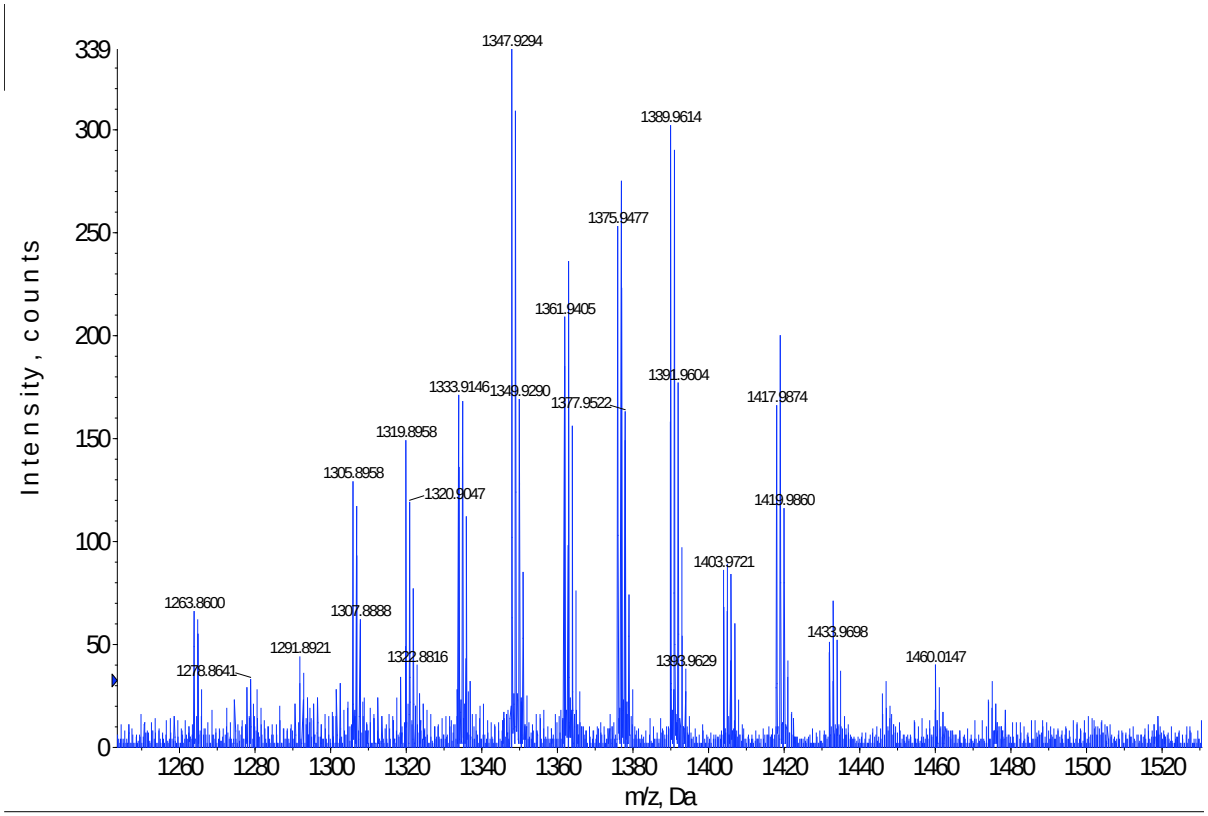

Figure 5.3. MALDI mass spectrum of PDIMs using DHB 25 mg mL^{-1} in 80 % MeOH (0.1 % TFA) as the matrix. Peaks present differ from one another by 14 u, which is characteristic of mycobacterial cell wall lipids; peaks from *m/z* 1306-1460 represent PDIM A, C_{87}-C_{97}. All peaks are believed to be $[M+Na]^+$ ions.

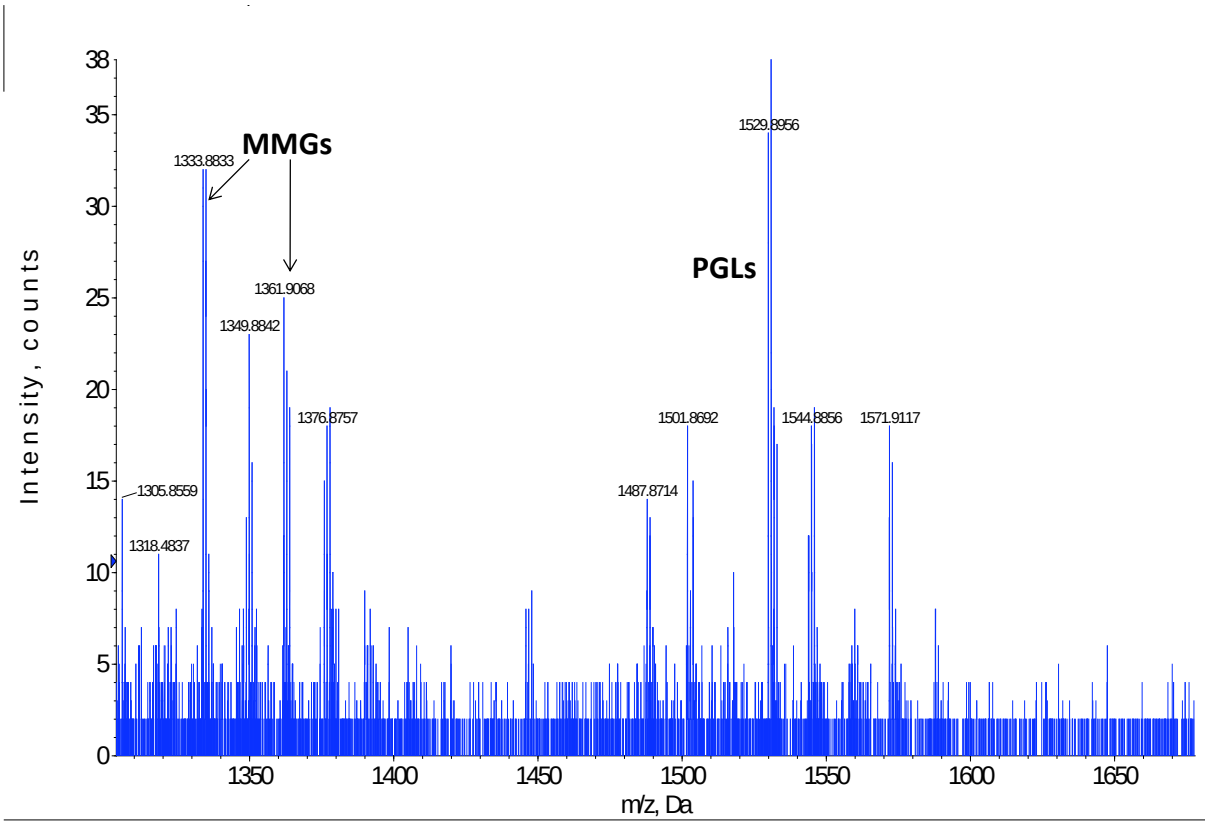

Figure 5.4. MALDI mass spectrum of PGL/MMG lipids using DHB 25 mg mL^{-1} in 80 % MeOH (0.1 %TFA). Peaks representing MMGs are observed at *m/z* 1333 and 1361; the ions ranging from *m/z* 1487-1571 represent PGLs. All peaks are believed to be $[M+Na]^+$ ions.

Previously published MALDI-MS data for the analysis of MAMEs, PDIMs and PGLs has shown DHB at 10 mg mL^{-1} in a solvent system of MeOH:$CHCl_3$ 1:1 (v/v) (0.1 TFA) to be suitable for the analysis of these species[132, 134, 193, 195, 200, 201, 287]. This solvent system was then applied to the analysis of free MAs to assess whether this enabled detection of these species. Free MAs were successfully desorbed, ionised and detected using this matrix and solvent system, as shown by the spectrum presented in figure 5.5. Peaks representing alpha-mycolates can be observed at *m/z* 1159 and 1187, the major homologue for the methoxy-mycolate can be seen at *m/z* 1275, and peaks representing keto-mycolates are observed at *m/z* 1302 and 1318. There is a substantial amount of background noise in this spectrum, however, the S/N for the alpha-, methoxy- and keto mycolates are improved. The ion counts for the MAME standard showed a five-fold increase when using MeOH:$CHCl_3$ 1:1 (v/v) (0.1 TFA) as the solvent system compared to the previously applied system, as demonstrated by comparing figure 5.6 to figure 5.1. This increase in sensitivity had enabled the detection of more species, as evidenced by the enriched spectrum in figure 5.6. The increased sensitivity observed with this system is thought to be attributed to the solubility of these analytes in $CHCl_3$, whereby a greater incorporation of the analytes into the matrix crystals is believed to be achieved. This matrix system was used for the analysis of the cattle extracts.

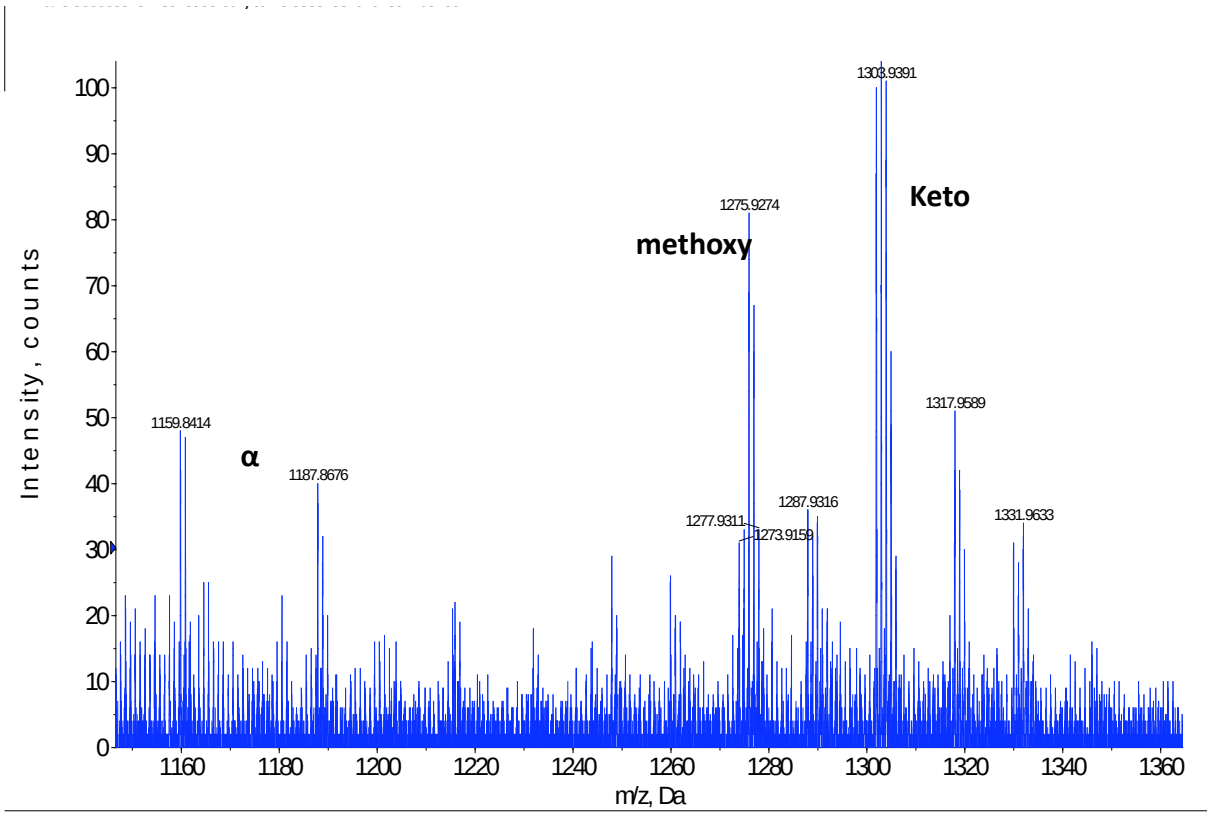

Figure 5.5. MALDI mass spectrum of free mycolic acids, using DHB 12.5 mg mL^{-1} in MeOH:$CHCl_3$ 1:1 (v/v), 0.1 TFA as the matrix.. The key peaks representing the alpha-, methoxy- and keto- MAs are labelled and are observed at *m/z* 1159 and 1187 (alpha), 1275 (methoxy) and 1303 (keto). All peaks are believed to be $[M+Na]^+$ ions.

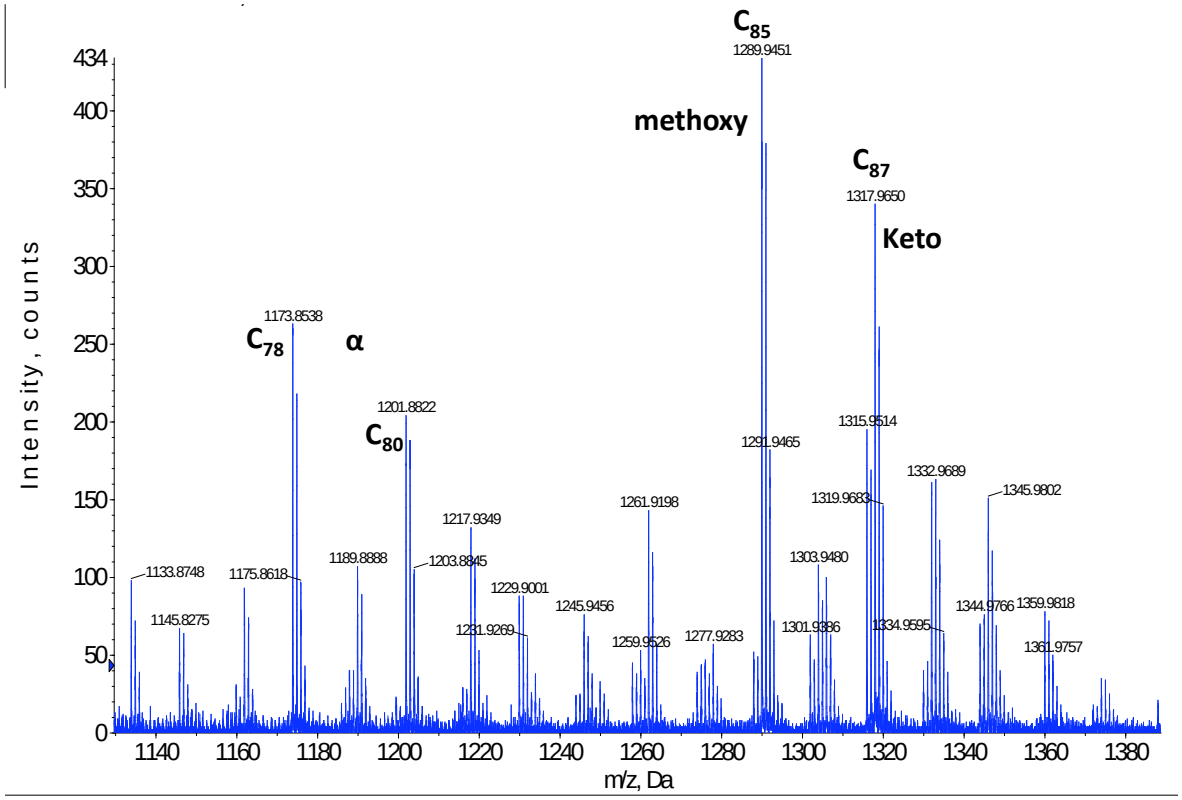

Figure 5.6. MALDI mass spectrum of mycolic acid methyl esters using DHB 12.5 mg mL^{-1} in MeOH:$CHCl_3$ 1:1 (v/v), 0.1 TFA as the matrix. The peaks representing the alpha-MAMEs are labelled at *m/z* 1173 and 1201, methoxy-MAMEs centre around the major homologue at *m/z* 1289, and the major homologue for keto-MAMEs can be seen at *m/z* 1317. All peaks are believed to be $[M+Na]^+$ ions.

5.3.2 Lymph and Blood Samples

Extracts of lymph samples 4465 A and B, representing PDIMs and PGLs/MMG respectively, were re-suspended in 200 µL of $CHCl_3$. Initially samples were mixed 1:1 (v/v) with the matrix solution and 1 µL were spotted onto the target plate for MALDI-MS analysis. The MALDI mass spectra acquired from analysis of these samples did not contain any peaks representing PDIMs, PGLs or MMGs within the *m/z* range of interest. Sample application to the target plate was then varied to assess whether this enabled detection of the lipids of interest. This involved 1 µL (2 x 0.5 µL) of each sample being spotted onto the target plate, followed by 0.5 µL of the matrix solution (the overlay method), using both 25 mg mL^{-1} and 12.5 mg mL^{-1} DHB concentrations. A varying laser power (25, 30 and 35 µJ) was also evaluated as the samples had a very different consistency to the standards, when deposited on the target plate, sample A was found to dry as a thick white crust/film. Detection of PDIMs and PGLs/MMGs from these samples was unsuccessful.

Lymph extract 4469 A and B, and blood extract 5005 A and B, representing PDIMs (A) and PGLs/MMG (B), were re-suspended in 50 µL of $CHCl_3$ to give more concentrated samples than those previously analysed. Samples were again applied to the plate as "overlays", this time with an equal concentration of analyte:matrix, analysis was carried out at 3 different laser powers, 25, 30 and 35 µJ. The MALDI mass spectrum acquired from the analysis of lymph sample A contained peaks that differed from one another by 14 mass units. These were observed within the *m/z* region 1151-1257, which is indicative of α-MAs. This sample, however, represents extracts of PDIMs which are observed within the mass range *m/z* 1306-1516 [132, 200, 201], no ions characteristic of these species were observed within this region, as shown in figure 5.7. It is also again worth noting that the alpha-MAs are the least polar of the mycolates, thus one would expect to see peaks representing the methoxy- and keto- MAs along with the alpha species, and showing

higher ion counts. These were not observed in this mass spectrum, thus care needs to be taken with the interpretation of these results, the peaks present are not believed to represent alpha-MAs.

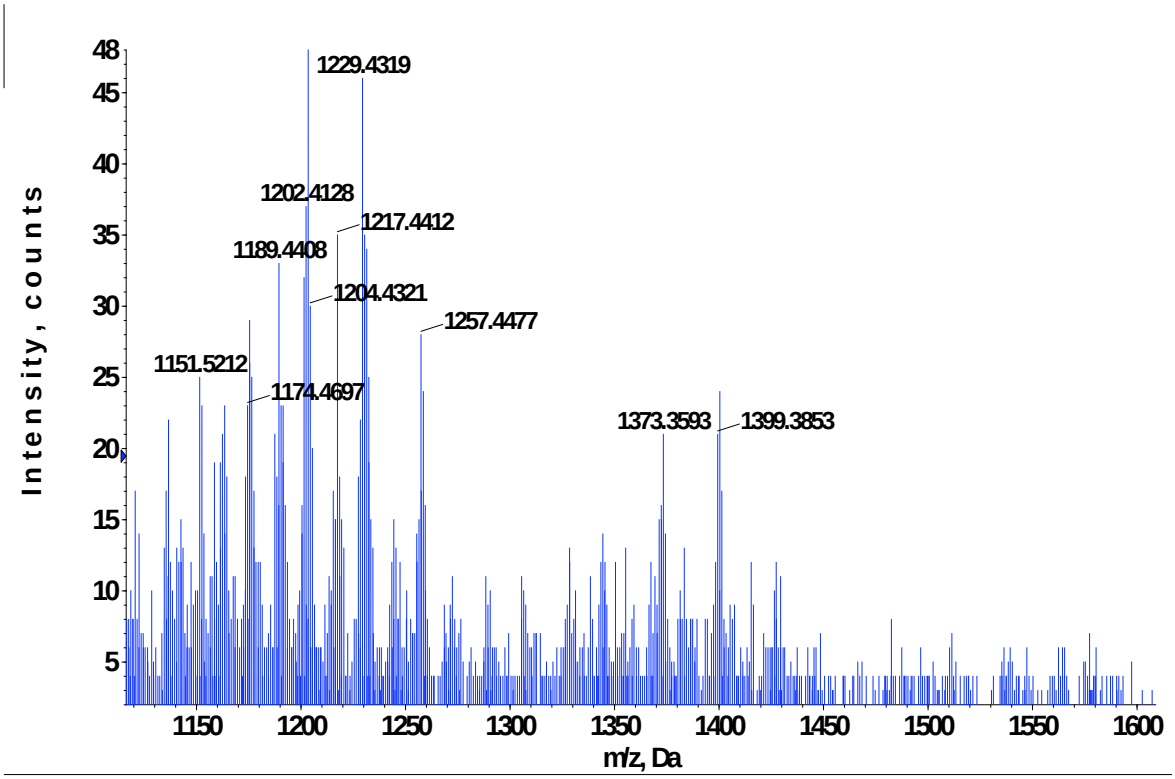

Figure 5.7. MALDI mass spectrum of lymph sample 4469 A, representing PDIMs. A characteristic peak pattern and mass range for mycolic acids are present at *m/z* 1151-1257. There are peaks present within the mass range for PDIMs, *m/z* 1306-1460; however the S/N ratio is extremely poor.

Lymph and blood extract samples were then dried down under a constant flow of nitrogen gas and re-suspended in 10 µL of $CHCl_3$. The purpose of this was to produce even more concentrated samples, in a hope this enabled detection of these lipids. Samples were applied to the MALDI target plate as 4 x 2.5 µL spots, followed by the same amount of matrix. MALDI mass spectra obtained from the more concentrated samples did not contain any peaks in the *m/z* region of interest. Increasing the amount applied the plate up to 12 x 2.5 µL drops, did not improve the detection of these species. For the entire set of samples representing PDIMs, depositing sample amounts over 1 µL inhibited the ionisation of any molecules in the sample, including matrix species. This is thought to be due to the sample drying as a thick white crust on the plate, resulting in poor co-crystallisation. The laser was also not able to penetrate the sample efficiently. A typical mass spectrum of these samples is shown in figure 5.8.

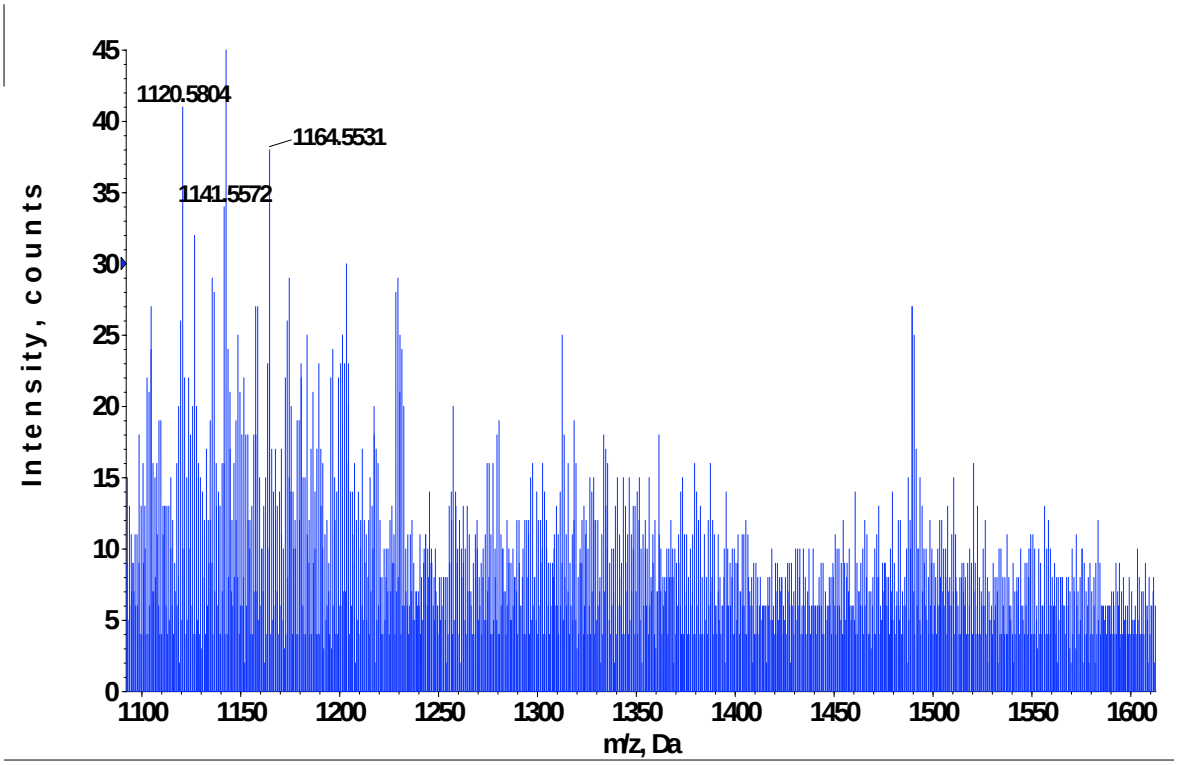

Figure 5.8. MALDI mass spectrum of lymph sample 4465 A, representing PDIMs. The ion counts are low and the background noise is quite high giving a low S/N ratio, resulting in a spectrum of very poor quality. Peaks representing the characteristic pattern of PDIMs are not present in this spectrum.

Samples of cattle lymph extracts labelled A1, B1 and C1, representing PDIMs, MAMEs and PGLs/MMGs respectively, were re-suspended in 50 µL of $CHCl_3$. Samples were applied to the target plate as either 2 x 2.5 µL or 4 x 2.5 µL, followed by either 0.5 or 1 µL of DHB. Sample A1 (PDIMs), when deposited onto the plate, the solvent evaporated leaving a thick white coating, and when initially analysed minimal ion counts were observed. Sample B1 (MAMEs) had the appearance of an oil slick on the plate, and also showed low to no ion counts. Sample C1 (PGLs/MMGs), when deposited onto the plate, the solvent evaporated leaving a yellow glossy film, resembling a thin plastic sheet, again low to no ion counts were observed for this sample. These more concentrated samples did not ionise well, even when 60 scans were summed per spectrum. Samples were diluted with a further 100 µL of $CHCl_3$, this resulted in an increase in ion counts for peaks in the *m/z* range 740-960, however peaks in the region of interest remained in the background noise. Samples A-C2 were re-suspended in 200 µL of $CHCl_3$ and applied to the plate as 2, 4, 6, 8 and 10 x 0.25 µL aliquots, followed by either 0.5 µL of the matrix solution, or the same volume of the matrix solution as the samples. MALDI mass spectra obtained from these preparation procedures again showed no ions were detected within the region of interest.

Although no ion counts were seen within the *m/z* range of interest for the selected cell wall associated lipid species, high ion counts were observed in the *m/z* range 800-930 and 760-960, for lymph and blood samples A and B respectively. An example spectrum for each type of extract, PDIMs (A) and PGLs/MMGs (B) is presented for lymph sample 4469 in figures 5.9 and 5.10 respectively. The peaks observed within this mass range differ by 14 mass units, which would correspond to one methlyene group (CH_2). These species could be associated with the mycobacterium lipids of interest, however due to their lower mass range it is thought they are mammalian or bacterial lipids that are present within this mass window. All MALDI-MS spectra acquired from the analysis of

lymph and blood extracts taken from cattle, contained the same peak profiles as those presented in figures 5.9 and 5.10.

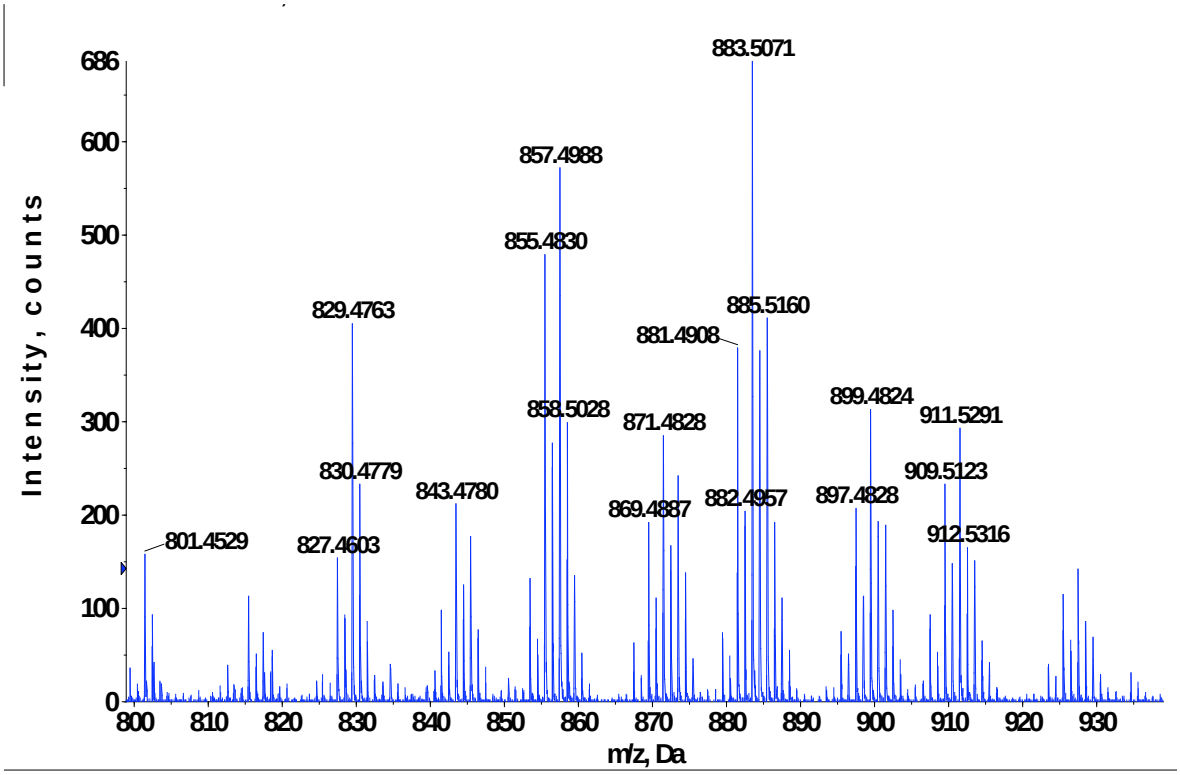

Figure 5.9. MALDI mass spectrum of lymph sample 4469 A, representing PDIMs. Peaks presented differ by 14 mass units which is characteristic of mycobacterium species, however due to their lower masses they are believed to be mammalian or bacterial lipid species that fall within this mass range and also differ from one another by a CH_2 group.

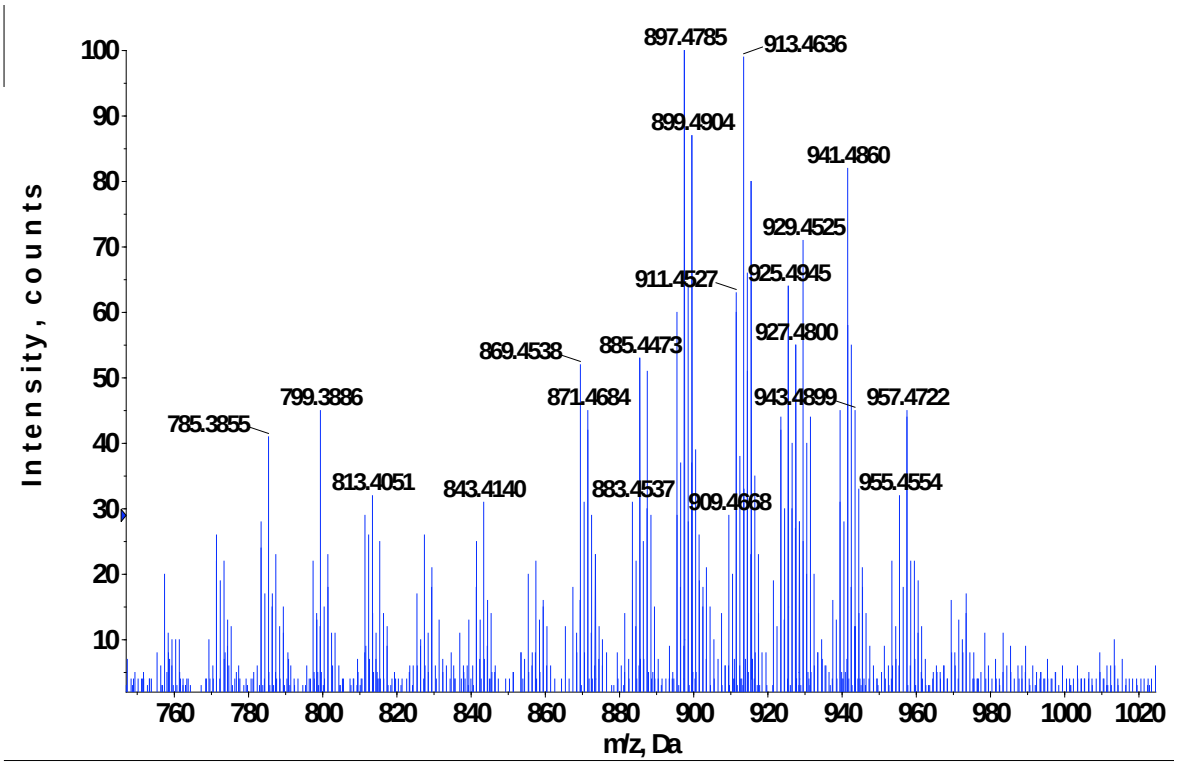

Figure 5.10. MALDI mass spectrum of lymph sample 4469 B, representing PGLs/MMGs. Peaks presented differ by 14 mass units which is characteristic of mycobacterium species, however due to their lower masses they are believed to be mammalian or bacterial lipid species that fall within this mass range and also differ from one another by a CH_2 group.

5.3.3 MALDI-MSI of TLC Plates

The analysis of the TLC plates proved rather problematic for a number of reasons. The matrix system used for the analysis of the standards and samples could not be used here as chloroform is toxic, and is a potent anaesthesia, thus spray deposition was not possible. DHB in 100 % MeCN (1% TFA) was used instead of chloroform; this solvent system had been successful in the detection of the PGL and PDIM standards (results not shown). The MALDI-MSI investigation of TLC plates also proved difficult due to each plate being prepared differently, regarding the number of lanes on each plate, the amount loaded onto each plate and the concentration of the amounts being loaded. These variations made it rather difficult to optimise matrix deposition and instrument parameters for analysis. Hence analysis of the first three plates, 2 controls and one sample plate (plate C), proved unsuccessful as the sample preparation and acquisition parameters had not been optimised, matrix ions were low and background noise high in all cases. In addition to this, at the time of analysis there were problems with the motor that controls the sample plate stepping distance in the oMALDI source; this resulted in laser oversampling, which may have completely ablated the matrix crystals, leading to no or low ion transmission.

Once matrix deposition and instrument parameters had been further optimised, evidenced by high TIC and matrix ion counts, several *Mycobacterium* cell wall associated lipid species of interest were detected. Ions at *m/*z 1333 and 1360 corresponding to keto-mycolate MMGs and ions between *m/*z 1494-1524, possible PGLs, were detected directly from TLC plate B. The MALDI-MS image presented in figure 5.11 shows these species at different migratory points along the plate, single point spectra were taken from the centre of these areas. This plate contained 5 control lanes, representing cholesterol, PDIMs, PGLs/MMGs, MAs, MAMEs and a non-polar blood extract lane. The images produced from this plate show different lipid species at different migratory points along the plate;

however these species were only detected in the lane representing the non-polar blood extract. Upon visualising the stained plate it is clear to see that a much larger amount or higher concentration of the sample had been added to this lane compared to the control lanes. As this is a sample extract and the visualisation for TLC is non-specific, this does not necessarily mean there is a greater amount or concentration of the lipids of interest within this lane. This could merely be a complex mixture containing many lipid species, some evidence for this was observed when analysing the images and spectra obtained within the mass region *m/z* 760-900 (data not shown). The ions previously observed in the blood extract samples were also detected from this lane. The detection of these lipids in the sample lane, and not the standard lanes, however, collectively indicates a higher concentration of these lipids were present within this sample compared to the controls. The detection of bacterial lipid species from TLC plates has been shown; these results indicate that a matrix solution of MeCN may not be suitable for the analysis of all species of interest, as MAs and MAMEs are not being detected. This is primarily thought to be due to them being insoluble in this solvent system. A suitable solvent matrix needs to be optimised for the ionisation of all species from TLC plates.

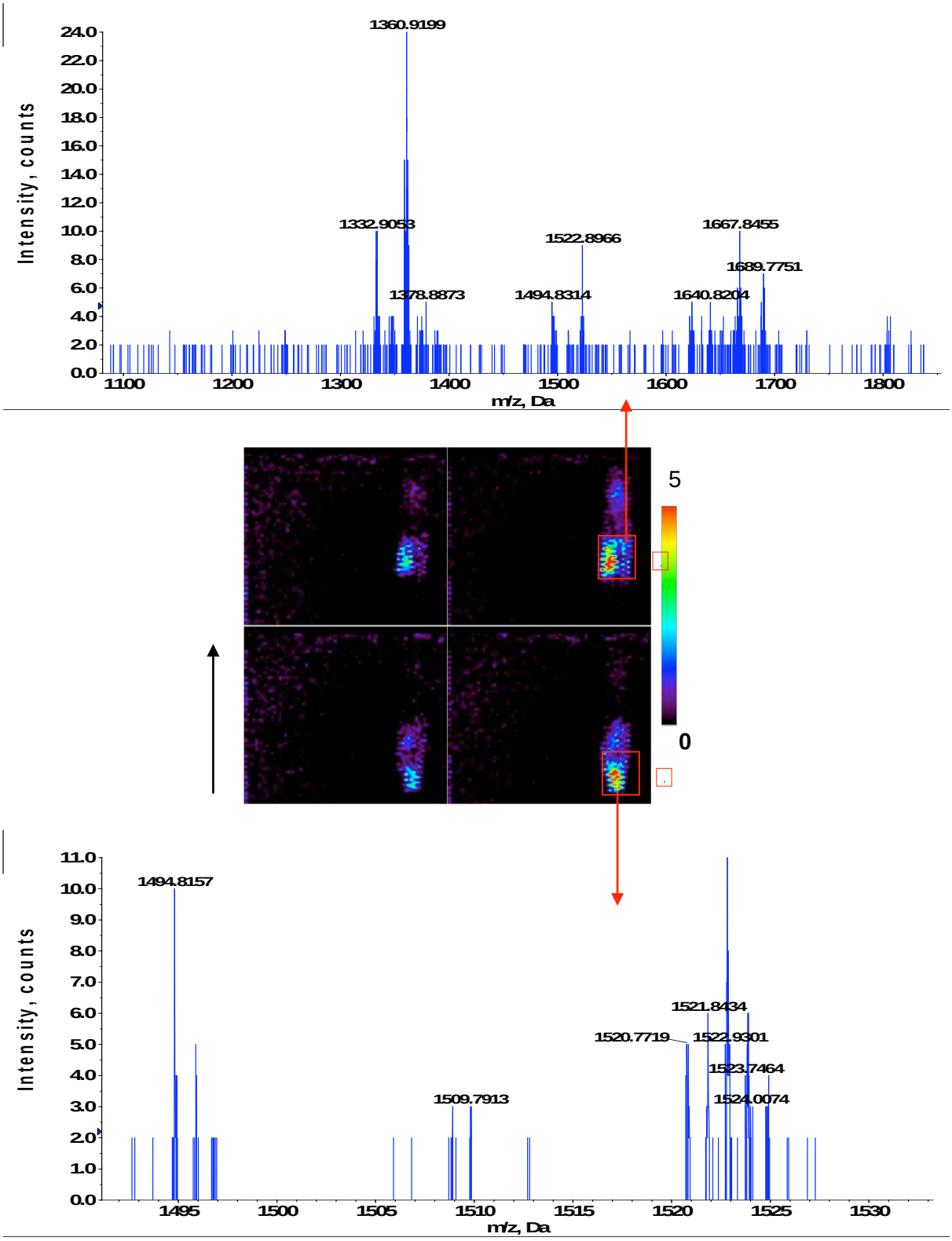

Figure 5.11. MALDI-MS image of *m/z* 1333 and 1360 representing MMGs (top images) and *m/z* 1494 and 1522, possible PGLs (bottom images) at different migrating points along the TLC plate. A single point spectrum taken from each specific migrating area is shown.

5.3.4 MALDI-MSI of Infected Lymph Node

The MALDI-MSI analysis of the lymph node excised from infected cattle was unsuccessful. Minimal ion counts were observed over the whole tissue section. Usually when analysing mammalian tissue sections high ion counts are observed for highly abundant lipid species that constitute cell membranes. The lymph node was classed as biohazard material, and following safety procedure was autoclaved to prevent potential infection. Autoclaving is carried out at high temperatures (typically 121 °C and above) to ensure all *Mycobacterium* are destroyed. These high temperatures will have also denatured or destroyed all heat sensitive peptides, proteins and lipids, the whole organ in essence. The heating also removes water from the tissue, which is why sections above 5 µm in thickness dried and crumbled off of the MALDI target plates. This process is believed to be the why extremely low ion counts were observed over the tissue area. Tissue that has been autoclaved does not suitable for MALDI-MS analysis.

5.4 Conclusion

The results presented in this chapter demonstrated two matrices, THAP and αCHCA to be unsuitable for the analysis of non-polar cell wall associated lipid species from *mycobacterium*. The MALDI-MS analysis of lipid standards using DHB in 80 % MeOH, proved successful in the detection of alpha-, methoxy-, and keto-MAMEs, PDIMs and PGLs/MMGs from lipid standards as $[M+Na]^+$, results corresponded well to those previously published for these lipids [132, 134, 193-197, 200, 201, 287]. The spectral quality and ion counts for PGLs/MMGs were rather poor however, and the detection of free MAs was unsuccessful. This lead to the application of a previously reported solvent system for the MALDI-MS analysis of MAMEs and other non-polar lipids[132-134, 193-197, 200, 201, 287]. This solvent system successfully detected free MA species,

evidenced by the presence of peaks representing alpha-mycolates, at *m/z* 1159 and 1187, methoxy-mycolate, at *m/z* 1275, and keto-mycolate at *m/z* 1302. There was also a five-fold increase in the detection of the major homologues for the alpha-, methoxy-, and keto-MAMEs using this solvent system compared to DHB in 80 % MeOH. The application of this system to more complex samples, however, proved unsuccessful, as demonstrated throughout this chapter. The MALDI-MS detection of MAs, PDIMs, PGLs and MMGs from lymph and blood extracts taken from infected cattle, was not possible with this method. Variation of extract concentration, amounts applied to the MALDI target plate, changing the matrix:analyte ratio, and altering the laser power, all had no effect on the outcome of the results. The MALDI mass spectrum of lymph extract 4469 A, presented in figure 5.7 does contain a cluster of peaks with a characteristic profile between *m/*z 1151 and 1257, which resembles those observed for these lipid species. These peaks could not be assigned to any of the lipids of interest, this is because they were detected in the sample representing PDIMs, and all data published to date for these lipids are at a higher *m/z* range, *m/z* 1306-1516[132, 200, 201]. These could be lipids with a similar polarity to PDIMs, and thus migrate with them along the TLC plate. They may be fragments or by-products of PDIMs, there is little to no literature on the analysis of MAs, PDIMs and PGLs directly from infected lymph extracts, thus building a lipid profile is difficult. Consistent findings with the analysis of these samples were the highly abundant peaks observed in the mass range *m/z* 740-960, the difficulty here is they may be attributed to either mammalian[288] or bacterial lipids[289]. The presence of these species indicate the extracts are quite complex and contain many species, this may be why no ions corresponding to *Mycobacterium* lipids were detected. The mixture may be too complex for efficient desorption and ionisation, especially when compared to the purer standards which were all sufficiently ionised and detected using this method.

A protocol has been optimised for the analysis of lipids directly from thin layer chromatography plates by MALDI-MSI. The detection of MMGs and possible PGLs

directly from TLC plates indicates this technique for analysis is useful for the MALDI-MSI analysis of complex mixtures, they are simplified as they are separated along the plate, thus providing a less complex sample mixture, however, at present it is still not well suited to the analysis of all *Mycobacterium* lipids of interest. This is thought to be primarily due to the insolubility of these molecules in the solvent system used. These structures are known for their insoluble nature, thus further optimisation is necessary to find a more sensitive solvent system.

MALDI-MSI investigation of a lymph node excised from infected cattle produced spectra and images with minimal to no ion counts. This result is attributed to the process of autoclaving the tissue, which is believed to have destroyed all lipid species and dehydrated the organ; making it unsuitable for MALDI-MS investigations. Future analysis of infected organs should be carried out on tissue fixed for a minimum of 24-48 h (size dependant) in formalin. This is the standard safety procedure applied in clinical histopathology laboratories for biohazard material, and tissue prepared this way is suitable for MALDI-MS analysis of phospholipids, as shown in chapter 3 of this thesis. There still remains a void in techniques that can rapidly diagnose infections caused by the *Mycobacterium tuberculosis complex*. MALDI-MS offers the speed of analysis, with further optimisation of matrix compounds and solvent systems the analysis of these lipids species, which play key roles in virulence, could be possible from highly complex solutions.

6. Solvent Optimisation for the MALDI-MS analysis of Cell Envelope Components of **Mycobacterium**

6.1 Introduction

Several research articles have been published evaluating MALDI matrix solvent systems, and how optimising such parameters can have dramatic effects on the acquired MALDI mass spectrum. Cohen and Chait (1996)[207] carried out an evaluation of 17 different matrix solvent systems, for the MALDI-MS analysis of peptides and proteins. The group showed matrix solvent composition greatly influenced the quality of the MALDI mass spectra, in addition to observing mass discriminatory effects. From this study the group were able to advise on suitable matrix solvent solutions for the analysis of higher mass, lower mass and complex mixtures of peptides. A study by Hattan *et al.* (2004)[290] demonstrated solvent composition significantly influenced the size, distribution, density and morphology of matrix crystals, which in turn greatly affected the signal intensity and quality of the MALDI mass spectra acquired from the analysis of peptides and proteins. A binary MALDI matrix solvent system has been optimised for the analysis of lipids from complex extracts[291]. Through the analysis of multiple combinations of matrices and solvents, Sun *et al.* (2008)[291], demonstrated a set of solvent conditions that increased S/N, and decreased spectral complexity in MALDI-MS analysis of complex lipids.

The matrix solvent system of choice for all MALDI-MS analysis of MAMEs, PGLs, and PDIMs, as is with other non-polar lipids, such as cholesterol and triacylglycerides, is chloroform:methanol at a ratio of either 1:1(v/v)[132, 134, 192, 193, 199-201] or 2:1(v/v)[133, 194, 196, 197]. In most instances the matrix selected is DHB, and as with other non-polar lipids, the lipids are observed in the mass spectrum as sodium adducts

$[M+Na]^+$. While this solvent system enables the ionisation and detection of these and other non-polar lipid species, a more sensitive solvent system is required for the analysis of free MAs from complex mixtures, and without the need for prior derivatisation. Results presented in Chapter 5 of this thesis showed MALDI-MS detection of specific mycobacterial cell wall lipids from purified lipid standards, using the previously published solvent system. The attempts made to detect these species from lymph and blood extracts proved unsuccessful. Addition issues were highlighted due to the solvent system of choice being unsuitable for airbrush deposition, thus it could not be used in MALDI-MSI investigations. Collectively these results highlighted the need for an optimised matrix solvent system that enhances sensitivity and could be used in MALDI-MSI investigations. In addition to this, a more sensitive solvent system could enable the analysis of MAs and related *Mycobacterium* lipids directly from complex mixtures, such a blood and sputum, thereby omitting the need to analyse bacterial cell extracts and the timely growth stage that accompanies such procedures. Such approaches would lead to faster and more rapid analysis times and would aid in a greater understanding of the lipids involved in growth and virulence.

Research presented in this chapter evaluates a number of matrix solvent systems and presents optimised routes for the analysis and detection of crude fatty acid mixtures of free MAs and their corresponding MAMEs. The optimised system was then used in MALDI-QqTOF analysis of complex bacterial extracts.

6.2 Experimental

6.2.1 Materials

2,5-dihydroxybenzoic acid (DHB) and trifluoracetic acid (TFA) were purchased from Sigma-Aldrich (Dorset, UK). Ethyl acetate (EA), 2-propanol (IPA), tetrahydrofuran (THF) and dichloromethane (DCM) were purchased from Fisher Scientific (Loughborough, UK). Free mycolic acids, mycolic acid methyl esters, BCG and strain C extracts were supplied by Professor D. Minnikin, Department of Biosciences, University of Birmingham.

6.2.2 Preparation of Lipid Standards and Bacterial Cell Extracts

Mycolic acids (4.2 mg) and mycolic acid methyl esters (7.2 mg) were re-suspended in 2 mL of chloroform, giving a concentration of 2.1 mg ml^{-1} and 3.6 mg ml^{-1}respectively. Strain C (7 mg) and BCG (22.9 mg) cell extracts were re-suspended in 1, 2, 3 and 4 mL of chloroform.

6.2.3 Matrix Preparation

DHB was prepared at 10 mg/mL in a range of solvents: EA, IPA, THF and DCM (0.1% TFA) and solvent mixtures of EA:THF (1:1 v/v), 0.1% TFA; EA:DCM (1:1 v/v), 0.1% TFA; IPA:THF (1:1 v/v), 0.1%TFA; IPA:DCM (1:1 v/v), 0.1% TFA and chloroform:methanol (1:1 and 2:1 v/v), 0.1% TFA.

6.2.4 Mass Spectrometry

MALDI mass spectrometric analysis was carried out using a QqTOF (Qstar XL – Applied Biosystems, Foster City, CA) mass spectrometer fitted with an orthogonal MALDI ion source. The nitrogen laser (337nm) has a band width of 3 ns and was operated at 35 µJ,

with a repetition rate of 20 Hz. Analysis was carried out in the positive ion reflectron mode. The mass range *m/z* 1000-2000 was used to avoid analyte suppression from highly abundant matrix ions and lipid species found in the lower mass range. Data were acquired using a Q1 scan time of 1 second, summing 30 scans per spectrum obtained. For the initial solvent evaluation 2.5 µL of the sample was applied to the plate and allowed to dry, followed by 2.5 µL of the matrix solution. For the comparison to the previously published matrix systems, 1 µL of the sample was applied to the plate and allowed to dry, followed by 0.5 µL of the matrix solution.

6.3 Results and Discussion

6.3.1 Crystal Formation for each Solvent System

Initially the optimisation of solvent systems for the analysis of free MA and MAME samples involved the single solvent systems of EA, IPA, THF and DCM, according to sample and matrix solubility. The alpha-, methoxy- and keto-MA and MAME subclasses were all present in the spectra obtained using these matrix solvent systems. The spectral quality and S/N was rather low (this will be discussed in detail in the following section), especially for the free MA and alpha subclasses, which are the least polar and thus most difficult to ionise. On observation it was noted that the crystal formation of DHB within these solvent systems varied quite significantly. This led to the inclusion of combinations of all four solvents into the analysis. The combination of EA:IPA and THF:DCM will not be discussed as the results produced from these combinations were extremely poor, with respect to crystal formation, ion counts, species present and spectral quality. The images presented in figure 6.1 show IPA alone produced a very fine coating of crystals; EA

produced slightly larger, more rounded crystals; DCM produced quite large needle-like crystals and THF produced large needle-like crystals that aggregated into a needle-like film. The combination of IPA with DCM and THF resulted in the increased crystal size compared to the former and greatly reduced crystal size compared to the latter two. The crystals for IPA:DCM appeared small, with slight aggregations, whereas the crystals produced using IPA:THF appeared small with a more homogenous distribution. The combination of EA:DCM produced an extremely fine coating of crystals, finer than those observed with IPA. Conversely EA:THF produced needle-like crystals, smaller than those observed with THF, but significantly larger than those seen with EA.

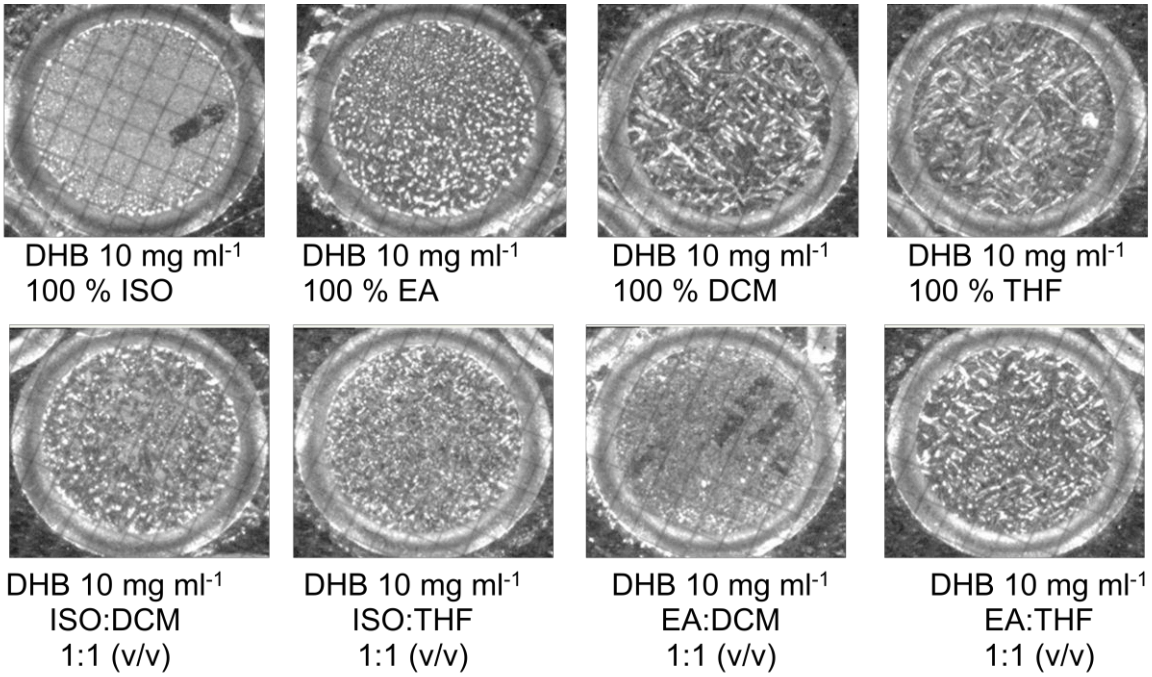

Figure 6.1. Optical images of DHB crystal formation within each solvent system. Images show crystal size growing from the finely dispersed coating observed with IPA, to a thick film of needle-like structures with THF, for the single solvents (top images). The combination of IPA with both THF and DCM greatly reduced the crystal size previously observed with the latter two solvents on their own. The combination of EA with DCM reduced the crystal size to an extremely fine coating, whereas EA with THF reduced the crystal size of those observed with THF (bottom images).

6.3.2 Matrix Solvent Evaluation for Analysis of Crude Fatty Acid Mixtures of Free Mycolic Acids and Mycolic Acid Methyl Esters

All of the matrix single solvent systems successfully incorporated the analytes into the matrix crystals to enable desorption/ionisation and detection of these molecules, evidenced by the presence of the alpha-, methoxy- and keto-MAs and MAMEs in the acquired spectra. The S/N was rather low however, especially for the MA and alpha

species which are the least polar and most difficult to ionise, which is a reason these molecules are usually derivatised prior to analysis. Analysis of the free MAs using the single solvent systems showed IPA resulted in the lowest ion counts and S/N for all mycolates detected, followed by THF, with EA and DCM producing similar results, as detailed in table 5. The spectral quality for IPA was also extremely poor compared to the other single solvents used, with respect to peak shape and the 'grassroots' appearance of the spectra acquired. The highest obtainable ion counts for IPA was 217 counts (mean 193, n=3) for the major homologue of the keto-mycolates, *m/*z 1302, which is the most polar of the mycolates and thus more readily ionised compared to the alpha-mycolates. Peak shape was poor, with peak shouldering present for the major homologues of the methoxy- and keto-mycolate peaks, *m/z* 1276 and 1302 respectively, and a 'split' in the peak representing the most abundant alpha-mycolate, *m/z* 1160, indicating poor resolving power. The 'grassroots' signal observed was above 20 % of the relative intensity of the base peak for all spectra acquired using IPA as the matrix solvent. The poor results observed for the analysis of free mycolic acids using IPA as the matrix solvent system are thought to be both due to the extremely non-polar nature of these molecules, along with the inefficient incorporation of the analytes into the matrix crystal, and the final crystal formation. As displayed in figure 6.1, IPA crystal formation was rather poor, which would lead to reduced desorption/ionisation. The spectral quality observed using THF as the matrix solvent system was greatly improved compared to IPA, with the S/N doubling, however the peak shape for the major homologue of the alpha-mycolate, *m/*z 1160 was still of rather low quality, demonstrating relatively poor mass resolution. As already mentioned, EA and DCM produced relatively similar results and produced the best overall results for the single solvents evaluated, achieving greater ion counts, higher S/N and improved peak/mass resolution.

The analysis of MAs using the mixed solvent systems showed EA combined with THF and DCM produced similar results to those achieved with the use of EA or DCM alone.

This is regarding ion counts, S/N and spectral quality. IPA, the least suitable solvent when used alone, in combination with DCM produced a two-fold increase in ion counts and S/N, and an increase in the resolution for the major homologue of the alpha- and methoxy-mycolates, *m/z* 1160 and 1276 respectively, compared to the latter used alone. There was also a three-fold increase in ion counts and S/N for the major homologue of the keto-mycolate, *m/*z 1302, compared to the latter used alone. IPA in combination with THF showed over a three-fold increase in ion counts and S/N for the major homologue of the alpha- and methoxy-mycolates, *m/z* 1160 and 1276 respectively, compared to the latter used alone. There was also over a five-fold increase in ion counts and S/N for the major homologue of the keto-mycolate, *m/*z 1302. The spectral quality was significantly improved for these solvent systems, the spectra are much clearer, and the peak shapes are uniform. Table 5 shows the mean ions counts, resolution and S/N for the major homologues of the alpha-, methoxy- and keto- mycolates obtained using each matrix solvent system. Figure 6.2a clearly highlights the far superior S/N achieved using IPA combined with either THF or DCM when compared to the other solvent systems evaluated. Figure 6.3 compares the mass spectra acquired from the two single solvents (EA and DCM) with the two mixed solvents (IPA:THF and IPA:DCM) that produced the best overall results. The improved ion counts, S/N and spectral quality for the latter two is evident.

The results for the analysis of the MAMEs showed similar results to those previously observed with the analysis of the free MAs, in which IPA combined with either THF or DCM produced far superior results compared to the other solvent systems evaluated, figure 6.2b this is again with respect to ion counts, S/N, resolution and spectral quality across all three major homologues, representing the alpha-, methoxy- and keto-mycolates, *m/z* 1174, 1290 and 1316 respectively. As these species are more readily ionised compared to free MAs, ion counts and spectral quality was greatly improved across all solvents used, however, the single solvents and combinations of EA with THF

and DCM all showed similar results for all MAME analysed and detected. The S/N again doubled for the combination of IPA with THF and DCM compared to all other solvents and combination of solvents evaluated, figure 6.2B. The standard deviation is shown in all cases for the analysis of the free MAs and their methyl esters, (n=3), and is quite large and often overlaps for most solvent systems, this is thought to be due to the 'overlay' method used for the application of the sample and matrix solutions to the MALDI target plate. This method, as with other dried droplet methods, is known to have poor spot-to-spot reproducibility, thus a large SD is observed. The SD is nearly always lower for analysis using DCM within the matrix solvent system. This is believed to be due to the crystal size and nature of the crystals produced with this solvent; they are quite robust and thus reduce the effect of the laser, never being fully ablated.

The superior results observed with the combination of IPA with either THF or DCM for both the analysis of free mycolic acids and mycolic acid methyl esters is thought to be due to the nature and speed in which these solvents dry, and thus the type of crystals formed from this. As previously discussed, the crystals formed from these solvents were quite small and rounded with quite a dense coverage, and in the case of IPA:THF a near homogenous distribution is achieved. These solvents are believed to induce a greater incorporation of the analytes into the matrix crystals, leading to greater desorption/ionisation and thus detection of the analytes.

Solvent	*m/z*	Centroid Mass	Ion Counts	Resolution	S/N
Ethyl Acetate	1160.3842	1160.3575	225 ± 37	6678 ± 381	32 ± 5
2-propanol	1160.3458	1160.3572	113 ± 17	6363 ± 1321	19 ± 3
Tetrahydrofuran	1160.397	1160.3692	157 ± 29	6269 ± 840	26 ± 5
Dichloromethane	1160.3714	1160.3657	266 ± 108	6602 ± 286	44 ± 18
IPA:THF	1160.2947	1160.3149	505 ± 309	7904 ± 68	126 ± 77
EA:THF	1160.3075	1160.3192	275 ± 85	6666 ± 462	31 ± 9
IPA:DCM	1160.3203	1160.323	527 ± 91	7289 ± 37	88 ± 15
EA:DCM	1160.2819	1160.3205	268 ± 58	6128 ± 77	34 ± 17
Ethyl Acetate	1276.4913	1276.4875	449 ± 109	6961 ± 305	64 ± 16
2-propanol	1276.4913	1276.4878	175 ± 28	7047 ± 337	29 ± 5
Tetrahydrofuran	1276.4645	1276.4853	298 ± 76	7189 ± 373	50 ± 13
Dichloromethane	1276.5047	1276.4901	524 ± 269	7279 ± 570	87 ± 45
IPA:THF	1276.4377	1276.4424	1261 ± 873	8278 ± 350	315 ± 218
EA:THF	1276.4511	1276.4439	556 ± 182	7072 ± 502	62 ± 20
IPA:DCM	1276.4511	1276.4463	1312 ± 135	7670 ± 174	219 ± 22
EA:DCM	1276.4645	1276.4404	582 ± 142	6825 ± 119	73 ± 18
Ethyl Acetate	1302.5239	1302.5174	538 ± 119	7217 ± 212	77 ± 17
2-propanol	1302.4968	1302.5169	193 ± 48	7581 ± 434	32 ± 8
Tetrahydrofuran	1302.5103	1302.5146	365 ± 99	7176 ± 37	61 ± 17
Dichloromethane	1302.5103	1302.5096	648 ± 346	7022 ± 189	108 ± 58
IPA:THF	1302.4697	1302.4719	2063 ± 1514	8934 ± 163	516 ± 378
EA:THF	1302.4562	1302.4711	665 ± 280.7	7201 ± 331	74 ± 31
IPA:DCM	1302.4697	1302.4741	2021 ± 282	8333 ± 180	337 ± 47
EA:DCM	1302.4562	1302.4739	755 ± 174	7136 ± 117	94 ± 22

Table 5. Average ion counts, resolution and signal-to-noise (± SD, n=3) for each of the major homologues of the mycolic acids analysed and detected using DHB in each solvent system. *m/z* 1160, 1276 and 1302 represents the alpha-, methoxy- and keto-mycolates of the free mycolic acids respectively. IPA combined with THF or DCM gave the best results across all MAs detected, with respect to ion counts, resolution and S/N.

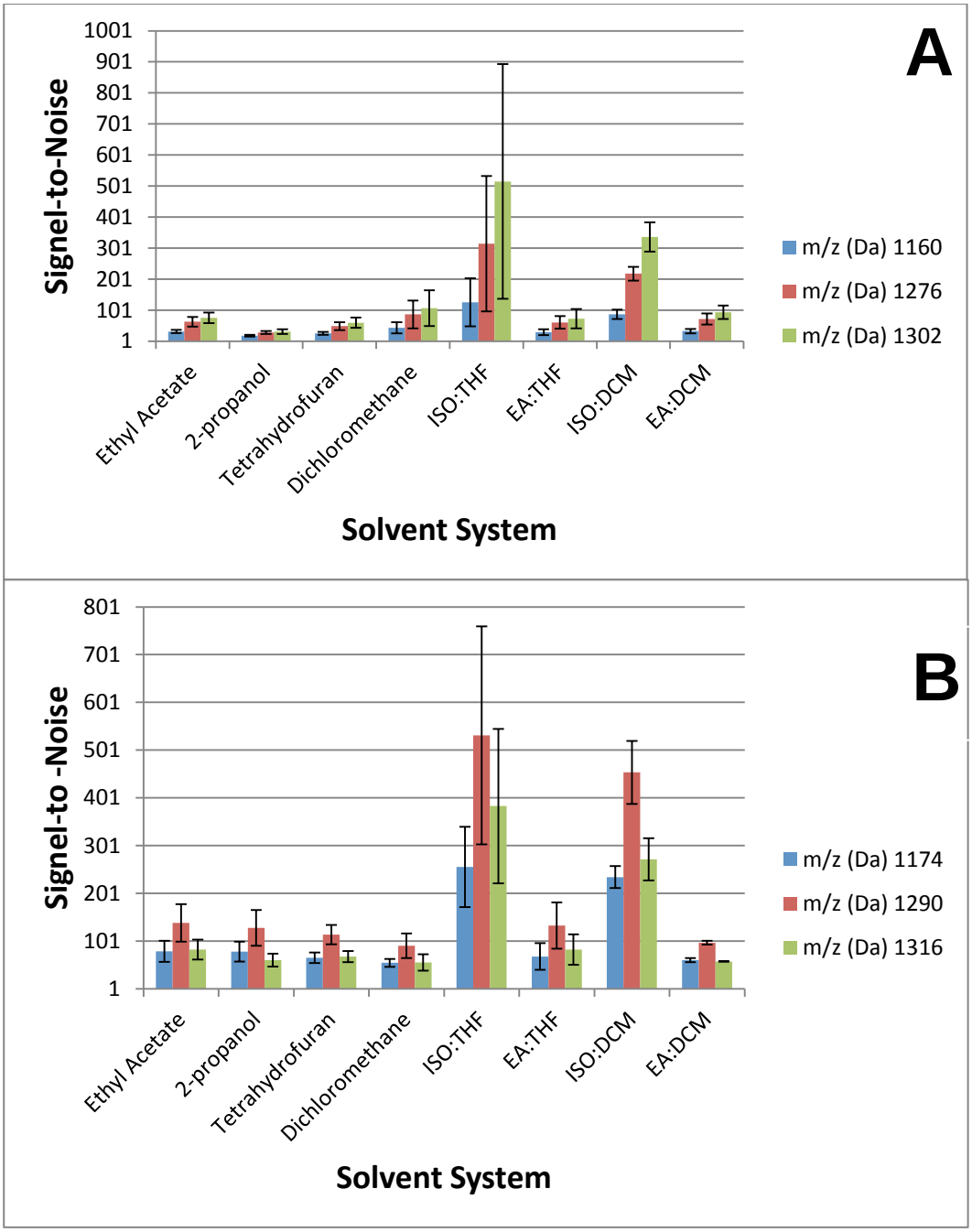

Figure 6.2. The analysis of MALDI mass spectra for the S/N for each solvent system based on the alpha-, methoxy- and Keto-mycolates of the free MA (A) and MAME (B) standards. Figure A *m/z* 1160, 1276 and 1302 represents the alpha, methoxy and keto-mycolic acids respectively. Figure B *m/z* 1174, 1290 and 1316 represents the alpha, methoxy and keto- mycolic acid methyl esters respectively. All peaks represent the $[M+Na]^+$ ion. IPA combined with THF and DCM produced far better S/N across both samples.

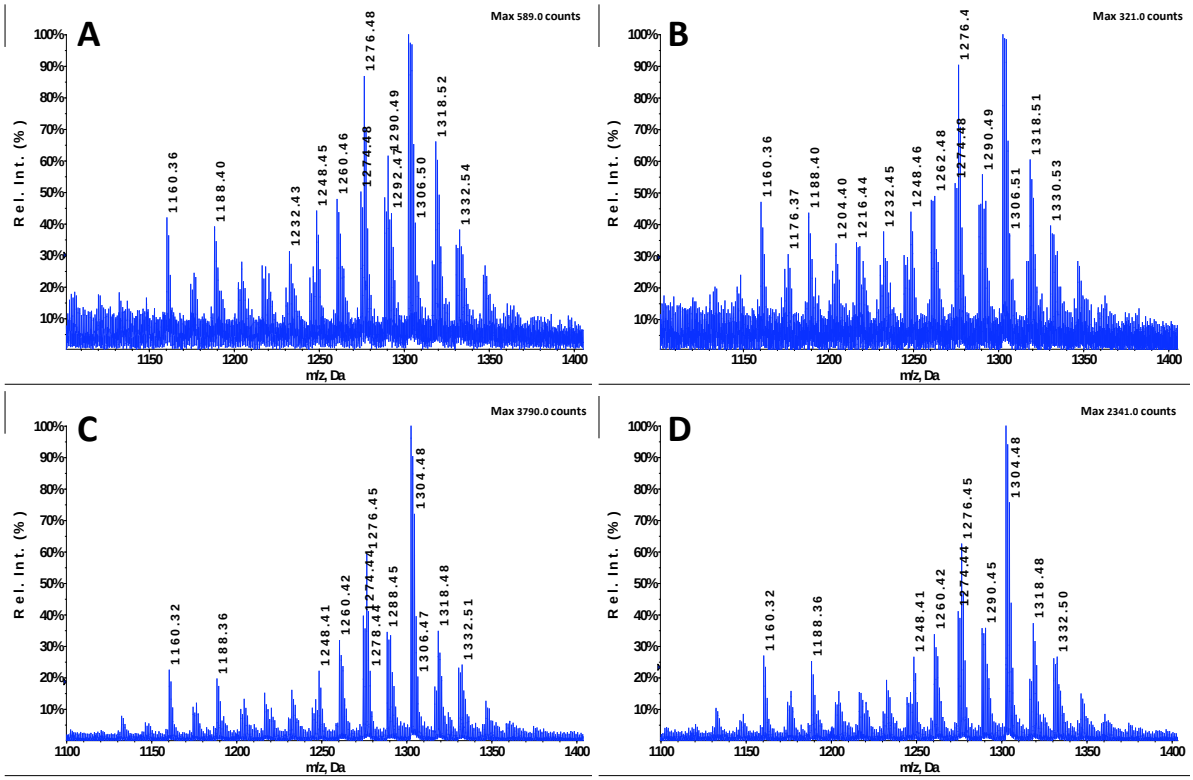

Figure 6.3. MALDI-MS spectra of free mycolic acids using the matrix solvent systems EA (A), DCM (B), IPA:THF (C) and IPA:DCM (D). The most abundant peaks for the alpha-, methoxy- and keto-mycolates are present at *m/z* 1160, 1276 and 1302 respectively. All peaks represent the $[M+Na]^+$ ion. The figure shows the ion counts, S/N and spectral quality is greatly improved using IPA combined with either THF or DCM compared to the single solvents of EA and DCM. EA, DCM, IPA:THF and IPA:DCM represent the solvent system that produced the best overall results for the single and mixed matrix solvent systems evaluated.

6.3.3 Subclasses Detected for Free MA and MAME Samples

Example spectra for the analysis of free MAs and their methyl ester derivatives (MAMEs) using 10 mg/ml DHB in IPA:THF 1:1 (v/v) as the matrix solvent system is shown in figure 6.4. A clear envelope of peaks is present that differ from one another by 14 or 28 mass units from *m/z* 1132 to 1374 for MAs and *m/z* 1134 to 1388 for MAMEs. The MALDI mass spectrum of the free mycolic acids shows two abundant alpha-mycolate peaks at *m/z* 1160 and 1188, representing C_{78} and C_{80} respectively, followed by slightly less abundant peaks at *m/z* 1174, 1202, 1216 and 1230, representing $C_{79,}$ C_{81}, C_{82} and C_{83} respectively. Less abundant but significant peaks for this mycolate are also observed in this spectrum at *m/z* 1132, 1146 1244, 1258, 1272 and 1286 representing alpha mycolates with carbon chain lengths C_{76}, $C_{77,}$ $C_{84,}$ $C_{85,}$ C_{86} and C_{87} respectively. The most abundant peak for the methoxy-mycolate is observed at *m/z* 1304 for C_{87}. At nearly 50% less relative intensity the next abundant peak for this subclass can be observed at *m/z* 1276, representing C_{85}, followed by peaks at *m/z* 1248, 1262, 1290, and 1318 representing $C_{83,}$ $C_{84,}$ $C_{86,}$ and C_{88} respectively. Less abundant but significant peaks for this mycolate are present at *m/z* 1220, 1234, 1332, 1346, 1360 and 1374, representing C_{81} through to C_{92}. The detection of keto-mycolates within this sample showed the most abundant peaks to be at *m/z* 1274 and 1302 for C_{85} and C_{87} respectively, followed by less abundant peaks at *m/z* 1260, 1288 and 1316 for $C_{84,}$ C_{86} and C_{88} respectively. Less abundant but significant peaks for this mycolate were also observed at *m/z* 1218, 1232, 1246, 1330, 1344 and 1358 representing C_{81} through to C_{91}. A characteristic MA profile can also be observed for *m/z* 1224, 1238, 1252, 1266, 1280, 1294, 1308, 1322, 1336 and 1340, due to their size these could possibly be assigned to methoxy- or keto-MAs, however structural characterisation is needed for full identification. A smaller cluster of peaks are also present at *m/z* 1010 to 1052 that have the characteristic mycolic acid pattern, these are yet to be identified but could be smaller alpha or the shorter chain alpha' mycolates. The same characteristic

peak profile was observed for the mycolic acid methyl esters, as was for the mycolic acids, a shift of 14 mass units was observed for each assignable mycolate, representing methylation. The relative intensity for almost all peaks has increased next to the base peak, when compared to the analysis of free MAs. This is thought to be due to the increased polarity of these species and thus an increase in desorption/ionisation, evidenced by the relative intensity of the alpha-mycolate methyl esters, *m/z* 1174 and 1202, compared to the relative intensity of the free alpha-mycolates, *m/z* 1160 and 1188, figure 6.4 top and bottom spectra respectively. Results found here correspond to those previously published for the MALDI-MS analysis of MAMEs from slow growing pathogenic mycobacterium, including *M.tb* and *M. bovis BCG[193-198].* Table 6 lists assignable mycolates according to literature, along with the number of carbons for each, for the analysis of free MAs and MAMEs.

Free mycolic acids

Mycolic	**Total number of carbons in mycolic acid**																		
acid type	74	75	76	77	78	79	80	81	82	83	84	85	86	87	88	89	90	91	92
Alpha			1132	1146	***1160***	*1174*	***1188***	*1202*	*1216*	*1230*	1244	1258	1272	1286					
Methoxy								1220	1234	*1248*	*1262*	***1276***	*1290*	***1304***	*1318*	1332	1346	1360	1374
Keto								1218	1232	1246	*1260*	**1274**	*1288*	***1302***	*1316*	1330	1344	1358	

Mycolic acid methyl etsers

Mycolic	**Total number of carbons in mycolic acid**																		
acid type	74	75	76	77	78	79	80	81	82	83	84	85	86	87	88	89	90	91	92
Alpha		1132	*1146*	1160	***1174***	1188	***1202***	1216	*1230*	1244	1258	1272	1286						
Methoxy							1220	1234	*1248*	*1262*	1276	***1290***	*1304*	***1318***	*1332*	*1346*	1360	1374	1388
Keto							1218	1232	1246	*1260*	1274	*1288*	*1302*	***1316***	*1330*	*1344*	1358	1372	

Table 6. Masses and carbon lengths of α-, methoxy- and keto-mycolates for free acids (top table) and their methyl esters (bottom table), values represent the $[M+Na]^+$ ions. The mass values for the major homologues are italicised in bold.

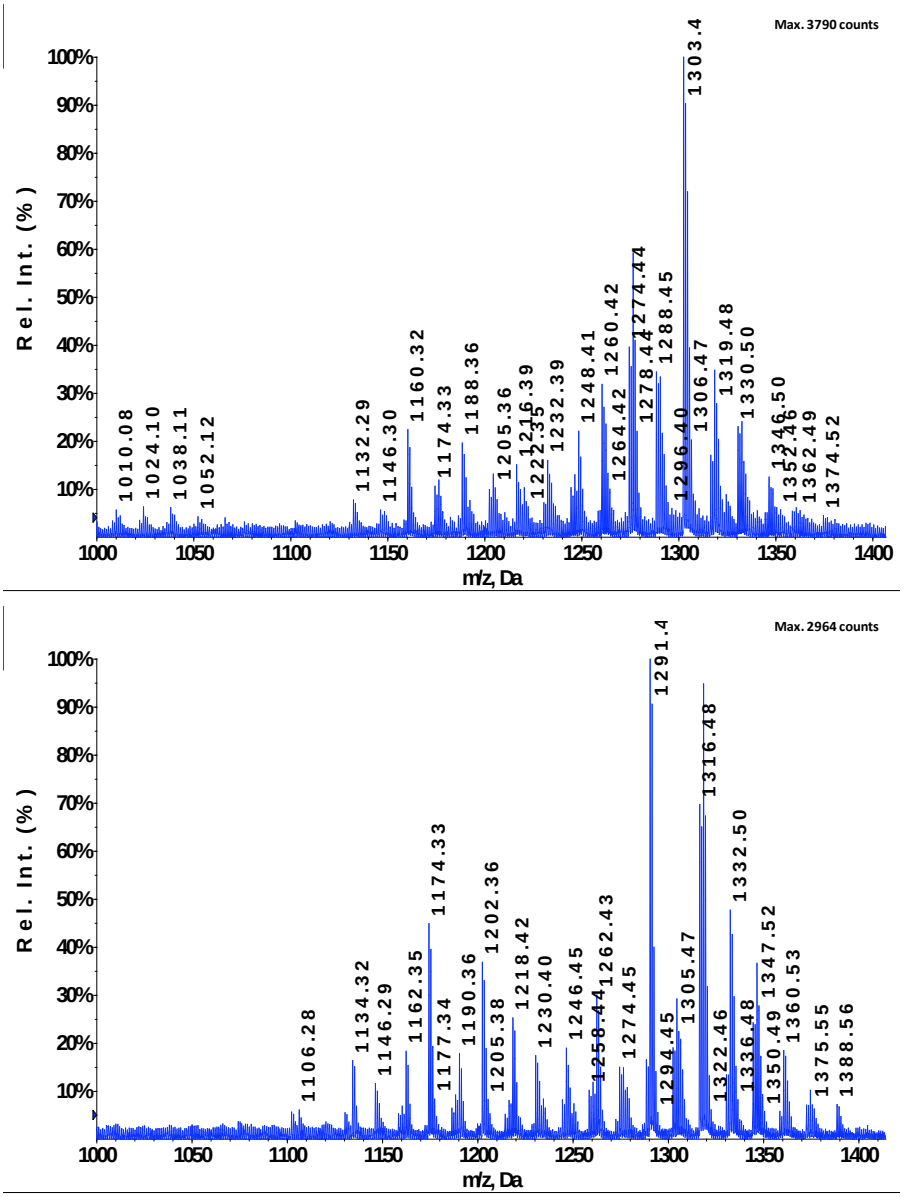

Figure 6.4. MALDI-TOF mass spectra of free mycolic acids (top spectrum) and mycolic acid methyl esters (bottom spectrum) using DHB 10 mg ml^{-1} IPA:THF 1:1 (v/v) 0.1 % TFA. The major homologues representing the alpha-, methoxy- and keto-mycolates can be observed at *m/z* 1160, 1303 and 1302 respectively. The major homologues representing the alpha-, methoxy- and keto-mycolic acid methyl esters can be observed at *m/z* 1174, 1290 and 1316 respectively. All peaks represent the $[M+Na]^+$ ion. The most abundant peak for the methoxy subclass has switched from C_{87} for the free MA sample to C_{85} in the MAME sample; however, there is only a slight difference in the relative intensity for these two peaks in the MAME sample.

6.3.4 Matrix Solvent System – Comparison to Published Literature

A comparison of MALDI-QqTOF-MS using the optimised solvent systems *vs*. previously published solvent systems[132-134, 193-201] shows the improved sensitivity of the new system: IPA:THF and IPA:DCM compared to $CHCl_3$:MeOH 1:1 and 2:1 (v/v). The ion counts for IPA:THF and IPA:DCM are again similar, however, IPA:THF produced slightly higher ion counts for all subclasses (alpha-, methoxy- and keto-) for both the free MA and the MAME samples, with less variance between analysis. For the analysis of the free mycolic acid sample, IPA:THF produced over a two-fold increase in ion counts for the major homologue of the alpha-MA at *m/z* 1160, compared to $CHCl_3$: MeOH 1:1 (v/v). Higher ion counts were also observed for this mycolate and solvent system compared to CHCL: MeOH 2:1 (v/v). As the polarity increases slightly with the methoxy- and keto-mycolates, the gap in ion counts also increases when comparing the optimised systems of, IPA:THF and IPA:DCM with $CHCl_3$:MeOH 1:1 and 2:1 (v/v). There is over a two-fold increase in ion counts for IPA:DCM and over a three-fold increase in ion counts for IPA:THF when compared to $CHCl_3$:MeOH 1:1 (v/v), the latter produced the poorest results over all mycolates for both samples, with respect to ion counts, resolution and S/N. IPA:DCM and $CHCL_3$:MeOH 2:1 (v/v) resulted in comparable findings with respect to ion counts and S/N. IPA:THF produced far superior results compared to both the optimised solvent system of IPA:DCM and the most useful of the previously published systems, which was $CHCl_3$:MeOH 2:1 (v/v), for both the purified MA and MAME samples. The S/N ratio shows over a ten-fold increase for the major homologues of the alpha-, methoxy- and keto-MAs, at *m/z* 1160, 1276 and 1302 respectively, when comparing, IPA:THF with $CHCl_3$:MeOH 1:1 (v/v), and over a three-fold increase when comparing IPA:THF with $CHCl_3$:MeOH 2:1 (v/v) or IPA:DCM, as shown in table 7. A similar trend is observed when analysing the S/N ratio acquired for the MAME sample. There is again a ten-fold increase for the alpha-MAME, *m/z* 1174, when comparing IPA:THF with $CHCl_3$:MeOH 1:1 (v/v) and

over a ten-fold increase for the methoxy- and keto-MAME, *m/z* 1290 and 1316 respectively. IPA:THF also yielded a four-fold increase in S/N for the alpha-MAME and over six-fold increase in S/N for the methoxy- and keto-MAME when compared to the previously published $CHCl_3$:MeOH 2:1 (v/v), as shown in the graphs presented in figure 6.5. Results presented here also show that an increase in the amount of sample applied to the plate compared to the amount of matrix, i.e 1 µL followed by 0.5 µL respectively, greatly increases the spot-to-spot reproducibility achieved, as shown by the reduction in error bars in figure 6.5 compared to those presented in figure 6.2. The effect of sample preparation on reproducibility in a MALDI experiment has long been known and greatly investigated [35, 206, 207, 209].

Solvent	*m/z*	Ion Counts	Resolution	S/N
CHCl3:MeOH 1:1	1160	107 ± 19	6788 ± 209	54 ± 10
CHCl3:MeOH 2:1	1160	201 ± 27	6660 ± 312	201 ± 27
IPA:THF	1160	314 ± 26	6874 ± 688	627 ± 52
IPA:DCM	1160	291 ± 88	6689 ± 316	146 ± 44
CHCl3:MeOH 1:1	1276	203 ± 61	6415 ± 542	101 ± 31
CHCl3:MeOH 2:1	1276	383 ± 38	6584 ± 446	383 ± 38
IPA:THF	1276	725 ± 45	7093 ± 238	1451 ± 90
IPA:DCM	1276	522 ± 123	6538 ± 146	261 ± 61
CHCl3:MeOH 1:1	1302	280 ± 67	6915 ± 597	140 ± 34
CHCl3:MeOH 2:1	1302	582 ± 107	6866 ± 120	582 ± 107
IPA:THF	1302	1015 ± 34	7407 ± 145	2031 ± 68
IPA:DCM	1302	852 ± 145	7515 ± 221	426 ± 72

Table 7. Average ion counts, resolution and signal-to-noise (± SD, n=3) for each of the major homologues of the mycolic acids analysed and detected using DHB in each solvent system. *m/z* 1160, 1276 and 1302 represents the alpha-, methoxy- and keto-mycolates of the free mycolic acids respectively. IPA:THF gave the best results across all MAs detected, with respect to ion counts, resolution and S/N.

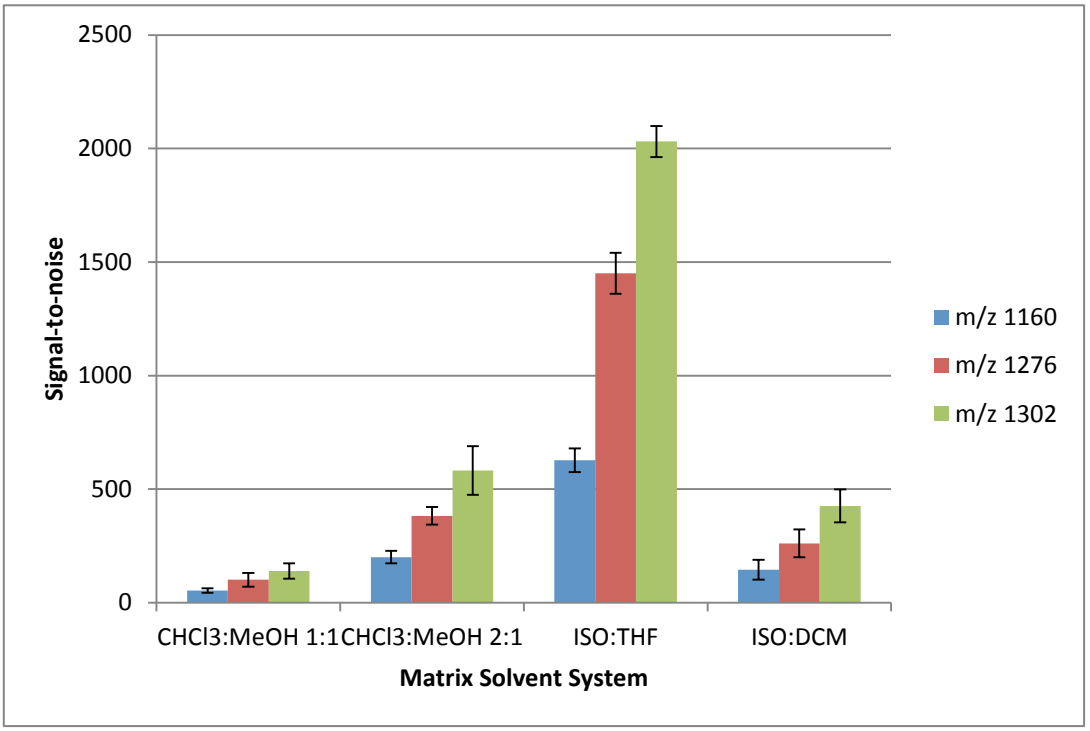

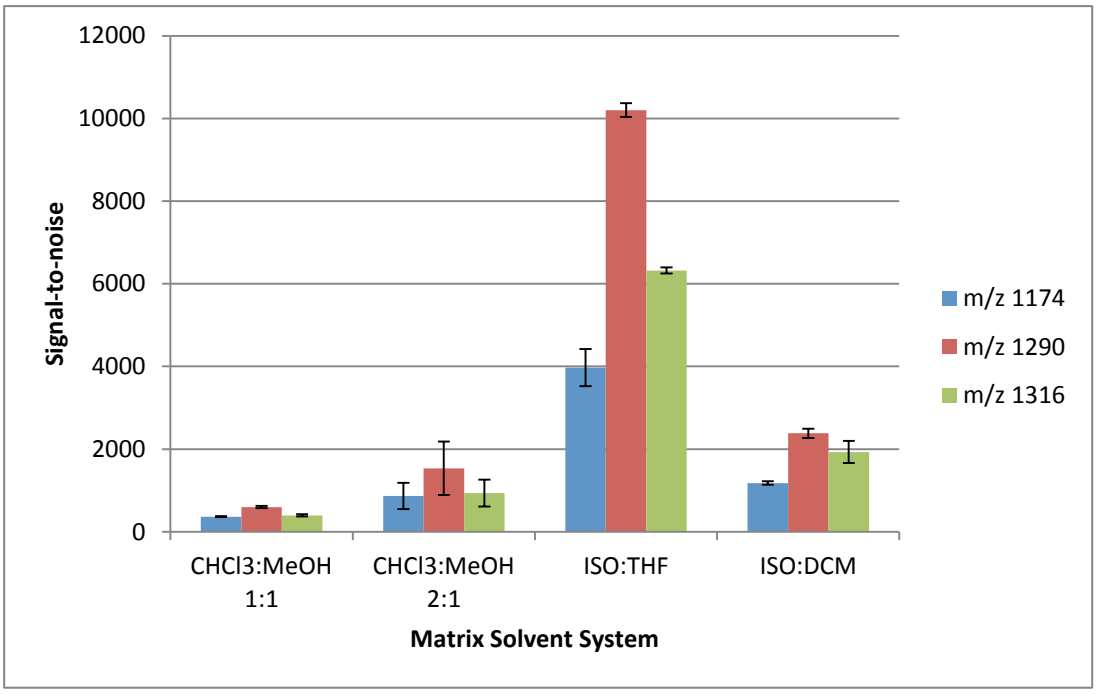

Figure 6.5. The analysis of MALDI mass spectra from each solvent system, for the S/N of the alpha-, methoxy- and Keto- mycolates of the free MA (A) and MAME (B) standards.

6.3.5 Analysis of Strain C Extracts

The analysis of the Strain C extract showed a clear characteristic peak pattern previously reported for the analysis of purified PDIMs from bacterial extracts[132, 200, 201]. The mass spectrum presented in figure 6.6 shows the major homologues of PDIMs are present at *m/*z 1474 and 1502 representing C_{98} and C_{100} respectively, but a characteristic peak pattern can be observed at *m/*z 1376, 1390, 1404, 1418, 1432, 1446, 1460, 1474, 1488, 1502 and 1516, representing C_{91} to C_{101}. This peak pattern, with respect to the masses present, corresponds to those previously published for the MALDI-TOF analysis of purified PDIM type A, also known as DIM A[132, 200, 201] and the MALDI-MS analysis of the standards of PDIMs analysed in Chapter 4 of this thesis. Peaks representing the major homologues of the methoxy- and keto-mycolic acids are also present in the mass spectrum acquired from this sample, and can be observed at *m/z* 1276 (C_{85}) and *m/z* 1302 (C_{87}) respectively. There are slightly lower abundant methoxy-mycolate peaks present at *m/*z 1304 and 1318. All masses correspond to those detected from the MA standards (figure 64 and table 5) and those previously published. Whilst the peak for the methoxy-MA is clearly visible above the background noise, the peak representing keto-MA is only just visible above this region of the spectrum. The peak shape is rather poor for both of these species, with peak broadening; this is thought to be due to the complexity of the sample. The alpha-mycolates were not detected from this sample, these are the least polar and thus most difficult to ionise of the MAs, it is thought the sample is too complex and the more polar lipids species are favourably ionised.

A number of possible cell wall associated lipid species were also detected in this sample, observed as peaks within the MALDI mass spectrum at *m/z* 1542 and 1556. In addition to these, a characteristic lipid profile can be observed at the higher mass range of the spectrum, *m/z* 1676-1768, these species are yet to be identified. The masses fall within the mass range of TMMs, however they do not correspond to any published masses of

these species to date. Structural characterisation will need to be carried out for full identification. *m/z* 1199 is a peak associated with the fractionation of solutions on Florisil columns. All significant peaks are listed in table 8, all masses are believed to be $[M+Na]^+$.

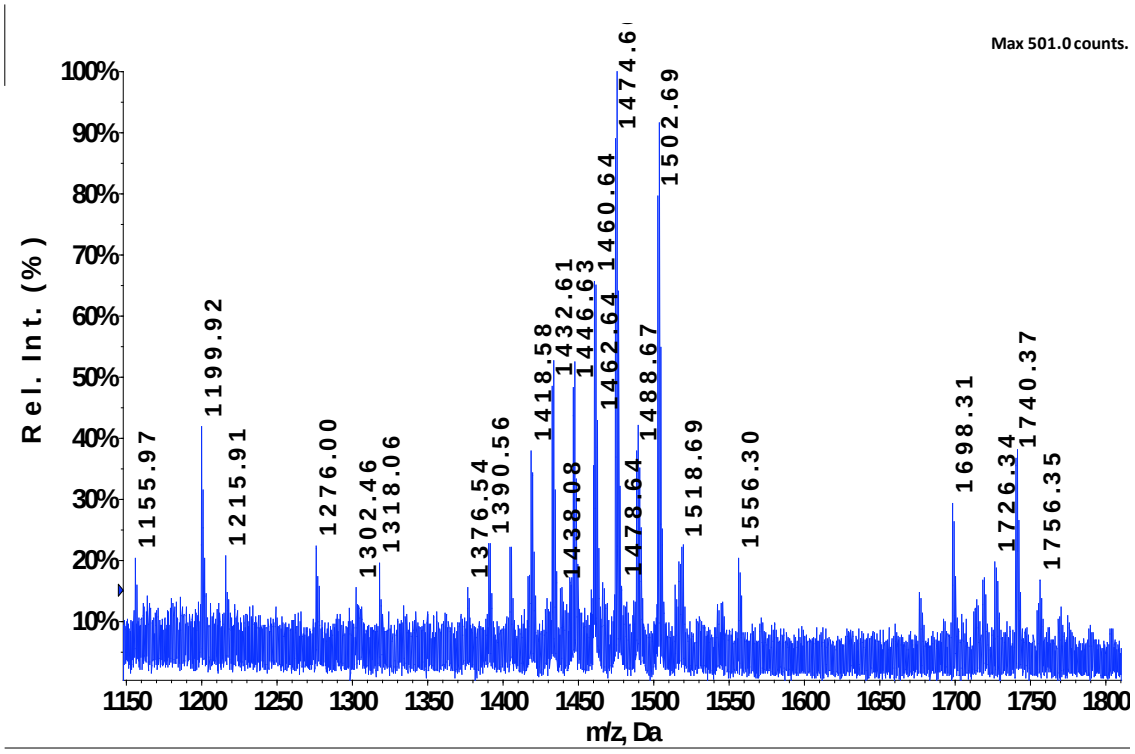

Figure 6.6. MALDI mass spectrum of bacterial extracts from Strain C using DHB 10 mg ml^{-1} IPA:THF (1:1, v/v). The peak for the major homologue of the methoxy-MA is present at *m/z* 1276. The main cluster of peaks *m/z* 1376-1516 represent PDIMs C_{92}-C_{101}, the maximum ion counts given is for the base peak which is *m/z* 1474 and represents the major homologue of PDIM A, C_{98}. The cluster of peaks seen at the higher mass range *m/z* 1677-1756 are believed to be cell envelope associated lipids with a similar structure, these are yet to be identified. The peak at *m/z* 1199 is a molecule associated with samples fractionated on Florisil columns.

m/z	Lipid	Reference
1276	Methoxy-MA	[193-195, 197]
1302.4605	Keto-MA	[193, 194, 197]
1304.09	Methoxy-MA	[193-195, 197]
1318.0576	Methoxy-MA	[193-195, 197]
1376.53	PDIM A	[132, 200, 201]
1390.55	PDIM A	[132, 200, 201]
1404.56	PDIM A	[132, 200, 201]
1418.58	PDIM A	[132, 200, 201]
1432.61	PDIM A	[132, 200, 201]
1446.63	PDIM A	[132, 200, 201]
1460.64	PDIM A	[132, 200, 201]
1474.66	PDIM A	[132, 200, 201]
1488.67	PDIM A	[132, 200, 201]
1502.69	PDIM A	[132, 200, 201]
1516.7	PDIM A	[132, 200, 201]
1542.29	Unidentified	
1556.3	Unidentified	
1676.32	Unidentified	
1698.31	Unidentified	
1712.33	Unidentified	
1714.31	Unidentified	
1726.34	Unidentified	
1740.37	Unidentified	
1754.39	Unidentified	
1768.37	Unidentified	

Table 8. MALDI-MS data of methoxy-, keto-MAs and PDIMs type A detected from the analysis of the Strain C extract, the references for all previously published masses are shown. The *m/z* of previously unpublished masses is listed as unidentified. All masses are the $[M+Na]^+$.

6.3.6 Analysis of BCG Extracts

The spectrum acquired from the analysis of the BCG extract is quite complex due to the number of lipids in the sample, as shown in figure 6.7. As the lipids within this sample are quite similar structurally and fall within the same mass range, leading to increased isobaric species, care must be taken with the interpretation of the spectrum.

At the lower mass range of the spectrum presented in figure 6.7 a cluster of peaks are present at *m/z* 1010-1084, these masses and characteristic peak pattern correspond to those observed in this region of the spectrum for the standard of free MAs (figure 6.4, top spectrum), indicating the presence of mycolic acids. As *M. bovis BCG* reportedly do not synthesise the shorter chain α'-MAs[292], these peaks could represent shorter chain α-MAs, which, to the best of the authors knowledge, have not previously been reported, structural characterisation is needed. The more polar methoxy-MAs were detected in this sample and can be observed in the mass spectrum at *m/z* 1234, 1248, 1262, 1276, 1290, 1304, 1318, 1332 and 1346, representing C_{81}-C_{89}. Keto-MAs were also detected from this sample and are observed in the mass spectrum at *m/z*1246, 1260, 1274 and 1288, representing C_{81}-$_{84.}$ All masses correspond to those detected from the MA standards (figure 6. 4) and those previously published[193-195, 197].

Peaks representing PDIM A are again present at *m/z* 1306-1516, representing C_{87} to C_{101} and correspond to those previously published for the MALDI-TOF analysis of these species from purified *M. bovis BCG* wild type and *M.tb* H37Rv (wild type) and Beijing extracts[132, 200, 201], and the MALDI-MS analysis of the standards of PDIMs analysed in Chapter 4 of this thesis. The characteristic peak pattern of these species is less evident in the spectrum due to the presence of PGLs in the sample, which shares the same mass range. The peak at *m/z* 1488 could be attributed to PDIM A C_{99} or PGL, however due the accuracy and resolution afforded by the TOF analyser, and as the peak is at *m/z* 1488.48 it is believed this is PGL. This corresponds to the *m/z* previously reported for this

species[201], whereas PDIM A C_{99} have been reported at *m/z* 1488.60 and 1488.67 in literature and the strain C sample (see previous section) respectively, both of which did not contain PGLs. *m/z* 1460 and 1502 are also isobars, according to literature they could be PDIMs or PGLs. The peak representing the major homologue for PGL is present at *m/z* 1530, with a series of less abundant peaks at *m/z 1488*, *1502*, 1544, 1558, 1572 and 1586. Masses of PGLs detected from this sample correspond to those previously reported for the MALDI-MS analysis of *M.* bovis BCG extracts [201], and those detected from the standards in Chapter 4 of this thesis. The *m/z* represented in italics correspond to isobaric species, thus these are tentative assignments. There are also two high abundant peaks within this mass spectrum at *m/z* 1334 and 1362 that correspond to the previously reported masses of the major homologues of a class of cell wall associated lipids known as monomycoloyl glycerol (MMG)[183]. MMGs are mycolate containing lipids often observed along with PGLs and it is believed these masses correspond to two keto-mycolate MMGs. Again a number of possible cell wall associated lipid species are also present in these mass spectra, observed within the higher mass range *m/z* 1677-1762; these peaks have the same masses and characteristic pattern as those observed in the Strain C extract and are yet to be identified. As mention for the analysis of the Strain C extract, the masses fall within the mass range of TMMs; however they do not correspond to any published masses of these species to date. Structural characterisation will need to be carried out for full identification. . All significant peaks are listed in table 9, all masses are believed to be $[M+Na]^+$.

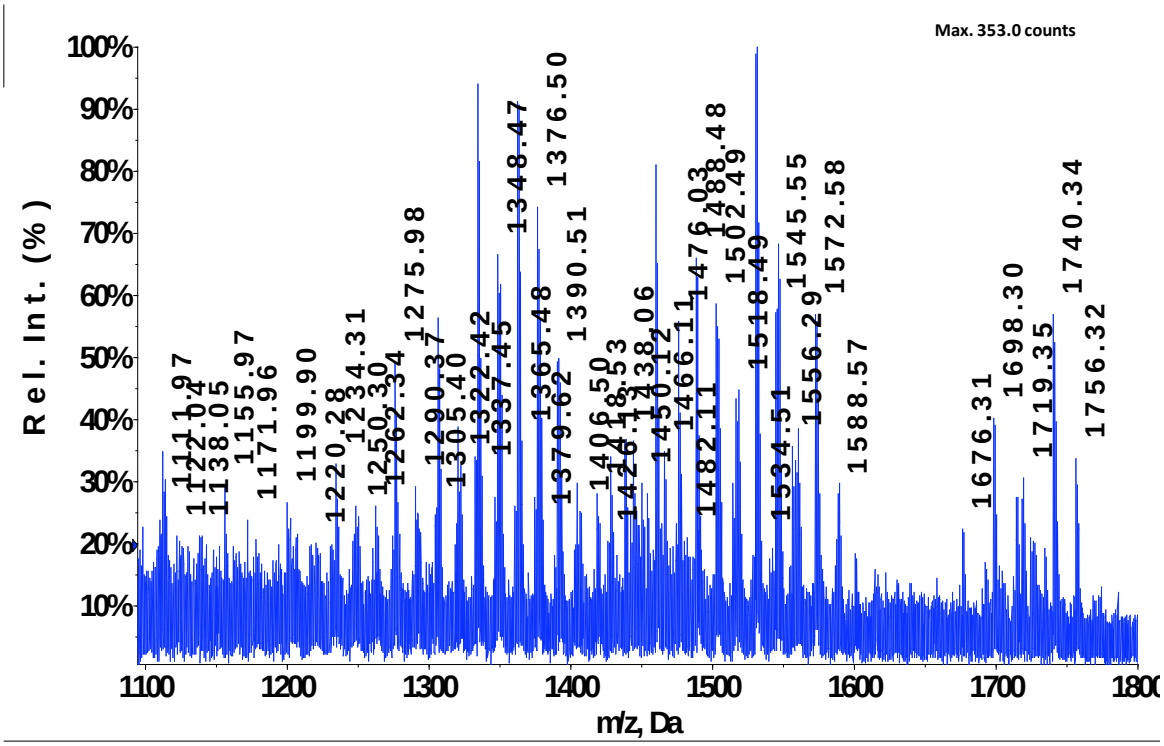

Figure 6.7. MALDI mass spectrum of bacterial extracts from *M. Bovis* BCG using DHB 10 mg ml^{-1} IPA:THF (1:1, v/v). The peak for the major homologue of the methoxy-MA is thought to be present at *m/z* 1275.98. The two high abundant peaks observed at *m/z* 1334 and 1362 represent the major homologue of MMG. Peaks from *m/z* 1306-1516 represent PDIM As C_{87}-C_{101}, whilst the peaks ranging from *m/z* 1446-1572 represent PGLs. The maximum ion count given is for the base peak which is at *m/z* 1530 and represents the major homologue of PGL. The cluster of peaks seen at the higher mass range *m/z* 1677-1756 are believed to be cell envelope associated lipids with a similar structure, but are yet to be identified.

m/z	Lipid	Reference
1012	Unidentified	
1026.04	Unidentified	
1040.01	Unidentified	
1054.05	Unidentified	
1070.05	Unidentified	
1084.06	Unidentified	
1234.31	Methoxy-MA	[193-195, 197]
1246.26	Keto-MA	[193, 194, 197]
1248.31	Methoxy-MA	[193-195, 197]
1260.31	Keto-MA	[193, 194, 197]
1262.34	Methoxy-MA	[193-195, 197]
1274.32	Keto-MA	[193, 194, 197]
1275.98	Methoxy-MA	[193-195, 197]
1288.33	Keto-MA	[193, 194, 197]
1290.37	Methoxy-MA	[193-195, 197]
1304	Methoxy-MA	[193-195, 197]
1318.39	Methoxy-MA	[193-195, 197]
1332.44	Methoxy-MA	[193-195, 197]
1346.46	Methoxy-MA	[193-195, 197]
1306.41	PDIM A	[132, 200, 201]
1320.43	PDIM A	[132, 200, 201]
1334.44	PDIM A/ MMG	[132, 200, 201] [183]
1348.47	PDIM A	[132, 200, 201]
1362.48	PDIM A/ MMG	[132, 200, 201] [183]
1376.5	PDIM A	[132, 200, 201]
1390.52	PDIM A	[132, 200, 201]
1404.5	PDIM A	[132, 200, 201]
1418.53	PDIM A	[132, 200, 201]
1446.43	PDIM A	[132, 200, 201]
1460.06	PDIM A	[132, 200, 201]
1474.47	PDIM A	[132, 200, 201]
1488.48	PDIM A/PGL	[132, 200, 201]
1502.49	PDIM A/PGL	[132, 200, 201]
1516.51	PDIM A	[132, 200, 201]
1530.26	PGL	[201]
1544.54	PGL	[201]
1558.55	PGL	[201]
1572.58	PGL	[201]
1676.32	Unidentified	
1690.16	Unidentified	
1698.3	Unidentified	
1714.27	Unidentified	
1718.35	Unidentified	
1726.33	Unidentified	
1734.32	Unidentified	
1740.34	Unidentified	
1742.35	Unidentified	
1756.32	Unidentified	

Table 9. MALDI-MS data of *m/z* of interest detected from the BCG extract.

6.4 Conclusion

The evaluation of numerous solvents that could be applied to the analysis of mycolic acids, without the need for prior derivatisation, led to the optimised combination of IPA:THF 1:1 (v/v). Whilst all of the solvent systems evaluated proved successful with respect to the detection of free MAs and their methyl esters, the spectral quality was rather poor for six of the eight systems. The experimental data for the initial solvent optimisation experiments showed IPA:THF, and IPA:DCM were the most sensitive systems to take forward for further experimentation. When analysing the spectra for both free MAs and MAMEs the quality was drastically improved compared to the other systems. Ion counts, S/N and resolving power was far greater with these solvents, particularly when analysing the extremely non-polar alpha-mycolates as free acids. All alpha-, methoxy- and keto-mycolates previously reported in literature were detected using IPA:THF as the matrix solvent system, with the addition of peaks that may be attributed to smaller chain alpha-MAs at the lower mass range of *m/z* 1012-1084, and possible methoxy- or keto-MAs at *m/z* 1224-1340, that, to the best of the authors knowledge, have not been previously reported. These molecules need further investigation to enable proper identification. In addition to this, most literature to date analyses MAMEs[193-195, 197, 198], as these are more readily ionised and thus increase sensitivity and detection of mycolates. The matrix solvent system presented here has proven sensitive enough to detect free MAs, including numerous alpha-MAs which are extremely non-polar by nature and thus difficult to ionise, thereby omitting the need for the derivatisation step. Most studies to date have also analysed individual mycolate subclasses after separation on TLC plates[193-195, 197, 198], whereas all data presented here is from complex lipid mixtures.

Numerous studies to date have shown the composition of the MALDI matrix solvent system greatly influences the resulting mass spectra and thus analysis[207, 209, 290,

293]. This is with respect to detection sensitivity and the relative intensities of the species/molecules detected[207, 209, 290]. In addition to this the matrix-sample solvent system has been shown to have mass discriminatory effects in the resulting MALDI-MS signal[293]; however most of the studies to date have been carried out for the analysis of peptides and proteins. The greater sensitivity achieved using IPA:THF as the solvent system is thought to be due to greater extraction and incorporation of the analytes into the matrix crystals, together with the size, shape and distribution of these crystals on the target plate, as presented in this chapter.

The comparison of IPA:THF and IPA:DCM to the matrix solvent systems currently used in literature, based around varying ratios of chloroform:methanol for the analysis of non-polar lipids, including MAMEs, TAGS and cholesterol[132-134, 192-201], showed IPA:THF to be a far more sensitive matrix solvent system. IPA:THF showed the greatest overall results for both the free MA and MAME samples. When analysing the major homologues of the alpha-, methoxy- and keto-mycolates at *m/z* 1160, 1276 and 1302 respectively IPA:THF showed a 3-4 times increase in S/N compared to those used in literature. By changing the ratio of analyte to matrix applied to the MALDI target plate the reproducibility also greatly increased for this solvent system. In addition to this, the change in sample preparation resulted in IPA:THF producing far greater results with respect to ion counts, S/N and thus spectral quality when compared to the other optimised solvent system of IPA:DCM. With these results in mind IPA:THF was applied to the analysis of whole mycobacterial lipid extracts from two bacterial species know as Strain C and *M. bovis* BGC.

The analysis of the Strain C extract using DHB in the optimised solvent system IPA:THF (v/v) was successful for the detection of numerous cell wall associated lipid species, known to be involved in virulence. The main cluster of peaks present in the MALDI mass spectrum correlate well with those previously published for the analysis of purified PDIMs type A analysed from, *M. tb* H37Rv (wild type)[200], *M. tb* Beijing strain (HN878)[132], *M.*

bovis BCG (PMM137:PM261) and *M. bovis* BCG wild type[201]. PDIMs are key virulence factors involved in both the replication of mycobacterium within the host, and the modulation of the host immune response[132, 199-201, 294]. In addition to the detection of PDIMs, methoxy- and keto-mycolic acids were also present within this mass spectrum, the sample proved too complex for the analysis of the extremely non-polar alpha-MAs. Whilst the analysis of the alpha-MAs is desirable from complex mixtures, it should be noted that these are the most widely distributed of the mycolate subclasses and are present in every species examined to date, followed by the least polar keto-MAs, it is the methoxy-MAs that are predominantly (not exclusively) found in slow-growing pathogenic species[292], and should thus possibly be the key species of interest. There is also a cluster of peaks present at the higher mass range of this mass spectrum that have the characteristic lipid profile, these could possibly be TMM, however, they do not correspond to any masses published in literature to date for these molecules. Structural characterisation is needed for full identification, as these lipids could prove to be important virulence factors that correspond to known lipids but have different chain lengths to those previously analysed. Strain C is believed to be a complimentary *M. tb* strain, this is due to the presence of mycolic acids and PDIMs, but a lack of PGLs, which are absent from most commonly used laboratory and clinical strains of *M. tb* due to a frame-shift mutation, as previously discussed[132, 136].

The MALDI-MS analysis of the *M. bovis* BCG extract produced a highly complex mass spectrum due to the number of lipid species detected from this sample. Several methoxy- and keto-MAs were detected from this sample that corresponds well to those previously published for the analysis of MAs from slow-growing pathogenic mycobacterium[193-198]. PDIMs type A was again present within this mass spectrum and again the masses correspond well with those previously published for this type of lipid for C_{87} to C_{101}[132, 200, 201]. In addition to those lipids detected from the Strain C extract, PGLs were detected from this sample and their masses correspond to those previously published for

the MALDI-MS analysis of purified lipid extracts from *M. bovis* BCG wild-type[201]. The peaks at *m/z* 1334 and 1362, although isobaric, are believed to be two species of keto-mycolate monomycoloyl glycerol (MMG) that are often found in association with or are separated with PGLs via TLC analysis[295]. These masses correspond to those reported for the $[M+Na]^+$ ions for C_{86} and C_{88} respectively from *M. bovis* BCG Danish 1331 strain[183]. MMGs have been shown to have potent immunostimulatory activity[183, 295]. There were also a number of unidentified peaks within this mass spectrum, that again, once identified could add the knowledge that already exists for mycobacterial lipid species involved in virulence. At the lower mass range *m/z* 1012-1084, a cluster of peaks are present that display the characteristic mycobacterium lipid profile, in that they differ from one another my 14 mass units. These share the same masses and profile as those observed in the mass spectrum of the free mycolic acid standards (figure 4) indicating the presence of shorter chain MAs. At the higher mass range, *m/z* 1676-1756 a cluster of peaks are present that also differ from one another by 14 mass units, these could possibly be TMM, but they are yet to be identified, they do share the same masses as the unidentified lipids detected from the Strain C sample. *M. bovis* BCG is an attenuated strain derived from the virulent *M. bovis* for use in vaccination against TB. The original vaccine strain has been subcultured and distributed to so many laboratories world-wide that today many substrains of the original exist, each with varying lipid profiles that are thought to have effects on attenuation, and thus have varying protective immunity[294]. Although the BCG strain supplied here is unknown, several substrains can be excluded due to the lipid profiles present. It is known that *M. bovis* BCG-Moreau, -Japan, and –Glaxo are deficient in PDIM and PGL biosynthesis, as these lipids are present these strains can be excluded[285]. Many BCG strains, those distributed from the Pasteur Institute after 1927, are deficient in the biosynthesis of methoxy-MAs due to a point mutation in the *mmA3* gene; these include Prague, Pasteur, Connaught, Denmark, Glaxo, Tice, Phipps and Frappier[296]. With the knowledge of the combined lipid profiles there

are only four remaining possibilities for this strain, they are Birkhaug, Japan, Russia and Sweden.

Mycolic acids and other cell envelope non-polar lipids including, PDIMs, PGLs and MMGs are important molecules as they play a central role in the pathogenicity of *M. tb* and *M. bovis*, thus methods that can rapidly analysis these species for aiding in diagnosis, identification of growth and virulence through the analysis of mutant models, and the identification of therapeutic targets/affects of pharmaceuticals is greatly needed. The application of MALDI-MS, using this solvent system could greatly contribute to such investigations. Work presented in this chapter has proven MALDI-MS as a viable tool for the investigation of lipids involved in the virulence of mycobacterium from highly complex mixtures. Several key lipids were detected along with numerous unknown species. In addition to this, this solvent system could be applied to MALDI-MS imaging studies, which was not previously possible using chloroform as part of the matrix solvent system, due to its toxicity and anaesthetic properties. The analysis of these lipids from formalin fixed samples could also be a possibility, lipid analysis from FF tissue was shown in chapter 3, and the analysis of fixed tissue would reduced the biohazard risk, as is common practice in histopathology laboratories. This solvent system may also be of more use when analysing other non-polar lipids including TAGs and cholesterol.

7.1 Conclusions and Future Work

MALDI-MSI is proven as a viable tool for the analysis of lipids in both normal and disease states, however, method development and sample preparation protocols can still be improved. This thesis reports the significant impact sample preparation has on MALDI-MS analysis, and further demonstrates the potential of this highly versatile technique in analysis of lipids in complex samples.

MALDI-MSI results demonstrated tissue sections that had been dehydrated resulted in much lower signal intensities compared to those that had not. The significant difference in signal intensity and spectral quality observed is thought to be due to alterations in surface/tissue properties, with 'dryer' sections resulting in reduced analyte extraction and co-crystallisation compared to the 'wetter' sections. Alternatively, the deposition of matrix onto the 'wetter' samples may decrease the solvent evaporation time, which in turn would decrease the crystal drying process, allowing more time for the analyte/s to be incorporated into the matrix crystals[206, 239]. It is unknown how these effects would translate to the analysis of larger molecules such as peptides and proteins. This would be an interesting investigation to carry out, as sample desiccation prior to matrix deposition is still a protocol in many MALDI-MSI investigations. Researchers do not really explain why samples are desiccated, other than to dehydrate the tissue, nor has anyone commented on the effects of such procedures. Many investigators have commented on the changes that occur within tissue immediately after death/during excision, prior to flash-freezing, even if this time period is minutes, it is still thought to affect the biological profiles in tissue. Investigators have attempted to minimise this by using processes such as rapid heating of the organs immediately after excision. Investigators also try to minimise the time tissue is out of the freezer, between storage periods and sectioning in the cryostat chamber, constant transfer between the two affects protein signal over time. With all this

knowledge in mind, it is postulated that sample desiccation or tissue 'dehydration' for time periods after sectioning will reduce the obtainable signal in MALDI-MSI, as demonstrated in chapter 2. Investigations should be carried out assessing time verses signal quality for a number of molecules, with an aim to provide a protocol or guidelines for analysts. Results presented also indicated matrix application and not sample thickness greatly affects the sensitivity and quality of a MALDI-MSI study.

The automated TM-sprayer was introduced at ASMS in 2007, there was little to no literature available on the application of this in MALDI-MS investigations, other than the technical note supplied by Leap Technologies. This deposition method demonstrated small crystal size and a homogenous coverage, high analyte extraction and co-crystallisation, and no analyte delocalisation, demonstrated by enhanced detection sensitivity and thus S/N, and high resolution images. The TM-sprayer showed over a two-fold reduction in variability compared to airbrush deposition, reproducibility is a key issue for the latter method. A more reproducible deposition method, as presented here, will aid in minimising the problems associated with *inter*- and *intra*- laboratory variability, due to irreproducible matrix deposition. Once optimised for a solvent system this method is both fast and efficient, and a much lower concentration and thus consumption of matrix material also make the TM Leap sprayer attractive tool for MALDI-MSI. The only problem with this instrument is its cost; at $50,000 it is beyond what is affordable by many research groups.

The MALDI-MSI analysis of phospholipids directly from formalin fixed tissue was presented for the first time in this thesis. High quality molecular lipid images were obtained, showing mutual distribution to fresh tissue preparation [10, 12, 14, 155, 165, 166, 172, 205, 230, 232, 233, 238, 275-278]. Sodium buffers associated with the formalin fixation protocol caused a change in previously reported ionisation pathways [10, 12, 14,

155, 165, 166, 172, 205, 230, 232, 233, 238, 275-278], and the $[M+Na]^+$ was found to be the most readily detected ion for each lipid species investigated. Dissociation of *m/z* 756, $[M+Na]^+$ in fixed tissue produced a more enriched CID mass spectrum, compared to those obtained from fresh tissue for the analysis of *m/z* 772, $[M+K]^+$. MALDI-MSI investigations were carried out on soft sarcoma sections that had been fixed in formalin, numerous suspected lipid species were detected, however, due to the absence of normal tissue architecture, and minimal pathological information, this investigation could not continue. Working alongside pathologists in the future would enable thorough MALDI-MSI investigations into the differential expression and distribution of PLs in disease states. There are a number of concerns regarding the interpretation of results obtained from MALDI-MSI investigations of PLs, as highlighted in chapter 1 of this thesis. Authors report results based on a single ion form for a given species, when the mass spectrum acquired is complex, containing protonated, cationised and fragment peaks of a single lipid. There are also discrepancies in the reported distribution of some PLs across tissue areas. It is postulated in this thesis that the method of sample preparation not only affects the quality of results, but may also result the discrepancies reported for the distribution of lipid species. This could be due to the use of different matrices, solvent systems, and matrix deposition methods across laboratories. The future analysis of these molecules should involve multi-laboratory efforts to build a database, not only of results acquired, but also of the experimental data used to obtain each result. This could be similar to the imzML initiative, which was set up to facilitate the exchange and processing of MALDI-MS imaging data, but with the addition of sample preparation and acquisition parameters. This would build a library of changes observed with each preparation, such as the use of methanol compared to acetonitrile. This would also help build a database of optimised strategies for lipid analysis. The importance of monitoring all ions for a given lipid species when discussing a difference in distribution, signal intensity and ratios needs to be recognised, as is reported in this thesis.

The MALDI-MS detection of MAs, PDIMs, PGLs and MMGs from lymph and blood extracts taken from infected cattle, was not possible with the method commonly used in literature. Variation of extract concentration, amounts applied to the MALDI target plate, changing the matrix:analyte ratio, and altering the laser power, all had no effect on the outcome of the results. A protocol has been optimised for the analysis of lipids directly from thin layer chromatography plates by MALDI-MSI; however, at present it is still not well suited to the analysis of all *Mycobacterium* lipids of interest. Analysis of tissue that had been autoclaved to remove biohazard risks proved this procedure to be unsuitable for MALDI-MSI investigations. Future analysis of infected organs should be carried out on tissue fixed for a minimum of 24-48hrs (size dependant) in formalin. This is the standard safety procedure applied in clinical histopathology laboratories for biohazard material, and tissue prepared this way is suitable for MALDI-MS analysis of phospholipids, as shown in chapter 3 of this thesis.

Solvent optimisation for MALDI-MS investigations of complex *Mycobacterium* cell wall lipids proved the binary matrix IPA:THF was far more sensitive than those used in literature, IPA:THF demonstrated a 3-4 times increase in S/N compared to those previously reported. The application of this solvent system to the analysis of complex bacterial extracts was successful in the detection of several key lipids known to be involved in virulence, including MAs, PDIMs, PGLs and MMGs, numerous unknown species were also detected. Further optimisation varying the ratios of these solvents may enhance detection sensitivity further. Protocols also need to be developed that enable low-energy CID of the unknown species, and thus aid in structurally elucidating these molecules. This solvent system could be applied to MALDI-MS imaging studies. The analysis of fixed organs taken from infected animals may provide distribution information of these lipids within organ systems, information that, to the best of the author's knowledge, has never been acquired before. Such studies may be able to complement

current MALDI-MSI investigations into the distribution of anti-mycobacterial drugs in lung tissue. The type and amount of MAs biosynthesised by *Mycobacterium* are affected by growth stages, temperature and growth medium, as analysis is nearly always carried out on bacteria grown in media it is unknown how these change in a host environment. Future work should aim to establish such information.

8. References

1. Karas, M. and F. Hillenkamp, *Laser desorption ionization of proteins with molecular masses exceeding 10,000 daltons.* Analytical chemistry, 1988. 60(20): p. 2299-2301.
2. Tanaka, k., H. Waki, Y. Ido, S. Akita, Y. Yoshida, and T. Yoshida, *Protein and polymer analyses up to m/z 100 000 by laser ionisation time-of-flight mass spectrometry.* Rapid Communications in Mass Spectrometry, 1988. 2 p. 151-153, .
3. Horneffer, V., K. Dreisewerd, H.C. Lüdemann, F. Hillenkamp, M. Läge, and K. Strupat, *Is the incorporation of analytes into matrix crystals a prerequisite for matrix-assisted laser desorption/ionization mass spectrometry? A study of five positional isomers of dihydroxybenzoic acid.* International Journal of Mass Spectrometry, 1999. 185-187: p. 859-870.
4. Stoeckli, M., D. Staab, A. Schweitzer, J. Gardiner, and D. Seebach, *Imaging of a [beta]-Peptide Distribution in Whole-Body Mice Sections by MALDI Mass Spectrometry.* Journal of the American Society for Mass Spectrometry, 2007. 18(11): p. 1921-1924.
5. Zhu, X. and I. Papayannopoulos, *Improvement in the detection of low concentration protein digests on a MALDI TOF/TOF workstation by reducing -cyano-4-hydroxycinnamic acid adduct ions.* Journal of Biomolecular Techniques: JBT, 2003. 14(4): p. 298.
6. Griffin, T.J., J.G. Hall, J.R. Prudent, and L.M. Smith, *Direct genetic analysis by matrix-assisted laser desorption/ionization mass spectrometry.* Proceedings of the National Academy of Sciences, 1999. 96(11): p. 6301-6306.

7. Bunch, J., M.R. Clench, and D.S. Richards, *Determination of pharmaceutical compounds in skin by imaging matrix-assisted laser desorption/ionisation mass spectrometry.* Rapid Communications in Mass Spectrometry, 2004. 18: p. 3051-3060.

8. Hsieh, Y., R. Casale, E. Fukuda, J. Chen, I. Knemeyer, J. Wingate, R. Morrison, and W. Korfmacher, *Matrix-assisted laser desorption/ionization imaging mass spectrometry for direct measurement of clozapine in rat brain tissue.* Rapid Communications in Mass Spectrometry, 2006. 20(6): p. 965-972.

9. Hsieh, Y., J. Chen, and W.A. Korfmacher, *Mapping pharmaceuticals in tissues using MALDI imaging mass spectrometry.* Journal of Pharmacological and Toxicological Methods, 2007. 55(2): p. 193-200.

10. Cerruti, C.D., D. Touboul, V. Guerineau, V.W. Petit, O. Laprevote, and A. Brunelle, *MALDI imaging mass spectrometry of lipids by adding lithium salts to the matrix solution.* Analytical and Bioanalytical Chemistry, 2011. 401(1): p. 75-87.

11. Strupat, K., M. Karas, and F. Hillenkamp, *2,5-Dihydroxybenzoic acid: a new matrix for laser desorption--ionization mass spectrometry.* International Journal of Mass Spectrometry and Ion Processes, 1991. 111: p. 89-102.

12. Hankin, J.A., R.M. Barkley, and R.C. Murphy, *Sublimation as a Method of Matrix Application for Mass Spectrometric Imaging.* Journal of the American Society for Mass Spectrometry, 2007. 18(9): p. 1646-1652.

13. Jackson, S.N., H.-Y.J. Wang, and A.S. Woods, *In Situ Structural Characterization of Phosphatidylcholines in Brain Tissue Using MALDI-MS/MS.* Journal of the American Society for Mass Spectrometry, 2005. 16(12): p. 2052-2056.

14. Jackson, S.N., H.-Y.J. Wang, and A.S. Woods, *Direct Profiling of Lipid Distribution in Brain Tissue Using MALDI-TOFMS.* Analytical Chemistry, 2005. 77(14): p. 4523-4527.

15. Gyémánt, G., A. Tóth, I. Bajza, L. Kandra, and A. Lipták, *Identification and structural analysis of synthetic oligosaccharides of Shigella sonnei using MALDI-TOF MS.* Carbohydrate Research, 2001. 334(4): p. 315-322.

16. Reis, A., M.R.M. Domingues, A.J. Ferrer-Correia, and M.A. Coimbra, *Structural characterisation by MALDI-MS of olive xylo-oligosaccharides obtained by partial acid hydrolysis.* Carbohydrate Polymers, 2003. 53(1): p. 101-107.

17. Sato, Y., Y. Fukuyama, H. Nonami, R. Erra-Balsells, C.A. Stortz, A.S. Cerezo, and M.C. Matulewicz, *Matrix-assisted ultraviolet laser desorption/ionization time-of-flight (UV-MALDI-TOF) mass spectra of N-acylated and N,O-acylated glycosylamines.* Carbohydrate Research, 2007. 342(17): p. 2567-2574.

18. Tang, W., J. Krause, L. Zhu, and L.M. Smith, *Factors influencing oligonucleotide stability in matrix-assisted laser desorption/ionization (MALDI) mass spectroscopy.* International Journal of Mass Spectrometry and Ion Processes, 1997. 169-170(0): p. 301-311.

19. Tang, W., C.M. Nelson, L. Zhu, and L.M. Smith, *Positive ion formation in the ultraviolet matrix-assisted laser desorption / ionization analysis of oligonucleotides by using 2,5-dihydroxybenzoic acid.* Journal of the American Society for Mass Spectrometry, 1997. 8(3): p. 218-224.

20. Farah, M.A., S. Bose, J.-H. Lee, H.-C. Jung, and Y. Kim, *Analysis of glycated insulin by MALDI-TOF mass spectrometry.* Biochimica et Biophysica Acta (BBA) - General Subjects, 2005. 1725(3): p. 269-282.

21. Schwartz, S.A., M.l. Reyzer, and R.M. Caprioli, *Direct tissue analysis using matrix-assisted laser desorption/ionisation mass spectrometry: practical aspects of sample preparation.* Journal of Mass Spectrometry, 2003. 38: p. 699-708.

22. Seeley, E.H., S.R. Oppenheimer, D. Mi, P. Chaurand, and R.M. Caprioli, *Enhancement of Protein Sensitivity for MALDI Imaging Mass Spectrometry After Chemical Treatment of Tissue Sections.* Journal of the American Society for Mass Spectrometry, 2008. 19(8): p. 1069-1077.

23. Low, W., J. Kang, M. DiGruccio, D. Kirby, M. Perrin, and W.H. Fischer, *MALDI-MS analysis of peptides modified with photolabile arylazido groups.* Journal of the American Society for Mass Spectrometry, 2004. 15(8): p. 1156-1160.

24. Tang, K., N.I. Taranenko, S.L. Allman, C.H. Chen, L.Y. Chág, and K.B. Jacobson, *Picolinic acid as a matrix for laser mass spectrometry of nucleic acids and proteins.* Rapid Communications in Mass Spectrometry, 1994. 8(9): p. 673-677.

25. Kirpekar, F., E. Nordhoff, L.K. Larsen, K. Kristiansen, P. Roepstorff, and F. Hillenkamp, *DNA sequence analysis by MALDI mass spectrometry.* Nucleic Acids Research, 1998. 26(11): p. 2554-2559.

26. Niemeyer, D., T. Elssner, K. Fahr, D. Peters, T. Wenzel, E. Petkovski, and M. Kostrzewa, *Detection of genetic variation by MALDI-TOF mass spectrometry: rapid SNP genotyping using the GENOLINK system.* International Congress Series, 2004. 1261(0): p. 9-11.

27. Sauer, S., P. Kepper, A. Smyra, A. Dahl, F.-T. Ferse, H. Lehrach, and R. Reinhardt, *Automated solid-phase extraction for purification of single nucleotide polymorphism genotyping products prior to matrix-assisted laser desorption/ionisation time-of-flight mass spectrometric analysis.* Journal of Chromatography A, 2004. 1049(1-2): p. 9-16.

28. Sascha, S., *The essence of DNA sample preparation for MALDI mass spectrometry.* Journal of Biochemical and Biophysical Methods, 2007. 70(2): p. 311-318.

29. Zagorevskii, D.V., M.F. Aldersley, and J.P. Ferris, *MALDI Analysis of Oligonucleotides Directly from Montmorillonite.* Journal of the American Society for Mass Spectrometry, 2006. 17(9): p. 1265-1270.

30. Zhang, L.-K. and M.L. Gross, *Location of abasic sites in oligodeoxynucleotides by tandem mass spectrometry and by a chemical cleavage initiated by an unusual reaction of the ODN with MALDI matrix.* Journal of the American Society for Mass Spectrometry, 2002. 13(12): p. 1418-1426.

31. Hunnam, V., D.J. Harvey, D.A. Priestman, R.H. Bateman, R.S. Bordoli, and R. Tyldesley, *Ionization and fragmentation of neutral and acidic glycosphingolipids with a Q-TOF mass spectrometer fitted with a MALDI ion source.* Journal of the American Society for Mass Spectrometry, 2001. 12(11): p. 1220-1225.

32. Stübiger, G. and O. Belgacem, *Analysis of lipids using 2, 4, 6-trihydroxyacetophenone as a matrix for MALDI mass spectrometry.* Anal. Chem, 2007. 79(8): p. 3206-3213.

33. Vakhrushev, S.Y., M.F. Snel, J. Langridge, and J. Peter-Katalinić, *MALDI-QTOFMS/MS identification of glycoforms from the urine of a CDG patient.* Carbohydrate Research, 2008. 343(12): p. 2172-2183.

34. Bouschen, W. and B. Spengler, *Artifacts of MALDI sample preparation investigated by high-resolution scanning microprobe matrix-assisted laser desorption/ionization (SMALDI) imaging mass spectrometry.* International Journal of Mass Spectrometry, 2007. 266(1-3): p. 129-137.

35. Dai, Y.Q., R.M. Whittal, and L. Li, *Two-layer sample preparation: A method for MALDI-MS analysis of complex peptide and protein mixtures.* Analytical chemistry, 1999. 71(5): p. 1087-1091.

36. Allwood, D.A., I.K. Perera, J. Perkins, P.E. Dyer, and G.A. Oldershaw, *Preparation of 'near' homogeneous samples for the analysis of matrix-assisted laser desorption/ionisation processes.* Applied Surface Science, 1996. 103(3): p. 231-244.

37. Önnerfjord, P., S. Ekström, J. Bergquist, J. Nilsson, T. Laurell, and G. Marko-Varga, *Homogeneous sample preparation for automated high throughput analysis with matrix-assisted laser desorption/ionisation time-of-flight mass spectrometry.* Rapid Communications in Mass Spectrometry, 1999. 13(5): p. 315-322.

38. Vorm, O. and M. Mann, *Improved mass accuracy in matrix-assisted laser desorption/ionization time-of-flight mass spectrometry of peptides.* Journal of the American Society for Mass Spectrometry, 1994. 5(11): p. 955-958.

39. Hensel, R.R., R.C. King, and K.G. Owens, *Electrospray sample preparation for improved quantitation in matrix-assisted laser desorption/ionization time-of-flight mass spectrometry.* Rapid Communications in Mass Spectrometry, 1997. 11(16): p. 1785-1793.

40. Jaskolla, T.W., M. Karas, U. Roth, K. Steinert, C. Menzel, and K. Reihs, *Comparison Between Vacuum Sublimed Matrices and Conventional Dried Droplet Preparation in MALDI-TOF Mass Spectrometry.* Journal of the American Society for Mass Spectrometry, 2009. 20(6): p. 1104-1114.

41. Meriaux, C., J. Franck, M. Wisztorski, M. Salzet, and I. Fournier, *Liquid ionic matrixes for MALDI mass spectrometry imaging of lipids.* Journal of Proteomics, 2010. 73(6): p. 1204-1218.

42. Holle, A., A. Haase, M. Kayser, and J. Höhndorf, *Optimizing UV laser focus profiles for improved MALDI performance.* Journal of Mass Spectrometry, 2006. 41(6): p. 705-716.

43. Qiao, H., V. Spicer, and W. Ens, *The effect of laser profile, fluence, and spot size on sensitivity in orthogonal injection matrix assisted laser desorption/ionization time of flight mass spectrometry.* Rapid Communications in Mass Spectrometry, 2008. 22(18): p. 2779-2790.

44. Zhu, L., G.R. Parr, M.C. Fitzgerald, C.M. Nelson, and L.M. Smith, *Oligodeoxynucleotide Fragmentation in MALDI/TOF Mass Spectrometry Using 355-nm Radiation.* Journal of the American Chemical Society, 1995. 117(22): p. 6048-6056.

45. Trim, P., M. Djidja, S. Atkinson, K. Oakes, L. Cole, D. Anderson, P. Hart, S. Francese, and M. Clench, *Introduction of a 20 kHz Nd: YVO4 laser into a hybrid quadrupole time-of-flight mass spectrometer for MALDI-MS imaging.* Analytical and Bioanalytical Chemistry, 2010: p. 1-11.

46. Dreisewerd, K., S. Berkenkamp, A. Leisner, A. Rohlfing, and C. Menzel, *Fundamentals of matrix-assisted laser desorption/ionization mass spectrometry with pulsed infrared lasers.* International Journal of Mass Spectrometry, 2003. 226(1): p. 189-209.

47. Kampmeier, J., K. Dreisewerd, M. Schürenberg, and K. Strupat, *Investigations of 2,5-DHB and succinic acid as matrices for IR and UV MALDI. Part: I UV and IR laser ablation in the MALDI process.* International Journal of Mass Spectrometry and Ion Processes, 1997. 169-170(0): p. 31-41.

48. Hess, W.P., H.K. Park, O. Yavas, and R.F. Haglund Jr, *IR-MALDI of low molecular weight compounds using a free electron laser.* Applied Surface Science, 1998. 127-129(0): p. 235-241.

49. Dreisewerd, K., *The Desorption Process in MALDI.* Chemical Reviews, 2003. 103(2): p. 395-426.

50. Dreisewerd, K., M. Schürenberg, M. Karas, and F. Hillenkamp, *Influence of the laser intensity and spot size on the desorption of molecules and ions in matrix-assisted laser desorption/ionization with a uniform beam profile.* International Journal of Mass Spectrometry and Ion Processes, 1995. 141(2): p. 127-148.

51. Ingendoh, A., M. Karas, F. Hillenkamp, and U. Giessmann, *Factors affecting the resolution in matrix-assisted laser desorption--ionization mass spectrometry.* International Journal of Mass Spectrometry and Ion Processes, 1994. 131: p. 345-354.

52. Aerni, H.-R., D.S. Cornett, and R.M. Caprioli, *Automated Acoustic Matrix Deposition for MALDI Sample Preparation.* Analytical Chemistry, 2006. 78(3): p. 827-834.

53. Hillenkamp, F., E. Wäfler, M.C. Jecklin, and R. Zenobi, *Positive and negative analyte ion yield in matrix-assisted laser desorption/ionization revisited.* International Journal of Mass Spectrometry, 2009. 285(3): p. 114-119.

54. Karas, M., U. Bahr, I. Fournier, M. Gluckmann, and A. Pfenninger, *The initial-ion velocity as a marker for different desorption-ionization mechanisms in MALDI.* International Journal of Mass Spectrometry, 2003. 226(1): p. 239-248.

55. Karas, M., M. Gluckmann, and J. Schafer, *Ionization in matrix-assisted laser desorption/ionization: singly charged molecular ions are the lucky survivors.* Journal of Mass Spectrometry, 2000. 35(1): p. 1-12.

56. Karas, M. and R. Krueger, *Ion formation in MALDI: the cluster ionization mechanism.* Chem. Rev, 2003. 103(2): p. 427-440.

57. Knochenmuss, R., *A quantitative model of ultraviolet matrix-assisted laser desorption/ionization.* Journal of Mass Spectrometry, 2002. 37(8): p. 867-877.

58. Knochenmuss, R., *A quantitative model of ultraviolet matrix-assisted laser desorption/ionization including analyte ion generation.* Anal. Chem, 2003. 75(10): p. 2199-2207.

59. Knochenmuss, R., *Photoionization pathways and free electrons in UV-MALDI.* Anal. Chem, 2004. 76(11): p. 3179-3184.

60. Knochenmuss, R., *Ion formation mechanisms in UV-MALDI.* The Analyst, 2006. 131(9): p. 966-986.

61. Knochenmuss, R., *Positive/negative ion ratios and in-plume reaction equilibria in MALDI.* International Journal of Mass Spectrometry, 2008. 273(1-2): p. 84-86.

62. Knochenmuss, R., *A bipolar rate equation model of MALDI primary and secondary ionization processes, with application to positive/negative analyte ion ratios and suppression effects.* International Journal of Mass Spectrometry, 2009. 285(3): p. 105-113.

63. Knochenmuss, R., F. Dubois, M.J. Dale, and R. Zenobi, *The matrix suppression effect and ionization mechanisms in matrix-assisted laser desorption/ionization.* Rapid Communications in Mass Spectrometry, 1996. 10(8): p. 871-877.

64. Knochenmuss, R., A. Stortelder, K. Breuker, and R. Zenobi, *Secondary ion-molecule reactions in matrix-assisted laser desorption/ionization.* Journal of Mass Spectrometry, 2000. 35(11): p. 1237-1245.

65. Knochenmuss, R. and A. Vertes, *Time-delayed 2-pulse studies of MALDI matrix ionization mechanisms.* Journal of Physical Chemistry B, 2000. 104(23): p. 5406-5410.

66. Knochenmuss, R. and R. Zenobi, *MALDI ionization: the role of in-plume processes.* Chem. Rev, 2003. 103(2): p. 441-452.

67. Knochenmuss, R. and L.V. Zhigilei, *Molecular dynamics simulations of MALDI: laser fluence and pulse width dependence of plume characteristics and consequences for matrix and analyte ionization.* Journal of Mass Spectrometry, 2010. 45(4): p. 333-346.

68. Krüger, R. and M. Karas, *Formation and fate of ion pairs during MALDI analysis: anion adduct generation as an indicative tool to determine ionization processes.* Journal of the American Society for Mass Spectrometry, 2002. 13(10): p. 1218-1226.

69. Krüger, R., A. Pfenninger, I. Fournier, M. Glückmann, and M. Karas, *Analyte Incorporation and Ionization in Matrix-Assisted Laser Desorption/Ionization Visualized by pH Indicator Molecular Probes.* Analytical Chemistry, 2001. 73(24): p. 5812-5821.

70. Vertes, A., G. Luo, L. Ye, Y. Chen, and I. Marginean, *Laser pulse length dependence of internal energy transfer in UV-MALDI-MS.* Applied Physics A: Materials Science & Processing, 2004. 79(4): p. 823-825.

71. Wong, C.K.L. and T.-W.D. Chan, *Cationization Processes in Matrix-assisted Laser Desorption/Ionization Mass Spectrometry: Attachment of Divalent and Trivalent Metal Ions.* Rapid Communications in Mass Spectrometry, 1997. 11(5): p. 513-519.

72. Zenobi, R. and R. Knochenmuss, *Ion formation in MALDI mass spectrometry.* Mass spectrometry reviews, 1998. 17(5): p. 337-366.

73. Zhigilei, L. and B. Garrison, *Molecular dynamics simulation study of the fluence dependence of particle yield and plume composition in laser desorption and ablation of organic solids.* Applied Physics Letters, 1999. 74: p. 1341.

74. Jaskolla, T.W. and M. Karas, *Compelling Evidence for Lucky Survivor and Gas Phase Protonation: The Unified MALDI Analyte Protonation Mechanism.* Journal of the American Society for Mass Spectrometry, 2011. 22(6): p. 976-988.

75. Brunnée, C., *The ideal mass analyzer: Fact or fiction?* International Journal of Mass Spectrometry and Ion Processes, 1987. 76(2): p. 125-237.

76. Dawson, P.H., D.J. Douglas, and C.L. John, *Quadrupoles, Use of in Mass Spectrometry*, in *Encyclopedia of Spectroscopy and Spectrometry*. 1999, Elsevier: Oxford. p. 1921-1930.

77. Karas, M., U. Bahr, A. Ingendoh, E. Nordhoff, B. Stahl, K. Strupat, and F. Hillenkamp, *Principles and applications of matrix-assisted UV-laser desorption/ionization mass spectrometry.* Analytica Chimica Acta, 1990. 241(2): p. 175-185.

78. Loboda, A.V. and I.V. Chernushevich, *A Novel Ion Trap That Enables High Duty Cycle and Wide m/z Range on an Orthogonal Injection TOF Mass Spectrometer.* Journal of the American Society for Mass Spectrometry, 2009. 20(7): p. 1342-1348.

79. McIver, R.T., Y. Li, and R.L. Hunter, *FTMS method for high resolution matrix-assisted laser desorption.* International Journal of Mass Spectrometry and Ion Processes, 1994. 132(3): p. L1-L7.

80. Todd, J.F.J., *A survey of the current state of quadrupole mass spectrometry.* International Journal of Mass Spectrometry and Ion Processes, 1984. 60(1): p. 3-10.

81. Amft, M., F. Moritz, C. Weickhardt, and J. Grotemeyer, *Instrumental measures to enhance the mass resolution in matrix assisted laser desorption/ionization (MALDI) time-of-flight experiments: computational simulations and experimental observations.* International Journal of Mass Spectrometry and Ion Processes, 1997. 167-168: p. 661-674.

82. Coles, J.N. and M. Guilhaus, *Resolution limitations from detector pulse width and jitter in a linear orthogonal-acceleration time-of-flight mass spectrometer.* Journal of the American Society for Mass Spectrometry, 1994. 5(8): p. 772-778.

83. Fetterolf, D.D. and R.A. Yost, *Energy-resolved collision-induced dissociation in tandem mass spectrometry.* International Journal or Mass Spectrometry and Ion Physics, 1982. 44(1-2): p. 37-50.

84. Franzen, J., *Improved resolution for MALDI-TOF mass spectrometers: a mathematical study.* International Journal of Mass Spectrometry and Ion Processes, 1997. 164(1-2): p. 19-34.

85. Glish, G.L. and D.J. Burinsky, *Hybrid Mass Spectrometers for Tandem Mass Spectrometry.* Journal of the American Society for Mass Spectrometry, 2008. 19(2): p. 161-172.

86. Dawson, P.H., *Experimental measurements of quadrupole mass analyser performance and comparison with theoretical predictions.* International Journal or Mass Spectrometry and Ion Physics, 1976. 21(3-4): p. 317-332.

87. Dawson, P.H., *Quadrupole mass filters with bent or bowed rod sets.* International Journal of Mass Spectrometry and Ion Processes, 1988. 84(1-2): p. 185-201.

88. Dawson, P.H., *Performance of the quadrupole mass filter with separated RF and DC fringing fields.* International Journal or Mass Spectrometry and Ion Physics, 1977. 25(4): p. 375-392.

89. Dawson, P.H., *Performance characteristics of an r.f.-only quadrupole.* International Journal of Mass Spectrometry and Ion Processes, 1985. 67(3): p. 267-276.

90. Dawson, P.H., *Quadrupole mass filters with varying mathieu parameter.* International Journal of Mass Spectrometry and Ion Processes, 1988. 83(3): p. 295-309.

91. Wiley, W.C. and I.H. McLaren, *Time-of-Flight Mass Spectrometer with Improved Resolution.* Review of Scientific Instruments, 1955. 26(12): p. 1150-1157.

92. Wilson, D.B., *A time-of-flight mass spectrometer.* Vacuum, 1969. 19(7): p. 323-325.

93. Standing, K.G., *Timing the flight of biomolecules: a personal perspective.* International Journal of Mass Spectrometry, 2000. 200(1-3): p. 597-610.

94. Mamyrin, B.A., *Time-of-flight mass spectrometry (concepts, achievements, and prospects).* International Journal of Mass Spectrometry, 2001. 206(3): p. 251-266.

95. Mamyrin, B.A., *Laser assisted reflectron time-of-flight mass spectrometry.* International Journal of Mass Spectrometry and Ion Processes, 1994. 131: p. 1-19.

96. Price, D. and G.J. Milnes, *Recent developments in techniques utilising time-of-flight mass spectrometry.* International Journal of Mass Spectrometry and Ion Processes, 1984. 60(1): p. 61-81.

97. Bahr, U., J. Stahl-Zeng, E. Gleitsmann, and M. Karas, *Delayed extraction time-of-flight MALDI mass spectrometry of proteins above 25000 Da.* Journal of Mass Spectrometry, 1997. 32(10): p. 1111-1116.

98. Ole, N.J., P. Alexandre, and M. Matthias, *Delayed Extraction Improves Specificity in Database Searches by Matrix-assisted Laser Desorption/Ionization Peptide Maps.* Rapid Communications in Mass Spectrometry, 1996. 10(11): p. 1371-1378.

99. Vestal, M.L., P. Juhasz, and S.A. Martin, *Delayed extraction matrix-assisted laser desorption time-of-flight mass spectrometry.* Rapid Communications in Mass Spectrometry, 1995. 9(11): p. 1044-1050.

100. Chernushevich, I.V., A.V. Lododa, and B.A. Thomson, *An Introduction to quadrupole-time-of-flight mass spectrometry.* Journal of Mass Spectrometry, 2001. 36: p. 849-865.

101. Corr, J.J., P. Kovarik, B.B. Schneider, J. Hendrikse, A. Loboda, and T.R. Covey, *Design Considerations for High Speed Quantitative Mass Spectrometry with MALDI Ionization.* Journal of the American Society for Mass Spectrometry, 2006. 17(8): p. 1129-1141.

102. Caprioli, R.M., T.B. Farmer, and J. Gile, *Molecular Imaging of Biological Samples: Localization of Peptides and Proteins Using MALDI-TOF-MS.* Analytical Chemistry, 1997. 69(23): p. 4751-4760, .

103. Stoeckli, M., P. Chaurand, E. Hallahan, and R.M. Capriopli, *Imaging mass spectrometry: A new technology for the analysis of protein expressions in mammalian tissues.* Nature Medicine, 2001. 7(4).

104. Stoeckli, M., D. Staab, M. Staufenbiel, K. Wiederhold, and L. Signor, *Molecular imaging of amyloid β peptides in mouse brain sections using mass spectrometry.* Analytical Biochemistry, 2002. 311: p. 33-39.

105. Hsu, F. and J. Turk, *Electrospray Ionisation/Tandem Quadrupole Mass Spectrometric Studies on Phosphatidylcholines: The Fragmentation Processes.* Journal of the American Society for Mass Spectrometry, 2003. 14: p. 352-363.

106. Navas-Iglesias, N., A. Carrasco-Pancorbo, and L. Cuadros-Rodríguez, *From lipids analysis towards lipidomics, a new challenge for the analytical chemistry of the 21st century. Part II: Analytical lipidomics.* TrAC Trends in Analytical Chemistry, 2009. 28(4): p. 393-403.

107. Burnum, K.E., D.S. Cornett, S.M. Puolitaival, S.B. Milne, D.S. Myers, S. Tranguch, H.A. Brown, S.K. Dey, and R.M. Caprioli, *Spatial and temporal alterations of phospholipids determined by mass spectrometry during mouse embryo implantation.* J. Lipid Res., 2009. 50(11): p. 2290-2298.

108. Florent-Béchard, S., C. Desbène, P. Garcia, A. Allouche, I. Youssef, M.-C. Escanyé, V. Koziel, M. Hanse, C. Malaplate-Armand, C. Stenger, B. Kriem, F.T. Yen-Potin, J.L. Olivier, T. Pillot, and T. Oster, *The essential role of lipids in Alzheimer's disease.* Biochimie, 2009. 91(6): p. 804-809.

109. Fuchs, B., J. Schiller, R. Suss, M. Schurenberg, and D. Suckau, *A direct and simple method of coupling matrix-assisted laser desorption and ionization time-of-flight mass spectrometry (MALDI-TOF MS) to thin-layer chromatography (TLC) for the analysis of phospholipids from egg yolk.* Analytical and Bioanalytical Chemistry, 2007. 389(3): p. 827-834.

110. Fujiwaki, T., M. Tasaka, N. Takahashi, H. Kobayashi, Y. Murakami, T. Shimada, and S. Yamaguchi, *Quantitative evaluation of sphingolipids using delayed extraction matrix-assisted laser desorption ionization time-of-flight mass spectrometry with sphingosylphosphorylcholine as an internal standard: Practical application to cardiac valves from a patient with Fabry disease.* Journal of Chromatography B, 2006. 832(1): p. 97-102.

111. Gross, R.W. and X. Han, *Shotgun lipidomics of neutral lipids as an enabling technology for elucidation of lipid-related diseases.* Am J Physiol Endocrinol Metab, 2009. 297(2): p. E297-303.

112. Hsu, F.-F., A. Bohrer, and J. Turk, *Formation of Lithiated Adducts of Glycerophosphocholine Lipids Facilitates their Identification by Electrospray Ionization Tandem Mass Spectrometry.* Journal of the American Society for Mass Spectrometry, 1998. 9(5): p. 516-526.

113. Hsu, F.-F. and J. Turk, *Differentiation of 1-O-alk-1'-enyl-2-acyl and 1-O-alkyl-2-acyl Glycerophospholipids by Multiple-Stage Linear Ion-Trap Mass Spectrometry with Electrospray Ionization.* Journal of the American Society for Mass Spectrometry, 2007. 18(11): p. 2065-2073.

114. Hsu, F.-F. and J. Turk, *Electrospray ionization with low-energy collisionally activated dissociation tandem mass spectrometry of glycerophospholipids: Mechanisms of fragmentation and structural characterization.* Journal of Chromatography B, 2009. 877(26): p. 2673-2695.

115. Pittenauer, E. and G. Allmaier, *The Renaissance of High-Energy CID for Structural Elucidation of Complex Lipids: MALDI-TOF/RTOF-MS of Alkali Cationized Triacylglycerols.* Journal of the American Society for Mass Spectrometry, 2009. 20(6): p. 1037-1047.

116. Schiller, J., R. Sub, J. Arnhold, B. Fuchs, J. LeBig, M. Muller, M. Petkovic, H. Spalteholze, O. Zscornig, and K. Arnold, *Matrix-assisted laser desorption and ionisation time-of-flight (MALDI-TOF) mass spectrometry in lipid and phospholipids research.* Progress in Lipid Research, 2004. 43: p. 449-488.

117. Teuber, K., J. Schiller, B. Fuchs, M. Karas, and T.W. Jaskolla, *Significant sensitivity improvements by matrix optimization: a MALDI-TOF mass*

spectrometric study of lipids from hen egg yolk. Chemistry and Physics of Lipids, 2010. 163(6): p. 552-560.

118. Ivanova, P.T., S.B. Milne, D.S. Myers, and H.A. Brown, *Lipidomics: a mass spectrometry based systems level analysis of cellular lipids.* Current Opinion in Chemical Biology, 2009. 13(5-6): p. 526-531.

119. Ståhlman, M., C.S. Ejsing, K. Tarasov, J. Perman, J. Borén, and K. Ekroos, *High-throughput shotgun lipidomics by quadrupole time-of-flight mass spectrometry.* Journal of Chromatography B, 2009. 877(26): p. 2664-2672.

120. Balazy, M., P. Braquet, and N.G. Bazan, *Determination of platelet-activating factor and alkyl-ether phospholipids by gas chromatography-mass spectrometry via direct derivatization.* Analytical Biochemistry, 1991. 196(1): p. 1-10.

121. Mansson, J.-E., P. Fredman, O. Nilsson, L. Lindholm, J. Holmgren, and L. Svennerholm, *Chemical structure of carcinoma ganglioside antigens defined by monoclonal antibody C-50 and some allied gangliosides of human pancreatic adenocarcinoma.* Biochimica et Biophysica Acta (BBA) - Lipids and Lipid Metabolism, 1985. 834(1): p. 110-117.

122. Medina, I. and R. Sacchi, *Acyl stereospecific analysis of tuna phospholipids via high resolution 13C-NMR spectroscopy.* Chemistry and Physics of Lipids, 1994. 70(1): p. 53-61.

123. Szücs, R., K. Verleysen, G.S.M.J.E. Duchateau, P. Sandra, and B.G.M. Vandeginste, *Analysis of phospholipids in lecithins comparison between micellar electrokinetic chromatography and high-performance liquid chromatography.* Journal of Chromatography A, 1996. 738(1): p. 25-29.

124. Yandrasitz, J.R., G. Berry, and S. Segal, *High-performance liquid chromatography of phospholipids: Quantitation by phosphate analysis.* Analytical Biochemistry, 1983. 135(1): p. 239-243.

125. Minnikin, D.E., L. Kremer, L.G. Dover, and G.S. Besra, *The methyl-branched fortifications of Mycobacterium tuberculosis.* Chemistry & Biology, 2002. 9(5): p. 545-553.

126. Guianvarc'h, D., T. Drujon, T.E. Leang, F. Courtois, and O. Ploux, *Identification of new inhibitors of E. coli cyclopropane fatty acid synthase using a colorimetric assay.* Biochimica et Biophysica Acta (BBA) - Proteins & Proteomics, 2006. 1764(8): p. 1381-1388.

127. Cardona, P.J., C.Y. Soto, C. Martín, B. Giquel, G. Agustí, E. Guirado, T. Sirakova, P. Kolattukudy, E. Julián, and M. Luquin, *Neutral-red reaction is related to virulence and cell wall methyl-branched lipids in Mycobacterium tuberculosis.* Microbes and Infection, 2006. 8(1): p. 183-190.

128. Jackson, M., G. Stadthagen, and B. Gicquel, *Long-chain multiple methyl-branched fatty acid-containing lipids of Mycobacterium tuberculosis: Biosynthesis, transport, regulation and biological activities.* Tuberculosis, 2007. 87(2): p. 78-86.

129. Hartmann, S., D.E. Minnikin, H.J. Römming, M.S. Baird, C. Ratledge, and P.R. Wheeler, *Synthesis of methyl 3-(2-octadecylcyclopropen-1-yl)propanoate and methyl 3-(2-octadecylcyclopropen-1-yl)pentanoate and cyclopropane fatty acids as possible inhibitors of mycolic acid biosynthesis.* Chemistry and Physics of Lipids, 1994. 71(1): p. 99-108.

130. D.M, C., *Virulence factors of Mycobacterium bovis.* Tuberculosis, 2001. 81(1-2): p. 97-102.

131. Harland, C.W., D. Rabuka, C.R. Bertozzi, and R. Parthasarathy, *The Mycobacterium tuberculosis Virulence Factor Trehalose Dimycolate Imparts Desiccation Resistance to Model Mycobacterial Membranes.* Biophysical Journal, 2008. 94(12): p. 4718-4724.

132. Huet, G., P. Constant, W. Malaga, M.A. Laneelle, K. Kremer, D. Van Soolingen, M. Daffe, and C. Guilhot, *A Lipid Profile Typifies the Beijing Strains of Mycobacterium tuberculosis IDENTIFICATION OF A MUTATION RESPONSIBLE FOR A MODIFICATION OF THE STRUCTURES OF PHTHIOCEROL DIMYCOCEROSATES AND PHENOLIC GLYCOLIPIDS.* Journal of Biological Chemistry, 2009. 284(40): p. 27101-27113.

133. Kai, M., Y. Fujita, Y. Maeda, N. Nakata, S. Izumi, I. Yano, and M. Makino, *Identification of trehalose dimycolate (cord factor) in Mycobacterium leprae.* FEBS letters, 2007. 581(18): p. 3345-3350.

134. Laval, F., R. Haites, F. Movahedzadeh, A. Lemassu, C.Y. Wong, N. Stoker, H. Billman-Jacobe, and M. Daffe, *Investigating the function of the putative mycolic acid methyltransferase UmaA - Divergence between the Mycobacterium smegmatis and Mycobacterium tuberculosis proteins.* Journal of Biological Chemistry, 2008. 283(3): p. 1419-1427.

135. Perez, E., P. Constant, A. Lemassu, F. Laval, M. Daffe, and C. Guilhot, *Characterization of three glycosyltransferases involved in the biosynthesis of the phenolic glycolipid antigens from the Mycobacterium tuberculosis complex.* Journal of Biological Chemistry, 2004. 279(41): p. 42574-42583.

136. Sinsimer, D., G. Huet, C. Manca, L. Tsenova, M.S. Koo, N. Kurepina, B. Kana, B. Mathema, S.A. Marras, B.N. Kreiswirth, C. Guilhot, and G. Kaplan, *The phenolic glycolipid of Mycobacterium tuberculosis differentially modulates the early host*

cytokine response but does not in itself confer hypervirulence. Infection and Immunity, 2008. 76(7): p. 3027-36.

137. Torrelles, J.B. and L.S. Schlesinger, *Diversity in Mycobacterium tuberculosis mannosylated cell wall determinants impacts adaptation to the host.* Tuberculosis, 2010. 90(2): p. 84-93.

138. Wang, Z., U. Schwab, E. Rhoades, P.R. Chess, D.G. Russell, and R.H. Notter, *Peripheral cell wall lipids of Mycobacterium tuberculosis are inhibitory to surfactant function.* Tuberculosis, 2008. 88(3): p. 178-186.

139. Watanabe, M., I. Honda, K. Kawajiri, S. Niinuma, S. Kudoh, and D.E. Minnikin, *Distribution of antibody titres against phenolic glycolipids from Mycobacterium tuberculosis in the sera from tuberculosis patients and healthy controls.* Research in Microbiology, 1995. 146(9): p. 791-797.

140. Wolf, C. and P.J. Quinn, *Lipidomics: Practical aspects and applications.* Progress in Lipid Research, 2008. 47(1): p. 15-36.

141. Hermansson, M., K. Hokynar, and P. Somerharju, *Mechanisms of glycerophospholipid homeostasis in mammalian cells.* Progress in Lipid Research, 2011. 50(3): p. 240-257.

142. Fahy, E., S. Subramaniam, H.A. Brown, C.K. Glass, A.H. Merrill, Jr., R.C. Murphy, C.R.H. Raetz, D.W. Russell, Y. Seyama, W. Shaw, T. Shimizu, F. Spener, G. van Meer, M.S. VanNieuwenhze, S.H. White, J.L. Witztum, and E.A. Dennis, *A comprehensive classification system for lipids.* J. Lipid Res., 2005. 46(5): p. 839-862.

143. Singer, S.J. and G.L. Nicolson, *The Fluid Mosaic Model of the Structure of Cell Membranes.* Science, 1972. 175(4023): p. 720-731.

144. Cunnane, S.C., M. Plourde, F. Pifferi, M. Bégin, C. Féart, and P. Barberger-Gateau, *Fish, docosahexaenoic acid and Alzheimer's disease.* Progress in Lipid Research, 2009. 48(5): p. 239-256.

145. Gorjão, R., A.K. Azevedo-Martins, H.G. Rodrigues, F. Abdulkader, M. Arcisio-Miranda, J. Procopio, and R. Curi, *Comparative effects of DHA and EPA on cell function.* Pharmacology & Therapeutics, 2009. 122(1): p. 56-64.

146. Huwiler, A. and J. Pfeilschifter, *Lipids as targets for novel anti-inflammatory therapies.* Pharmacology & Therapeutics, 2009. 124(1): p. 96-112.

147. Beel, A.J., M. Sakakura, P.J. Barrett, and C.R. Sanders, *Direct binding of cholesterol to the amyloid precursor protein: An important interaction in lipid–Alzheimer's disease relationships?* Biochimica et Biophysica Acta (BBA) - Molecular and Cell Biology of Lipids, 2010. 1801(8): p. 975-982.

148. Fathi, R., N. Isbel, L. Short, B. Haluska, D. Johnson, and T.H. Marwick, *The effect of long-term aggressive lipid lowering on ischemic and atherosclerotic burden in patients with chronic kidney disease.* American Journal of Kidney Diseases, 2004. 43(1): p. 45-52.

149. Kawata, S., A. Chitranukroh, J.S. Owen, and N. McIntyre, *Membrane lipid changes in erythrocytes, liver and kidney in acute and chronic experimental liver disease in rats.* Biochimica et Biophysica Acta (BBA) - Biomembranes, 1987. 896(1): p. 26-34.

150. Montine, T.J., M.D. Neely, J.F. Quinn, M.F. Beal, W.R. Markesbery, L.J. Roberts Ii, and J.D. Morrow, *Lipid peroxidation in aging brain and Alzheimer's disease.* Free Radical Biology and Medicine, 2002. 33(5): p. 620-626.

151. Tanea T, R., *Lipid peroxidation and neurodegenerative disease.* Free Radical Biology and Medicine, 2011. 51(7): p. 1302-1319.

152. Vered, A., M. Eugenio, D. Arie, P. Augusto, M. Sergio, and G. Shimon, *Fluorescence-based diagnosis of lipid storage diseases by analysis of the culture medium of skin fibroblasts.* Clinica Chimica Acta, 1993. 218(2): p. 139-147.

153. Williams, M.L., R.A. Coleman, D. Placezk, and C. Grunfeld, *Neutral lipid storage disease: a possible functional defect in phospholipid-linked triacylglycerol metabolism.* Biochimica et Biophysica Acta (BBA) - Molecular Basis of Disease, 1991. 1096(2): p. 162-169.

154. Xianlin, H., *Multi-dimensional mass spectrometry-based shotgun lipidomics and the altered lipids at the mild cognitive impairment stage of Alzheimer's disease.* Biochimica et Biophysica Acta (BBA) - Molecular and Cell Biology of Lipids, 2010. 1801(8): p. 774-783.

155. Garrett, T.J., M.C. Prieto-Conaway, V. Kovtoun, H. Bui, N. Izgarian, G. Stafford, and R.A. Yost, *Imaging of small molecules in tissue sections with a new intermediate-pressure MALDI linear ion trap mass spectrometer.* International Journal of Mass Spectrometry, 2007. 260(2-3): p. 166-176.

156. Jackson, S., M. Ugarov, T. Egan, J. Post, D. Langlais, J. Albert Schultz, and A. Woods, *MALDI ion mobility TOFMS imaging of lipids in rat brain tissue.* Journal of Mass Spectrometry, 2007. 42(8): p. 1093-1098.

157. Shimma, S., Y. Sugiura, T. Hayasaka, N. Zaima, M. Matsumoto, and M. Setou, *Mass imaging and identification of biomolecules with MALDI-QIT-TOF-based system.* Anal. Chem, 2008. 80(3): p. 878-885.

158. Caprioli, R.M., M.R. Groseclose, M. Andersson, and W.M. Hardesty, *Identification of proteins directly from tissue: in situ tryptic digestions coupled with imaging mass spectrometry.* Journal of Mass Spectrometry, 2007. 42(2): p. 254-262.

159. Caprioli, R.M., S. Khatib-Shahidi, M. Andersson, J.L. Herman, and T.A. Gillespie, *Direct molecular analysis of whole-body animal tissue sections by imaging MALDI mass spectrometry.* Analytical chemistry, 2006. 78(18): p. 6448-6456.

160. Reyzer, M.L., Y. Hsieh, K. Ng, W.A. Korfmacher, and R.M. Caprioli, *Direct analysis of drug candidates in tissue by matrix-assisted laser desoption/ionisation mass spectrometry.* Journal of Mass Spectrometry, 2003. 38(10): p. 1082-1092.

161. Rubakhin, S.S., J.C. Jurchen, E.B. Monroe, and J.V. Sweedler, *Imaging mass spectrometry: fundamentals and applications to drug discovery.* Drug Discovery Today, 2005. 10(12): p. 823-837.

162. Stauber, J., R. Lemaire, J. Franck, D. Bonnel, D. Croix, R. Day, M. Wisztorski, I. Fournier, and M. Salzet, *MALDI Imaging of Formalin-Fixed Paraffin-Embedded Tissues: Application to Model Animals of Parkinson Disease for Biomarker Hunting.* Journal of Proteome Research, 2008. 7(3): p. 969-978.

163. Touboul, D., S. Roy, D.P. Germain, P. Chaminade, A. Brunelle, and O. Laprévote, *MALDI-TOF and cluster-TOF-SIMS imaging of Fabry disease biomarkers.* International Journal of Mass Spectrometry, 2007. 260(2-3): p. 158-165.

164. Chen, Y., J. Allegood, Y. Liu, E. Wang, B. Cachon-Gonzalez, T.M. Cox, A.H. Merrill, and M.C. Sullards, *Imaging MALDI Mass Spectrometry Using an Oscillating Capillary Nebulizer Matrix Coating System and Its Application to Analysis of Lipids in Brain from a Mouse Model of Tay−Sachs/Sandhoff Disease.* Analytical Chemistry, 2008. 80(8): p. 2780-2788.

165. Wang, H.-Y.J., S.N.J.J. Post, and A.S. Woods, *A minimalist approach to MALDI imaging of glycerophospholipids and sphingolipids in rat brain sections.* International Journal of Mass Spectrometry, 2008. 278(2-3): p. 143-149.

166. Puolitaival, S.M., K.E. Burnum, D.S. Cornett, and R.M. Caprioli, *Solvent-Free Matrix Dry-Coating for MALDI Imaging of Phospholipids.* Journal of the American Society for Mass Spectrometry, 2008. 19(6): p. 882-886.

167. Hsu, F.-F. and J. Turk, *Structural characterization of triacylglycerols as lithiated adducts by electrospray ionization mass spectrometry using low-energy collisionally activated dissociation on a triple stage quadrupole instrument.* Journal of the American Society for Mass Spectrometry, 1999. 10(7): p. 587-599.

168. Dogruel, D., R.W. Nelson, and P. Williams, *The Effects of Matrix pH and Cation Availability on the Matrix-assisted Laser Desorption/Ionization Mass Spectrometry of Poly(methyl methacrylate).* Rapid Communications in Mass Spectrometry, 1996. 10(7): p. 801-804.

169. Scrivens, J.H., A.T. Jackson, H.T. Yates, M.R. Green, G. Critchley, J. Brown, R.H. Bateman, M.T. Bowers, and J. Gidden, *The effect of the variation of cation in the matrix-assisted laser desorption/ionisation-collision induced dissociation (MALDI-CID) spectra of oligomeric systems.* International Journal of Mass Spectrometry and Ion Processes, 1997. 165-166(0): p. 363-375.

170. Benard, S., J. Arnhold, M. Lehnert, J. Schiller, and K. Arnold, *Experiments towards quantification of saturated and polyunsaturated diacylglycerols by matrix-assisted laser desorption and ionization time-of-flight mass spectrometry.* Chemistry and Physics of Lipids, 1999. 100(1-2): p. 115-125.

171. Sugiura, Y., Y. Konishi, N. Zaima, S. Kajihara, H. Nakanishi, R. Taguchi, and M. Setou, *Visualization of the cell-selective distribution of PUFA-containing phosphatidylcholines in mouse brain by imaging mass spectrometry.* J. Lipid Res., 2009. 50(9): p. 1776-1788.

172. Shanta, S.R., L.-H. Zhou, Y.S. Park, Y.H. Kim, Y. Kim, and K.P. Kim, *Binary Matrix for MALDI Imaging Mass Spectrometry of Phospholipids in Both Ion Modes.* Analytical Chemistry, 2011. 83(4): p. 1252-1259.

173. Berry, K.A.Z., B. Li, S.D. Reynolds, R.M. Barkley, M.A. Gijón, J.A. Hankin, P.M. Henson, and R.C. Murphy, *MALDI imaging MS of phospholipids in the mouse lung.* Journal of lipid research, 2011. 52(8): p. 1551-1560.

174. Kobayashi, Y., T. Hayasaka, M. Setou, H. Itoh, and N. Kanayama, *Comparison of Phospholipid Molecular Species between Terminal and Stem Villi of Human Term Placenta by Imaging Mass Spectrometry.* Placenta, 2010. 31(3): p. 245-248.

175. Miyamura, N., T. Nakamura, N. Goto-Inoue, N. Zaima, T. Hayasaka, T. Yamasaki, S. Terai, I. Sakaida, M. Setou, and H. Nishina, *Imaging mass spectrometry reveals characteristic changes in triglyceride and phospholipid species in regenerating mouse liver.* Biochemical and Biophysical Research Communications, 2011. 408(1): p. 120-125.

176. Shimma, S., Y. Sugiura, T. Hayasaka, Y. Hoshikawa, T. Noda, and M. Setou, *MALDI-based imaging mass spectrometry revealed abnormal distribution of phospholipids in colon cancer liver metastasis.* Journal of Chromatography B, 2007. 855(1): p. 98-103.

177. Kaneko, Y., Y. Obata, T. Nishino, H. Kakeya, Y. Miyazaki, T. Hayasaka, M. Setou, A. Furusu, and S. Kohno, *Imaging mass spectrometry analysis reveals an altered lipid distribution pattern in the tubular areas of hyper-IgA murine kidneys.* Experimental and Molecular Pathology, 2011. 91(2): p. 614-621.

178. Koizumi, S., S. Yamamoto, T. Hayasaka, Y. Konishi, M. Yamaguchi-Okada, N. Goto-Inoue, Y. Sugiura, M. Setou, and H. Namba, *Imaging mass spectrometry*

revealed the production of lyso-phosphatidylcholine in the injured ischemic rat brain. Neuroscience, 2010. 168(1): p. 219-225.

179. Hankin, J., S. Farias, R. Barkley, K. Heidenreich, L. Frey, K. Hamazaki, H.-Y. Kim, and R. Murphy, *MALDI Mass Spectrometric Imaging of Lipids in Rat Brain Injury Models.* Journal of the American Society for Mass Spectrometry, 2011. 22(6): p. 1014-1021.

180. www.who.int/topics/tuberculosis/en/.

181. Daffé, M. and P. Draper, *The Envelope Layers of Mycobacteria with Reference to their Pathogenicity.* Advances in Microbial Physiology, 1997. Volume 39: p. 131-203.

182. Brennan, P.J., *Structure, function, and biogenesis of the cell wall of Mycobacterium tuberculosis.* Tuberculosis, 2003. 83(1-3): p. 91-97.

183. Andersen, C.S., E.M. Agger, I. Rosenkrands, J.M. Gomes, V. Bhowruth, K.J.C. Gibson, R.V. Petersen, D.E. Minnikin, G.S. Besra, and P. Andersen, *A Simple Mycobacterial Monomycolated Glycerol Lipid Has Potent Immunostimulatory Activity.* Journal of Immunology, 2009. 182(1): p. 424-432.

184. Asselineau, C., J. Asselineau, G. Laneelle, and M.A. Laneelle, *The biosynthesis of mycolic acids by Mycobacteria: current and alternative hypotheses.* Progress in Lipid Research, 2002. 41(6): p. 501-523.

185. Barkan, D., Z. Liu, J.C. Sacchettini, and M.S. Glickman, *Mycolic Acid Cyclopropanation is Essential for Viability, Drug Resistance, and Cell Wall Integrity of Mycobacterium tuberculosis.* Chemistry & Biology, 2009. 16(5): p. 499-509.

186. Lea-Smith, D.J., J.S. Pyke, D. Tull, M.J. McConville, R.L. Coppel, and P.K. Crellin, *The reductase that catalyzes mycolic motif synthesis is required for*

efficient attachment of mycolic acids to arabinogalactan. Journal of Biological Chemistry, 2007. 282(15): p. 11000-11008.

187. Minnikin, D.E., M. Ridell, J.H. Parlett, and R.C. Bolton, *Direct Detection of Mycobacterium-Tuberculosis Lipid Antigens by Thin-Layer Chromatography.* Fems Microbiology Letters, 1987. 48(1-2): p. 175-177.

188. Watanabe, M., Y. Aoyagi, H. Mitome, T. Fujita, H. Naoki, M. Ridell, and D.E. Minnikin, *Location of functional groups in mycobacterial meromycolate chains; the recognition of new structural principles in mycolic acids.* Microbiology-Sgm, 2002. 148: p. 1881-1902.

189. Beukes, M., Y. Lemmer, M. Deysel, R.A.D. Juma'a, S.B. Mark, G. Koza, M.I. Maximiliano, R.R. Richard, C. Theunissen, J. Grooten, G. Toschi, V.R. Vanessa, L. Pilcher, S. Van Wyngaardt, N. Mathebula, M. Balogun, C.S. Anton, and J.A. Verschoor, *Structure-function relationships of the antigenicity of mycolic acids in tuberculosis patients.* Chemistry and Physics of Lipids, 2010. 163(8): p. 800-808.

190. Minnikin, D.E., R.C. Bolton, S. Hartmann, G.S. Besra, P.A. Jenkins, A.I. Mallet, E. Wilkins, A.M. Lawson, and M. Ridell, *An Integrated Procedure for the Direct-Detection of Characteristic Lipids in Tuberculosis Patients.* Annales De La Societe Belge De Medecine Tropicale, 1993. 73: p. 13-24.

191. Minnikin, D.E., O.Y.C. Lee, M. Pitts, M.S. Baird, and G.S. Besra, *Essentials in the use of mycolic acid biomarkers for tuberculosis detection: response to "High-throughput mass spectrometric analysis of 1400-year-old mycolic acids as biomarkers for ancient tuberculosis infection" by Mark et al., 2010.* Journal of Archaeological Science, 2010. 37(10): p. 2407-2412.

192. Rafidinarivo, E., M.A. Laneelle, H. Montrozier, P. Valero-Guillen, J. Astola, M. Luquin, J.C. Prome, and M. Daffe, *Trafficking pathways of mycolic acids:*

structures, origin, mechanism of formation, and storage form of mycobacteric acids. Journal of lipid research, 2009. 50(3): p. 477-490.

193. Laval, F., M.-A. Lanéelle, C. Déon, B. Monsarrat, and M. Daffé, *Accurate Molecular Mass Determination of Mycolic Acids by MALDI-TOF Mass Spectrometry.* Analytical Chemistry, 2001. 73(18): p. 4537-4544.

194. Uenishi, Y., Y. Fujita, N. Kusunose, I. Yano, and M. Sunagawa, *Comprehensive analysis of mycolic acid subclass and molecular species composition of Mycobacterium bovis BCG Tokyo 172 cell wall skeleton (SMP-105).* Journal of Microbiological Methods, 2008. 72(2): p. 149-156.

195. Watanabe, M., Y. Aoyagi, M. Ridell, and D.E. Minnikin, *Separation and characterization of individual mycolic acids in representative mycobacteria.* Microbiology-Sgm, 2001. 147: p. 1825-1837.

196. Fujita, Y., T. Naka, T. Doi, and I. Yano, *Direct molecular mass determination of trehalose monomycolate from 11 species of mycobacteria by MALDI-TOF mass spectrometry.* Microbiology-Sgm, 2005. 151: p. 1443-1452.

197. Fujita, Y., T. Naka, M.R. McNeil, and I. Yano, *Intact molecular characterization of cord factor (trehalose 6,6 '-dimycolate) from nine species of mycobacteria by MALDI-TOF mass spectrometry.* Microbiology-Sgm, 2005. 151: p. 3403-3416.

198. Alahari, A., L. Alibaud, X. Trivelli, R. Gupta, G. Lamichhane, R.C. Reynolds, W.R. Bishai, Y. Guerardel, and L. Kremer, *Mycolic acid methyltransferase, MmaA4, is necessary for thiacetazone susceptibility in Mycobacterium tuberculosis.* Molecular Microbiology, 2009. 71(5): p. 1263-1277.

199. Perez, E., P. Constant, F. Laval, A. Lemassu, M.A. Laneelle, M. Daffe, and C. Guilhot, *Molecular dissection of the role of two methyltransferases in the biosynthesis of phenolglycolipids and phthiocerol dimycoserosate in the*

Mycobacterium tuberculosis complex. Journal of Biological Chemistry, 2004. 279(41): p. 42584-42592.

200. Simeone, R., P. Constant, W. Malaga, C. Guilhot, M. Daffe, and C. Chalut, *Molecular dissection of the biosynthetic relationship between phthiocerol and phthiodiolone dimycocerosates and their critical role in the virulence and permeability of Mycobacterium tuberculosis.* Febs Journal, 2007. 274(8): p. 1957-1969.

201. Simeone, R., M. Leger, P. Constant, W. Malaga, H. Marrakchi, M. Daffe, C. Guilhot, and C. Chalut, *Delineation of the roles of FadD22, FadD26 and FadD29 in the biosynthesis of phthiocerol dimycocerosates and related compounds in Mycobacterium tuberculosis.* Febs Journal, 2010. 277(12): p. 2715-2725.

202. Chaurand, P., D.S. Cornett, and R.M. Caprioli, *Molecular imaging of thin mammalian tissue sections by mass spectrometry.* Current Opinion in Biotechnology, 2006. 17(4): p. 431-436.

203. Cornett, D.S., M.L. Reyzer, P. Chaurand, and R.M. Caprioli, *MALDI imaging mass spectrometry: molecular snapshots of biochemical systems.* Nature Methods, 2007. 4(10): p. 828-833.

204. Walch, A., S. Rauser, S.-O. Deininger, and H. Hofler, *MALDI imaging mass spectrometry for direct tissue analysis: a new frontier for molecular histology.* 2008, Journal of Histochem Cell Biology. p. 421-434.

205. Astigarraga, E., G. Barreda-GoÌ mez, L. Lombardero, O. Fresnedo, F. CastanÌƒo, M.a.T. Giralt, B. Ochoa, R. RodriÌ• guez-Puertas, and J.A. FernaÌ• ndez, *Profiling and Imaging of Lipids on Brain and Liver Tissue by Matrix-Assisted Laser Desorption/Ionization Mass Spectrometry Using 2-Mercaptobenzothiazole as a Matrix.* Analytical Chemistry, 2008. 80(23): p. 9105-9114.

206. Bird, G.H., A.R. Lajmi, and J.A. Shin, *Manipulation of temperature to improve solubility of hydrophobic proteins and cocrystallization with matrix for analysis by MALDI-TOF mass spectrometry.* Analytical chemistry, 2002. 74(1): p. 219-225.

207. Cohen, S.L. and B.T. Chait, *Influence of matrix solution conditions on the MALDI-MS analysis of peptides and proteins.* Analytical chemistry, 1996. 68(1): p. 31-37.

208. Distler, A. and J. Allison, *Improved MALDI-MS analysis of oligonucleotides through the use of fucose as a matrix additive.* Anal. Chem, 2001. 73(20): p. 5000-5003.

209. Domin, M.A., K.J. Welham, and D.S. Ashton, *The effect of solvent and matrix combinations on the analysis of bacteria by matrix-assisted laser desorption/ionisation time-of-flight mass spectrometry.* Rapid Communications in Mass Spectrometry, 1999. 13(4): p. 222-226.

210. Fuchs, B. and J. Schiller, *Recent developments of useful MALDI matrices for the mass spectrometric characterization of apolar compounds.* Current Organic Chemistry, 2009. 13(16): p. 1664-1681.

211. Jens Soltwisch, S.B.K.D., *A binary matrix of 2,5-dihydroxybenzoic acid and glycerol produces homogenous sample preparations for matrix-assisted laser desorption/ionization mass spectrometry.* Rapid Communications in Mass Spectrometry, 2008. 22(1): p. 59-66.

212. Ceuppens, R., D. Dumont, L. Van Brussel, B. Van de Plas, R. Daniels, J.-P. Noben, P. Verhaert, E. Van der Gucht, J. Robben, S. Clerens, and L. Arckens, *Direct profiling of myelinated and demyelinated regions in mouse brain by imaging mass spectrometry.* International Journal of Mass Spectrometry, 2007. 260(2-3): p. 185-194.

213. Chan, K., P. Lanthier, X. Liu, J.K. Sandhu, D. Stanimirovic, and J. Li, *MALDI mass spectrometry imaging of gangliosides in mouse brain using ionic liquid matrix.* Analytica Chimica Acta, 2009. 639(1-2): p. 57-61.

214. Drexler, D.M., T.J. Garrett, J.L. Cantone, R.W. Diters, J.G. Mitroka, M.C. Prieto Conaway, S.P. Adams, R.A. Yost, and M. Sanders, *Utility of imaging mass spectrometry (IMS) by matrix-assisted laser desorption ionization (MALDI) on an ion trap mass spectrometer in the analysis of drugs and metabolites in biological tissues.* Journal of Pharmacological and Toxicological Methods, 2007. 55(3): p. 279-288.

215. Grey, A.C., A.K. Gelasco, J. Section, R.A. Moreno-Rodriguez, E.L. Krug, and K.L. Schey, *Molecular Morphology of the Chick Heart Visualized by MALDI Imaging Mass Spectrometry.* The Anatomical Record: Advances in Integrative Anatomy and Evolutionary Biology, 2010. 293(5): p. 821-828.

216. Laurens Minerva, S.C.G.B.L.A., *Direct profiling and identification of peptide expression differences in the pancreas of control and ob/ob mice by imaging mass spectrometry.* PROTEOMICS, 2008. 8(18): p. 3763-3774.

217. Prideaux, B., S.J. Atkinson, V.A. Carolan, J. Morton, and M.R. Clench, *Sample preparation and data interpretation procedures for the examination of xenobiotic compounds in skin by indirect imaging MALDI-MS.* International Journal of Mass Spectrometry, 2007. 260(2-3): p. 243-251.

218. Schwamborn, K. and R.M. Caprioli, *MALDI Imaging Mass Spectrometry - Painting Molecular Pictures.* Molecular Oncology, 2010. 4(6): p. 529-538.

219. Stoeckli, M., R. Knochenmuss, G. McCombie, D. Mueller, T. Rohner, D. Staab, K. Wiederhold, and W. Indu Kheterpal and Ronald, *MALDI MS Imaging of Amyloid*, in *Methods in Enzymology*. 2006, Academic Press. p. 94-106.

220. Taban, I.M., A.F.M. Altelaar, Y.E.M. van der Burgt, L.A. McDonnell, R.M.A. Heeren, J. Fuchser, and G. Baykut, *Imaging of Peptides in the Rat Brain Using MALDI-FTICR Mass Spectrometry.* Journal of the American Society for Mass Spectrometry, 2007. 18(1): p. 145-151.

221. Tanaka, H., N. Zaima, N. Yamamoto, D. Sagara, M. Suzuki, M. Nishiyama, Y. Mano, M. Sano, T. Hayasaka, N. Goto-Inoue, T. Sasaki, H. Konno, N. Unno, and M. Setou, *Imaging Mass Spectrometry Reveals Unique Lipid Distribution in Primary Varicose Veins.* European Journal of Vascular and Endovascular Surgery, 2010. 40(5): p. 657-663.

222. Valdes-Gonzalez, T., W. Hirano, H. Ishiyama, and T. Taki, *Scanning analysis of human brain ganglioside molecular species by a combination of TLC-Blot and MALDI-TOF MS.* Journal of Neurochemistry, 2010. 113: p. 29-30.

223. Verhaert, P.D., M.C.P. Conaway, T.M. Pekar, and K. Miller, *Neuropeptide imaging on an LTQ with vMALDI source: The complete [`]all-in-one' peptidome analysis.* International Journal of Mass Spectrometry, 2007. 260(2-3): p. 177-184.

224. Zaima, N., T. Hayasaka, N. Goto-Inoue, and M. Setou, *Imaging of metabolites by MALDI mass spectrometry.* Journal of Oleo Science, 2009. 58(8): p. 415-419.

225. Chaurand, P., S.A. Schwartz, and R.M. Caprioli, *Imaging mass spectrometry: a new tool to investigate the spatial organization of peptides and proteins in mammalian tissue sections.* Current Opinion in Chemical Biology, 2002. 6(5): p. 676-681.

226. Chaurand, P., J.L. Norris, D.S. Cornett, J.A. Mobley, and R.M. Caprioli, *New Developments in Profiling and Imaging of Proteins from Tissue Sections by MALDI Mass Spectrometry.* Journal of Proteome Research, 2006. 5(11): p. 2889-2900.

227. Sugiura, Y., S. Shimma, and M. Setou, *Thin Sectioning Improves the Peak Intensity and Signal-to-Noise Ratio in Direct Tissue Mass Spectrometry.* Journal of Mass Spectrometry. Soc. Jpn, 2006. 54(2): p. 45-48.

228. Crossman, L., N.A. McHugh, Y. Hsieh, W.A. Korfmacher, and J. Chen, *Investigation of the profiling depth in matrix-assisted laser desorption/ionization imaging mass spectrometry.* Rapid Communications in Mass Spectrometry, 2006. 20: p. 284-290.

229. Hsieh, Y., R. Casale, E. Fukuda, J. Chen, I. Knemeyer, J. Wingate, R. Morrison, and W. Korfmacher, *Matrix-assisted laser desorption/ionization imaging mass spectrometry for direct measurement of clozapine in rat brain tissue.* Rapid Communications in Mass Spectrometry, 2006. 20: p. 965-972.

230. Murphy, R.C., J.A. Hankin, and R.M. Barkley, *Imaging of lipid species by MALDI mass spectrometry.* J. Lipid Res., 2009. 50(Supplement): p. S317-322.

231. Yuki, S. and S. Mitsutoshi, *Selective imaging of positively charged polar and nonpolar lipids by optimizing matrix solution composition.* Rapid Communications in Mass Spectrometry, 2009. 23(20): p. 3269-3278.

232. Jackson, S.N., M. Ugarov, J.D. Post, T. Egan, D. Langlais, J.A. Schultz, and A.S. Woods, *A Study of Phospholipids by Ion Mobility TOFMS.* Journal of the American Society for Mass Spectrometry, 2008. 19(11): p. 1655-1662.

233. Jackson, S.N. and A.S. Woods, *Direct profiling of tissue lipids by MALDI-TOFMS.* Journal of Chromatography B, 2009. 877(26): p. 2822-2829.

234. Folch, J., M. Lees, and G.H.S. Stanley, *A Simple Method for the Isolation and Purification of Total Lipides from Animal Tissues.* Journal of Biological Chemistry, 1957. 226(1): p. 497-509.

235. Stubiger, G., E. Pittenauer, and G. Allmaier, *MALDI seamless postsource decay fragment ion analysis of sodiated and lithiated phospholipids.* Anal. Chem, 2008. 80(5): p. 1664-1678.

236. Vér, Á., P. Csermely, T. Bányász, T. Kovács, and J. Somogyi, *Alterations in the properties and isoform ratios of brain Na+/K+-ATPase in streptozotocin diabetic rats.* Biochimica et Biophysica Acta (BBA) - Biomembranes, 1995. 1237(2): p. 143-150.

237. Balluff, B., C. Schöne, H. Höfler, and A. Walch, *MALDI imaging mass spectrometry for direct tissue analysis: technological advancements and recent applications.* Histochemistry and Cell Biology, 2011. 136(3): p. 227-244.

238. Baluya, D.L., T.J. Garrett, and R.A. Yost, *Automated MALDI Matrix Deposition Method with Inkjet Printing for Imaging Mass Spectrometry.* Analytical Chemistry, 2007. 79(17): p. 6862-6867.

239. Heeren, R.M.A., *MALDI Techniques in Mass Spectrometry Imaging*, in *Encyclopedia of Spectroscopy and Spectrometry*, C. Editor in, xA, and L. John, Editors. 2010, Academic Press: Oxford. p. 1443-1451.

240. Franck, J., K. Arafah, A. Barnes, M. Wisztorski, M. Salzet, and I. Fournier, *Improving Tissue Preparation for Matrix-Assisted Laser Desorption Ionization Mass Spectrometry Imaging. Part 1: Using Microspotting.* Analytical Chemistry, 2009. 81(19): p. 8193-8202.

241. Leap, T., *Optimization of Automated Matrix Spraying for MALDI Imaging.* LEAP Technologies, Inc.Technical Note, 2007.

242. Bruker, D., *Comprehensive and Reliable Tissue Sample Preparation for MALDI Imaging.* Bruker Daltonics Inc., 2008.

243. Franck, J., M. Wisztorski, J. Stauber, M. Elayed, M. Salzet, and I. Fournier, *Shimadzu CHIP-1000 for clinical tissue application in MALDI imaging.* Shimazdu Application Note, 2007.

244. Végvári, Á., T.E. Fehniger, L. Gustavsson, A. Nilsson, P.E. Andrén, K. Kenne, J. Nilsson, T. Laurell, and G. Marko-Varga, *Essential tactics of tissue preparation and matrix nano-spotting for successful compound imaging mass spectrometry.* Journal of Proteomics, 2010. 73(6): p. 1270-1278.

245. Baluya, D., T. Garrett, and R. Yost, *Automated MALDI matrix deposition method with inkjet printing for imaging mass spectrometry.* Anal. Chem, 2007. 79(17): p. 6862-6867.

246. Caprioli, R.M., M. Andersson, M.R. Groseclose, and A.Y. Deutch, *Imaging mass spectrometry of proteins and peptides: 3D volume reconstruction.* Nature Methods, 2008. 5(1): p. 101-108.

247. Jurchen, J.C., S.S. Rubakhin, and J.V. Sweedler, *MALDI-MS Imaging of Features Smaller than the Size of the Laser Beam.* Journal of the American Society for Mass Spectrometry, 2005. 16(10): p. 1654-1659.

248. Lagarrigue, M., M. Becker, R. Lavigne, S.O. Deininger, A. Walch, F. Aubry, D. Suckau, and C. Pineau, *Revisiting Rat Spermatogenesis with MALDI Imaging at 20-mu m Resolution.* Molecular & Cellular Proteomics, 2011. 10(3).

249. Kaletaş, B.K., I.M. van der Wiel, J. Stauber, J.D. Lennard, C. Güzel, J.M. Kros, T.M. Luider, and R.M.A. Heeren, *Sample preparation issues for tissue imaging by imaging MS.* PROTEOMICS, 2009. 9(10): p. 2622-2633.

250. Jun, J.H., Z. Song, Z. Liu, B.J. Nikolau, E.S. Yeung, and Y.J. Lee, *High-Spatial and High-Mass Resolution Imaging of Surface Metabolites of Arabidopsis thaliana*

by Laser Desorption-Ionization Mass Spectrometry Using Colloidal Silver. Analytical chemistry, 2010. 82(8): p. 3255-3265.

251. Passarelli, M.K. and N. Winograd, *Characterizing in situ Glycerophospholipids with SIMS and MALDI Methodologies.* Surface and Interface Analysis, 2011. 43(1-2): p. 269-271.

252. Norris, J.L., D.S. Cornett, J.A. Mobley, M. Andersson, E.H. Seeley, P. Chaurand, and R.M. Caprioli, *Processing MALDI mass spectra to improve mass spectral direct tissue analysis.* International Journal of Mass Spectrometry, 2007. 260(2-3): p. 212-221.

253. Stoeckli, M., D. Staab, and A. Schweitzer, *Compound and metabolite distribution measured by MALDI mass spectrometric imaging in whole-body tissue sections.* International Journal of Mass Spectrometry, 2007. 260(2-3): p. 195-202.

254. Cooks, R.G., N.E. Manicke, J.M. Wiseman, and D.R. Ifa, *Desorption electrospray ionization (DESI) mass Spectrometry and tandem mass spectrometry (MS/MS) of phospholipids and sphingolipids: Ionization, adduct formation, and fragmentation.* Journal of the American Society for Mass Spectrometry, 2008. 19(4): p. 531-543.

255. Yamada, Y., K. Hidefumi, H. Shion, M. Oshikata, and Y. Haramaki, *Distribution of chloroquine in ocular tissue of pigmented rat using matrix-assisted laser desorption/ionization imaging quadrupole time-of-flight tandem mass spectrometry.* Rapid Communications in Mass Spectrometry, 2011. 25(11): p. 1600-1608.

256. Klöppel, G., *Tumour biology and histopathology of neuroendocrine tumours.* Best Practice & Research Clinical Endocrinology & Metabolism, 2007. 21(1): p. 15-31.

257. Pileri, S.A., E. Sabattini, C. Agostinelli, L. Bodega, M. Rossi, P.L. Zinzani, and T. Marafioti, *Histopathology of B-cell chronic lymphocytic leukemia.* Hematology/Oncology Clinics of North America, 2004. 18(4): p. 807-826.

258. Allred, D.C. and S. Moshin, *The Assessment of Hormone Receptors in Breast Cancer by Immunohistochemistry.* Seminars in Breast Disease: Radiologic, Pathologic and Surgical Considerations, 2005. 8(2): p. 57-61.

259. Giordano, G., *Value of immunohistochemistry in uterine pathology: Common and rare diagnostic dilemmas.* Pathology - Research and Practice, 2009. 205(10): p. 663-676.

260. Benabdellah, F., H. Yu, A. Brunelle, O. Laprévote, and S. De La Porte, *MALDI reveals membrane lipid profile reversion in MDX mice.* Neurobiology of Disease, 2009. 36(2): p. 252-258.

261. Deininger, S.r.-O., M.P. Ebert, A. FuÌˆtterer, M. Gerhard, and C. RoÌˆcken, *MALDI Imaging Combined with Hierarchical Clustering as a New Tool for the Interpretation of Complex Human Cancers.* Journal of Proteome Research, 2008. 7(12): p. 5230-5236.

262. Fuchsberger, C., K. Kofler, M. Hammerer, W. Wieder, S. Ongarello, I. Feuerstein, G.K. Bonn, G. Bartsch, A.E. Pelzer, and H. Klocker, *IMAGING OF PROSTATE TISSUE SECTIONS BY MALDI PROTEIN MASS SPECTROMETRY - TISVIS, A TOOL FOR THE VISUAL DATA PROCESSING.* The Journal of Urology, 2008. 179(4, Supplement 1): p. 389-390.

263. Rohner, T.C., D. Staab, and M. Stoeckli, *MALDI mass spectrometric imaging of biological tissue sections.* Mechanisms of Ageing and Development, 2005. 126(1): p. 177-185.

264. Schwartz, S.A., R.M. Caprioli, V. Károly, T. András, and V. Akos, *Molecular imaging by mass spectrometry*, in *Medical Applications of Mass Spectrometry*. 2008, Elsevier: Amsterdam. p. 533-554.

265. Buesa, R.J., *Histology without formalin?* Annals of Diagnostic Pathology, 2008. 12(6): p. 387-396.

266. Moreau, A., T. Le Neel, M. Joubert, A. Truchaud, and C. Laboisse, *Approach to automation in immunohistochemistry.* Clinica Chimica Acta, 1998. 278(2): p. 177-184.

267. Shi, S.-R., R.J. Cote, and C.R. Taylor, *Antigen Retrieval Immunohistochemistry: Past, Present, and Future.* J. Histochem. Cytochem., 1997. 45(3): p. 327-344.

268. Shi, S.-R., C. Liu, B.M. Balgley, C. Lee, and C.R. Taylor, *Protein Extraction from Formalin-fixed, Paraffin-embedded Tissue Sections: Quality Evaluation by Mass Spectrometry.* J. Histochem. Cytochem., 2006. 54(6): p. 739-743.

269. Werner, M., A. Chott, A. Fabiano, and H. Battifora, *Effect of Formalin Tissue Fixation and Processing on Immunohistochemistry.* The American Journal of Surgical Pathology, 2000.

Volume 24(7): p. 1016-1019.

270. Ramos-Vara, J.A., *Technical Aspects of Immunohistochemistry.* Veterinary Pathology Online, 2005. 42(4): p. 405-426.

271. Lemaire, R., A. Desmons, J.C. Tabet, R. Day, M. Salzet, and I. Fournier, *Direct Analysis and MALDI Imaging of Formalin-Fixed, Paraffin-Embedded Tissue Sections.* Journal of Proteome Research, 2007. 6(4): p. 1295-1305.

272. Yutaka AOKI, Atsuhiko TOYAMA, Takashi SHIMADA, Tetsuyoshi SUGITA, Chikage AOKI, Yukari UMINO, Atsushi SUZUKI, Daisuke AOKI, Yataro DAIGO, Y. NAKAMURA, and T.-A. SAT, *A novel method for analyzing*

formalin-fixed paraffin embedded (FFPE) tissue sections by mass spectrometry imaging. Proceedings of the Japan Academy, Series B, 2007. 83(7): p. 205-214.

273. Chaurand, P., S.A. Schwartz, D. Billheimer, B.J. Xu, A. Crecelius, and R.M. Caprioli, *Integrating Histology and Imaging Mass Spectrometry.* Analytical Chemistry, 2004. 76(4): p. 1145-1155.

274. Rujol, M., R. Estrada, and M.C. Yappert, *In Situ MALDI-TOF MS Regional Analysis of Neutral Phospholipid in Lens Tissue.* Analystical Chemistry, 2004. 76: p. 1657-1663.

275. Chen, Y., J. Allegood, Y. Liu, E. Wang, B. Cachon-Gonzalez, T.M. Cox, A.H. Merrill, and M.C. Sullards, *Imaging MALDI Mass Spectrometry Using an Oscillating Capillary Nebulizer Matrix Coating System and Its Application to Analysis of Lipids in Brain from a Mouse Model of Tayâ^'Sachs/Sandhoff Disease.* Analytical Chemistry, 2008. 80(8): p. 2780-2788.

276. Jackson, S.N., H.-Y.J. Wang, A.S. Woods, M. Ugarov, T. Egan, and J.A. Schultz, *Direct tissue analysis of phospholipids in rat brain using MALDI-TOFMS and MALDI-ion mobility-TOFMS.* Journal of the American Society for Mass Spectrometry, 2005. 16(2): p. 133-138.

277. Jaskolla, T., B. Fuchs, M. Karas, and J. Schiller, *The New Matrix 4-Chloro-[alpha]-Cyanocinnamic Acid Allows the Detection of Phosphatidylethanolamine Chloramines by MALDI-TOF Mass Spectrometry.* Journal of the American Society for Mass Spectrometry, 2009. 20(5): p. 867-874.

278. Mikawa, S., M. Suzuki, C. Fujimoto, and K. Sato, *Imaging of phosphatidylcholines in the adult rat brain using MALDI-TOF MS.* Neuroscience Letters, 2009. 451(1): p. 45-49.

279. Al-Saad, K.A., W.F. Siems, H.H. Hill, V. Zabrouskov, and N.R. Knowles, *Structural analysis of phosphatidylcholines by post-source decay matrix-assisted laser desorption/ionization time-of-flight mass spectrometry.* Journal of the American Society for Mass Spectrometry, 2003. 14(4): p. 373-382.

280. Brosch, R., S.V. Gordon, M. Marmiesse, P. Brodin, C. Buchrieser, K. Eiglmeier, T. Garnier, C. Gutierrez, G. Hewinson, K. Kremer, L.M. Parsons, A.S. Pym, S. Samper, D. van Soolingen, and S.T. Cole, *A new evolutionary scenario for the Mycobacterium tuberculosis complex.* Proceedings of the National Academy of Sciences, 2002. 99(6): p. 3684-3689.

281. Milián-Suazo, F., L. Pérez-Guerrero, C. Arriaga-Díaz, and M. Escartín-Chávez, *Molecular epidemiology of human cases of tuberculosis by Mycobacterium bovis in Mexico.* Preventive Veterinary Medicine, 2010. 97(1): p. 37-44.

282. Ricardo, d.l.R.-D., *Human Mycobacterium bovis infection in the United Kingdom: Incidence, risks, control measures and review of the zoonotic aspects of bovine tuberculosis.* Tuberculosis, 2006. 86(2): p. 77-109.

283. Hope, J.C. and B. Villarreal-Ramos, *Bovine TB and the development of new vaccines.* Comparative Immunology, Microbiology and Infectious Diseases, 2008. 31(2-3): p. 77-100.

284. http://archive.defra.gov.uk/foodfarm/farmanimal/diseases/atoz/tb/documents/expenditure-stats.pdf.

285. Chen, J.M., S.T. Islam, H. Ren, and J. Liu, *Differential productions of lipid virulence factors among BCG vaccine strains and implications on BCG safety.* Vaccine, 2007. 25(48): p. 8114-8122.

286. Rehren, G., S. Walters, P. Fontan, I. Smith, and A.M. Zárraga, *Differential gene expression between Mycobacterium bovis and Mycobacterium tuberculosis.* Tuberculosis, 2007. 87(4): p. 347-359.

287. Andersen, C.S., E.M. Agger, I. Rosenkrands, J.M. Gomes, V. Bhowruth, K.J.C. Gibson, R.V. Petersen, D.E. Minnikin, G.S. Besra, and P. Andersen, *A Simple Mycobacterial Monomycolated Glycerol Lipid Has Potent Immunostimulatory Activity.* The Journal of Immunology, 2009. 182(1): p. 424-432.

288. Picariello, G., R. Sacchi, and F. Addeo, *One-step characterization of triacylglycerols from animal fat by MALDI-TOF MS.* European Journal of Lipid Science and Technology, 2007. 109(5): p. 511-524.

289. Stadthagen, G., J. Korduláková, R. Griffin, P. Constant, I. Bottová, N. Barilone, B. Gicquel, M. Daffé, and M. Jackson, *p-Hydroxybenzoic Acid Synthesis in Mycobacterium tuberculosis.* Journal of Biological Chemistry, 2005. 280(49): p. 40699-40706.

290. Hattan, S.J., J. Marchese, M. Albertinetti, S. Krishnan, N. Khainovski, and P. Juhasz, *Effect of solvent composition on signal intensity in liquid chromatography-matrix-assisted laser desorption ionization experiments.* Journal of Chromatography A, 2004. 1053(1-2): p. 291-297.

291. Sun, G., K. Yang, Z. Zhao, S. Guan, X. Han, and R.W. Gross, *Matrix-Assisted Laser Desorption/Ionization Time-of-Flight Mass Spectrometric Analysis of Cellular Glycerophospholipids Enabled by Multiplexed Solvent Dependent Analyte−Matrix Interactions.* Analytical chemistry, 2008. 80(19): p. 7576-7585.

292. Barry III, C.E., R.E. Lee, K. Mdluli, A.E. Sampson, B.G. Schroeder, R.A. Slayden, and Y. Yuan, *Mycolic acids: structure, biosynthesis and physiological functions.* Progress in Lipid Research, 1998. 37(2-3): p. 143-179.

293. Yalcin, T., Y. Dai, and L. Li, *Matrix-assisted laser desorption/ionization time-of-flight mass spectrometry for polymer analysis: solvent effect in sample preparation.* Journal of the American Society for Mass Spectrometry, 1998. 9(12): p. 1303-1310.

294. Hotter, G.S. and D.M. Collins, *Mycobacterium bovis lipids: Virulence and vaccines.* Veterinary Microbiology, 2011. 151(1-2): p. 91-98.

295. Andersen, C.A.S., I. Rosenkrands, A.W. Olsen, P. Nordly, D. Christensen, R. Lang, C. Kirschning, J.M. Gomes, V. Bhowruth, D.E. Minnikin, G.S. Besra, F. Follmann, P. Andersen, and E.M. Agger, *Novel Generation Mycobacterial Adjuvant Based on Liposome-Encapsulated Monomycoloyl Glycerol from Mycobacterium bovis Bacillus Calmette-Guérin.* The Journal of Immunology, 2009. 183(4): p. 2294-2302.

296. Belley, A., D. Alexander, T. Di Pietrantonio, M. Girard, J. Jones, E. Schurr, J. Liu, D.R. Sherman, and M.A. Behr, *Impact of methoxymycolic acid production by mycobacterium bovis BCG Vaccines.* Infection and Immunity, 2004. 72(5): p. 2803-2809.